Inkjet Printing of Cadmium-Free Quantum Dots-Based Electroluminescent Devices

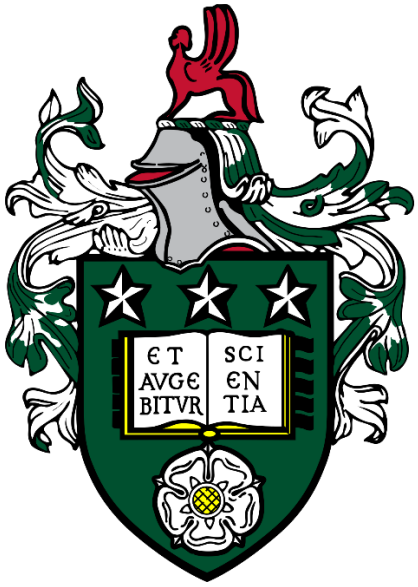

Min Fu

University of Leeds

School of Physics and Astronomy

January 2025

Submitted in accordance with the requirements for the degree of Doctor of Philosophy

Declaration

The candidate confirms that the work submitted is his own and that appropriate credit has been given where reference has been made to the work of others. This copy has been supplied on the understanding that it is copyright material and that no quotation from the thesis may be published without proper acknowledgment. In some parts of the thesis, figures have been reproduced from publications with permission from the copyright holder.

The partial work in chapters 1, 3, and 4 of this thesis has appeared in publication as follows:

Fu, M., Critchley, K. Inkjet printing of heavy-metal-free quantum dots-based devices: a review. *Nanotechnology* **2024**, 35, 302002.

Fu, M., Santaella J., Evans S., Critchley, K. Inkjet printing of cadmium-free quantum dots-based electroluminescent devices, *ACS Appl. Mater. & Interfaces*, **2025**, 17, 22952

The work discussed in Chapter 5 of this thesis has appeared in the paper under preparation for publication:

Min Fu, Stephen Evans, Kevin Critchley. Studying photoluminescence degradation of InP/$ZnSe_xS_{1-x}$/ZnS quantum dot films.

MF was responsible for the preparation, characterization, and enhancement of InP quantum dot films, data analysis, and draft preparation. In Chapter 5, all near ambient pressure X-ray photoelectron spectroscopy data was collected by Dr. Liam Dwyer and analyzed by MF. The contribution of the other authors involved data discussion and assisting with proofreading.

The right of Min Fu to be identified as the Author of this work has been asserted by him in accordance with the Copyright, Designs and Patents Act 1988.

Acknowledgments

I would like to thank my main supervisor, Dr. Kevin Critchley, for his constant support, assistance, advice, and encouragement over the last four years. I would also like to thank Prof. Stephen Evans for his less frequent but equally invaluable advice.

I gratefully acknowledge the CSC and the University of Leeds for funding this research project and sponsoring me to study at Leeds. My gratitude goes to Dr. Zabeada Aslam of Leeds Electron Microscopy and Spectroscopy Centre for her support & assistance in TEM characterization. Dr. Alex Walton and Dr. Liam Dwyer at the University of Manchester deserve huge thanks for the NAP-XPS measurement. I thank Dr. Ben Johnson for the instrumental designs and all the arrangements. Dr. Dan Baker and Dr. Andrew Hobson deserve enormous credit for letting me use their laboratories.

Many thanks to Joel Whipp for training me in the synthesis of QDs and helping me move house. I thank Matthew Huges for helping me with rheology experiments. I would like to mention Prof. Richard Bushby for helping set up the Schlenk line and sharing his little things. Thanks to Christa Brown for training me on the optical microscope and ImageJ. I thank Richard Oliver for his craft and electronic designs. Except for academic contributions, my gratitude also goes to the rest of the MNP group members for their continuing encouragement, entertainment, and company. I thank Nizzy James for helping me with inkjet printing and the exchange of instrumental time slots. Xinhui Lan is inheriting lots of my consumables and QD messes and has helped me with purchasing orders.

Lastly, I would like to thank my family who always support and encourage me. Big thanks to my friends Yunhao Liang and Sunjie Ye who are always there for me and taught me many life skills in the UK, and I really enjoyed all the trips with you. Qi Chen inherited many of my kitchen messes during my last move. Thanks to Youxing Zhang and Jihai Zhong for letting me stay in their house during the gap in my accommodation contracts. I thank Jianting Feng and Chao Sun for their banters and company. I acknowledge the use of ChatGPT-3.5 (Open AI, https://chat.openai.com/) and Grammarly to proofread my draft.

Abstract

InP quantum dots (QDs) have excellent optoelectronic properties and less toxicity than Cd-based QDs, making them excellent candidates for QD-based light-emitting diodes (QD-LEDs). Inkjet printing (IJP) is a promising technology to substitute the spin coating method for assembling lower-cost and high-resolution QD-LEDs. However, IJP faces the challenge of the coffee ring effect (CRE). To address this, we combined the solutal and thermal Marangoni effects by employing a binary solvent system (cyclohexylbenzene and decane) and heating the substrate during printing. The thermal Marangoni effect, which has been underexplored in previous studies of inkjet-printed QD-LEDs, is a focal point of this work. Uniform patterns were obtained with a volume ratio of 20% decane and a substrate temperature (T_{sub}) of 60 °C. The evaporation of the solvents from QD ink droplets behaved differently at different T_{sub}, i.e., stick jump mode at 20 °C and 40 °C, and stick slide mode at 60 °C. Consequently, the inkjet-printed InP QD-LEDs without the CRE were successfully assembled. Furthermore, increasing the electron transport layer thickness reduced trap density when it was exposed to the air and prevented the deterioration of the QD layer from water vapor and oxygen exposure. This is likely due to the decrease in oxygen vacancies in the ETL, mitigating the defect-dependent exciton quenching at the ETL/QD interface.

Although InP/$ZnSe_xS_{1-x}$/ZnS QDs show a big potential in state-of-the-art electroluminescent devices, they remain vulnerable to air, leading to PL quenching over time. Most degradation studies of InP QDs have focused on InP/$ZnSe_xS_{1-x}$/ZnS QD dispersion rather than QD films. The impact of oxygen, moisture, and heat on PL quenching and the chemical state changes in InP/$ZnSe_xS_{1-x}$/ZnS QD films are less understood. Additionally, IJP is typically an open-air fabrication process. In this work, we investigated the PL quenching of InP/$ZnSe_xS_{1-x}$/ZnS QD films by varying their thicknesses, humidity levels, and temperature. The PL quenching rate slowed under higher relative humidity due to the photoinduced fluorescence enhancement effect. Increasing QD films' thickness from 19 nm to 100 nm extended the PL decay half-life ($\tau_{1/2}$) by 5.6 times. Heating above 100 °C under vacuum (1 mbar) significantly reduced the $\tau_{1/2}$ due to the formation of trap states from strain misfit and increased atomic mobility. Chemical state changes in QD films by oxygen and moisture have been identified by in-situ near-ambient atmosphere X-ray photoelectron spectroscopy. For example, several oxidation species, including In_2O_3, $InPO_x$, ZnO, SeO_2, and SO_x^-, were detected. To improve the air stability of QD films, a 47-nm-thick layer of polymethyl

methacrylate (PMMA) was applied, dramatically increasing the $\tau_{1/2}$ by 12 times compared to QD films without the PMMA barrier.

Table of Contents

List of Abbreviations and Symbols

QDs – Quantum dots

CQDs – Colloidal quantum dots

NCs – Nanocrystals

NPs – Nanoparticles

HM – Heavy-metal

HMF – Heavy-metal-free

LFP – Lead-free perovskite

PQDs – Perovskite QDs

QCE – Quantum confinement effect

FWHM - Full width at half maximum

QD-LEDs – Quantum dots-based light-emitting diodes

OLEDs – Organic light-emitting diodes

LCDs – Liquid crystal displays

PL – Photoluminescence/photoluminescent

TRPL – Time-resolved photoluminescence

EL – Electroluminescence/electroluminescent

EQE – External quantum efficiency

SCLC – Space charge limited conduction

PLQY – Photoluminescence quantum yield

CB – Conduct band

CBM – Conduct band minimum

VB – Valance band

VBM – Valance band maximum

HOMO – Highest occupied molecular orbit

LUMO – Lowest unoccupied molecular orbit

AR – Auger recombination

FRET – Förster resonance energy transfer

FIQ – Field-induced quenching

IJP – Inkjet print/printing

SC – Spin coat/coating

DOD – Drop-on-demand

DS – Drop spacing

CRE – Coffee ring effect

ME – Marangoni effect

CE – Capillary effect

CA – Contact angle

CAM – Constant angle mode

CRM – Constant radius mode

ST – Surface tension

BP – Boiling point

RH – Relative humidity

RPM – Rotates per minute

RCF – Relative centrifugal force

HIL – Hole injection layer

HTL – Hole transport layer

ETL – Electron transport layer

NAP-XPS – Near ambient pressure X-ray photoelectron spectroscopy

BE – Binding energy

UV-Vis-NIR – Ultra-violet/visible/near-Infra-red

AFM – Atomic force microscopy

TEM – Transmission electron microscopy

EDS – Energy dispersive X-ray spectroscopy

SAED – Selected area electron diffraction

SE – Spectroscopic ellipsometry

PI – Photoinitiator

ITO – Indium tin oxide

CHB – Cyclohexylbenzene

COB – Chlorobenzene

TFB – Poly(9,9-dioctylfluorene-co-N-(4butylphenyl)diphenylamine)

PVK – Poly(9-vinylcarbazole)

PEDOT:PSS – Poly(ethylenedioxythiophene): polystyrenesulfonate

CBP – 4,4′-bis(carbazol-9-yl)biphenyl

TPBi – 1,3,5-tri(phenyl-2-benzimidazolyl)-benzene

TCTA – 4,4′,4″-Tris(carbazol-9-yl)triphenylamine

FLTA-V – 4,4′-(9,9-dimethyl-9H-fluorene-2,7-diyl)bis(N-phenylN-(4-vinylphenyl)aniline)

S – Sulphur

Se – Selenium

Al – Aluminium

Cd – Cadmium

$InCl_3$ – Indium chloride

$ZnCl_2$ – Zinc chloride

DMAP – Tris(dimethylamino)phosphine

$Zn(acet)_2$ – Zinc acetate

$Zn(St)_2$ – Zinc stearate

TOP – Trioctylphosphine

ODE – Octadecane

IPA – Isopropyl alcohol

N_2 – Nitrogen

TMAH – Tetramethylammonium hydroxide

EA – Ethanolamine

DMSO – Dimethyl sulfoxide

PMMA – Polymethyl methacrylate

PEN – Polyethylene naphthalate

DOE – Dodecane

CHB – Cyclohexylbenzene

DE – Decalin

NPT – Naphthane

TD – N-Tridecane

NN – Nonane

CHX – Cyclohexane

oDCB – Orthodichlorobenzene

NMP – N-Methyl-2-pyrrolidone

BTA – N-butylamine

λ_{em} – EL peak

V_{on} – Turn-on voltage

L_m – Maximum luminance

T_{sub} – Substrate temperature

List of Figures

List of Tables

1. Introduction

1.1 Motivation

This work aimed to inkjet print InP quantum dots (QDs)-based light-emitting diodes (QD-LEDs) which are regarded as the promising next-generation display technology. QDs are promising fluorescent semiconductor nanoparticles (NPs) and are capable of emitting high-purity colors from visible to near-infrared by tuning their sizes [1]. The past three decades have witnessed the development of various colloidal QDs, especially the heavy-metal (HM) QDs. However, heavy metals such as cadmium and lead pose serious risks to human health and the environment [2], making the synthesis process hazardous and environmentally unfriendly. The Restriction of Hazardous Substances directive in the European Union has limited the use of cadmium and lead in consumer electronics since 2011 [3]. This restricts their application in wearable devices and biomedical imaging [1]. Hence, researchers have turned their attention to developing heavy-metal-free (HMF) QDs, including II-VI QDs (ZnO, ZnS, ZnSe, and ZnTe) [4], III-V QDs (III = In, Ga, Al; V = N, P, Sb) [5], I-III-VI QDs (I = Cu, Ag; III = In, Al, Ga; VI = S, Te, Se) [6], lead-free perovskite QDs (LFP QDs) [7], carbon-based QDs (CQDs) [8] and graphene QDs [9], silicon QDs (SiQDs) [10].

As a member of HMF QDs, state-of-the-art InP QDs have high photoluminescence (PL) quantum yield (PLQY, near 100%), wide tuneable emission wavelength (from blue to near-infrared), narrow full width at half maximum (FWHM, < 40 nm), and similar synthesis methods to Cd-based QDs [11]. Compared with CdSe QDs, InP QDs have a slightly smaller bulk band gap (1.34 eV vs 1.74 eV), much larger exciton Bohr radius (10 nm vs 3 nm), and reduced toxicity, showing great potential for wider technological use, for example, QD-LEDs [12]. Therefore, InP QDs are a good candidate to replace toxic Cd-based QDs to be applied in state-of-the-art QD-LEDs. State-of-the-art display technologies include liquid crystal diodes (LCDs), organic LEDs (OLEDs), and QD-LEDs [13]. The use of color filters in LCDs limits their color gamut, and the need for a backlight makes them have a thicker form. OLEDs are susceptible to burn-in over time due to organic material degradation. QD-LEDs have higher color accuracy, faster response time, and lower power consumption than LCDs and OLEDs due to the advantages of QDs mentioned above [13]. Therefore, QD-LEDs are beneficial for high-end televisions/monitors and augmented/virtual reality. Apart from QD-LEDs, QDs can be also used in humidity sensors [14], UV shields [15], synaptic transistors [16], photodetectors (PDs) [17], anti-counterfeiting tags [18], color conversion layers [19], photovoltaic cells (PVCs) [20].

Yet, manufacturing high-resolution, large-scale, and low-cost QD-LEDs remains challenging. Spin coating (SC) is a widely used solution-processed method because it is well-established for lithographic techniques and enables the wet deposition of smooth and uniform thin films rapidly [21]. However, SC has the disadvantage that the majority of the material being coated is lost as waste. Vacuum evaporation is commonly used to manufacture large-scale organic LEDs, but some colloidal QDs cannot be sublimated or evaporated [22]. The remaining materials deposited on the mask are wasted, and this method must be performed under high-vacuum conditions. Lithography can precisely pattern high-resolution QD pixels through selective illumination [23]. However, exposure to UV light and the use of harsh chemicals during the process can degrade the optical properties of the QDs. In contrast, inkjet printing (IJP) technology uses fewer materials, creates patterns without masks, and achieves high resolution, making it a promising candidate for industrial QD-LED assembly [24]. Despite its advantages, IJP is challenged by the coffee ring effect (CRE), where capillary flow, driven by a faster evaporation rate at the droplet's edge, causes liquid from the interior to move outward [25]. This movement transports solutes to the fixed contact line, forming a ring of deposited material at the contact line. This challenge is general for inkjet printing most materials.

Several methods have been proposed to mitigate the CRE, including enhancing the Marangoni effect (ME) [26], engineering the substrate surface with two-dimensional or three-dimensional structures [27], and electrowetting [28]. ME involves the transport of solvents from regions of lower surface tension to those with higher surface tension and therefore will transport solutes from the edge back into the interior of the droplet. There are two types of Marangoni flows. One is the concentration-driven Marangoni flow achieved by introducing an additional solvent or surfactant [29]. For a binary solvent system, as the droplet evaporates, a difference in surface tension between the edge and the center generates an inward Marangoni flow, balancing the outward capillary flow. The second type of Marangoni flow, which is thermally driven and exhibits a circulating motion, is less studied in previous reports. The initial flow direction depends on the thermal conductivity ratio ($K_R = K_s/K_l$) between the substrate (K_s) and the liquid (K_l) [30]. If K_R is greater than 2, indicating an efficient conductor substrate, heat transfers from the contact line to the droplet center because it is warmest at the contact line. Conversely, when K_R is less than 1.45, the flow reverses due to the highest evaporation rate at the contact line, and the droplet temperature cannot be maintained without sufficient energy. For $1.45 < K_R < 2$, the Marangoni flow direction depends on the critical contact angle. To balance the capillary flow with the Marangoni flow, it is

crucial to optimize the ink formulation, particularly the selection of solvents based on their rheological properties, boiling points, thermal conductivity, and compatibility.

Currently, most inkjet-printed QD-LEDs are based on CdSe QDs and Pb-based perovskite QDs, with a record EQE of 23.1% and 14.3%, respectively [31, 32]. The inkjet-printed red, green, and blue InP QD-LEDs have only appeared in the past three years, achieving the highest EQE of 8.1%, 0.7%, and 0.15%, respectively [33-35], which are much lower than that of spin-coated analogs, i.e., 23.5% [36], 26.7% [37], and 2.6% [38]. This results from the increased vulnerability of In and P to air and the difference in energy band alignments [39]. The higher covalency of InP has hindered synthetic advancements, as it requires highly reactive precursors for lattice formation, making the resulting nanocrystals more susceptible to lattice defects. Therefore, shell engineering and optimizing the QD ink formulation and device structure have been proposed to enhance the electrical performance of inkjet-printed InP QD-LEDs [33-35]. Additionally, it was reported that the electrical performance of QD-LEDs deteriorates when the electron transport layer (ETL, $Zn_{1-x}Mg_xO$) is exposed to air [40]. This may be attributed to the increase of trap density (density of carriers occupying trap states) in the ETL, especially oxygen vacancies, resulting in exciton quenching at the QD/ETL interface [41].

QDs can reportedly degrade due to water, oxygen, UV irradiation, and heat, which lead to the formation of trap states [42-45]. This physical and, or, chemical adsorption of oxygen and water can greatly affect the overall behavior of QDs, resulting in photoactivation [42], photooxidation [44], and photocorrosion [45]. In and P are easily oxidized, forming In_2O_3 and $InPO_x$, which degrades their PL properties quickly under ambient atmosphere, thus restricting their practical applications [46, 47]. A ZnS shell coating effectively alleviates the PL degradation because of the physical barrier it provides as well as a large bandgap which gives strong exciton confinement [48, 49]. Yet, the large lattice strain between InP and ZnS (7.6%) causes anomalous interfacial reconstruction and surface defects, limiting its ability to passivate trap states at the interface between the core and the shell. Introducing an alloyed $ZnSe_{1-x}S_x$ middle shell can further reduce the misfit strain to below 3.4% and promote the PLQY to beyond 90% [50, 51]. Despite these improvements, the PL of core-shell InP/$ZnSe_{1-x}S_x$/ZnS QDs can still be quenched in ambient conditions, with the shell passivation only delaying this process [52].

IJP typically takes place in ambient conditions, while thermal evaporation of electrodes

subjects them to heat, which degrades the PL performance of QDs [35]. As the emissive layer in QD-LEDs, the stability of the QD layer significantly affects the device's electrical performance, including external quantum efficiency (EQE), lifetime, and luminance [53]. Furthermore, the operating temperature of QD-LEDs rises under high voltage conditions, leading to efficiency roll-off in the devices [54]. Although the oxidation of InP QDs during synthesis and the thermal stability of InP QD dispersions have been studied [47, 55], the stability of InP/$ZnSe_xS_{1-x}$/ZnS QD films, particularly the effects of moisture, oxygen, and heat on degradation, remains underexplored. QD films, being densely packed solids with an exposed surface, differ from QD dispersions, which are protected by a solvent.

1.2 Inkjet Printing Technology

IJP has become a promising technology to replace the commonly used SC method, lithography, and thermal evaporation for assembling QD-LEDs. Selecting proper ink solvents is important to formulate printable inks for IJP.

1.2.1 Basics of IJP

IJP technology has been under development for over 50 years. The advantages over other thin film deposition techniques such as SC [56], lithography [57], and vacuum evaporation [58] include low material waste, high lateral resolution (10-50 μm), mask-free operation, and flexible designability [59], thereby showcasing its significant potential for the industry. SC is the simplest solution-based method for preparing thin films; however, it results in significant material waste and struggles to produce high-resolution patterns. Vacuum evaporation is commonly used to manufacture large-scale OLEDs, but some colloidal QDs (CQDs) cannot be sublimated or evaporated [22]. The remaining materials deposited on the mask are wasted, and this method must be performed under high-vacuum conditions. Lithography can precisely pattern high-resolution QD pixels through selective illumination [23]. However, exposure to UV light and the use of harsh chemicals during the process can degrade the optical properties of the QDs.

IJP operates by expelling micro-sized inks from μm-sized nozzles onto a designated substrate under computer control [60]. Upon droplet evaporation through heating, distinct patterns are formed. IJP has two standard ejection modes: continuous and drop-on-demand (DOD) modes. DOD printing emits ink through the nozzle to form a

short jet that condenses into a droplet only when required for printing (Figure 1a). The DOD mode, favored for its lower cost and higher ink utilization ratio, prevails over the continuous mode. Ink droplets are managed using either a piezoelectric transducer or a thermal resistor. However, the nozzle size limits the lateral printing resolution (> 10 μm), and IJP instruments struggle to handle highly viscous inks (> 30 mPa s). Electrohydrodynamic jet printing relies on the electric field generated between the substrate and the inkjet nozzle, making the use of a conductive substrate essential [61, 62]. The applied electric field shapes the ink meniscus into a Taylor cone, allowing for the creation of patterns at the submicrometer scale with high precision. Although IJP does not claim the top spot among printing methods such as screen printing [63], offset printing [64], and gravure printing [65], it strikes a favorable balance between high resolution and printing speed.

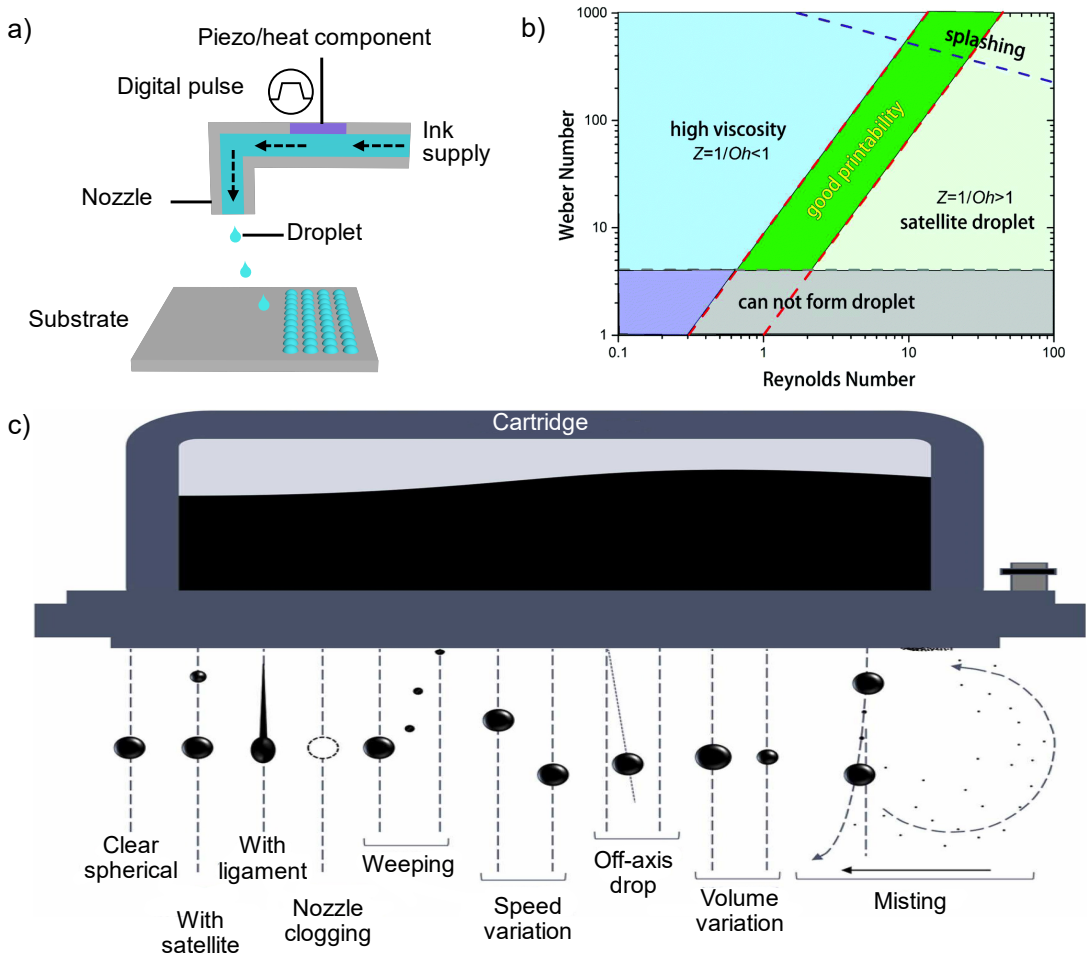

Figure 1. a) A schematic diagram of IJP. b) The printability of the ink expressed by Reynolds and Weber numbers. Reprinted with permission from [66]. Copyright 2017 RSC. c) Possible behavior of ejected droplets from cartridge nozzles. Reprinted with permission from [67]. Copyright 2023 Elsevier.

1.2.2 Printability of QD Inks

Optimizing ink formulation is crucial for ensuring good printability before printing. Key factors affecting ink formulation include viscosity, surface tension (ST), suspended particle size, solute concentration, substrate wettability, and solvent properties [68]. The particle size in the ink should ideally be smaller than 1/100th of the nozzle size. Low viscosity and ST often result in the generation of satellite droplets, while high viscosity and ST can lead to nozzle clogging or lack of control over droplet formation. In general, printability can be assessed by the Ohnesorge number *Oh* or *Z*-number [69],

$$Oh = Z^{-1} = \frac{\eta}{\sqrt{\rho\gamma a}} = \frac{\sqrt{W_e}}{R_e} \quad (1)$$

Where η, ρ, γ, a, and v represent the viscosity (mPa s), density (g mL^{-1}), ST (mN m^{-1}) of the ink, the nozzle diameter (μm), and the droplet velocity (m s^{-1}), respectively. The Weber number (W_e) and the Reynolds number (R_e) are defined by,

$$W_e = \frac{v^2 a\rho}{\gamma} \quad (2)$$

And

$$R_e = \frac{va\rho}{\eta} \quad (3)$$

Figure 1b illustrates the correlation between printability and the associated numerical values, with the optimal *Z* value falling within the range of 1 to 14 [70, 71]. At low values of *Z*, the viscosity dominates, damping the actuating pulse. At higher values of *Z*, the ST dominates, which can cause satellites. This condition is sufficient but not strictly necessary. The *Z* number describes only the ratio of inertial and ST forces to viscosity, without accounting for changes in the actuating signal (i.e., voltage). Given that energy is required to move an object or droplet, this limitation reduces *Z*'s reliability as a predictor of printability.

1.2.3 Optimisation of QD Inks

Regarding solvent selection, specific requirements must be met. Firstly, solvents should allow QDs to form a stable dispersion without compromising their PLQY [72].

In some cases, longer ligands are replaced by shorter ones for faster carrier transportation in QD-LEDs [73], influencing solvent selection. Secondly, solvents should not damage the inner printer cartridge, making some specific organic solvents unsuitable. Thirdly, these solvents should have low volatility and a high boiling point (BP, ideally > 100 °C) to avoid risks of nozzle blockage. Fourthly, solvent viscosity and ST should fall within appropriate ranges to achieve a favourable *Z* value and avoid the generation of undesirable droplet behaviour such as satellites, weeping, off-axis droplets, etc. (Figure 1c) [74]. Additionally, compatibility with the substrate or the pre-deposited layer on the substrate is essential [75, 76]. Table 1 shows the physical properties and printability of some reported QD inks. Most ink solvent systems include two or more solvents, the QD loading is between 15 and 40 mg mL^{-1}, and the density of QDs is close to 1 g cm^{-3}. Sometimes, a small amount of polymer is added to adjust the ink's viscosity and ST, which also impacts the CRE [77, 78]. Moreover, the substrate's surface energy should surpass that of the ink's ST, resulting in a low contact angle (<< 90°), which facilitates the spreading of ink droplets and droplets drying after depositing on the substrate.

Table 1. A summary of the physical properties and printability of different QD ink formulations.

QDs	Solvents	Volume ratio	QD loading (mg mL^{-1})	ρ (g cm^{-3})	η (mPa s)	γ (mN m^{-1})	Nozzle dia. (μm)	*Z* value	Ref.
InP	Hexane/octane	19/1	15	0.7	2.2	30.5	21	9.7	[35]
InP	Octane/DOE	5/5	20	-	0.90	23.2	30	-	[33]
InP	CHX/octane	5/5	2.5 wt%	-	-	22.8	12	-	[74]
CdSe	CHB/decane	9/1	-	-	2.35	32.8	30	-	[72]
CdSe	CHB/oDCB	8/2	30	-	2.45	31.77	20	-	[79]
CdSe	CHB/Indane	9/1	15	0.78	1.64	28.0	-	12.7	[75]
CdSe	DE/TD	7/3	-	0.82	1.59*	27.33*	20	13.3	[76]
$CsPbX_3$	NPT/TD/NN	7/2/2	20	0.76	1.57	24.67	21	12.3	[26]
$CsPbBr_3$	DOE/TOL	6/4	15	-	0.9	24.61	80	-	[80]
PbS	NMP/BTA	99/1, w	-	1.11	1.38	28.16	21	18.56	[81]

η and *γ* were tested at room temperature (RT, values indicated by * were measured at 35 °C). w means weight ratio.

To ensure the formation of single droplets without satellites, various printing factors, such as jetting waveform, firing frequency, and voltage, need examination. Drop ejection, triggered by the electrical signal controlled by the jetting waveform with

multiple segments, can be optimized by adjusting the amplitude and duration of each segment. For less viscose ink, a low firing frequency and voltage are set, resulting in a lower drop velocity and smaller volume. Drop spacing (DS), the center distance between neighboring droplets, affects printed pattern behavior [82]. Furthermore, substrate temperature is a crucial factor affecting the uniformity and morphology of the resultant pattern [83], which will be discussed in the following section.

1.3 QD Droplet Drying

For small droplets of binary solvents, two main physical effects are the capillary effect [84] and the Marangoni effect [85] which drive the flow of material within the droplet during the evaporation process.

1.3.1 Capillary Effect

The capillary effect (CE) is a phenomenon, first described by Thomas Young and Laplace – to form the Young-Laplace equation [84]. In the CE, the liquid moves within narrow spaces due to the balance between cohesive forces within the liquid and adhesive forces between the liquid and a surface. In the context of droplets, the CE can cause liquid within the droplet to move toward the edges where the droplet's surface meets the substrate. This effect is driven primarily by ST, which can pull liquid outward as the droplet loses moisture.

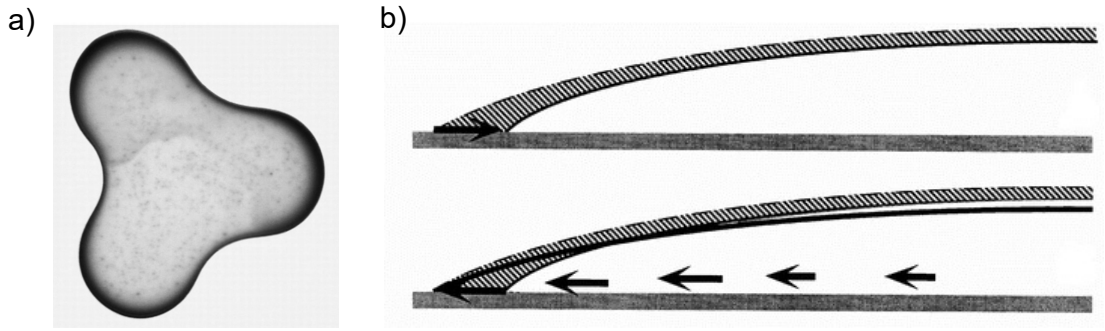

Figure 2. a) A 2-cm-diameter drop of coffee with 1% solids by weight dried to form a perimeter ring. b) Cross-section view of droplet evaporation. The contact line recedes without outward compensating flow while fixed with the capillary flow. Reprinted with permission from [25]. Copyright 1997 Nature Springer.

When a small droplet dries on a surface, the CE leads to an interesting pattern of evaporation. As the solvent within the droplet begins to evaporate, the contact line (the edge where the droplet meets the surface) often becomes fixed, especially if the

droplet is pinned to the surface. Because evaporation occurs faster at the droplet's edge than at the center, the liquid is continually drawn outward to compensate for the loss at the perimeter. This outward flow transports suspended particles to the edge, where they accumulate, eventually forming a ring-like deposit, coined the CRE by Deegan et al. [25] (Figure 2). This phenomenon has been observed in drying different solvents (e.g. water, acetone, and ethanol) on many substrates such as glass, metal, and polymer films [86]. The CRE requires two conditions: a pinned contact line and evaporation at the contact line. If either condition is unmet, particle deposits may form patterns other than rings.

1.3.2 Marangoni Effect

The Marangoni effect was first reported by Carlo Marangoni in his doctoral thesis in 1865, titled "*On the expansion of a drop of liquid floating on the surface of another liquid* [85]." The effect involves transporting solvents from regions of lower ST to those with higher ST. There are two types of Marangoni flows. The first is the concentration-driven Marangoni flow, achieved by introducing an additional solvent [29, 79] or surfactant [78, 87], such as a binary solvent system. As the low-BP solvent evaporates first at the contact line, a difference in ST between the edge and the center generates an inward Marangoni flow and can balance the outward capillary flow (see section 1.3.1). This can be used to mitigate the CRE, by balancing the CE and ultimately achieving a uniform pattern (Figure 3a) [88]. The strength of the Marangoni flow, u, was reported to be proportional to the ST gradient along the liquid-vapor surface ($\Delta\gamma$) [89] which is dependent on the volume ratio of the two solvents.

$$u \propto \frac{\Delta\gamma}{\eta} \tag{4}$$

A strong Marangoni flow reportedly causes a bump at the center of the droplet (not the usual droplet shape), and a balance is reached when the ratio of solvents is appropriately adjusted. In addition to the binary-solvent system, a ternary-solvent strategy was proposed for more precise manipulation of the Marangoni flow [26, 90].

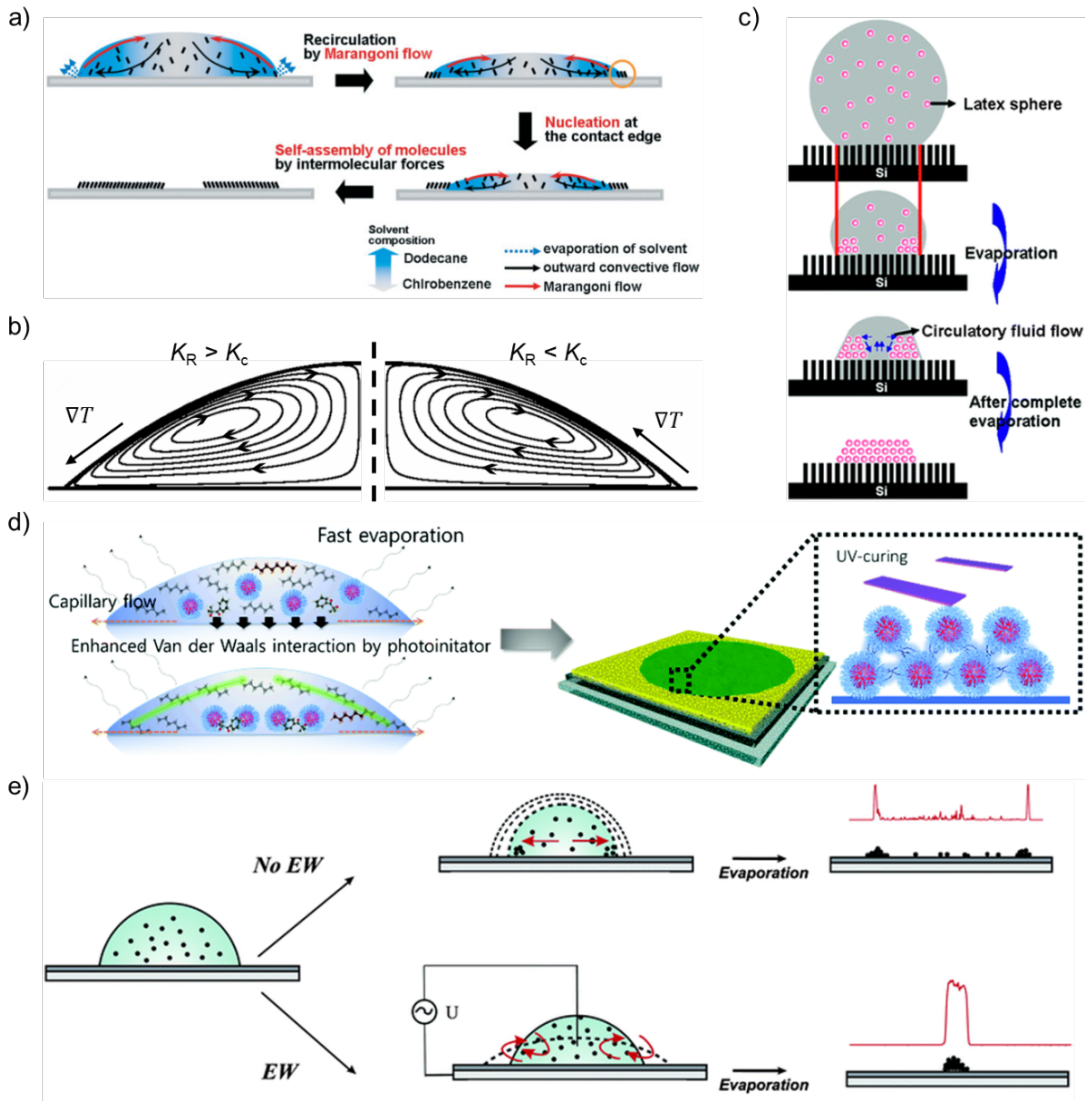

Figure 3. a) The evaporation process of a binary solvent system with 75 vol. % chlorobenzene (COB) and 25 vol. % dodecane, leading to the self-assembly of molecules. Reprinted with permission from [88]. Copyright 2008 Wiley. b) The thermal Marangoni flow direction is determined by K_R. The temperature increases in the direction of the arrows outside the half droplets. Reprinted with permission from [30]. Copyright 2007 APS. c) The droplet evaporates on the silicon surface with micropillar arrays. Reprinted with permission from [91]. Copyright 2012 RSC. d) Cross-linking PI and surface ligands of QDs to prepare a densely packed QD film through UV curing. Adapted from [35]. CC BY 3.0. e) A schematic of the droplet drying process with and without EW. Adapted with permission from [28]. Copyright 2011 RSC.

Another type of Marangoni flow is thermally driven by a nonuniform temperature distribution, exhibiting circulating motion in the droplet. The initial flow direction depends on the thermal conductivity ratio ($K_R = K_s/K_l$) between the substrate (K_s) and the liquid (K_l) [30]. If K_R is greater than 2, indicating an efficient conductor substrate, heat transfers from the contact line to the droplet center because it is warmest at the

contact line. Conversely, when K_R is less than 1.45, the flow reverses due to the highest evaporation rate at the contact line, and the droplet temperature cannot be maintained without sufficient energy. For 1.45 < K_R < 2, the Marangoni flow direction depends on the critical CA (θ_c, Figure 3b), with the critical thermal conductivity ratio given by,

$$K_c = \tan\theta_c \cot\left(\frac{\theta_c}{2} + \frac{\theta_c^2}{\pi}\right) \quad (5)$$

Heating the substrate introduces a thermal gradient, impacting the flow direction, and therefore the substrate temperature can adjust the strength of the ME [83, 92, 93].

In addition to introducing the ME, researchers have proposed alternative methods to prevent the occurrence of CRE. Surface engineering of the substrate surface, involving modification in roughness and topography with structures like two-dimensional micro-pillar arrays [91] and three-dimensional porous structures with small pore sizes [27], confines solutes in these structures, making it difficult for them to migrate due to internal flows and resulting in a flat pattern (Figure 3c). Surface engineering, although a direct approach, is time-consuming and involves processes like lithography and etching. Lee et al. addressed the issue by adding a photoinitiator (PI) into the ink to bond QDs by crosslinking the ligands. The QD film polymerized upon UV exposure once the droplets were deposited on the substrate (Figure 3d) [35]. Some low-BP solvents can be used, and the addition of the PI helps increase the viscosity of the ink. However, proper matching of ligands and PI is crucial; otherwise, polymerization may not occur under UV curing. EW employs alternating current with a frequency between a few Hz and a few tens of kHz to prevent contact line pinning due to time-dependent electrostatic forces and internal flows (Figure 3e) [28]. This method eliminates the need for additives or heat in the system, and the ink does not directly contact the electrode. However, the liquid must be conductive, limiting its application with certain QD inks.

1.3.3 Evaporation Modes

The two simplest and most studied evaporation modes are the constant radius mode (CRM) and the constant angle mode (CAM). In the CRM, typically observed on rough surfaces, the contact line (CL) is pinned, keeping the radius fixed while the CA gradually decreases to zero (Figure 4a) [94]. Conversely, in the CAM, usually seen on smooth surfaces, the CL is unpinned, allowing the radius to shrink while the CA remains constant (Figure 4b) [95]. Although these extreme modes are possible,

droplets more commonly evaporate in mixed modes that combine aspects of both.

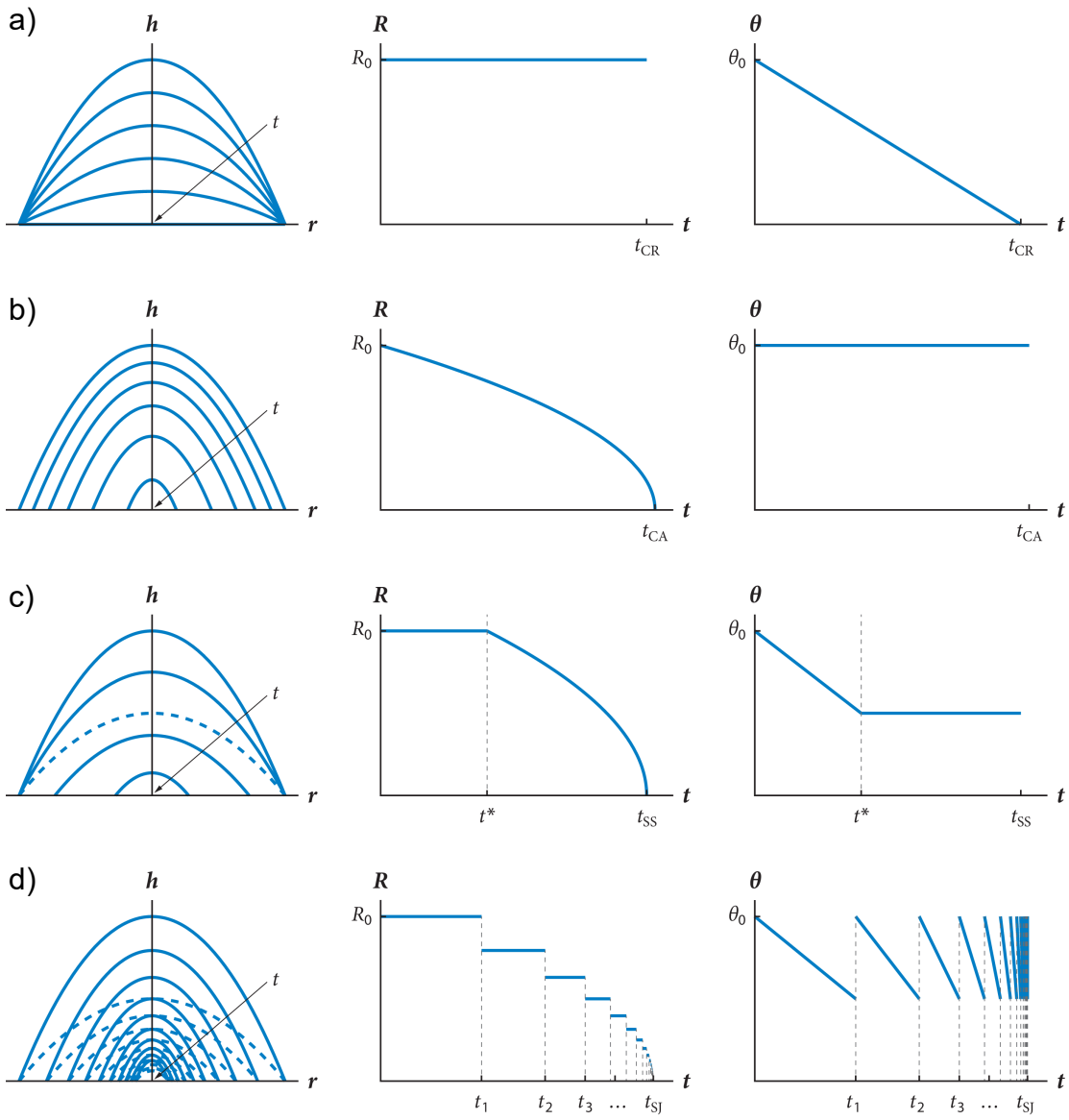

Figure 4. Sketches of the progression of free surface height (h), contact radius (R), and CA (θ) for droplets in a) constant radius, b) constant angle, c) stick-slide, and d) stick-jump modes. Reprinted from [96]. CC BY 4.0.

The most commonly observed mixed mode is the stick–slide (SS) mode, which begins with a constant radius (CR) phase, followed by a constant angle phase (Figure 4c) [97]. In the CR phase, the contact radius (R) remains fixed while the CA decreases from its initial value θ_0 to a critical receding angle θ^* (where $0 \leq \theta^* \leq \theta_0$). Once the CA reaches θ^*, the CL depins, entering the constant angle phase, while R decreases to zero. Depinning occurs at time $t = t^*$, and the total lifetime of a droplet in the SS mode is t_{SS}. Special cases, $\theta^* = 0$ and $\theta^* = \theta_0$, correspond to pure CRM and CAM, respectively.

The stick–jump (SJ) mode, another commonly observed mixed mode, consists of multiple CR phases separated by rapid, nearly instantaneous jumps (Figure 4d) [98]. In each n-th CR phase (n = 1, 2, 3, ...), the contact radius remains constant at $R = R_n$ while the CA decreases from a maximum (θ_{max}) to a minimum ($0 \leq \theta_{min} \leq \theta_{max}$), triggering the CL to depin. During each jumping phase, the CL retracts inward from R_n to R_{n+1} ($< R_n$), and the CA resets to θ_{max}. The jumps occur at times t_n (n = 1, 2, 3, ...), starting from t_0 = 0, with the total droplet lifetime in SJ mode denoted by t_{SJ} (approaching the limit as $n \rightarrow \infty$).

1.4 QDs

QDs refer to semiconductor nanocrystals (NCs) with a diameter that is similar to or smaller than the Bohr exciton diameter (which can be up to 50 nm for some materials, but more commonly ~10 to 20 nm). The QDs therefore comprise hundreds to tens of thousands of atoms. QDs are deemed ideal light emitters due to their high PLQY, narrow emission width, and nanosecond PL lifetime (from a few ns to hundreds of ns) [99], which has been applied in display technologies (Figure 5). The emission color varies with the size of the QDs due to shifts in both the energy positions of the conduction band (CB) and valance band (VB) with respect to the vacuum level [100]. This section discusses the fundamentals and properties of colloidal QDs.

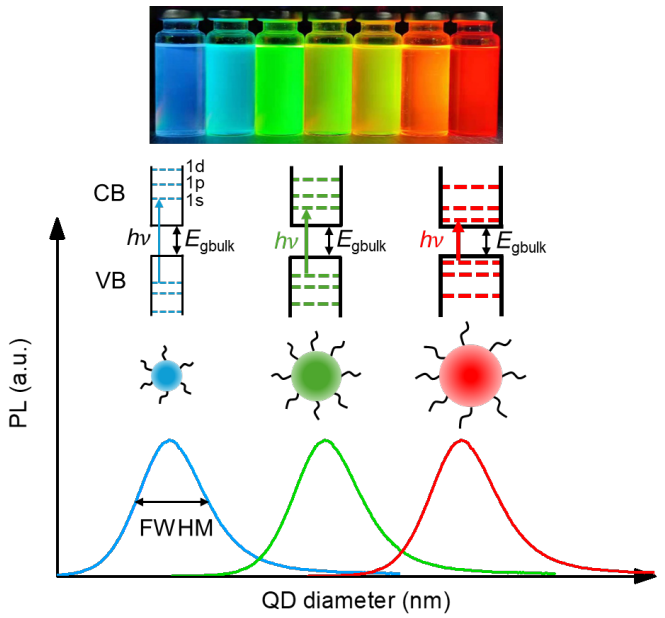

Figure 5. Size-dependent emission and energy level diagram of QDs. The top photograph shows different emission colors of InP QDs by varying the size upon UV illumination. Reprinted with permission from [101]. Copyright 2021 ACS.

1.4.1 Basics of Semiconductors

In bulk crystalline materials, the atomic lattice consists of a large collection of atoms, where the electron orbitals associated with these atoms broaden to form continuous energy bands. The VB represents the lower-energy band of occupied orbitals, while the CB consists of orbitals that electrons can occupy after being excited from the VB [102]. The interaction between the wavelike electrons and the crystal's atomic cores creates forbidden regions in momentum space, known as band gaps [103], where no electronic states exist. Electrons, being fermions, follow the Pauli Exclusion Principle [104], which dictates that no two fermions can share the same quantum state.

The classification of a crystalline material as an insulator, metal, or semiconductor depends on how electrons are distributed across these bands and the size of the band gaps (Figure 6a). In the case of semiconductors, the smaller E_g allows the thermal excitation of carriers into the CB at finite temperatures via lattice vibrations and photon absorption [105]. Semiconductors can be classified by their band gap as either direct or indirect (Figure 6b). A direct band gap occurs when the CB minimum (CBM) and the VB maximum (VBM) are aligned at the same crystal momentum in the energy-momentum (dispersion) relation. In contrast, an indirect band gap arises when the CBM and VBM are located at different momentum states. Transitions in such semiconductors require additional momentum transfer, typically facilitated by the emission or absorption of a phonon, the quantized unit of crystal lattice vibrations [105]. Doping is capable of altering the electronic properties of semiconductors, involving introducing impurities with a different valence to the lattice [106]. These impurities act as electron donors or acceptors, significantly influencing the carrier concentration and the semiconductor's conductivity.

When an electron is excited to the CB, it leaves behind a hole in the VB, which has an effective mass and an opposite charge to the electron. The electrostatic attraction between the electron and hole binds them together unless they are given enough kinetic energy to overcome this attraction. This electron-hole pair can be treated as a quasi-particle, known as an exciton, with a reduced mass (μ) determined by the following equation [102]:

$$\frac{1}{\mu} = \frac{1}{m_e} + \frac{1}{m_h} \tag{6}$$

Where m_e and m_h are the electron and hole effective mass, respectively.

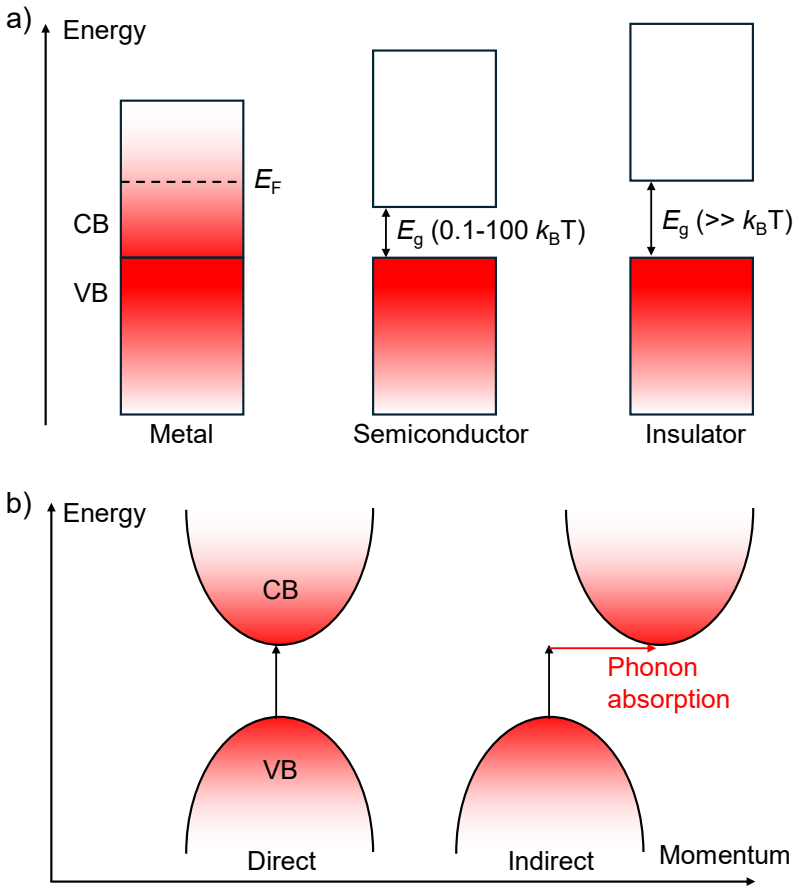

Figure 6. a) Schematic diagram shows how a material's classification as an insulator, semiconductor, or metal depends on the size of its E_g. b) Illustration of energy-momentum relations in direct and indirect band gap semiconductors.

1.4.2 Quantum Confinement in QDs

One fascinating characteristic of QDs is their confinement of electrons and holes in all three dimensions, known as the quantum confinement effect (QCE) [107]. QCE leads to a separation of the continuous energy bands in a bulk material, forming discrete states near the band edge. The shape of the density of energy states $g(E)$ is highly relative to material dimensions (Figure 7). The density of states in a material represents the number of available states per energy interval at each energy level.

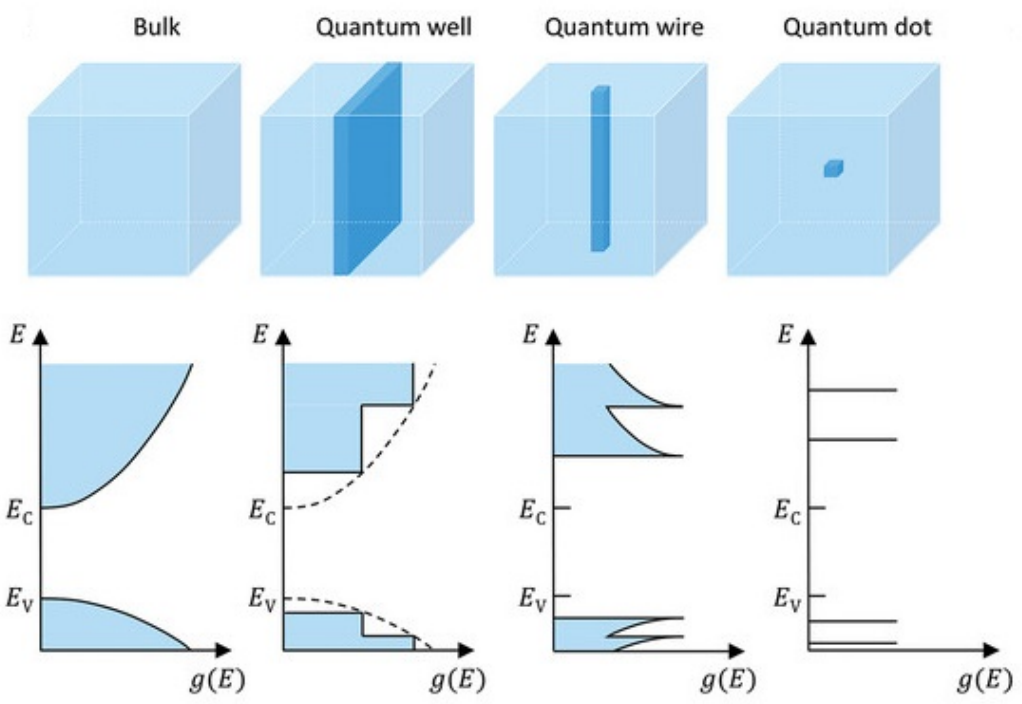

Figure 7. Density of energy states for bulk crystals and structures of reduced dimensionality. Reprinted with permission from [108]. Copyright 2023 Wiley.

QCE is not equally important for all semiconductor NCs but becomes significant when the NC size approaches the natural length scale of the electron and hole. When examining the QCE on excitons in semiconductors, it is helpful to compare the exciton's characteristic radius to the semi-classical Bohr model of an atom. This radius is determined by the balance between the electron-hole pair's electric potential energy and the kinetic energy associated with their relative motion:

$$\frac{1}{2}\mu v^2 = \frac{e^2}{4\pi\varepsilon r} \tag{7}$$

Where v is the regular angular velocity of the electron-hole pair, e is the charge of the electron, ε is the static dielectric constant, and r is the exciton separation. The Bohr model describes a quantized angular momentum $L = \mu v r$ with minimum value $h/(2\pi)$. Therefore, r at this value, i.e., Bohr radius of the exciton (a_B), can be calculated by

$$a_B = \frac{h^2\varepsilon}{4\pi^2 e^2 \mu} \tag{8}$$

Where h is the Planck constant. The confinement energy increases the effective band gap, making it strongly dependent on the semiconductor's size when below a_B.

Based on a particle in a sphere model, a QD with a radius R has a spheric potential:

$$V(r,\varphi,\theta) = \begin{cases} 0, & r < R \\ \infty, & r \geq R \end{cases} \tag{9}$$

Where r, φ, and θ represent the radial distance, azimuthal angle, and polar angle, respectively. The infinite potential beyond a defined radius R ensures the exciton's wavefunction $\psi(r,\varphi,\theta)$ is zero outside that boundary. The time-independent Schrödinger equation for this scenario is expressed as follows:

$$\left[\frac{-\hbar^2}{2\mu}\left(\frac{\partial^2}{\partial r^2}+\frac{2}{r}\frac{\partial}{\partial r}-\frac{L^2}{\hbar^2 r^2}\right)+V(r)\right]\psi(r,\varphi,\theta) = E\psi(r,\varphi,\theta) \tag{10}$$

Here, $\hbar$ is the reduced Planck constant ($\hbar = h/(2\pi)$). The total energy needed to achieve the first excited state in a QD is equivalent to its band gap energy, expressed as follows :

$$E_{\mathrm{QD}} = E_{\mathrm{g}} + \frac{h^2}{8R^2u} - \frac{1.8e^2}{4\pi\varepsilon R} \tag{11}$$

Where E_{g} is the bulk band gap. The last term is the stabilization correction for exciton binding energy (BE) [109]. Since it is inversely proportional to the particle radius R, its influence becomes significant primarily for larger QDs, where it contributes to a reduction in the band gap.

1.4.3 Photon Absorption in QDs

QDs are significantly smaller than the wavelength of light, allowing them to absorb photons with energies exceeding the band gap effectively. Generally, a photon with energy $E_{i,f} = \hbar\omega_{i,f}$, corresponding to the energy difference between the ground state $|i\rangle$ and an excited state $|f\rangle$, excites an electron from the ground state to the excited state. While QDs do not fit perfectly into the categories of purely 0D or bulk 3D materials, their density of states, $N_{0\mathrm{D}}(E)$, can still be effectively described using a specific expression:

$$N_{0D}(E) = \frac{1}{V_{\mathrm{QD}}}\sum_{n,l}(2l+1)\delta(E-E_n) \tag{12}$$

Here, E_n represents the energy levels with a degeneracy n, and V_{QD} denotes the volume of a QD. Based on this framework, Sun and Goldys calculated the linear optical absorption coefficient, $\alpha_{QD}(\hbar\omega)$, of an individual QD under incident light of angular frequency ω by using the envelope function approximation [110]:

$$\alpha_{QD}(\hbar\omega) = \frac{\pi e^2 E_p a_p}{2m_e c n_r \varepsilon_0 \omega} \frac{1}{V_{QD}} \sum_{n,l} (2l+1)\delta(\hbar\omega - E_{n,l}) \tag{13}$$

Where e is the elementary charge, E_p is the momentum matrix element, a_p is the average over polarisation directions for incident light, m_e is the electron mass, c is the speed of light, n_r is the refractive index of the QD, and ε_0 is the vacuum permittivity. The broad size distribution of QDs results in a range of quantized energy levels with a width of $\Delta E_{n,l}$ [111], leading to the replacement of the delta function with a Gaussian distribution:

$$\alpha_{QD}(\hbar\omega) = \frac{\pi e^2 E_p a_p}{2m_e c n_r \varepsilon_0 \omega} \frac{1}{V_{QD}} \sum_{n,l} \frac{(2l+1)}{E\sqrt{2\pi}\Delta E_{n,l}} \exp\left(-\frac{(\hbar\omega - E_{n,l})^2}{2\Delta E_{n,l}^2}\right) \tag{14}$$

The molar absorption coefficient, $\varepsilon(E)$, derived from $\alpha_{QD}(E)$ for a monodisperse QD solution using the Beer-Lambert law, quantifies the strength of light absorption by QDs at a specific wavelength. It is represented as a function of photon energy E.

$$\varepsilon(E) = \frac{N_A V_{QD} \alpha_{QD}(E)}{\ln 10} \tag{15}$$

Here, N_A is Avogadro's number. QD states lie between those of bulk semiconductors and individual atoms, exhibiting greater discreteness at lower excitation energies. At higher excitation energies, these states become closer together, resembling excitation bands, leading to increased absorption at shorter wavelengths. The absorption spectrum of a typical InP QD dispersion will be discussed in section 2.4.4.

1.4.4 Excited State Dynamics of QDs

When a QD absorbs a photon with energy exceeding the band gap, it enters an excited state, with the electron elevated above the CBM and the hole below the VBM. Excited electrons quickly decay to the bottom of CB through phonon emission, while holes relax to the VBM in a process called thermalization. In bulk semiconductors, where

energy states are continuous, hot exciton cooling—nonradiative relaxation to the band edge—occurs within a few picoseconds [112]. In QDs, the discrete energy states increase separation with the QD size reduces, with this spacing growing bigger than typical acoustic phonon energies. This creates a ‘phonon bottleneck,’ where direct thermalization requires precise resonance between phonon and transition energies, leading to prolonged carrier relaxation times [113]. However, despite this bottleneck, observed lifetimes of carriers in smaller QDs remain short, in the range of picoseconds, indicating the presence of additional relaxation mechanisms [114].

When an electron from the (N+1)-th shell fills a hole in the N-th shell, the resulting transition energy can cause the emission of an electron from the (N+2)-th shell, a phenomenon known as the Auger effect [115]. Such Auger processes provide an alternate pathway for breaking the ‘phonon bottleneck’ by enabling energy swaps between electrons and holes, thereby introducing additional relaxation mechanisms. Since the energy levels in the VB are more densely packed, holes tend to relax faster than electrons. This allows energy transfer from excited electrons to relaxed holes at the VBM through phonon emission. The emitted photon during electron decay corresponds to the energy difference between the electron and hole, typically spanning from the CBM to the VBM unless intra-gap states are present.

In addition to radiative relaxation via Auger energy transfer, structural defects play a significant role in overcoming the ‘phonon bottleneck’ as well. Due to the nanoscale dimensions of QDs, a substantial proportion of their atoms are located at the surface, regardless of shape [116]. This high surface-to-volume ratio amplifies surface effects, greatly influencing electron relaxation from the excited state. Defects introduced during synthesis can create shallow trap states, where trapped electrons become spatially delocalized and depopulate in a short time [117]. These shallow traps are typically located near the band edges (within a few $k_B T$), arising from under-coordinated atoms with unpaired valences or unsaturated dangling bonds at the crystal's surface. Although many surface atoms are passivated by stabilizing ligands, steric hindrance often leaves some dangling bonds, which act as trap states that contribute to non-radiative recombination, reducing PLQY by transferring energy to CB electrons rather than emitting photons [118]. Internal point defects, caused by deviations from the ideal crystal structure, generate deep intra-gap trap states that are further from the band edges (several $k_B T$) [119]. Deep trap states are characteristic of defect-tolerant materials and exhibit longer lifetimes, facilitating efficient radiative exciton recombination.

1.4.5 Growth Kinetics of Colloidal QDs

Colloidal QDs generally consist of a core, shell, and ligands. The shell serves to passivate surface trap states and protect the core from degradation caused by oxygen and water [120]. The shell engineering, including the shell materials and thickness, greatly influences the PL property of QDs, which will be discussed in detail in section 3.1. Ligands enhance monodispersity during synthesis and provide colloidal stability to QDs while also passivating surface defects. Common ligands used in QD synthesis are long-chain organic hydrocarbons with anchoring end groups. While these molecules offer high chemical flexibility, they act as bulky insulating barriers between QDs, hindering charge transport. Replacing larger ligands with smaller ones or cross-linking surface ligands can improve carrier transport in QD-LEDs [121, 122].

LaMer model is used to describe the growth kinetics of most NCs (Figure 8), including four stages: (I) monomer supersaturation, (II) nucleation, (III) growth, and (IV) Ostwald ripening. During the monomer accumulation stage (Stage I), [A] and [B] precursors transform into A–B monomers through chemical bond breaking and recombination. When the concentration of A–B monomers is over the saturation limit ($C_{Saturation}$), nucleation begins through the self-assembly of monomers (Stage II). This nucleation process halts abruptly as the rapid consumption of A–B monomers reduces their concentration below $C_{Saturation}$. The remaining A–B monomers then deposit onto the preformed AB nuclei, marking the crystal growth stage (Stage III). When the concentration of A–B monomers reaches an equilibrium ($C_{Equilibrium}$), Ostwald ripening takes over, characterized by the dissolution of smaller AB NCs and the redeposition of the dissolved species onto larger ones (Stage IV). Since Ostwald ripening typically broadens the size distribution, QD synthesis should be terminated promptly to prevent detrimental interparticle reactions.

For the formed nuclei to achieve thermodynamic stability, they must reach a minimum critical radius, r_C, as defined by:

$$r_c = \frac{2\gamma V_m}{RT \ln S} \tag{16}$$

Where γ is the specific surface energy, V_m is the molar volume, R is the universal gas constant, and S is the supersaturation [123]. Oswald ripening suggests that nuclei with a radius smaller than the r_C dissolve due to their high surface free energy, whereas nuclei with a radius greater than the r_C continue to grow. The maximum growth rate

occurs as $r = 2r_C$, where smaller crystals grow faster than larger ones. This results in size focusing, producing crystals with a narrow size distribution at the cost of nanoparticle concentration. This effect is typically achieved by the continuous injection of precursors to maintain the monomer concentration. Monomers can also be supplied by the dissolution of already-formed NCs. The smallest particles, having the highest surface free energy, are most susceptible to this process, resulting in a reduction in the number of NCs and an increase in their average size.

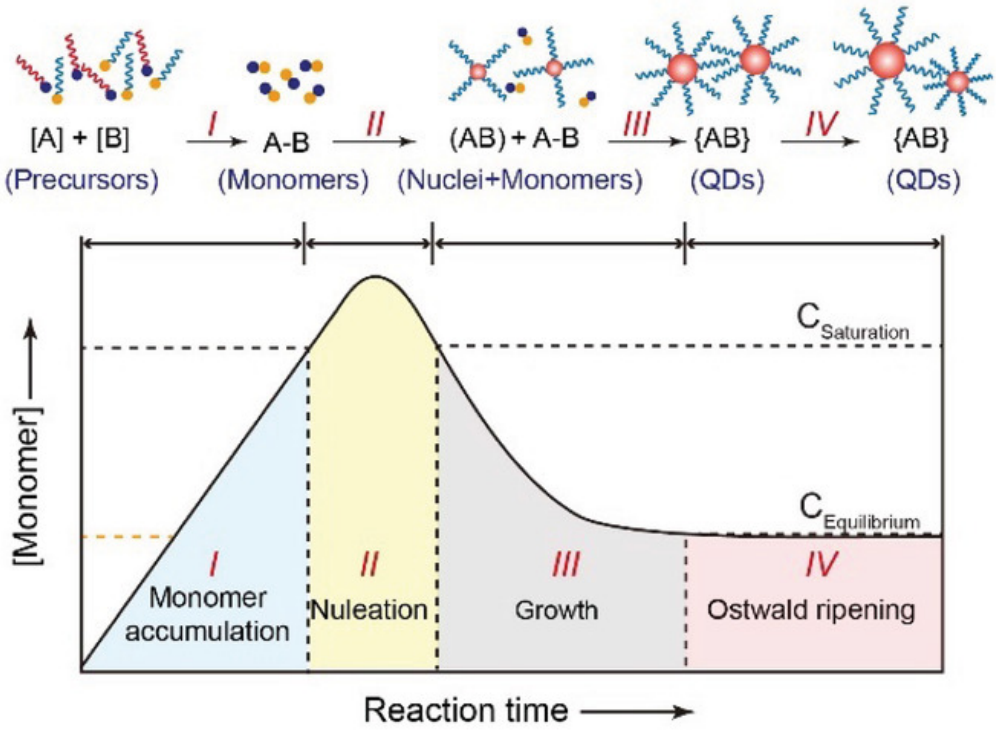

Figure 8. LaMer plot and corresponding schematic diagram of the grow kinetic of colloidal NCs. Reprinted with permission from [124]. Copyright 2020 Wiley.

1.5 QD-LEDs

QD-LEDs are promising next-generation display technology, which has been developed for more than two decades. However, their electrical performance is still not desirable, which struggles to meet the requirements of the industry, especially for HMF QD-based LEDs. Key challenges include unbalanced charge injection [125] and nonradiative recombination mechanisms such as FRET [126] and Auger recombination (AR) [127].

1.5.1 Fundamentals of QD-LEDs

QD-LEDs are considered to be the next generation of self-emissive displays, offering

a longer lifespan, faster response time (ns), lower power consumption, and higher viewing angles compared to LCD and OLED devices [128]. The structure of QD-LEDs is similar to OLEDs, consisting of a substrate, anode, hole injection layer (HIL), hole transport layer (HTL), emissive layer (EL), electron transport layer (ETL), electron injection layer (EIL), and cathode (Figure 9a, b). For QD-LEDs, the EML is QD film while organic fluorescent film for OLEDs. The cathode's work function should be close to the LUMO of EIL/ETL, which facilitates electron injection and decreases heat production to improve the device's lifetime. The carrier injection layers reduce the potential barrier of electrons or holes injection and enable more efficient carrier injection. The carrier transport layers (CTLs) are usually designed with higher exciton energy than EML to ensure that the excitation energy of the EML is not transferred to the transport layer and balance the injection of electrons and holes. The CTLs can be organic and inorganic materials, leading to all-organic, all-inorganic, and hybrid structures (Figure 9c).

QD-LEDs with different structures show different EL mechanisms. For the all-organic structure, it has been suggested that holes or electrons could move through the QD layer to the neighboring donor layer, where they form excitons with charge carriers of the opposite type. Rather than undergoing radiative recombination to produce photons, these excitons transfer their energy to QDs via FRET which significantly enhances the device's performance and stability [129]. Since FRET is distance-sensitive, it is crucial to control the spacing between the donor and acceptor to ensure effective FRET. In the hybrid configuration, electrons and holes form excitons on the QDs directly, then either recombine radiatively or dissipate through non-radiative decays [130]. The charge injection depends on the carrier mobility of CTLs and the energy barrier between CTLs and QDs. The hybrid structure has prevailed owing to its excellent electrical performance. Jin et al. deciphered the formation of excitons in hybrid QD-LEDs using electrically pumped single-NC spectroscopy [131]. A negatively charged QD is formed firstly by injecting an electron and then the hole injection follows, forming an exciton. The intermediate negatively charged QD reduces the hole injection barrier, accelerating the hole injection and hindering excessive electron injection due to the Coulomb interaction. Regarding the all-inorganic structure, QDs ionized when the voltage is applied across the device rather than undergoing FRET or direct charge injection [132]. An electron is removed from the VB of one QD and moves into the CB of a neighboring QD, resulting in the creation of an electron and a hole on a pair of adjacent QDs. Ultimately, excitons are formed through multiple such ionization events.

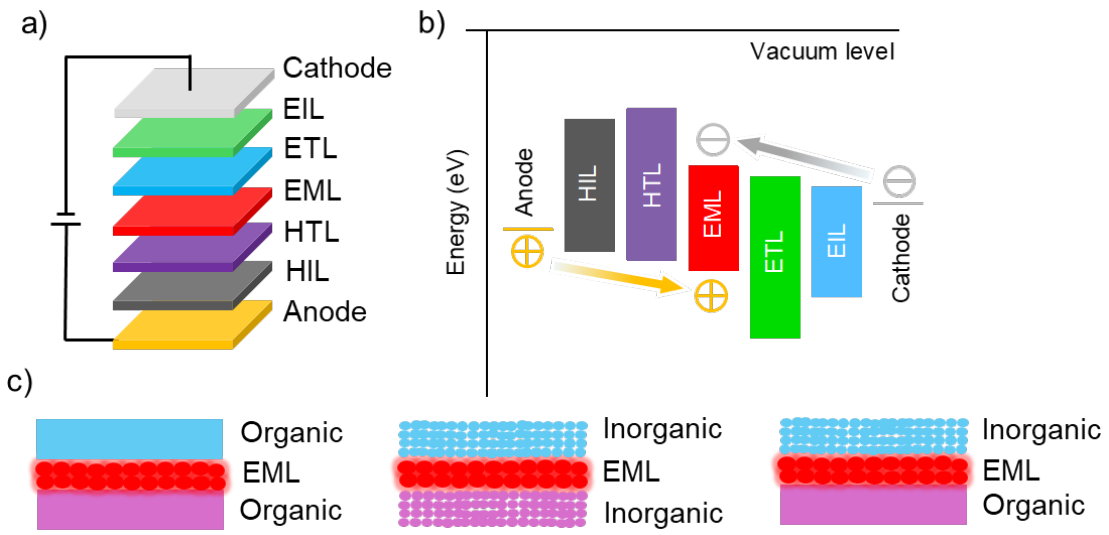

Figure 9. a) The basic structure and b) energy band alignment of QD-LEDs. Reprinted with permission from [133]. Copyright 2018 Wiley. c) Configurations of all-organic, all-inorganic, and hybrid QD-LEDs from left to right. Reprinted with permission from [134]. Copyright 2021 Elsvier.

1.5.2 Challenges of QD-LEDs

Apart from radiative recombination, there are a few kinds of nonradiative recombination such as AR, FRET, and filed-induced quenching (FIQ), resulting in low EQE and hindering commercialization (Figure 10).

AR is a non-radiative process in which an electron and hole recombine, transferring their energy to a third charge carrier (electron or hole) instead of emitting a photon [135]. This process generates "hot" carriers (high-energy electrons or holes) that dissipate their energy as heat, resulting in trions and biexcitons and reducing the overall quantum efficiency of the device [127]. AR is closely linked to the volume of QDs, with an inverse relationship between the two [136]. Additionally, AR is associated with blinking, a random switching between the emitting and non-emitting states, caused by excess charge carriers and charge fluctuations at surface sites that capture electrons [137, 138]. These two types of blinking can interconvert by varying the bias potentials. AR can be mitigated through interface engineering, such as by coating QDs with shells and adjusting the shell thickness [139].

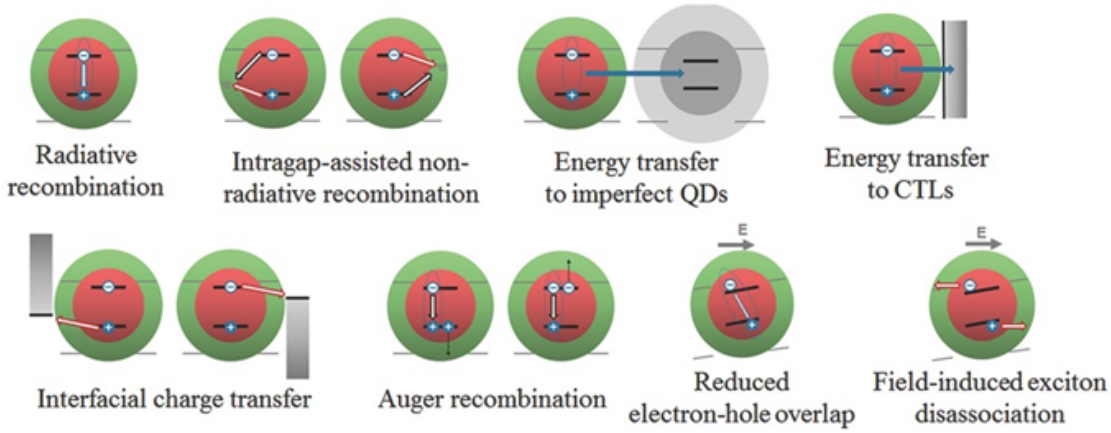

Figure 10. Schematic diagram of possible exciton decay in QD-LEDs. Reprinted with permission from [140]. Copyright 2017 Wiley.

The mechanism of FRET involves the transfer of recombination energy from an exciton to another radiative site via nonradiative dipole-dipole coupling [126]. Specifically, energy transfer occurs from the organic layer to the QD layer (layer-to-layer FRET) or between neighboring QDs (inter-dot FRET) in QD-LEDs [129, 141]. FRET is highly sensitive to the distance between QDs, which is influenced by the length and morphology of the ligand. Controlling the distance and fine structural design of QDs can reduce the FRET rate. FIQ leads to a drop in external quantum efficiency (EQE) as the current density increases, likely due to high electric fields and the resulting delocalized carrier wave functions [142]. Therefore, QD-LEDs should be protected from direct exposure to high electric fields through encapsulation.

Moreover, charge balance is also a significant issue for the efficiency and lifetime of QD-LEDs, depending on the charge mobility and energy band alignment of CTLs. Initially, organic small molecules were used, however, the instability of organic CTLs under the ambient atmosphere raises manufacturing costs for environmental packaging, and their relatively low mobilities limit charge carrier densities. In contrast, inorganic wide bandgap CTLs such as ZnO [143], TiO_2 [144], and MoO_x [145] were developed due to their higher stability and easier preparation. Among these, ZnO is the most widely used metal oxide as the ETL due to its high electron mobility and efficient electron injection [143]. However, ZnO's electron mobility is significantly higher than the hole mobility of most HTLs (Table 2), creating an imbalance in electron and hole injection. To address this issue, solutions include doping ZnO with Mg, Co, or Li [125], inserting an insulating layer between QDs and ZnO [56, 146], and adding additives to the QD solution [147]. Besides, the interaction between QDs and ZnO is not fully understood. Direct contact between these inorganic oxides and QDs can

cause emissive quenching, and energy band alignment must also be considered. Currently, state-of-the-art QD-LEDs mainly employ hybrid organic and inorganic materials as HTLs and ETLs, respectively (Figure 11).

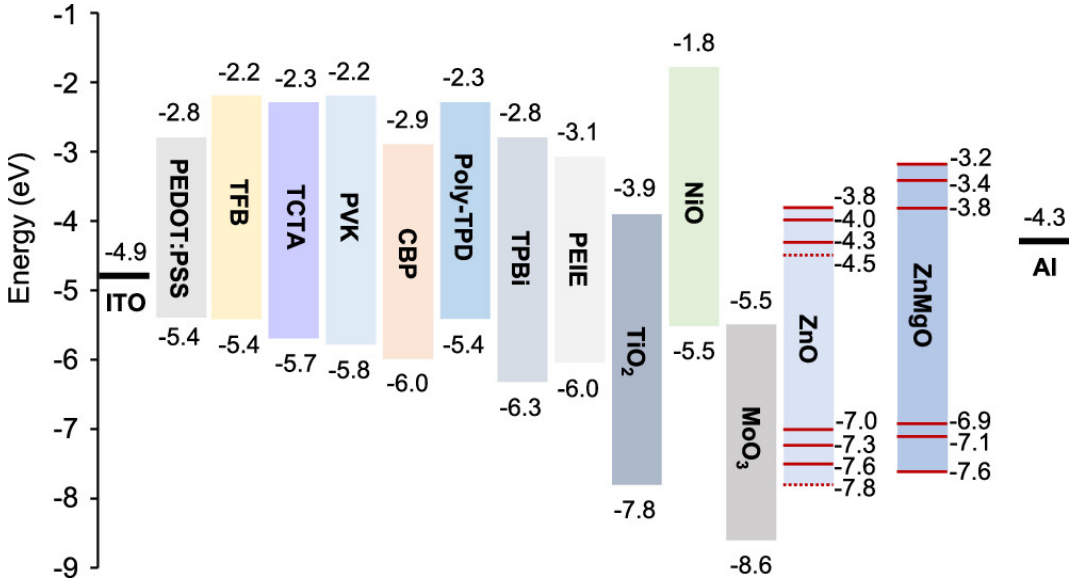

Figure 11. Energy band alignment of organic and inorganic functional CTLs and electrodes. The dashed lines in ZnO are the CB and VB of bulk ZnO. Reprinted with permission from [13]. Copyright 2023 ACS.

Table 2. The carrier mobility of commonly used CTL materials.

Material	CTL	Hole/electron mobility ($cm^2\ V^{-1}\ S^{-1}$)	Ref.
TFB	HTL	1×10^{-2}	[148]
PVK	HTL	2.5×10^{-6}	[149]
Poly-TPD	HTL	1.0×10^{-4}	[150]
TCTA	HTL	4×10^{-4}	[151]
CBP	HTL	1.0×10^{-3}	[151]
ZnO	ETL	4.5×10^{-4}	[143]

1.6 Scope of Project and Chapter Overview

The scope of the thesis was to use the IJP technique to assemble QD-LEDs based on InP/$ZnSe_xS_{1-x}$/ZnS QDs and study the degradation of QDs upon exposure to oxygen, water, and heat. To overcome the CRE, ME was introduced by forming a binary solvent system and heating the substrate. The process of evaporation for a liquid droplet on a surface is intricate, involving particle-particle, particle-substrate, particle-flow, and particle-interface interactions. Observing the evolution and lifetime of QD droplets

facilitates understanding of the CRE. As the most popular ETL of QD-LEDs, ZnO is normally doped with magnesium to align with the energy levels of QDs and reduce electron mobility. However, the impact of $Zn_{0.9}Mg_{0.1}O$ films exposed to wet air on the electrical performance of InP QD-LEDs is rarely reported. Optimizing the thickness can achieve a more balanced charge injection.

The stability of the QD layer significantly influences the stability and lifetime of QD-LEDs. Although the oxidation of InP core and InP/$ZnSe_xS_{1-x}$/ZnS QDs have been studied by X-ray photoelectron spectroscopy (XPS) and scanning transmission electron microscopy, the real-time degradation of InP/$ZnSe_xS_{1-x}$/ZnS QD films by oxygen, water, and heat was rarely reported. Here, the quenching of InP/$ZnSe_xS_{1-x}$/ZnS QD films was investigated by varying the thicknesses of QD films, RH, temperatures, and encapsulating layers of polymethyl methacrylate (PMMA). Besides, the stability of InP/ZnSeS/ZnS QDs by oxygen and water was studied separately by near ambient pressure (NAP) XPS, providing an understanding of how the QD films oxidized by oxygen and water, respectively.

The structure of the thesis is as follows. Chapter 2 gives the experimental details and techniques used in the thesis, including theories of some methods. Chapter 3 characterizes the optical properties, chemical composition, size distribution, and morphology of InP/$ZnSe_xS_{1-x}$/ZnS QDs and $Zn_{1-x}Mg_xO$ NPs. In Chapter 4, four QD inks with different volume ratios of CHB and decane were formulated and their basic physical properties including viscosity, density, ST, and CA were measured. The optimal volume ratio was confirmed by checking the CRE and film uniformity of the printed QD patterns. Different evaporation modes were revealed by observing the real-time drying of the QD ink at various substrate temperatures (T_{sub}). InP QD-LEDs were assembled by IJP and the electrical performance was compared with that of spin-coated analogues. Additionally, the electrical performance of InP QD-LEDs with different $Zn_{0.9}Mg_{0.1}O$ layer thicknesses was also studied. Chapter 5 studied the stability of QD films with different thicknesses at different humidity levels and temperatures by fluorescence spectroscopy. The in-situ degradation of QD films by oxygen, water, and heat was characterized by NAP-XPS. Furthermore, surface engineering was adopted to enhance the air stability of QD films by encapsulating a thin PMMA layer.

2. Experimental Methods

2.1 Synthesis of InP QDs

The protocol of InP QDs synthesis was based on the hot-injection method with minor modifications [152], including InP nucleation, $ZnSe_xS_{1-x}$/ZnS shell growth, and QDs cleaning. The reaction of InP QDs is described by the equation (24) [153],

$$InCl_3 + 4P(N(CH_3)_2)_3 + 12C_{18}H_{35}NH_2 \rightarrow InP + 3P(NHC_{18}H_{35})_4Cl + 12HN(CH_3)_2 \quad (17)$$

InP nucleation. 0.100 g indium chloride ($InCl_3$, 99.99%, Sigma-Aldrich) and 0.300 g zinc chloride ($ZnCl_2$, >98%, Thermo Fisher Scientific) were added into a 100-mL three-neck flask in the glove box. $ZnCl_2$ was added to facilitate the shell growth, minimize surface defects, and reduce the InP core's size distribution by stabilizing the QD surface and lowering the critical nucleus size [154]. Meantime, dissolving 9.47 mg of elemental selenium (Se, 99.9%, Alfa Aesar) powder in 1.0 mL trioctylphosphine (TOP, >97%, Sigma-Aldrich), 4.8 mg Se with 64.1 mg elemental sulfur (S, 99.98%, Sigma-Aldrich) powder in 1.6 mL TOP, and 1.6 mg Se with 0.128 g S in 2.0 mL TOP at 140 °C for 1 h. TOP was used to dissolve S and Se, as well as a stabilizer. 6.0 mL oleylamine (70%, Sigma-Aldrich) was injected into the 100-mL three-necked flask on a Schlenk line and degassed at 120 °C for 1 h. Then the temperature was heated to 180 °C under nitrogen (N_2) flow and was monitored by the thermometer. In the meantime, 3.000 g Zinc stearate ($Zn(St)_2$, 10-12% Zn basis, Sigma-Aldrich) was dissolved in 12.0 mL squalane (>92%, Sigma-Aldrich) under the N_2 atmosphere. 0.35 mL tris(dimethylamino)phosphine ($(DMA)_3P$, 97%, Sigma-Aldrich) was quickly injected into the flask and kept for 10 min at 180 °C to form the InP core. The pale yellow solution changed into dark red in 2 min (Figure 12). Protic molecules like oleylamine contain labile H^+ that can be released into surrounding reagents. This proton is expected to hydrolyze or activate $(DMA)_3P$, producing highly reactive phosphine (PH_3), which then triggers a nucleation burst by reacting with the In-oleylamine complex to form high-quality InP QDs.

Shell growth. The shells were deposited on the InP core using the successive ion layer adsorption and reaction technique. Inject 1.0 mL Se/TOP solution, 4.0 mL $Zn(st)_2$/squalane (0.4 M), 1.6 mL Se/S/TOP solution, 4.0 mL $Zn(st)_2$/squalane, 2.0 mL Se/S/TOP solution, and 4.0 mL $Zn(st)_2$/squalane solution into the core solution in turn and reacted at 200 °C, 220 °C, 240 °C, 260 °C, 280 °C for 30 min, respectively, and then 300 °C for 60 min. Here, the middle $ZnSe_xS_{1-x}$ shell was formed, and an outmost

ZnS shell would grow afterward. 5.0 mL octanethiol (>98.5%, Sigma-Aldrich) was added and reacted at 190 °C for 1 h. Dissolve 0.659 g zinc acetate ($Zn(acet)_2$, 99.99%, Sigma-Aldrich) in 3.0 mL oleic acid (97%, VWR Chemicals) and then inject into the flask at 190 °C for 2 h and then cool to RT after the reaction.

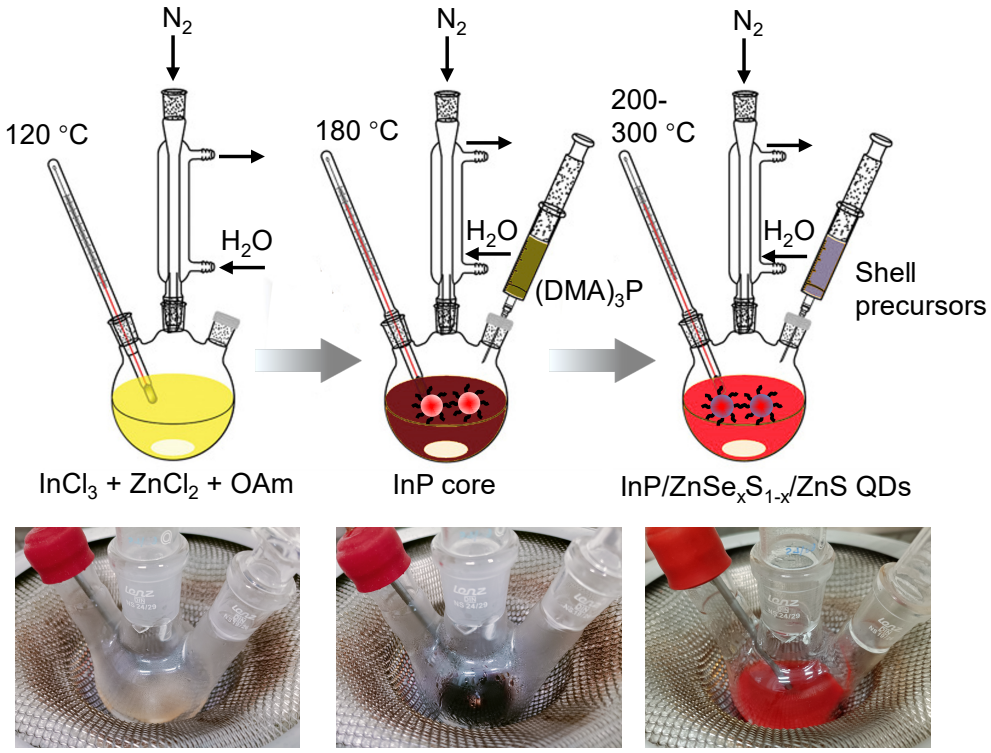

Figure 12. Schematic of InP/$ZnSe_xS_{1-x}$/ZnS QD synthesized by the hot-injection method. The bottom photographs show the corresponding synthesis stages.

QD cleaning. The as-synthesised InP QD solution was equally divided and the quantity of hexane with a volume ratio of 1:1 was added and then centrifuged at 15000 RCF for 10 min. The precipitation was discarded and three times the amount of isopropyl alcohol (IPA) was added into the supernatant and centrifuged at 15000 RCF for 10 min. The supernatant was then removed, and 5 mL hexane was added to disperse the pellets and centrifuged at 15000 RCF for 10 min. The above cleaning protocols were repeated three times. The cleaned InP/$ZnSe_xS_{1-x}$/ZnS QDs were dispersed in anhydrous octane (>99%, Sigma-Aldrich) for characterization.

2.2 Synthesis of $Zn_{0.9}Mg_{0.1}O$ NPs

The synthesis protocol of colloidal $Zn_{0.9}Mg_{0.1}O$ NPs was based on a previously published solution precipitation method, with minor modification [155]. Initially, 576.2 mg of zinc acetate dihydrate ($Zn(acet)_2$ $2H_2O$, >98%, Sigma-Aldrich) and 80.4 mg of

magnesium acetate tetrahydrate ($Mg(acet)_2$ $4H_2O$, 98%, Alfa Aesar) were dissolved in 30.0 mL of dimethyl sulfoxide (DMSO, 99%, Alfa Aesar) at RT for 1 h. Meanwhile, 5.0 mmol of tetramethylammonium hydroxide (TMAH, 97%, Sigma-Aldrich) was dissolved in 10.0 mL ethanol (>99%, Fisher Chemical) and stirred at RT for 1 h. TMAH is a strong organic alkali used to easily adjust the pH level to around 14. Unlike strong inorganic alkali like NaOH, TMAH does not introduce alkali metal cations that could contaminate metal oxides and negatively impact their ohmic conductivity [156]. The TMAH/ethanol solution was then slowly injected into another solution and reacted at RT for 4 h until the mixed solution was clear. $Zn_{0.9}Mg_{0.1}O$ NPs were precipitated by acetone and purified by centrifugation at 10000 RCF for 10 min. The cleaned $Zn_{0.9}Mg_{0.1}O$ NPs were dispersed in IPA for characterization. Then, 0.2 vol.% ethanolamine (EA, >99%, Sigma-Aldrich) was added into the $Zn_{0.9}Mg_{0.1}O$ dispersion to improve its dispersity by sonication in the water bath for 2 h, and the final NPs were denoted as $Zn_{0.9}Mg_{0.1}O$-EA. The ratio is calculated by the volume of EA divided by the net mass of $Zn_{0.9}Mg_{0.1}O$ NPs in the dispersion.

2.3 Assembly of QD-LEDs

The QD layer in QD-LEDs was assembled by SC and IJP separately in this work to compare their electrical performance. In both spin-coated and inkjet-printed QD-LEDs, the HIL, HTL, and ETL were spin-coated, and the Al cathode was deposited by thermal evaporation.

2.3.1 Spin Coating of InP QD-LEDs

SC is a simple and efficient way to prepare thin films with a thickness between a few nm and a few μm, including static SC and dynamic SC [157]. The final thickness of spin-coated thin films varies with the spinning speed and the ink's viscosity, which can be expressed by

$$h_f \propto \eta^{\frac{1}{3}}\omega^{-a} \tag{18}$$

Where *a* ranges from 2/3 to 1/2 [158, 159], depending on the drying rate.

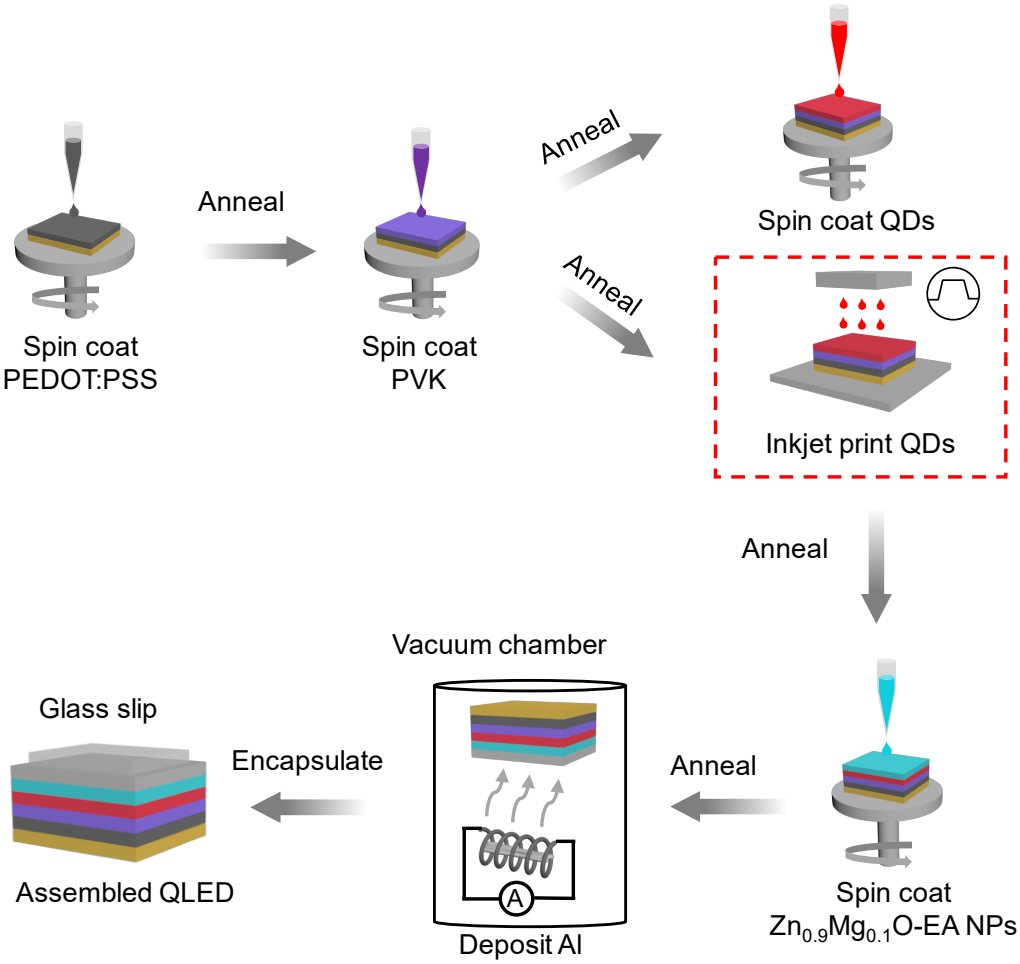

Figure 13. The step-by-step assembly process of inkjet-printed and spin-coated InP QD-LEDs.

The fabrication process of spin-coated InP QD-LEDs is shown as follows. Firstly, ITO glass (S211, Ossila, sheet resistance: 20 Ω/sq) was sonicated in Decon 90 (3%), MilliQ water, and IPA consecutively for 15 min and rinsed three times in MilliQ water. One piece of ITO glass contains 8 pixels with a size of 2 × 2 mm^2 for each pixel. The ITO glass was then dried under N_2 flow and exposed to UV-ozone for 10 min to improve its surface energy and hydrophilicity. Next, poly(3,4-ethylenedioxythiophene) polystyrene sulfonate (PEDOT:PSS, 3-4%, Sigma-Aldrich), polyvinylcarbazole (PVK, Sigma-Aldrich) or Poly(9,9-dioctylfluorene-alt-N-(4-sec-butylphenyl)-diphenylamine) (TFB, Sigma-Aldrich), QDs, and $Zn_{0.9}Mg_{0.1}O$-EA NPs were spin-coated on ITO-coated glass as the HIL, HTL, EML, and ETL of InP QD-LEDs, respectively. PEDOT:PSS was diluted by MilliQ water with a volume ratio of 2:1 and then diluted by IPA with a volume ratio of 4:1 to improve the conductivity of PEDOT:PSS [160]. $Zn_{0.9}Mg_{0.1}O$-EA and PEDOT:PSS were filtered by the 0.2 μm and 0.45 μm PTFE filter, respectively. Their thicknesses were controlled by varying the spin speeds. Then, they were annealed at

150 °C, 200 °C, 150 °C, 80 °C, and 30 °C for 10 min, respectively after spin coating (Figure 13). Their spin speeds and corresponding thicknesses will be discussed in section 4.5.1. Table 3 shows the ink formulations and corresponding spin coating and annealing parameters. Subsequently, a 100-nm-thick aluminum cathode was deposited by the thermal evaporator (Edwards 306) with a deposition rate of ~0.2 nm/s under vacuum (2×10^{-6} bar). Finally, the devices were sealed with encapsulation epoxy and a cover slip under UV light for 15 min.

Table 3. Ink formulations and spin coating parameters of spin-coated InP QD-LEDs.

Materials	PEDOT:PSS	PVK	TFB	InP	$Zn_{0.9}Mg_{0.1}O$
Concentration	1.75%	10 mg/mL	8 mg/mL	10 mg/mL	14 mg/mL
Solvent	MilliQ/IPA	COB	COB	octane	IPA
Spin speed (RPM)	4000	3000	3000	2000	4000
Spin time	60 s	45 s	45 s	30 s	45 s
Spin volume	30 µL	30 µL	30 µL	30 µL	30 µL
Annealing parameters	150 °C, 10 min	200 °C, 10 min	150 °C, 10 min	80 °C, 10 min	RT, 10 min

2.3.2 Inkjet Printing of InP QD-LEDs

For inkjet-printed QD-LEDs, the assembly procedures were the same as spin-coated QD-LEDs except the QD layer which was printed using the Fujifilm DMP-2850 inkjet printer (Figure 14a).

The main components of an inkjet printer include a cartridge, platen, and image system (drop watcher and fluidical camera, Figure 14b, c). Before jetting, optimizing the firing frequency and jetting voltage by observing the jetting process of the droplets using the drop watcher is necessary. The fluidical camera can be used to position the print head, set the printing route, and observe printed patterns. The fluid bag in the cartridge is made from polypropylene, making some organic solvents not compatible. The maximum platen and cartridge temperature can reach 60 °C and 70 °C, respectively. DS can be adjusted by the saber angle; a smaller DS corresponds to a smaller saber angle (see Table 4). The smaller the DS, the closer drop to each other, allowing higher resolution (defined as dot per inch).

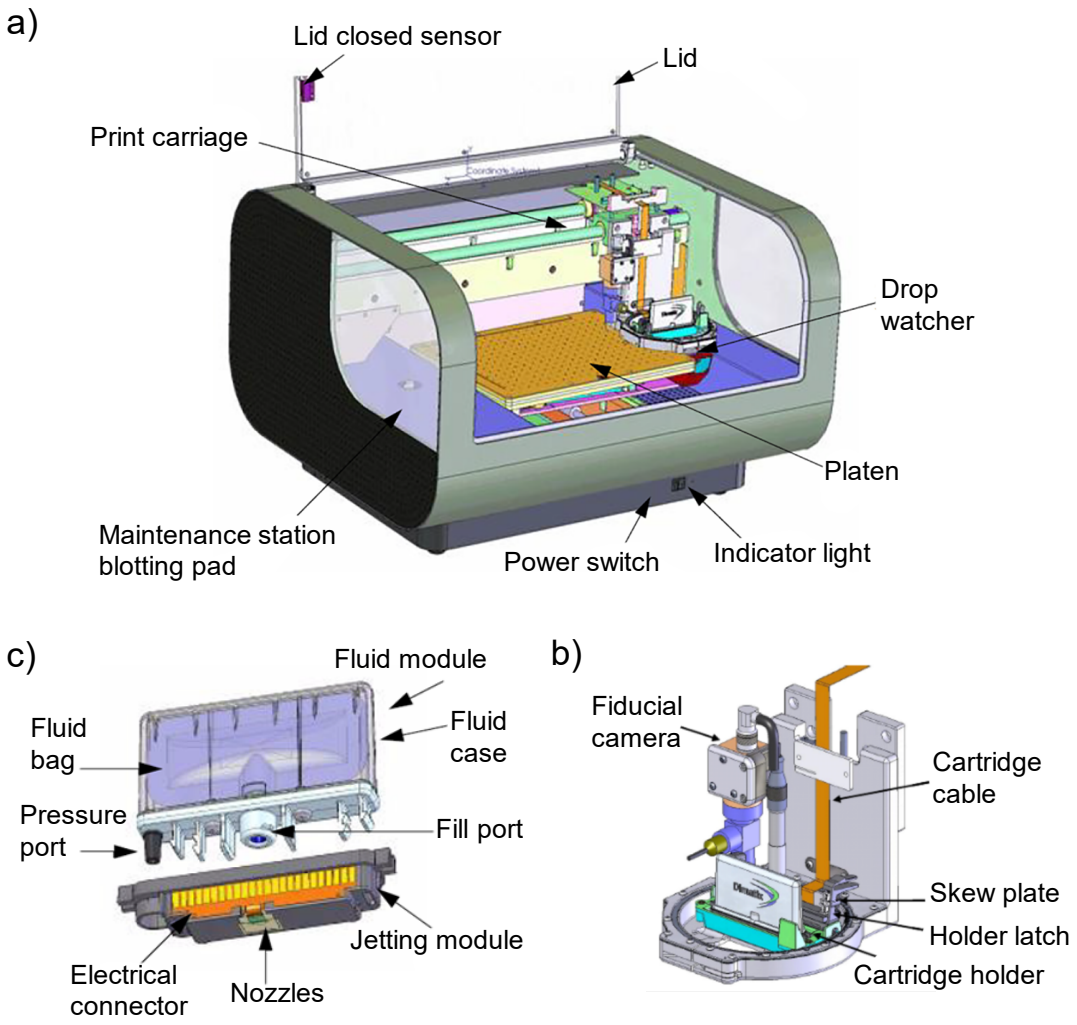

Figure 14. Schematics of a) Fujifilm DMP-2850 inkjet printer, b) print carriage, and c) cartridge components. Images adapted from the inkjet printer manual.

Table 4. Relationships between resolution, saber angle, and DS. Taken from the inkjet printer manual.

Resolution (dpi)	5080.00	2540.00	1693.33	1270.00	1016.00	846.67	725.71
Saber angle (°)	1.1	2.3	3.4	4.5	5.6	6.8	7.9
DS (μm)	5	10	15	20	25	30	35

Figure 15a shows the starting or standby position of the piezo-electric printhead's pumping chamber before the jetting pulse begins. The fluid chamber is slightly compressed by a bias voltage. When the pulse starts, the voltage drops to zero, returning the piezo to a neutral or relaxed state, which expands the chamber to its maximum volume (Figure 15b). During phase 1, fluid is drawn into the chamber

through the inlet, and the meniscus at the nozzle is pulled inward, as shown in the diagram. In phase 2, the chamber compresses, generating pressure to eject a droplet. The voltage then resets to its initial state, preparing for the next jetting cycle (Figure 15c). To achieve good printability, the manual recommends some parameters with proper ranges, i.e., viscosity of 10-12 mPa s and ST of 28-42 mN/m at jetting temperature, BP of solvents higher than 100 °C, specific gravity greater than 1, a pH-value of 4-9.

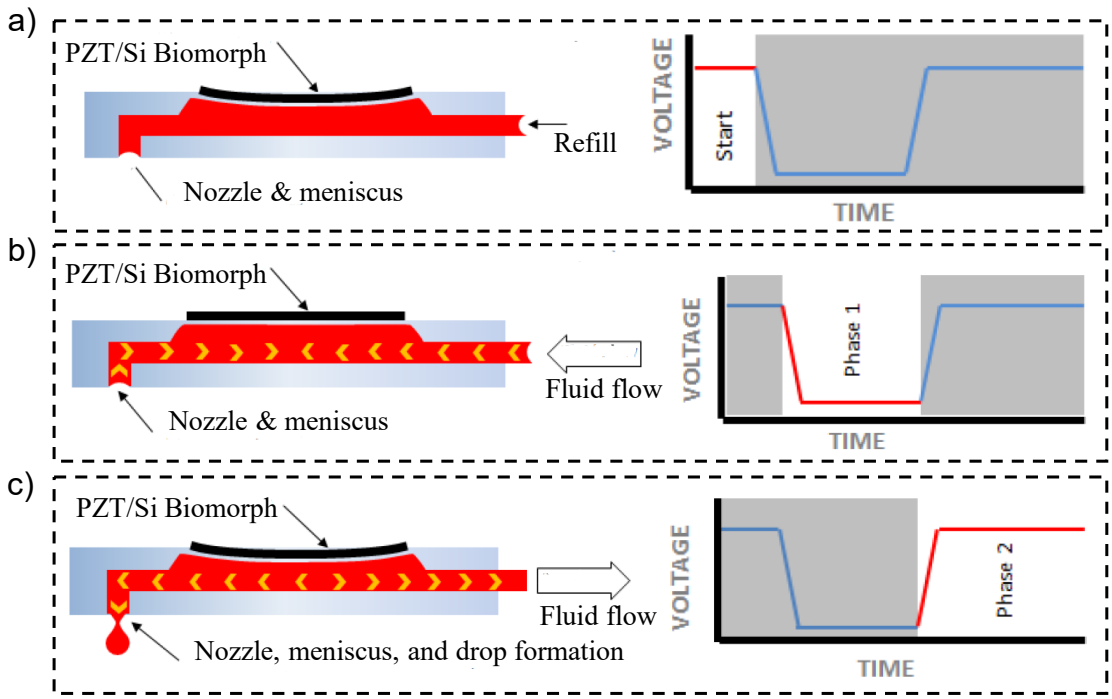

Figure 15. a) Standby, b) phase 1, and c) phase 2 of the status of the piezo-electric transducer and corresponding waveform. Images adapted from the inkjet printer manual.

Table 5. Physical properties of ink solvents [161].

Solvents	Density (g/cm^3)	Viscosity (mPa s, @20°C)	ST (mN/m)	BP (°C)	Vapor pressure (mmHg, @25°C)
Decane	0.73	0.92	23.8	174	1.4
CHX	0.78	0.93	24.7	81	96.9
CHB	0.94	2.81	34.6	239	0.1
Octane	0.70	0.50	20.0	125	13.6

The inkjet printing steps of QD inks are shown as follows. Initially, QDs were dispersed in the mixture of octane and cyclohexane (CHX) with a volume ratio of 1:1 [74], but the

nozzles were blocked shortly due to the low BP of the solvents. Hence, another ink formulation was tried by using higher-BP solvents, i.e., CHB and decane (Figure 16 inset) [72, 74]. Table 5 shows the physical properties of the solvents used, including density, ST, viscosity, BP, and vapor pressure. The inks were infilled in a cartridge (DMC-11601) with 16 1-pL nozzles at 254 μm spacing (nozzle diameter of ~12 μm) and then installed in the cartridge holder. The printing schematic and jetting waveform are shown in Figure 16. Drop space (DS), firing frequency, and voltage were optimized to be 20 μm (corresponding to the saber angle of 4.5°), 2 kHz, and 9.5 V, respectively. The distance between the nozzles and the substrate was set as the default value, i.e., 1 mm. After depositing the ink on the PVK film, the pattern was transferred into the glove box and annealed on a hot plate at 110 °C to evaporate the remaining solvents. Fluorescence images of inkjet-printed circular patterns by printing the QD ink with different T_{sub} and annealing temperatures (T_a) are provided in Appendix 9.3.

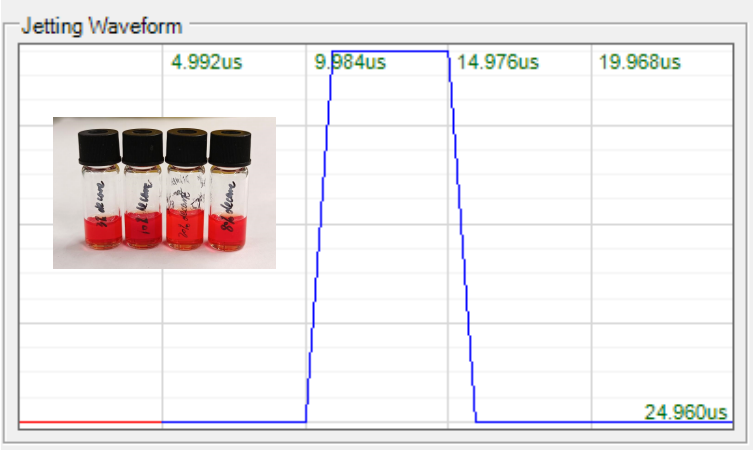

Figure 16. The jetting waveform for IJP. The inset is a photograph of QD inks with different volume ratios of decane (3%, 10%, 20%, and 80% from left to right).

2.4 Optical Spectroscopy

Optical spectroscopy is a non-invasive technique that measures the interactions between light and matter, including absorption, PL emission, and reflection, with outcomes influenced by factors such as polarization, wavelength, and intensity.

2.4.1 Steady-State PL Spectroscopy

PL spectroscopy measures the properties of QD's PL emissions by utilizing an Edinburgh Instruments FLS 980 spectrometer in this work (Figure 17). In a standard steady-state PL spectroscopy experiment, the QD dispersion in a sealed quartz

cuvette is continuously illuminated by a collimated beam of unpolarised light generated from a steady-state xenon lamp, with its wavelength controlled by an excitation monochromator and kept constant. Emitted light from the sample is collected using an emission monochromator and photomultiplier detector (PMT-900). Temperature was consistently maintained at 20 °C and controlled with a liquid Peltier cooler and resistance heater system.

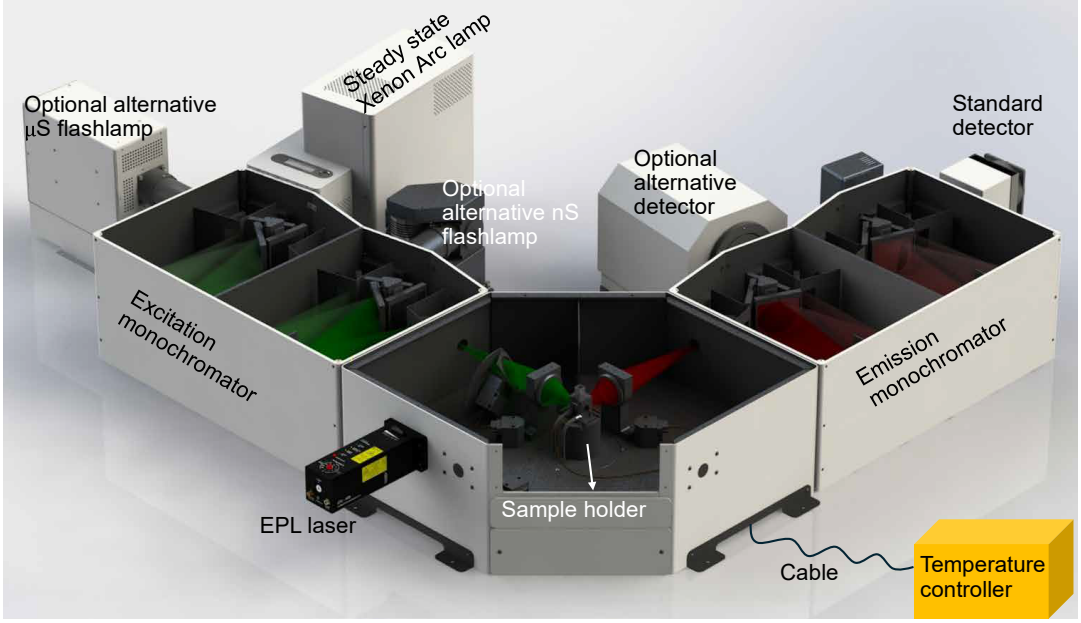

Figure 17. A schematic of Edinburgh Instruments FLS 980 spectrometer system. Image adapted from Edinburgh Instruments FLS980 manual.

2.4.2 PL Lifetime

Time-resolved PL (TRPL) spectroscopy, also known as fluorescence lifetime spectroscopy, was measured by Edinburgh Instruments FLS 980 spectrometer system combined with a highly controllable pulsed laser source (EPL 475) and highly sensitive, time-accurate photomultiplier. A typical lifetime experiment operated on the principle of time-correlated single photon counting. In this method, the QD dispersion in a sealed cuvette was illuminated by a short laser pulse of 79.5 ps at the wavelength of 473 nm, and the pulse period was set to 1000 ns. The time between the pulse and the first detection of an emitted photon was recorded using a photomultiplier and fast electronics for many pulses, and the data was plotted on a histogram. The experiment concluded when the largest histogram bin reached a user-defined value (1024). With sufficient data, the frequency density of each histogram bin was proportional to the probability of detecting the first photon at a specific time after excitation. Immediately

after photoexcitation, the maximum number of QDs was excited, making the probability of emission highest. As some excited states depopulate over time, the probability decreases. The resulting plot shows emission intensity over time after excitation, typically fitted as a sum of exponential decays:

$$I = A_0 + \sum_i A_i \, e^{-\frac{t}{\tau_i}} \tag{19}$$

Here, A_i and τ_i are the amplitudes and decay times of components, respectively. The fit can be evaluated by calculation of the χ^2.

$$\chi^2 = \sum_{k=1}^{n} \frac{[N(t_k) - N_c(t_k)]^2}{N(t_k)} \tag{20}$$

Here, $N(t_k)$, $N_c(t_k)$, and n are the measured fluorescence decay function, calculated decay function, and the number of data points, respectively. In this work, the plots were fitted by a biexponential function (i = 2) using the F980 software. The average lifetime of QDs was calculated by,

$$\tau_{avg} = \frac{A_1 * \tau_1^2 + A_2 * \tau_2^2}{A_1 * \tau_1 + A_2 * \tau_2} \tag{21}$$

This provides extensive insight into the excited state dynamics of the photoluminescent system. The dominant process's time constant, known as the PL lifetime, characterizes the timescale for excited states leading to radiative recombination. In QDs, the excited state dynamics are complex, and factors such as size polydispersity result in a wide range of recombination processes within a given ensemble.

2.4.3 PLQY Measurements

PLQY is the ratio of photons emitted via photoluminescence to the photons absorbed by the sample. To accurately determine PLQY, precise measurement of both photon absorption and emission is essential. This is achieved using an integrating sphere, an alternative sample holder of the aforementioned Edinburgh Instruments FLS 980. It includes a 120 mm diameter spherical cavity made from a polytetrafluoroethylene (PTFE)-like material with over 99% reflectance between 400 nm and 1500 nm and more than 95% reflectance from 250 nm to 2500 nm. The sphere has two ports placed 90° apart: one with a lens to focus the excitation beam on the sample, and another

open aperture to monitor emission or scatter with the FLS980 emission arm. A baffle near the exit aperture ensures only diffusely scattered radiation exits the sphere. An internal mirror directs the incident light either to the side for measuring QD dispersion (Figure 18a) or toward the bottom for the measurement of QD films (Figure 18b), positioned to prevent directly reflected light from leaving the sphere.

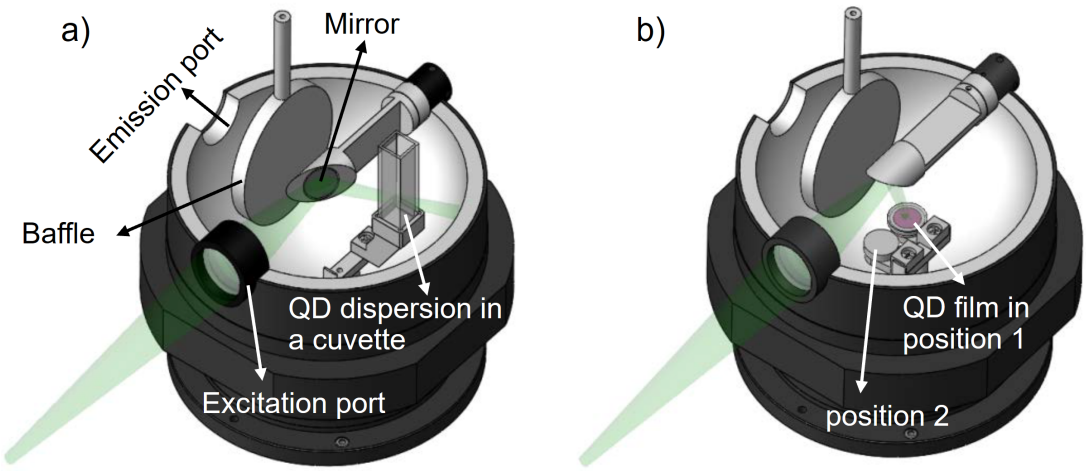

Figure 18. Integrating sphere configurations for measuring a) QD dispersions and b) QD films. Images adapted from Edinburgh Instruments FLS980 manual.

Spectra recorded for measuring the PLQY of QD dispersions include the reference solvent (octane, spectrum A in Figure 19a) and QDs dispersed in octane (spectrum B). The absolute fluorescence quantum yield, calculated with the “Direct Excitation” method is calculated as follows:

$$\eta = \frac{E_B - E_A}{S_A - S_B} \tag{22}$$

In terms of QD film’s PLQY, three spectra are scanned (Figure 19b). Spectrum A measures glass coverslips (reference) against blanking plugs in positions 1 and 2. For spectrum B, QD-coated glass coverslips against a PTFE plug and a glass coverslip against a blanking plug are placed in positions 1 and 2, respectively, while spectrum C is the opposite. The absolute fluorescence quantum yield, calculated with the “Direct and Indirect Measurement” method is calculated as follows:

$$\eta = \frac{S_B(E_C - E_A) - S_C(E_B - E_A)}{(S_B - S_C)S_A} \tag{23}$$

PLQY was calculated from these spectra using the F980 software. The relative humidity of 35% and 55% was controlled by saturated salt solutions of $MgCl_2 \cdot 6H_2O$ and $Mg(NO_3)_2 \cdot 6H_2O$, respectively with a weight ratio of 80% [162]. The RH and temperature were monitored using a digital temperature humidity meter (± 3% accuracy of RH and ± 1 °C accuracy of temperature).

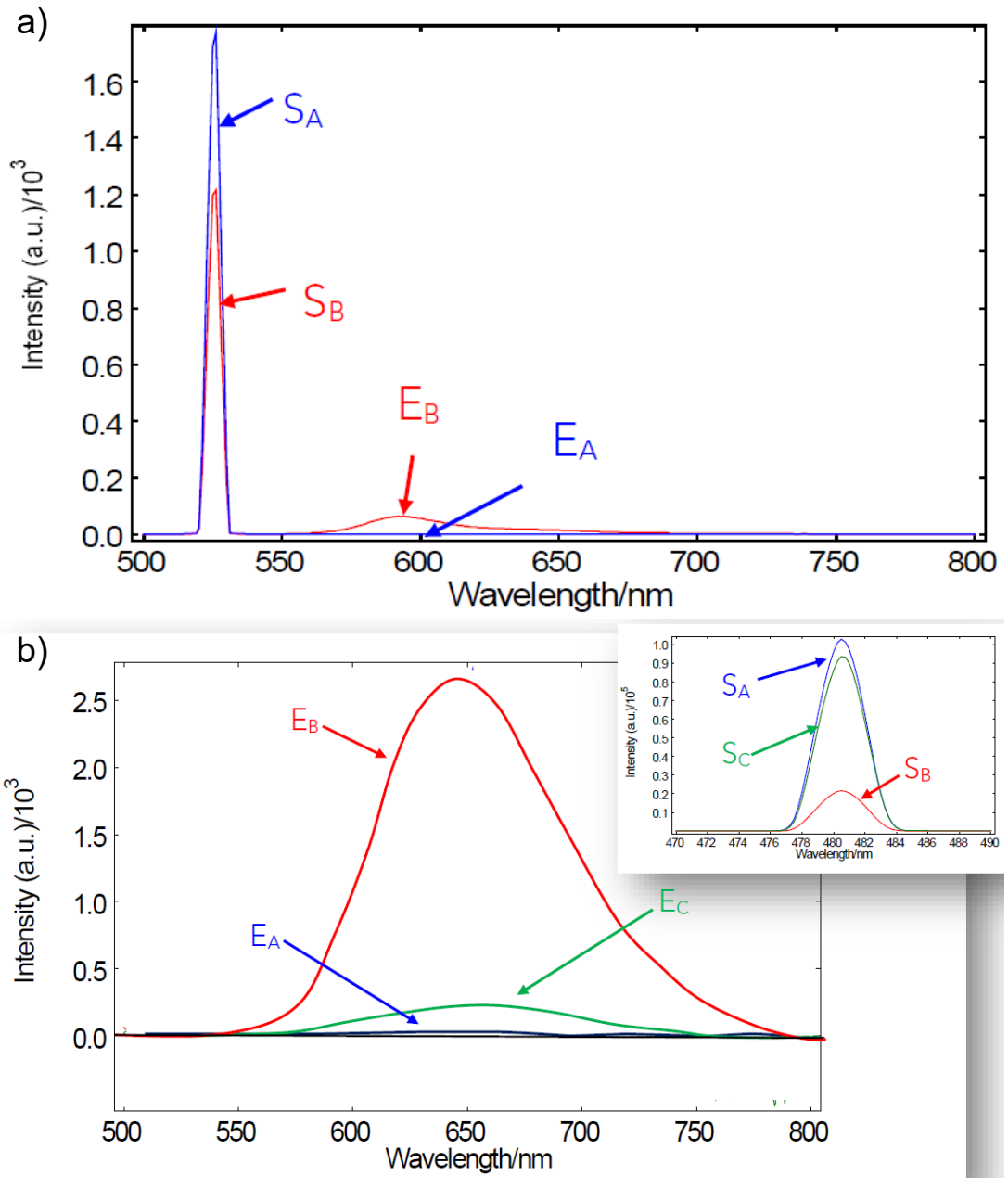

Figure 19. Spectral scans of the excitation scatter region (S-region) and the emission region (E-region) of a) QD dispersion and reference solvent and b) QD films and reference plug. Images adapted from Edinburgh Instruments FLS980 manual.

2.4.4 UV-Vis-NIR

UV-Vis-NIR absorption spectroscopy is a steady-state technique used to measure a sample's light absorption across ultraviolet, visible, and near-infrared wavelengths. This method is particularly suitable for studying the optoelectronic properties of semiconductor NPs, as many electronic transitions in NPs occur within this range of the electromagnetic spectrum. As discussed in section 1.4.3, when a photon has enough energy to excite an electron beyond the bandgap into discrete energy levels, the QD enters an excited state. If the photon's energy is below the minimum required for this excitation, no absorption occurs, which corresponds to the higher wavelength region. As the energy of the photon increases (i.e., the wavelength decreases), the first excitation peak appears, known as the first excitation peak. However, it's important to note that QDs in a sample are typically polydisperse, meaning they vary in size, which causes the first excitation peak to occur at slightly different energies for different particles. Consequently, the width of this peak reflects the degree of particle polydispersity. Beyond the first excitation peak, the energy levels become more closely spaced. This close packing makes it difficult to distinguish individual absorption peaks at higher photon energies (lower wavelengths).

The absorbance of a colloidal QD sample (*A*) is directly proportional to its molar concentration (*C*), allowing the molar concentration to be determined using the Beer-Lambert law, provided the molar extinction coefficient is known.

$$A = \varepsilon C l \tag{24}$$

Where *l* and *ε* are the path length of the light through the sample (10 mm in this work) and wavelength-dependent molar extinction coefficient, respectively. The molar extinction coefficient varies with the size and material of the QDs. For InP QDs, *ε* (in L mol^{-1} cm^{-1}) can be determined by [163]

$$\varepsilon = 3046.1 * D^3 - 76532 * D^2 + 551370 * D - 898390 \tag{25}$$

Here, *D* is the diameter of InP QDs. In UV-Vis-NIR spectroscopy, a blank solvent sample is first tested to serve as a reference. The sample's absorbance is calculated by comparing the intensity difference between the solvent and the QDs. The UV-Vis-NIR spectra for this study were obtained using an Agilent Technologies Cary 5000 UV-Vis-NIR spectrophotometer.

2.5 Fluorescence Microscopy

Fluorescence spectroscopy can analyze fluorescence from fluorophores (Figure 20). A light source, usually a mercury lamp, emits white light, which is then collimated and filtered to the specific wavelength needed to excite the fluorophore. This filtered light is reflected by a dichroic mirror and directed onto the back of an objective lens, which focuses it on the fluorescent sample. The emitted fluorescence is collected by the same objective lens, transmitted through the dichroic mirror, and passes through an additional filter to remove any extraneous light before reaching the camera or detection optics. A dichroic mirror is an optical component that reflects shorter wavelengths while transmitting longer ones, with the cut-off wavelength chosen based on the fluorophore in use. To ensure that the excitation light is reflected, and the emitted light is transmitted and detected, the appropriate dichroic mirror must be selected.

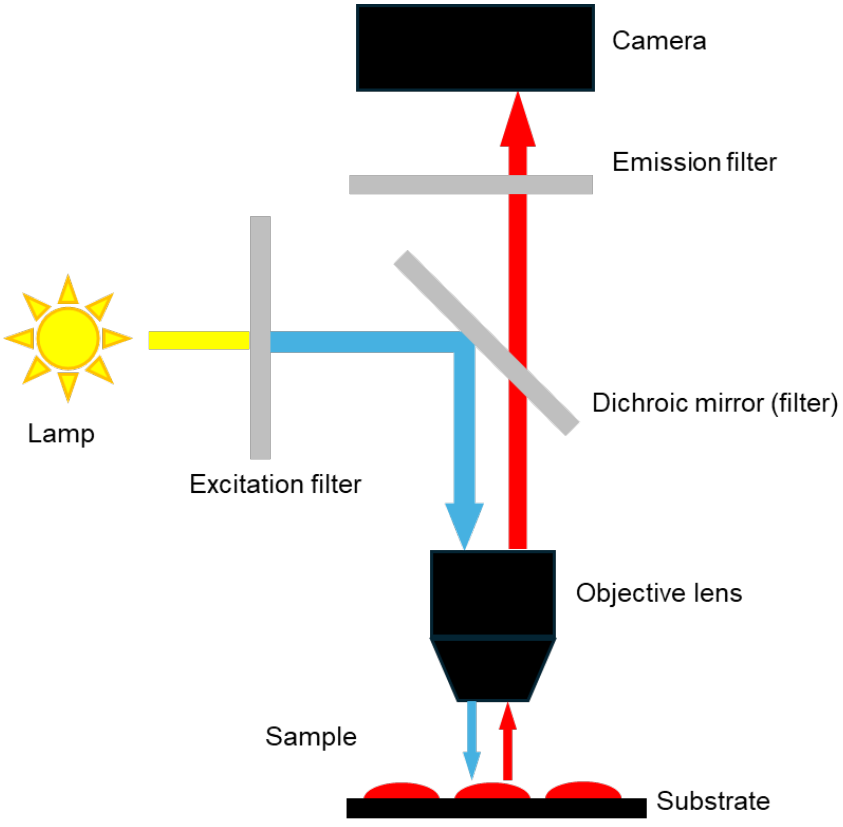

Figure 20. A schematic of the fluorescence microscope.

The resolution in epifluorescence microscopy is limited by the Abbe limit:

$$d = \frac{\lambda}{2n\sin\theta} \tag{26}$$

Where d, λ, n, and θ are the minimum resolvable distance, the wavelength of the light, the refractive index of the medium, and the half convergence angle of the focus of the lens, respectively. The inkjet-printed patterns and top-view evaporation of QD inks were characterized by the fluorescence microscope (E600, Nikon) facilitated with the Texas red filter and Edmund blue band pass filter (product code: 28-435), respectively. The line profiles of inkjet-printed patterns and the diameter evolution of droplet drying were analyzed using the ImageJ software.

2.6 Electron Spectroscopy

Transmission electron microscopes (TEM) achieve much higher resolution than optical microscopes due to the smaller de Broglie wavelength of electrons, as described by

$$\lambda = \frac{h}{p} \tag{27}$$

Where h is the Planks constant, and P is the momentum of electrons. This allows the TEM to capture extremely fine details, even down to a single column of atoms—thousands of times smaller than what can be resolved by optical microscopes. A TEM consists of several key components: a vacuum system for electron travel, an electron emission source to generate the electron stream, electromagnetic lenses, and a specimen stage (Figure 21). The electron source, typically a field emission gun, serves as the cathode and is maintained at a high potential with the anode, usually between 100-300 kV. Electrons are accelerated by this potential and focused into a tight beam by condenser lenses. The TEM operates at very low pressure (10^{-4} to 10^{-7} Pa) to prevent electron beam collisions with air molecules. After passing through a condenser aperture, the electron beam interacts with the sample, where electrons are either absorbed, scattered, or transmitted. High-resolution images are primarily generated by detecting scattered electrons, which appear darker against the transmitted beam. The transmitted beam is focused onto a charge-coupled device detector to create a bright-field image, with its resolution depending on the electron beam's wavelength. The electron beam can also eject inner orbital electrons from the sample atoms, creating vacancies that are filled by higher orbital electrons, releasing characteristic X-rays. Energy Dispersive X-ray spectroscopy (EDS) analyses these X-rays to identify and quantify the sample's elemental composition.

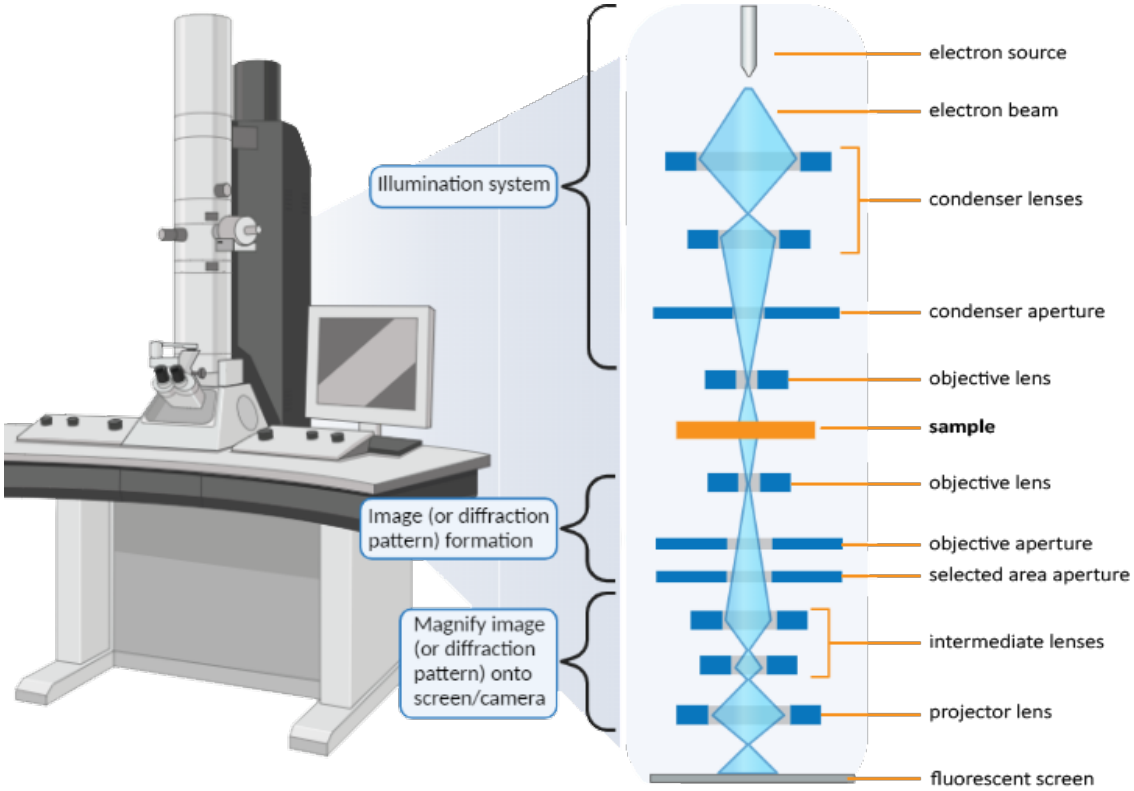

Figure 21. A schematic of a TEM system. Image taken from Nanoscience Instruments.

In this work, the size distribution and selected area electron diffraction (SAED) of InP/$ZnSe_xS_{1-x}$/ZnS QDs and $Zn_{0.9}Mg_{0.1}O$-EA NPs were measured by a transmission electron microscope (TEM, FEI Titan Cubed Themis 300 G2). The stock QD and NP dispersions were diluted 1000 times and then deposited on the graphene/carbon film-coated copper grids and annealed overnight under vacuum at 100 °C. The grids were also cleaned under argon plasma for 10 min to further remove contaminants and organic materials. The size was analyzed by using the Digital Micrograph software. The elemental ratio of $Zn_{0.9}Mg_{0.1}O$-EA NPs was characterized by EDX accompanied by the TEM. The crystal faces shown in the SAED images refer to standard PDF cards No. 32-0452 and No. 36-1451 for InP and ZnO, respectively.

2.7 Atomic Force Microscopy

Atomic force microscopy (AFM), a type of scanning probe microscopy, achieves resolution at nm-scale, over 1000 times finer than the optical diffraction limit. It gathers information by ‘feeling’ or ‘touching’ the surface with a mechanical probe. Piezoelectric elements in the cantilever enable precise and minute movements, allowing accurate scanning (Figure 22). AFM typically operates in three modes based on tip motion: contact mode (static), tapping mode (intermittent contact), and non-contact mode

(frequency modulation). Tapping mode is the most used AFM technique, especially under ambient conditions or in liquids.

In tapping mode, the cantilever oscillates up and down at or near its resonance frequency, typically driven by a small piezo element in the cantilever holder. The oscillation amplitude usually ranges from a few nm to 200 nm. The driving signal's frequency and amplitude are kept constant, ensuring a steady cantilever oscillation unless surface interaction occurs. As the tip nears the surface, forces like van der Waals, dipole-dipole interactions, and electrostatic forces cause a change, typically a decrease, in the oscillation amplitude. This change is monitored by an electronic servo, which adjusts the cantilever's height to maintain the set oscillation amplitude as it scans the sample. Tapping mode AFM images are thus produced by capturing the forces during these intermittent tip-sample contacts. Although peak forces can be higher than in contact mode, tapping mode generally reduces damage to both the surface and tip due to the shorter force application and significantly lower lateral forces.

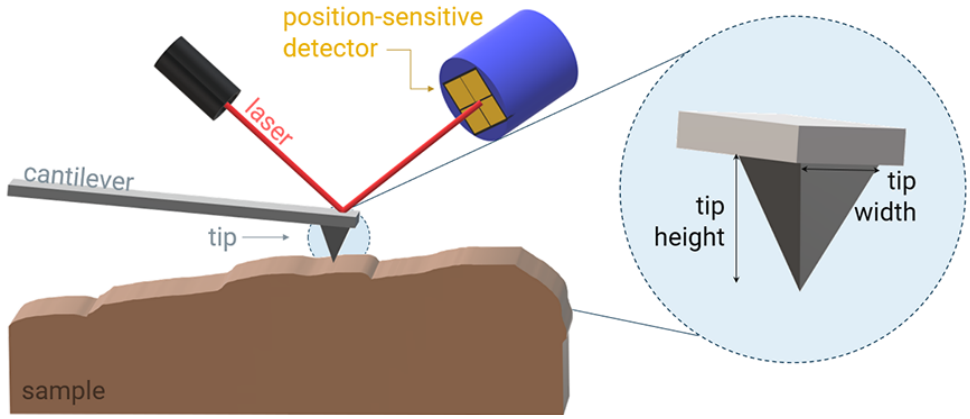

Figure 22. A schematic diagram of AFM. Image taken from Bruker.

In this study, the functional materials used in QD-LEDs were spin-coated on the ITO glass. The QD films were both inkjet printed and spin-coated. The spin-coating and inkjet-printing parameters were mentioned in section 2.3. The surface morphology and thickness of spin-coated and inkjet-printed films were measured by the tapping-mode AFM (Multimode 8, Bruker) with a TESPA-V2 tip (270-370 kHz). It was indicated by the root mean square average of height deviation taken from the mean image data plane (R_q). For measuring the thickness, the spin-coated films were scratched gently using a sharp wooden stick to make a clear step. The data were analyzed using Nanoscope Analysis software, and the step thickness was used as the film's thickness.

2.8 Spectroscopic Ellipsometry

Spectroscopic ellipsometry (SE) measures changes in light polarization as it reflects or transmits through a thin film (Figure 23). A light source emits unpolarized light, which then passes through a polarizer that filters it to a preferred electric field orientation. The polarizer axis is set between the p- and s-plane. Upon reflection, the linearly polarized light becomes elliptically polarized and passes through a continuously rotating polarizer (the analyzer). The amount of light passing through depends on the analyzer's orientation relative to the electric field 'ellipse' from the sample. A detector then converts the light into an electronic signal, determining the reflected polarization. By comparing this with the known input polarization, the change in polarization due to the sample reflection is measured, which is the ellipsometry measurement of amplitude - Psi (Ψ) and phase change - Delta (Δ). The measured response is influenced by the optical properties and thickness of the materials, making ellipsometry a key technique for determining film thickness and optical constants. A known polarization is reflected or transmitted from the sample, and the resulting polarization is measured. The change in polarization is the ellipsometry measurement, typically expressed as:

$$\rho = \tan(\psi)\, e^{i\Delta} = \frac{r_p}{r_s} \tag{28}$$

Where r_p and r_s are the Fresnel reflection coefficients for the p- and s-polarized light, respectively. As the film thickness increases, the separation between the light reflected from the surface and the light passing through the film also increases, creating a phase delay. This phase delay is influenced by both the film's physical thickness and its refractive index. Therefore, spectroscopic ellipsometry can accurately measure both thickness and refractive index.

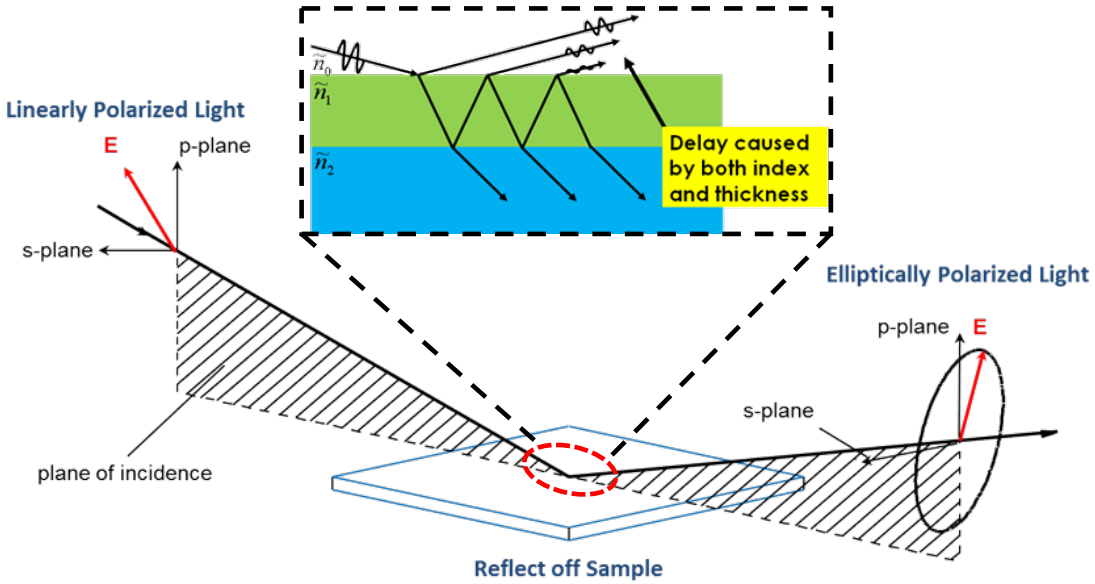

Figure 23. Interaction of polarized light with a sample. Image adapted from the CompleteEASE software manual.

In this work, the thickness of spin-coated functional films on the ITO glass or Si wafer was characterized using the ellipsometer (M-2000, J A Woollam) from 250 to 1000 nm. For the ITO glass substrate, a layer of magic tape was attached to the backside to avoid the backside reflection. The angles of light incidence were operated between 50° and 75° relative to the surface normal in steps of 5°. Ellipsometric data was analyzed on the CompleteEASE software and fitted by the Cauchy model initially in the transparent region (> 600 nm) with acceptable mean square error (MSE < 10). Cauchy model describes the relationship between refractive index (n) and wavelength (λ) as shown in the following equation:

$$n = A + \frac{B}{\lambda^2} + \frac{C}{\lambda^4} + \cdots \tag{29}$$

Where the three coefficients A, B, and C are optimized by CompleteEASE software and extinction coefficient (k) is assumed as 0. Mean square error (MSE), which quantifies the difference between data and model, is described as the following equation:

$$\text{MSE} = \sqrt{\frac{1}{3n-m}\sum_{i=1}^{n}\left[\left(N_{E_i} - N_{G_i}\right)^2 + \left(C_{E_i} - C_{G_i}\right)^2 + \left(S_{E_i} - S_{G_i}\right)^2\right] * 1000} \tag{30}$$

Where n and m are the number of wavelengths and the number of fit parameters, respectively, $N = \mathrm{Cos}(2\Psi)$, $C = \mathrm{Sin}(2\Psi)\mathrm{Cos}(\Delta)$, $S = \mathrm{Sin}(2\Psi)\mathrm{Sin}(\Delta)$. Then converted to the B-spline model to expand the fitting range down to 250 nm. Finally, the model was converted to the Gen-Osc model and fitted by Tauc-Lorentz oscillators with an MSE < 20. In the Gen-Osc model, the material's complex relative permittivity (ε) is fitted.

$$\varepsilon = \varepsilon_1 + i\varepsilon_2 \tag{31}$$

Where ε_1 and ε_2 are real and imaginary parts, respectively. For the Tauc-Lorentz oscillator,

$$\varepsilon_2(E) = \frac{A_n E_{On} Br_n \left(E - E_{gn}\right)^2}{(E^2 - E_{On}^2)^2 + Br_n^2 E^2} \frac{1}{E} \tag{32}$$

Where E, A, B_r, E_O, E_g, and n are the energy of light, amplitude, broadening, center energy, bandgap of material, and number of oscillators, respectively.

2.9 Rheology

Viscosity is a fluid property that indicates resistance to shear deformation or flow, driven by cohesive intermolecular forces that create friction between moving fluid layers. It depends on the attractive forces between molecules and the momentum exchange between layers in motion. Temperature affects viscosity differently in liquids and gases: in liquids, viscosity primarily arises from molecular cohesion. As temperature rises, molecules gain energy and move further apart, reducing cohesive forces and thereby lowering viscosity.

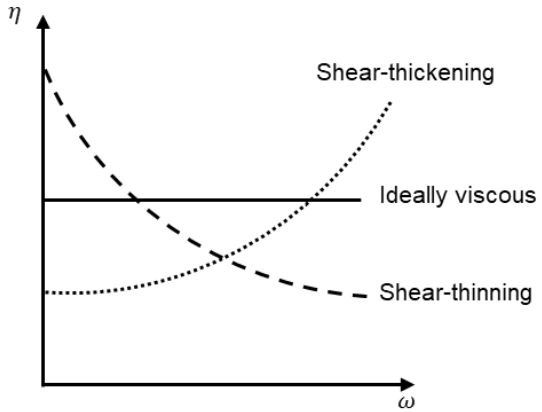

Figure 24. The viscosity of Newtonian and non-Newtonian fluids with respect to the shear rate. Image taken from Anton Paar.

Viscosity, specifically shear viscosity, is crucial for regulating fluid flow through the printhead nozzle. High flow rates and small nozzle diameters result in fluids operating under high shear rates (> 10^3 s^{-1}) [71]. Viscosity also affects how ink fills the printhead chamber. Many inks are classified as 'Newtonian,' meaning their viscosity remains constant regardless of the applied shear rate (Figure 24). Additives such as polymers can alter the fluid's behavior, resulting in viscosity that changes with shear rate, known as 'non-Newtonian' behavior. Typically, viscosity decreases with increasing shear rate, a characteristic of 'shear-thinning' fluids [164]. The opposite effect, where viscosity increases with shear rate, is known as 'shear-thickening' behavior [165]. The viscosity can be calculated by

$$\eta = \frac{\tau}{\omega} = \frac{\frac{F}{A}}{\frac{v}{h}} \tag{33}$$

Where τ, ω, F, A, v, and h are shear stress, shear rate, shear force, shear area, velocity, and shear gap, respectively. In this study, the viscosity of QD inks was measured at 20 °C by a rheometer (MCR302, Anton Paar) with a CP-50 measuring tool under a shear rate of 10^3 s^{-1}.

2.10 Contact Angle

CA is the angle formed at the intersection of the liquid, gas, and solid at the three-phase boundary. The shape of a droplet on a surface depends on the fluid's ST and the surface's properties (Figure 25). ST at the droplet's boundary with the surrounding gas creates a curved contour. The CA (θ) can be calculated by the Young's equation [84],

$$\cos\theta = \frac{\gamma^{\mathrm{sv}} - \gamma^{\mathrm{sl}}}{\gamma^{\mathrm{lv}}} \tag{34}$$

Where γ^{sl}, γ^{sv}, and γ^{lv} represent the solid/liquid interfacial free energy, solid surface free energy, and liquid surface free energy, respectively. If CA is between 0° and 90°, the surface is wettable and called hydrophilic. CA measures how well a liquid wets a solid surface and determines the droplet height on the substrate [166]. Reducing CA increases the contact area between the droplet and the solid surface while decreasing the droplet's thickness [167]. This enhances heat conduction through the droplet, accelerating its evaporation rate. If evaporation occurs significantly faster than particle

movement, the formation of a coffee ring may be suppressed [168].

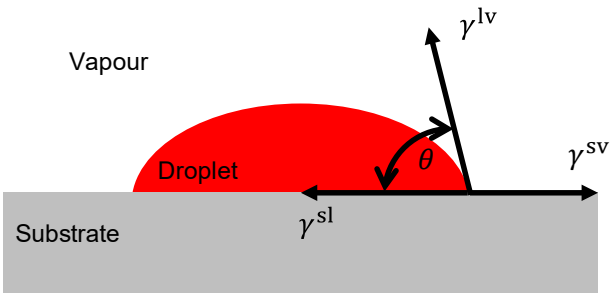

Figure 25. The CA of a droplet deposited on a solid surface.

In this work, CA was tested by a tensiometer (OCA 15EC, DataPhysics Instruments GmbH) via the sessile drop method for this study. The sessile drop method is the standard technique for measuring CA. In this method, a sessile drop is illuminated from one side with diffuse light, and its contour is observed from the other side. QD inks with different volume ratios of decane were deposited on the PVK-coated glass substrate at RT. For the CA evolution of the ink-20 at different temperatures, the PVK-coated glass was put on a hot plate. The CA was analyzed using the dpiMAX software.

2.11 Tensiometry

Surface tension is crucial in IJP, influencing drop formation, satellite creation, and interactions with the substrate. The shape of a pendant drop is primarily determined by two forces: gravity, which elongates the drop based on its mass, and ST, which tries to maintain a spherical shape to minimize surface area. In equilibrium, the drop's curvature is defined by the Young-Laplace equation, allowing ST to be calculated from the drop's shape and size, particularly when the drop is large enough to deviate from a perfect sphere. The ST can be expressed by:

$$\gamma = \frac{\Delta\rho g R}{\beta} \tag{35}$$

Where γ is the ST, $\Delta\rho$ is the density difference between fluids, g is the gravitational constant, R is the drop radius of curvature at the apex, and β is the shape factor. ST arises from cohesive forces among liquid molecules. In the liquid's bulk, molecules are equally pulled in all directions, resulting in no net force. However, surface molecules lack neighboring molecules on all sides, causing them to be pulled inward, generating internal pressure and contracting the liquid surface to minimize area. Before measuring

the ST of QD inks, the density was checked by dividing the mass weighed by its volume. The ST was tested by the tensiometer (OCA 15EC, DataPhysics Instruments GmbH) via the pendent drop method and analyzed using the dpiMAX software.

2.12 Electrical Properties of InP QD-LEDs

When characterizing QD-LEDs, three critical data sets are reported: current-voltage (*J-V*) characteristics, external quantum efficiency (EQE), and the EL spectrum. EQE is defined as the ratio of the number of photons emitted per second to electrons injected into the device as a function of time, which can be calculated by

$$\mathrm{EQE}\ (\%) = \frac{e\ \Phi_p}{I} \tag{36}$$

Where *e*, Φ_p, and *I* represent the elementary charge, total photon flux, and current, respectively. Φ_p is derived either from the spectral radiant flux ($\Phi_e(\lambda)$, unit: W) or the spectral luminous flux ($\Phi_v(\lambda)$, unit: lm) with the knowledge of the emission spectrum.

$$\Phi_p = \int \frac{\Phi_e(\lambda)}{\frac{hc}{\lambda}} d\lambda = \int \frac{\frac{\Phi_v(\lambda)}{K_m V(\lambda)}}{\frac{hc}{\lambda}} d\lambda \tag{37}$$

Where *h*, *c*, and *λ* are the Plank constant, the speed of light in the vacuum, and the emission wavelength, respectively. K_m represents the peak luminous efficacy at the wavelength of 555 nm (683 lm/W). $V(\lambda)$ is the standard spectral luminous efficiency function, which defines the human eye's relative sensitivity to light across different wavelengths (Table 6).

Table 6. Normalized standard spectral luminous efficiency function [169].

Wavelength (nm)	620	621	622	623	624	625
CIE-1931 V(λ)	0.381	0.369	0.357	0.345	0.333	0.321

Radiometric (signal response to Φ_e) and photometric (signal response to Φ_v) measurements are essentially equivalent. Photometric methods are capable of directly measuring the luminous intensity and luminance of a single QD-LED device. Since QD-LEDs typically display axially symmetric intensity characteristics, the luminous intensity is related to the total luminous flux via the following equation:

$$\Phi_v = \int I_v d\Omega = \int_0^{\pi/2} 2\pi I_v(\theta)\, sin\theta d\theta \tag{38}$$

Where θ is the viewing angle with respect to the direction perpendicular to the device surface. For the bottom-emitting QD-LEDs, the devices show Lambertian-type angular distribution of EL intensities. The luminance can be derived from the reduced integration of the total luminous flux,

$$\Phi_v = \int_0^{\pi/2} 2\pi I_v(0°)\, cos\theta\, sin\theta d\theta = \pi A L_v \tag{39}$$

Where L_v is the luminous intensity per area and A is the active area of the QD-LEDs.

2.12.1 *I-V* Behavior

For QD-LEDs with organic small molecule CTLs, the shape of the *J-V* curves can be analyzed using the theory for crystals with low mobility, which suggests a $J \sim V^n$ relation [170]. This includes four distinctive regions: ohmic conduction (n = 1), trap-limited space charge-limited conduction (T-SCLC, n = 1-2), trap-filled limited (TFL, n = 2-100) conduction, and space charge-limited conduction (SCLC, n = 2), as shown in Figure 26. Ohmic conduction usually occurs only in defect-free devices and at very low voltages. Steeper slopes suggest the presence of trap states. This analysis allows temperature-dependent *J-V* measurements to estimate the energy of these trap states. The current density-voltage (*J-V*) characteristic was collected via a push-fit test board (P2008A1, Ossila) and computer-controlled Keithley 2400 source meter. The data were recorded by Kevin Critchley's Python code.

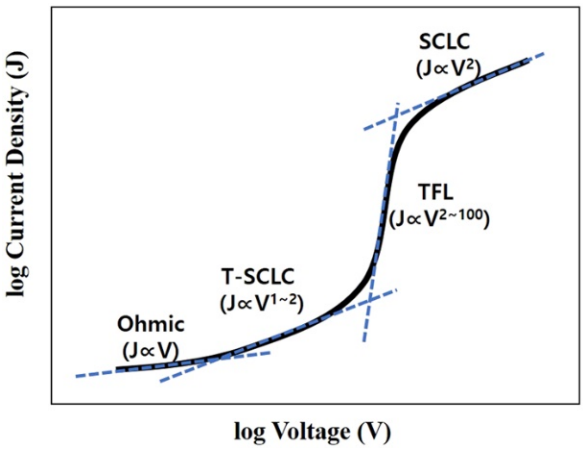

Figure 26. *J-V* behavior is characterized by a different power law relationship in a semiconductor layer. Reprinted with permission from [171]. Copyright 2019 AIP.

2.12.2 Steady-State EL Spectroscopy

The steady-state EL spectroscopy measures the emission wavelength and intensity of QD-LEDs under different applied voltages. The luminescence spectra are crucial for understanding and characterizing QD-LED's operation. Differences between the PL spectra of the QD solution and QD film in the device can indicate damage to the QD layer during fabrication or a microcavity effect due to varying refractive indices in the thin film stack. In this study, the EL spectra of QD-LEDs were recorded using the bioluminescent mode of the fiber-optic spectrometer (LS55, Perkin-Elmer) connected to the computer-controlled Keithley 2400 source meter.

2.12.3 Luminance Measurement

A luminance meter is a commonly used photometric device for measuring the luminance of extended light sources. It can also be used to determine the total luminous flux (or radiant flux) of LEDs. The meter collects light from a small area of the emitting device and measures the luminance within that specific field of view. The absolute luminance needs to be calibrated using a luminance-standard source with uniform brightness. To ensure accurate measurement, the light source should be significantly larger than the measurement field. In this work, the power was supplied with the 2400 source meter, and the luminance of QD-LEDs was measured by the digital luminance meter (TEN01070). The distance between the detector of the luminance meter and QD-LEDs is approximately 18 mm.

2.13 NAP-XPS

X-ray photoelectron spectroscopy (XPS) is a surface-sensitive, quantitative technique that analyses the topmost 10 nm of any surface, equivalent to about 200 atoms. XPS leverages the photoelectric effect to determine the elemental composition, chemical state, electronic structure, and density of electronic states in a material. It is commonly used to investigate chemical processes in materials either in their original state or after treatment, such as heat exposure, reactive gases, and UV light. A typical XPS spectrum plots the number of electrons detected at a specific BE, with each element producing characteristic peaks corresponding to its electron configuration (e.g., 1s, 2s, 2p). The BE can be expressed by

$$E_{\mathrm{b}} = E_{\mathrm{p}} - (E_{\mathrm{k}} + \phi) \tag{40}$$

Where E_b, E_p, E_k, and ϕ are the BE of the electron measured relative to the chemical potential, the energy of the X-ray photons being used, the kinetic energy of the electron as measured by the instrument, and a work function-like term for the specific surface of the material, respectively. The intensity of each peak is proportional to the element's concentration within the sampled volume. To obtain atomic percentages, the raw XPS signals are corrected by dividing the intensity by a relative sensitivity factor (RSF) and then normalized across all detected elements.

However, XPS has a significant limitation: it is a post-mortem technique. Since samples are in a high vacuum during measurement, XPS can only examine the state of a sample before and after a chemical reaction, not during the reaction itself, which is often the most insightful phase. NAP-XPS addresses this limitation by enabling XPS characterization in a gaseous environment (Figure 27). This is done by placing the sample in a high-pressure cell with a small aperture connected to the analyzer. A series of pumping stages after the aperture quickly reduces the pressure to a high vacuum, minimizing the distance electrons travel through the gas. By positioning the sample surface close to the aperture, the area under analysis can be exposed to high gas pressure while still allowing a detectable fraction of emitted photoelectrons to reach the detector.

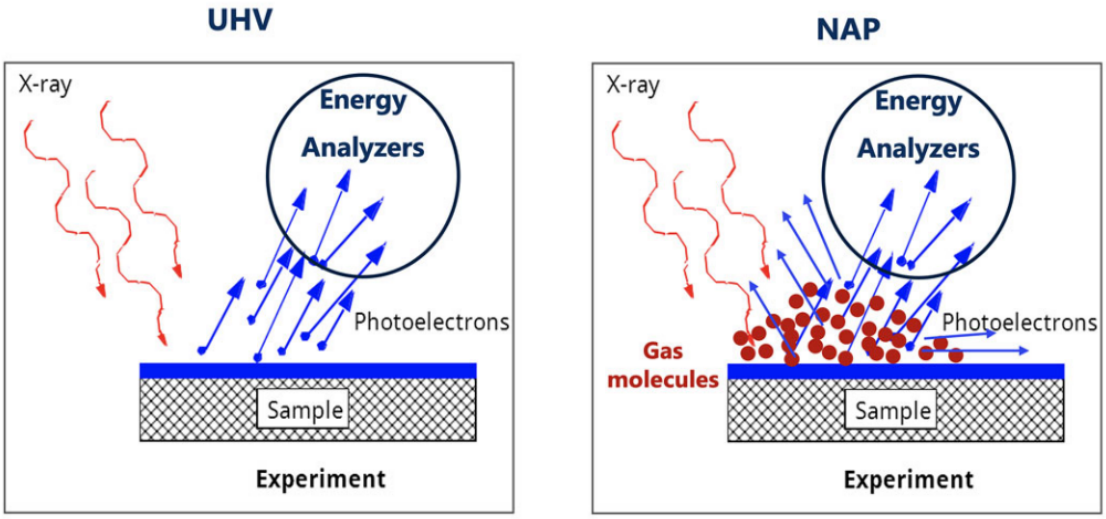

Figure 27. Schematics of interactions between X-ray and sample's surface atoms in the UHV (left) and NAP (right) experiments. Images were taken from the SPECSgroup website.

In this work, 19-nm-thick QD films were spin-coated at the spin speed of 2000 RPM for 30 s in the glove box. After annealing at 80 °C for 10 min, the QD films were

transferred to the XPS UHV chamber. XPS was performed in a SPECS NAP-XPS system consisting of a UHV (~5 x 10^{-10} mbar) analysis chamber equipped with an Ar cluster source for surface preparation and e-beam heating capability. Monochromated Al Kα X-rays (1.486 keV photon energy, 14.5 kV, 120 W/25 W) were focussed to a spot of 300 μm or 1 mm diameter, and the emitted photoelectrons were detected using a SPECS Phoibos 150 NAP differentially pumped analyzer. Here, 120 W/1 mm for measurements using the 'Micro 1' setting (UHV only), and 25 W/300 μm for measurements using the 'Micro 4' setting (NAP). After measuring the survey and fine scans of C 1s, Zn 2p, S 2p, Se 3p, In 3d, P 2p, Zn LMM, and O 1s, the QD films were transferred to the NAP cell. NAP experiments were performed by placing the sample inside a NAP cell which was maneuvered into the analysis chamber and docked directly to the analyzer. This cell was sealed, except for a 300 μm aperture which allows pressures within the cell to reach up to 3 mbar through the controlled addition of oxygen or water vapor. X-rays entered the cell through an X-ray transparent silicon nitride window and were focussed onto the sample which was held approximately 300 μm from the aperture leading to the detector. This optimized distance between the sample surface and the entrance to the differentially pumped detector ensures that minimal signal is lost due to attenuation of the photoelectrons by the gas in the NAP cell, which in turn ensures sufficient signal can reach the detector. Survey spectra were measured with a pass energy of 60 eV, and high-resolution core level spectra with a pass energy of 20/30 eV. Scanning was performed cyclically to allow the identification of any changes in the sample due to exposure to the experimental conditions. The QD films were measured at RT in the NAP cell for 8 h, and then the temperature was elevated to 100 °C and measured for 8 h. Subsequently, the QD films were transferred to the UHV cell for measurement. The $Zn_{0.9}Mg_{0.1}O$ and $Zn_{0.9}Mg_{0.1}O$-EA NPs were measured under UHV at RT. Analysis of the data was performed in CasaXPS software, and the BE scale was calibrated from hydrocarbon ligands using the C-C/C-H peak at 284.8 eV. All photoelectron BEs are quoted to a precision of ± 0.05 eV. Regions and components were fitted to each peak with the appropriate RSF taken from the Scofield library file within CasaXPS. Core peaks were analyzed using a nonlinear Shirley-type background. The peak positions and areas were optimized by a weighted least-squares fitting method using 70% Gaussian, and 30% Lorentzian line shapes. The atomic percentage (at%) of elemental core level peaks was calculated by [172],

$$\mathrm{At}\% = \frac{\frac{A_x}{RSF_x}}{\sum_n \frac{A_i}{RSF_i}} \tag{41}$$

Here, A_x represents the area under the peak for element x, while the relative sensitivity factor (RSF_x) ensures consistent scaling of the measured area regardless of the chosen peak. RSF values were determined using the same instrument settings, including pass energy, anode power, and aperture size.

3. Characterisation of InP QDs and $Zn_{0.9}Mg_{0.1}O$ NPs

Understanding the optical properties and morphology of specific QDs is essential for advancing their application in QD-LEDs. InP/$ZnSe_xS_{1-x}$/ZnS QDs are attractive candidates for the development of QD-LEDs due to their reduced toxicity and optical performance comparable to that of Cd-based QDs. The optical properties are inherently linked to the QD's structure, particularly with respect to the composition and thickness of the shell. $Zn_{1-x}Mg_xO$ NPs are widely used as ETL materials owing to their high electron mobility and chemical stability [143, 173]. The Mg doping ratio in $Zn_{1-x}Mg_xO$ greatly impacts the electron mobility of the NP films, which in turn affects the carrier injection balance in QD-LED devices. The following study was to explore the structure and chemical composition of InP/$ZnSe_xS_{1-x}$/ZnS core/shell/shell QDs and $Zn_{1-x}Mg_xO$ NPs, and how this relates to their optical properties.

3.1 Background

Bulk InP has a slightly smaller bandgap compared to bulk CdSe (1.34 eV vs 1.74 eV), allowing InP QDs to emit across the visible spectrum and into the lower infrared range. InP's higher covalency causes greater carrier mobility (4600 vs 900 $cm^2/V \cdot s$) and a much larger Bohr exciton radius than CdSe (10.8 nm vs 3.0 nm), providing enhanced optical tunability [12]. However, this tunability comes at the cost of a rapidly widening bandgap as the NC size decreases. The higher covalency of InP also complicates synthesis, requiring more reactive precursors, which increases the likelihood of lattice defects and broadens emission linewidths [5]. This creates a growth barrier and heightens sensitivity to oxidative degradation. InP QDs have similar synthesis protocols as Cd/Pb/Hg-based QDs, which can be synthesized by hot injection [154]. In the hot-injection method, a rapid nucleation burst followed by a slow growth stage is ideal for obtaining monodisperse colloidal NCs, as described in section 1.4.5. The room-temperature precursor solution is quickly injected into the hot reaction medium, triggering monomer formation and a nucleation burst. Within seconds, the solution temperature drops, causing a decrease in monomer concentration and terminating nucleation. The growth stage then begins, with no further nuclei formation. The nucleation of covalent InP QDs requires higher temperature, longer time, and reactive precursor than ionic CdSe QDs. However, the crystallization of InP QDs does not follow the LaMer model completely because the unavoidable overlap of nucleation and growth processes hinders precise size control, leading to a broad distribution [174].

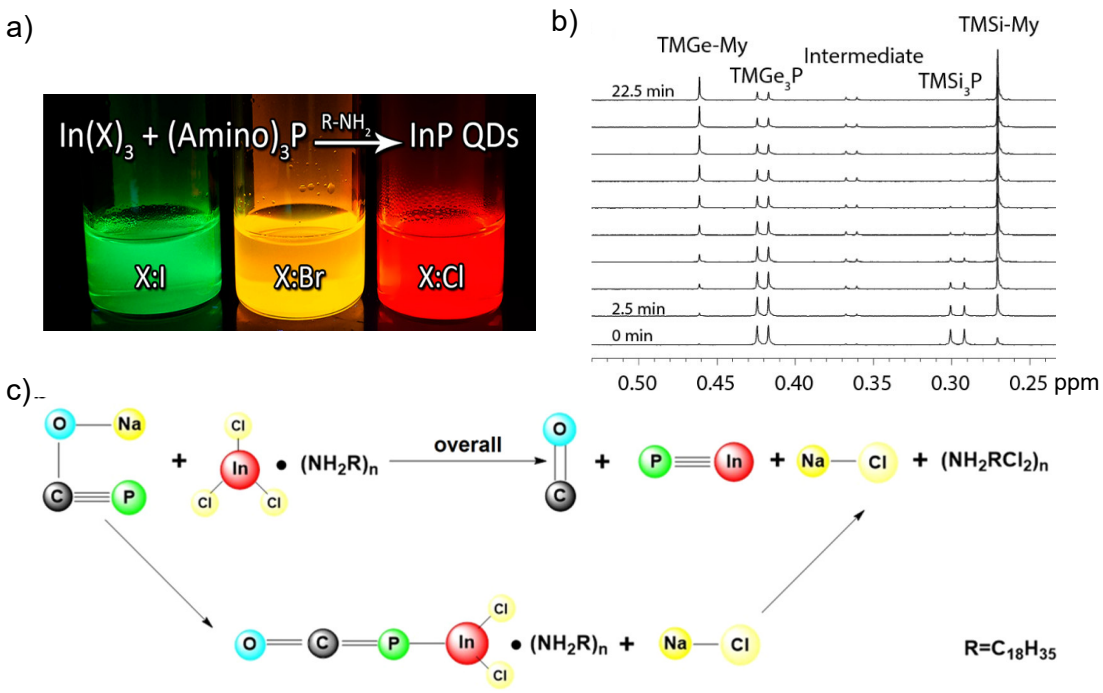

Figure 28. a) A photograph of illuminated InP QDs synthesized by InI_3, $InBr_3$, and $InCl_3$. Reprinted with permission from [175]. Copyright 2015 ACS. b) Temporal evolution of NMR spectra showing the simultaneous reaction of $P(SiMe_3)_3$ and $P(GeMe_3)_3$ precursors with indium myristate. Reprinted with permission from [176]. Copyright 2012 ACS. c) Schematic illustration for the formation of InP QDs using inorganic P source of NaOCP. Reprinted with permission from [101]. Copyright 2021 ACS.

The selection of In and P precursors greatly influences the resultant size and optical properties of InP QDs. Most indium precursors are simple In(III) salts such as indium halides $In(X)_3$ (X = Cl, Br, I) or indium acetate. The halogens can affect the resultant size of InP QDs by tuning the rate constants of the surface reaction and solute solubility (Figure 28a) [175]. $P(SiMe_3)_3$ (Me = CH_3) serves as the [P] precursor for most InP syntheses adapted from Wells' dehalosilylation reactions. However, the high reactivity of the P-Si bond depletes [P] precursor rapidly, causing the broad size distribution of NCs [177, 178]. And expensive $P(SiMe_3)_3$ is responsible for most of the chemical cost. $P(SiMe_3)_3$ derivatives were therefore proposed to reduce its reactivity and cost by introducing bulky side chains [174, 179] and substitute stronger P-X (X = Ge [180], Sn [176], or N [154]) for the fragile P-Si bond (Figure 28b). Except for organic [P] precursor, inorganic alternatives like P_4 [181] and PH_3 [182] were reported but they are very toxic and dangerous, and the size distribution is undesirable. Recently, Yu et al. adopted a cheaper and greener [P] source, sodium phosphaethynolate (NaOCP), to synthesize red, green, and blue InP QDs with corresponding high PLQY of 95%, 97%, and 43%, respectively (Figure 28c) [101].

The QD surface significantly influences their optical properties due to the large surface-volume ratio. Upon excitation, when electrons delocalize across the entire QD, they are easily trapped by surface ions or vacancies. This creates localized defect states within the bandgap, leading to the dissipation of excitation energy. Despite the QD surface being passivated by ligands, surface-related quenching cannot be prevented, such as surface oxides and dangling bonds, which are the primary reasons for their low PLQY (<1%). Covalent InP QDs show more and deeper trap states than ionic CdSe QDs [183]. Hence, composition engineering and surface engineering were introduced to suppress surface states and enhance optical performance.

Composition engineering dopes metal ions into InP QDs, such as Zn^{2+} [184], Cu^{+} [106], and Ag^{+} [185], and the bandgap of the doping material is generally larger than that of InP. Among them, Zn-doping has been widely applied to synthesize high-quality InP QDs. By increasing the In/Zn ratio, the emission peak and first excitonic peak show a blue shift because of the replacement of In^{3+} with Zn^{2+}, the formation of Zn-P, and size reduction (Figure 29a) [184]. However, adding excessive Zn precursor deteriorates QDs' optical properties, so the In/Zn ratio, the type of Zn precursor, and reaction temperature need to be precisely controlled.

Surface engineering includes ion passivation and shell coating. Ion passivation is an easy post-treatment method that suppresses trap states by binding added ions to dangling bonds. Fluorides (e.g., HF, NH_4F, etc.) and Lewis acids are utilized as agents to etch away the P dangling bonds and displace In^{3+} ions, respectively [186, 187], mitigating the quenching effect (Figure 29b). However, despite its simplicity, ion passivation has not proven to be an effective method for producing high-quality InP QDs. The resulting QDs exhibit low PLQY and poor stability.

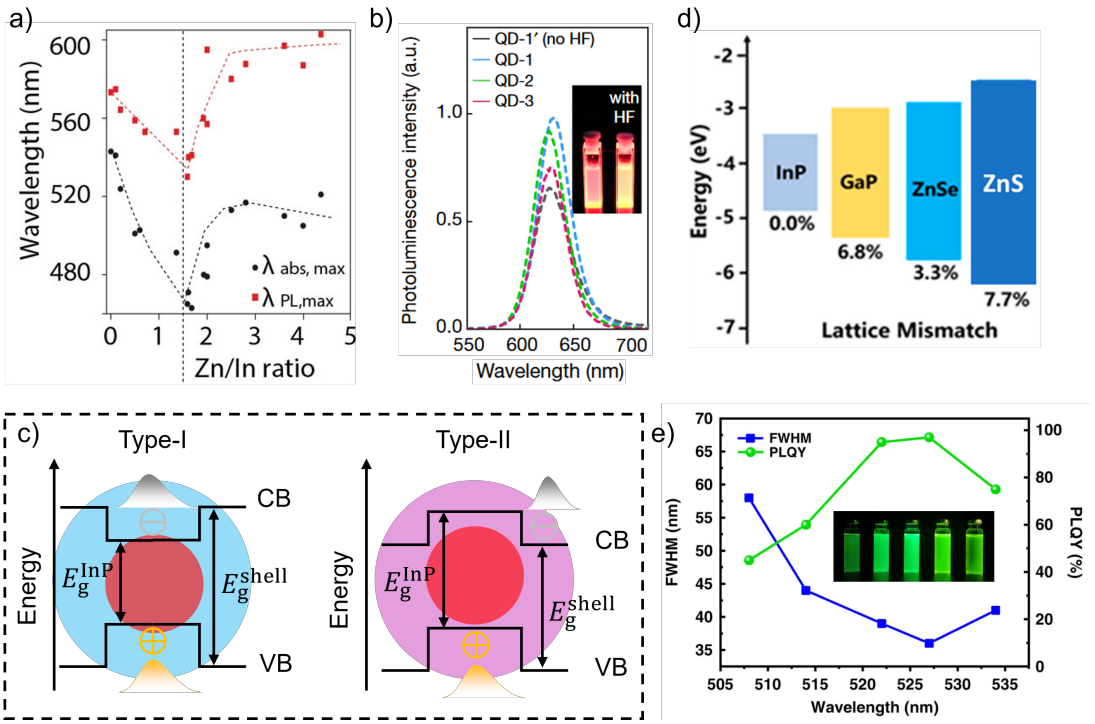

Figure 29. a) Maximum absorbance and PL emission wavelength as a function of the Zn/In molar ratio. Reprinted with permission from [184]. Copyright 2016 ACS. b) PL spectra and PL photos of the InP core before and after adding HF. Reprinted with permission from [148]. Copyright 2019 Nature Springer. c) The band alignment of type-I and type-II configurations. d) Lattice mismatches between InP and other semiconductors that were usually used as shells. Reprinted with permission from [188]. Copyright 2020 ACS. e) FWHM and PLQY of InP/$ZnSe_xS_{1-x}$/ZnS (x = 0, 0.3, 0.5, 0.7, and 1 from left to right). The inset photo is the corresponding PL of QDs irradiated by an ultraviolet lamp. Reprinted with permission from [50]. Copyright 2022 Nature Springer.

Compared with ion passivation, embedding shell materials into the core can further improve the PLQY of InP QDs, including a single shell, multiple shells, and gradient shell. When choosing a suitable shell material, the following parameters should be taken into consideration. Firstly, the band gap of the shell material should be greater than that of the core to effectively confine charge carriers within the core. Secondly, large offsets for both the VB and CB edges are preferable. Lastly, it is desirable for the crystal structures and lattice parameters of the core and shell materials to closely match. A core-shell QD can be classified into type-I and type-II structures based on the alignment of electronic bands between the core and shell. For the type-I structure, the CB edge of the shell material has a higher energy, whereas its VB edge has a lower energy compared to the core material (Figure 29c). This configuration effectively confines both electrons and holes within the core, enhancing luminescence and stability for lighting applications. Examples are ZnS [189], ZnSe [148], and GaP [190]

because the II-VI group atoms (Zn, S, and Se) are easily doped into III-V atoms and vice versa.

ZnS shell is adopted from the CdSe/ZnS system, which provides strong electron confinement and high stability because of its large bulk bandgap (3.54 eV) and suitable band alignment. But the large lattice strain regarding InP (7.6%) limits the thickness of ZnS, ZnSe with a smaller misfit strain (3.4%) is an alternative to replace ZnS (Figure 29d) [188]. Although narrower FWHM was obtained with InP/ZnSe QDs, the weaker QC makes it lower PLQY than InP/ZnS QDs (50% vs 60%). Therefore, a multi-shell structure with ZnSe as the middle shell and ZnS as the outer shell (InP/ZnSe/ZnS) was proposed to realize both strong QC and small misfit strains [99]. Moreover, alloyed InP/$ZnSe_{1-x}S_x$ QDs also work effectively by varying the injection molar ratio of Se and S, which is attributed to the lower reaction rate of TOP/S than that of TOP/Se (Figure 29e) [50, 191]. Regarding the type-II structure, both the valance and conduction band edges of the core are situated either below or above the corresponding band edges of the shell material, facilitating spatial separation of hole and electron wavefunctions and leading to an extended exciton lifetime, which is ideal for photovoltaic application, such as CdSe [192] and ZnO [193].

3.2 Characterisation of InP QDs

The optical properties (absorbance, steady-state PL, PLQY, and TRPL) of the InP core, InP/$ZnSe_xS_{1-x}$, and InP/$ZnSe_xS_{1-x}$/ZnS QDs were measured and analyzed. The morphology, size distribution, and chemical composition of InP/$ZnSe_xS_{1-x}$/ZnS QDs were characterized.

3.2.1 Optical Properties of QDs

Sequential products, including InP core, InP/$ZnSe_xS_{1-x}$, and InP/$ZnSe_xS_{1-x}$/ZnS QDs, were synthesized from the same batch. The synthesis protocol is described in detail in section 2.1. The color of the precursor solution changed from pale yellow to dark red following the core nucleation and then to an orange-reddish hue after the shell coating (Figure 12). UV-vis spectra of the samples at different stages of synthesis (i.e., core, shell, and double shell) show the characteristic features expected for QDs (Figure 30a). The higher absorption at lower wavelengths corresponds to an increase in available states at higher energies, as described in section 2.4.4. The peak is known as the first excitation peak and its position is dependent on the composition and size of the QD.

Generally, the more monodisperse the sample is, the narrower the peak width will be.

The short width of the first excitation peak indicated good monodispersity or narrow size distribution. The optical band gap was determined from the intercept between the wavelength axis and the tangent to the linear portion of the Tauc plot, i.e., $(\alpha h\nu)^2$ versus $h\nu$, where α is the absorption coefficient (absorbance divided by the thickness of sample), h is Planck's constant, and ν is the frequency of light (Figure 30b). The InP core showed a first excitation peak of 539 nm and an optical band gap of 2.13 eV but had almost no PL and therefore a very low PLQY of 1.6% was measured based on the method in section 2.4.3 (Figure 30c and Table 7). This indicates many surface traps on the core surface and/or partial oxidation. Trap states and defects can offer an alternative pathway for the free electron-hole pair to recombine, which is typically orders of magnitude faster (ps) than PL recombination (ns) [117], as described in section 1.4.4.

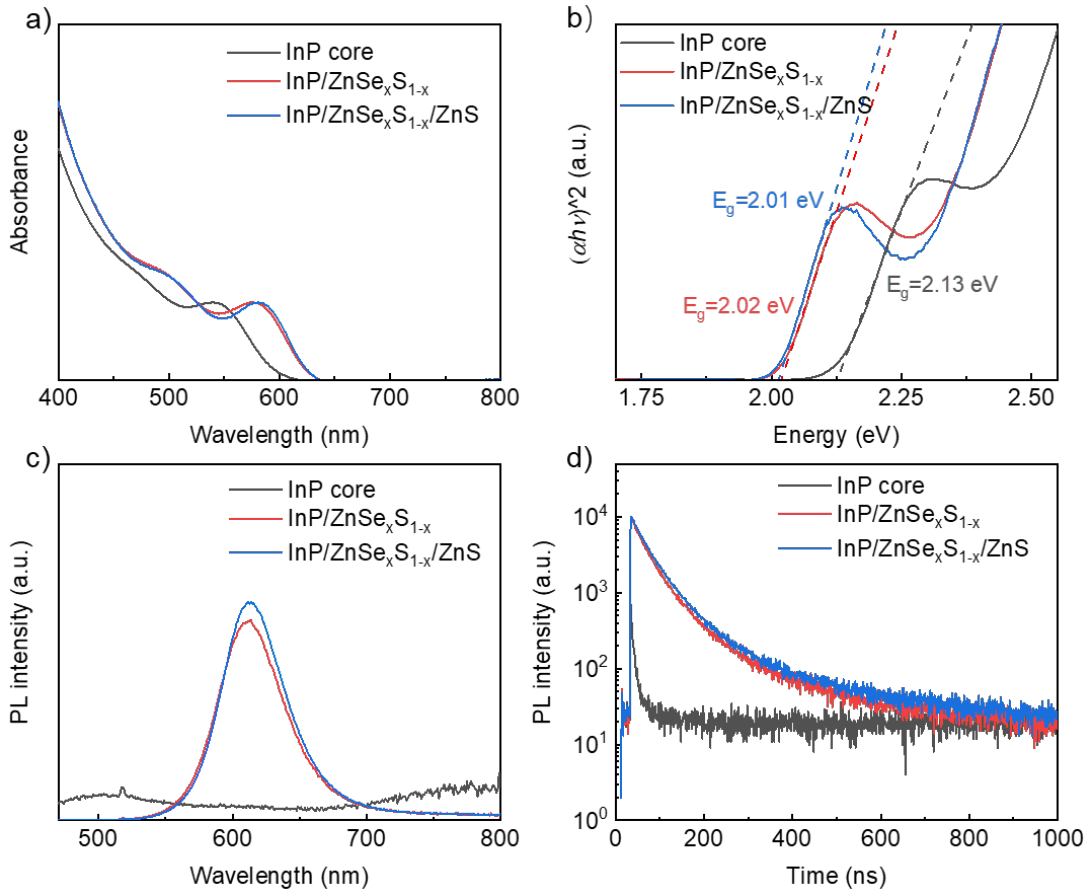

Figure 30. The optical properties of InP QDs synthesized. a) UV-Vis spectrum, b) Tauc plot, c) PL spectrum, and d) TRPL spectrum of InP core, InP/$ZnSe_xS_{1-x}$, and InP/$ZnSe_xS_{1-x}$/ZnS QDs.

After the double shell ($ZnSe_xS_{1-x}$/ZnS) was grown onto the InP cores, the first excitation peak red-shifted to 581 nm, corresponding to a reduced band gap of 2.01 eV due to fine structure and stronger absorption. The PL emission spectrum from the InP/$ZnSe_xS_{1-x}$/ZnS QD dispersion showed a single peak with a maximum of 614 nm and an FWHM of 56 nm (Figure 30c) which is comparable to some reported values but is inferior to that of state-of-the-art InP QDs (< 40 nm, see Table 8). The relatively broader emission than Cd-based QDs associated with structural and electronic disorders [47, 194]. The peak was slightly asymmetric with a slight tail into the red region due to the presence of a small amount of larger QDs. This is common for large QDs, as described in section 1.4.5. The difference between the first excitation peak and the emission peak gives a Stokes shift of 33 nm. The PLQY of InP/$ZnSe_xS_{1-x}$ and InP/$ZnSe_xS_{1-x}$/ZnS QDs was significantly improved to 58% and 81%, respectively, suggesting that the multiple shells were effective in protecting and removing the surface trap states from the core-shell interface. The composition-gradient $ZnSe_xS_{1-x}$ intermediate shell reportedly relieves interfacial compressive strain at the InP/ZnS interface, contributing to the higher PLQY [175].

Table 7. Optical properties of InP core, InP/$ZnSe_xS_{1-x}$, and InP/$ZnSe_xS_{1-x}$/ZnS QDs.

	InP core	InP/$ZnSe_xS_{1-x}$	InP/$ZnSe_xS_{1-x}$/ZnS
First excitation peak (nm)	539	576	581
Emission peak (nm)	-	613	614
FWHM (nm)	-	58	56
Stokes shift (nm)	-	37	33
Average lifetime (ns)	10.7	59.6	63.1
PLQY (%)	1.6 ± 1	57.9 ± 0.4	80.8 ± 1.6
E_g (eV)	2.13 ± 0.02	2.02 ± 0.01	2.01 ± 0.01

Figure 30d shows the TRPL curves of QDs, and the decay times of components of QDs are summarized in Table 9. The decay is clearly faster for the core only than the core-shell-shell sample. None of the decay curves can be fitted to a single component exponential decay function which suggests, as expected, that there are competing pathways for relaxation. In this work, a two-component decay model was required to fit the fluorescence decay. Although there may be more processes, for example, processes with similar rates which we cannot resolve, the two carrier relation processes in the QDs can be approximately assigned to a fast component (τ_1) resulted from the capture process of carriers by defect states [195, 196] and a slow component

(τ_2) due to the band-edge electron-hole radiative recombination process [117]. The two lifetime components were fixed, with only their amplitudes adjusted, as the decay pathways were assumed to remain consistent. More combinations of lifetime fitting of InP core, InP/$ZnSe_xS_{1-x}$, and InP/$ZnSe_xS_{1-x}$/ZnS QDs were tried and summarized in the table in Appendix 9.1.

Table 8. The optical performance of state-of-the-art InP QDs compared with this work.

Structure	Synthesis method	Mean Size (nm)	PL peak (nm)	FWHM (nm)	PLQY (%)	Ref.
InP/GaP/ZnS	Hot injection	5.2-12.8	537-558	48-61	72-83	[190]
InP/ZnSe/ZnS	Hot injection	11	630	35	100	[148]
InP/$ZnSe_{0.7}S_{0.3}$/ZnS	Hot injection	11.25	~527	35	97	[50]
InP/ZnSe/ZnSeS/ZnS	Hot injection	10.5	680	66	95	[197]
InP/ZnS/ZnS	Hot injection	6.2	474	52	93	[198]
Mn:InP/ZnS	Hot injection	3.6-5.0	485-524	-	55-79	[189]
InP/ZnS/ZnS	Heat-up	10.6	465	38	96	[34]
InP/ZnSeS/ZnS	Hot injection	5.4	510	45	95	[51]
InP/$ZnSe_xS_{1-x}$/ZnS	**Hot injection**	**8.1**	**614**	**56**	**81**	**This work**

Table 9. PL lifetime components and nonradiative rates of InP core, InP/$ZnSe_xS_{1-x}$, and InP/$ZnSe_xS_{1-x}$/ZnS QDs.

	InP core	InP/$ZnSe_xS_{1-x}$	InP/$ZnSe_xS_{1-x}$/ZnS
A_1	36.7	8307.7	8803.5
τ_1 (ns)	10.5 (99.8%)	33.6 (68.0%)	33.6 (63.7%)
A_2	0.006	1140.7	1466.5
τ_2 (ns)	114.9 (0.2%)	114.9 (32.0%)	114.9 (36.3%)
τ_{avg} (ns)	10.7	59.6	63.1
χ^2	1.5	1.5	1.8
k_n (μs^{-1})	92.0	7.0	3.0

However, the τ_1 of the core was shorter than that of the core-shell QDs because partial surface trap states on the core were passivated after the shell coating. The average lifetime (τ_{avg}) and amplitudes increased after coating the shell, but QDs with a single shell and double shell did not show big changes, suggesting a thin outmost shell. τ_{avg} was calculated by equation (21) in section 2.4.2. Notably, the τ_1% of core-shell QDs

dramatically decreased from 99.8% to 63.7%, but the τ_2% enhanced from 0.2% to 36.3%, indicating effective surface passivation. These results were comparable to the values reported by Duan et al., but the authors held an opposite opinion that the shorter lifetime component τ_1 originated from the band-edge transition emission instead of τ_2 [47].

The portion of each lifetime component was expressed by the equation:

$$\tau_i\ (\%) = \frac{A_i\tau_i}{A_1\tau_1 + A_2\tau_2} \tag{42}$$

The nonradiative decay rates (k_n) greatly decreased from 92.0 to 3.0 μs^{-1} after coating double shells, preventing the nonradiative decay that resulted from trap states and energy transfer in QDs. k_n was calculated based on the PLQY and τ_{avg} [155].

$$\mathrm{PLQY} = \frac{k_r}{k_t} = \frac{k_r}{k_n + k_r} = k_r\tau_{avg} \tag{43}$$

Here, k_t and k_r represent total and radiative decay rates, respectively.

1-octadecene (ODE) was commonly used as a non-coordinating solvent to synthesize high-quality InP QDs, which was first proposed by Peng et al. [199]. However, it was replaced with squalane in this work because ODE can polymerize at high temperatures (especially >240 °C), forming poly(ODE), which is difficult to clean by centrifugation [200]. The existence of Poly(ODE) reduces the efficiency of InP QD-LED as it hinders carrier transport in solid films [201]. The optical properties of QDs synthesized using squalane were slightly enhanced than those of QDs using ODE, especially the Stocks' shift and FWHM decreased by 7 nm and 5 nm, respectively (Figure 31).

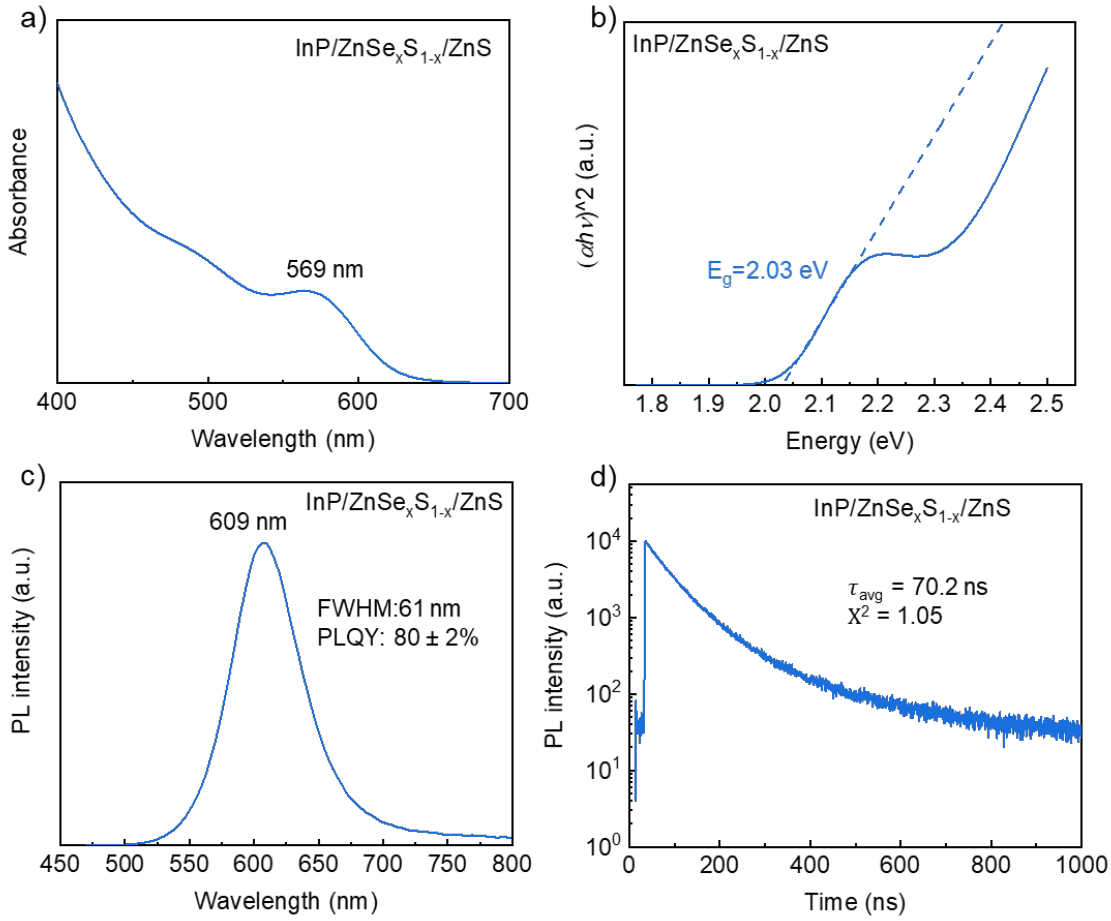

Figure 31. a) Absorbance, b) Tauc plot, c) PL, and d) TRPL spectrum of InP/$ZnSe_xS_{1-x}$/ZnS QDs synthesized by ODE.

3.2.2 Morphology of QDs

TEM images of QDs showed that the nanocrystals were irregular in shape (Figure 32a, b), with an interplanar spacing of 3.37 Å corresponds to the cubic crystalline plane of (111) (calculated by the distance measured divided by the number of peaks, Figure 32b, c). Crystal planes of (111), (220), and (311) can be interpreted from the SAED pattern (Figure 32d). The interpretation details of QD's SAED pattern were summarised in the table in Appendix 9.2. The average size of QDs was 8.1 ± 0.7 nm, measured as the longest distance (Figure 32e), with a core size of 3.6 nm, which is comparable to reported values (see Table 8). Assuming that InP cores are spherical, the diameter of InP core (D in nm) was estimated using the following equation [163]:

$$D = (-3.7707*10^{-12})\lambda^5 + (1.0262*10^{-8})\lambda^4 - (1.0781*10^{-5})\lambda^3 + (5.455*10^{-3})\lambda^2 - 1.3122*\lambda + 119.9 \quad (44)$$

Here, λ is the first excitation peak (539 nm).

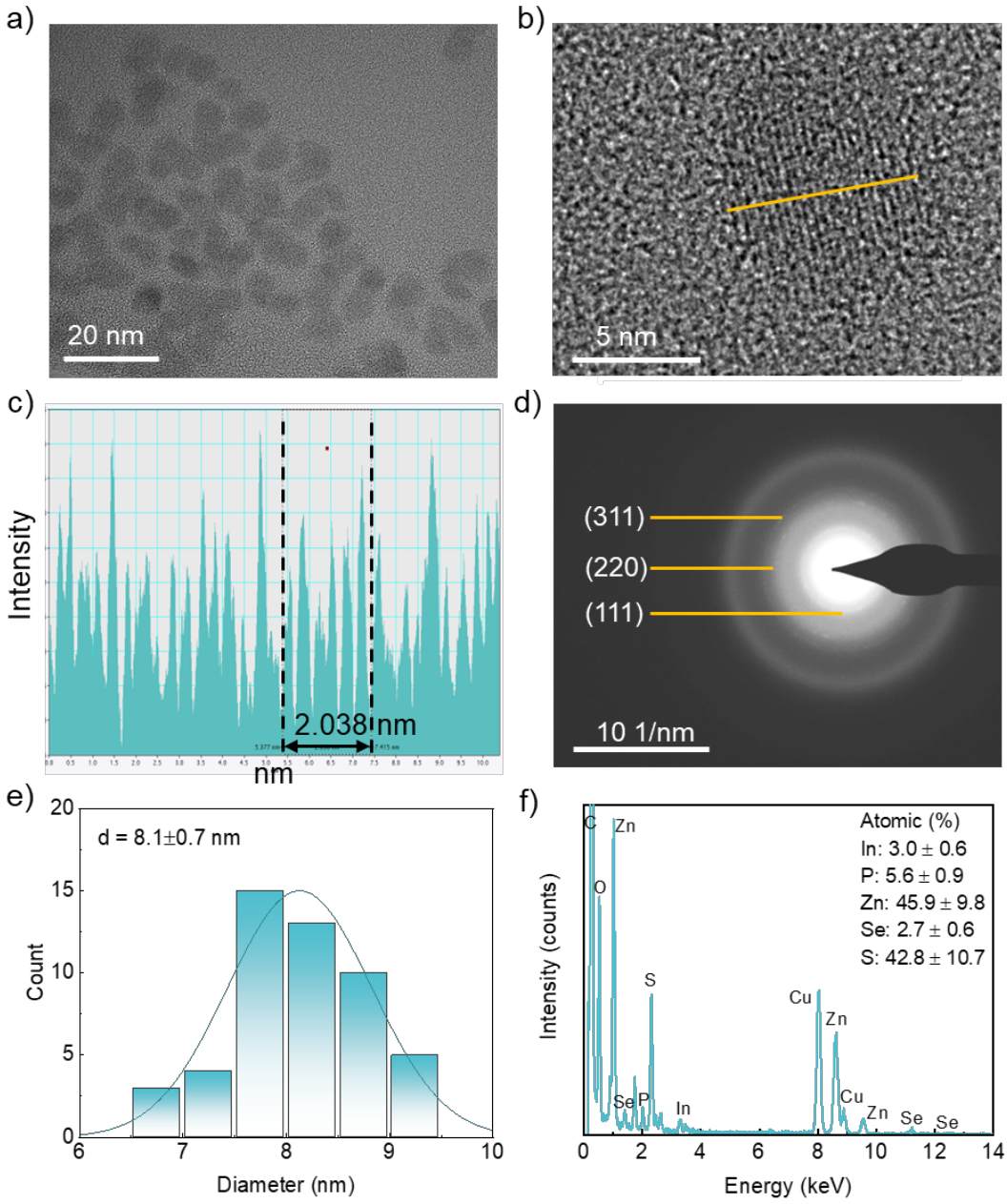

Figure 32. a-b) HR-TEM images and c) corresponding line profile of InP/ZnSe$_x$S$_{1-x}$/ZnS QDs. d) SAED pattern of QDs. e) size distribution (fitted with the Gaussian model) and f) EDS spectra (with atomic percentages inset) of QDs.

The EDS result showed that Se accounted for 2.7 at% of the middle shell (Figure 32f) and P-rich surface due to the undercoordinated surface P atoms [202], which was comparable to the XPS result (3.7 at%) discussed in Section 3.2.3. The shell can be assumed as ZnS because the Se amount was very small in the middle shell, thus obtaining a shell thickness of 2.3 nm (c.a. 4.3 monolayers, calculated based on the lattice constant of ZnS – 0.541 nm [203]). The thicker shell can enhance the stability

and suppress nonradiative FRET in InP/ZnSe$_x$S$_{1-x}$/ZnS core/shell QDs, contributing to more stable and efficient QD-LEDs [175].

3.2.3 XPS of QDs

The main peak positioned at 284.8 eV corresponds to C-C/C-H bonds (Figure 33a), while the tail extending to higher BE is associated with the C-S bonds from the QD ligands (octanethiol) [204]. The In 3d spectrum exhibited two contributions due to the spin-orbit splitting of 7.5 eV, In 3d$_{5/2}$ and In 3d$_{3/2}$, at 444.7 and 452.2 eV, respectively (Figure 33b). The P 2p spectrum reveals two distinct chemical environments for phosphorus atoms (Figure 33c). The spectrum was fitted using two resolved doublets, with a spin-orbit splitting of 0.9 eV between 2p$_{3/2}$ and 2p$_{1/2}$. The first, dominant doublet appears at 128.4−129.3 eV and is characteristic of InP [205]. The second, more intense doublet is located at higher BE, 133.3−134.2 eV, corresponding to phosphorus in an oxidized environment, likely InPO$_x$ (x = 3 and/or 4), as supported by the literature [47, 205]. The presence of InPO$_x$ without air exposure suggests that it was formed during the synthesis, which reduced the PLQY [148].

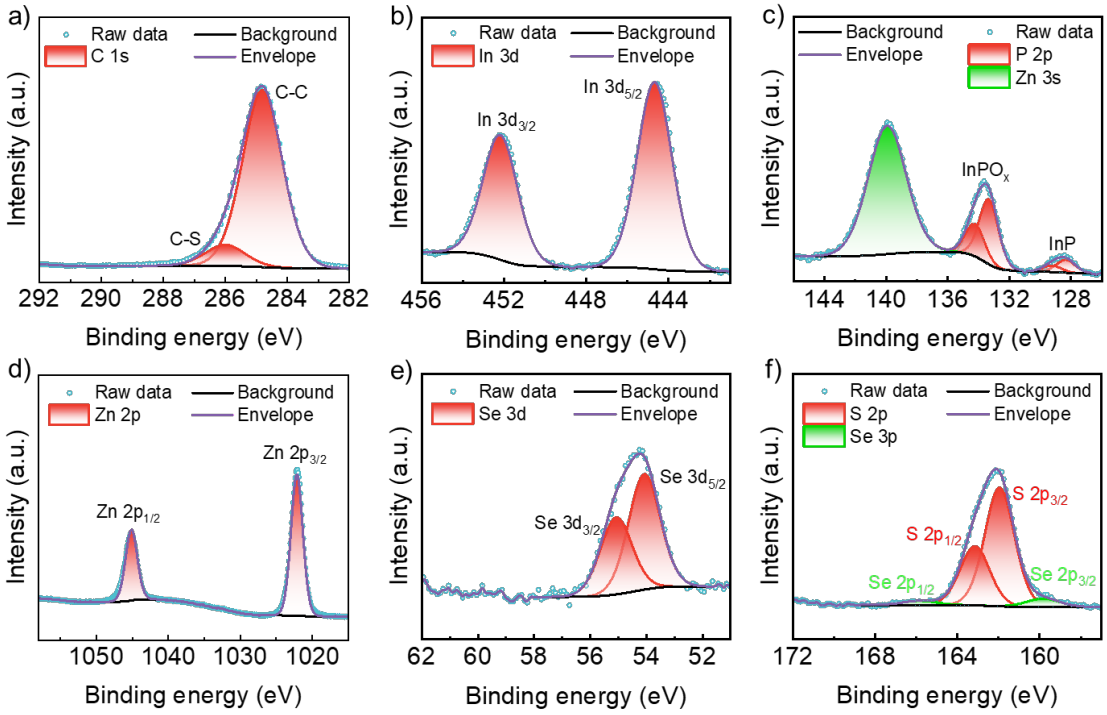

Figure 33. XPS spectra of a) C 1s, b) In 3d, c) Zn 3s & P 2p, d) Zn 2p, e) Se 3d, and f) S 2p & Se 2p of InP/ZnSe$_x$S$_{1-x}$/ZnS QDs.

Isolated Zn 2p$_{3/2}$ and Zn 2p$_{1/2}$ peaks present at 1022.1 and 1045.1 eV, respectively

with a spin-orbit splitting of 23.0 eV (Figure 33d) [172, 206]. The Se $3d_{3/2}$ and Se $3d_{5/2}$ peaks at 55.3 and 54.3 eV, respectively (Figure 33e), with an overlapping spin-orbit separation of 1.0 eV, are comparable to the reported results [172, 207]. The S 2p spectrum initially exhibited two contributions, $2p_{3/2}$ and $2p_{1/2}$, at 161.9 and 163.1 eV (Figure 33f), respectively, which can be assigned to the $ZnSe_xS_{1-x}$/ZnS shell [172, 208]. The peaks at 166.0 and 160.0 eV were attributed to Se $3p_{1/2}$ and Se $3p_{3/2}$, respectively, which is in line with the literature [172, 209]. Se accounted for 3.7 at% of the sum of S 2p and Se 3p, so the middle shell can be expressed as $ZnSe_{0.04}S_{0.96}$. Since XPS is highly surface sensitive and Se is covered by an organic ligand layer, the inner shell may be underestimated. The atomic percentage was calculated by equation (41) in section 2.13.

3.3 Characterisation of $Zn_{0.9}Mg_{0.1}O$ NPs

The absorbance, morphology, size distribution, and chemical composition of the synthesized $Zn_{1-x}Mg_xO$ and $Zn_{1-x}Mg_xO$-EA NPs were measured and analyzed.

3.3.1 Optical Properties of $Zn_{0.9}Mg_{0.1}O$ NPs

Doping magnesium into ZnO NPs can reduce electron mobility and adjust the energy level between the QD layer and the ETL, promoting more balanced electron and hole injection [143]. This is important because the electron mobility of ZnO is 2-3 orders of magnitude higher than that of most HTLs (see Table 2). The doping ratio significantly affects the electron mobility and energy level of ZnO NPs, with 12.5% of the total metal molar ratio found to be optimal [143]. To prevent agglomeration and improve the mono-dispersity of $Zn_{0.9}Mg_{0.1}O$ NPs, 0.2 vol.% EA was used as a capping agent. The synthesis protocol is described in detail in section 2.2. The transparency of $Zn_{0.9}Mg_{0.1}O$-EA NP dispersion was visibly improved in ambient lighting conditions (Figure 34a inset). The absorbance of $Zn_{0.9}Mg_{0.1}O$-EA NPs followed a similar pattern to $Zn_{0.9}Mg_{0.1}O$ NPs, showing a plateau above 500 nm and a sharp increase below 400 nm (Figure 34a), indicating a large band gap. The increased absorption of $Zn_{0.9}Mg_{0.1}O$-EA NP dispersion below 350 nm might be attributed to the absorbance of EA. Using the Tauc method to analyze the absorption spectra, the estimated band gaps were 3.66 eV and 3.65 eV for $Zn_{0.9}Mg_{0.1}O$ NPs and $Zn_{0.9}Mg_{0.1}O$-EA NPs, respectively. This value is comparable to previously reported results [210] but higher than that of bulk ZnO (3.2−3.3 eV) [211], indicating greater spatial confinement of photogenerated charge carriers in the smaller ZnO NPs (Figure 34b) [212].

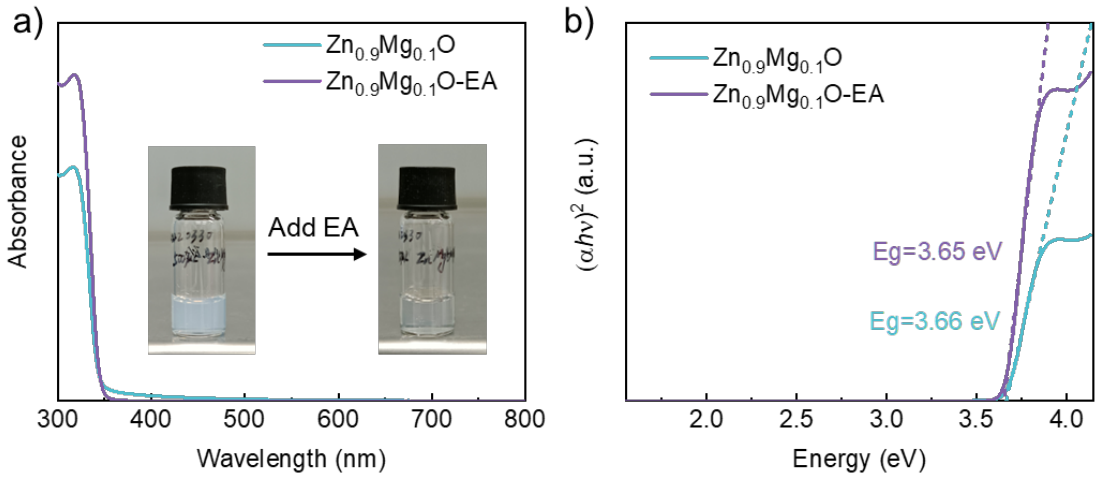

Figure 34. a) Absorption spectra and b) Tauc plots of $(\alpha hv)^2$ of $Zn_{0.9}Mg_{0.1}O$ and $Zn_{0.9}Mg_{0.1}O$-EA NPs. The insets are photos of $Zn_{0.9}Mg_{0.1}O$ NPs before and after adding EA.

3.3.2 Morphology of $Zn_{0.9}Mg_{0.1}O$ NPs

$Zn_{0.9}Mg_{0.1}O$-EA NPs exhibited irregular shapes but excellent crystallinity with a clear interplanar spacing of 2.73 Å on the (110) plane (Figure 35a-c). The selected area electron diffraction (SAED) image revealed lattice planes of (100), (002), (102), (110), (103), (200), and (203) (Figure 35d). The interpretation details of $Zn_{0.9}Mg_{0.1}O$-EA NPs' SAED pattern were summarised in a table in Appendix 9.2. $Zn_{0.9}Mg_{0.1}O$-EA NPs had a narrow size distribution of 3.9 ± 0.5 nm (Figure 35e), measured as the longest distance. EDS showed peaks corresponding to Zn, Mg, and O, with additional carbon and copper peaks originating from the TEM grid. The atomic percentage was 18.4 ± 3.0% Zn, 2.5 ± 0.5% Mg, and 79.1 ± 7.1% O (Figure 35f), with Mg accounting for 12.0% of the total atomic ratio of Zn and Mg, which was comparable to the XPS results (15.1%) discussed in Section 3.3.3.

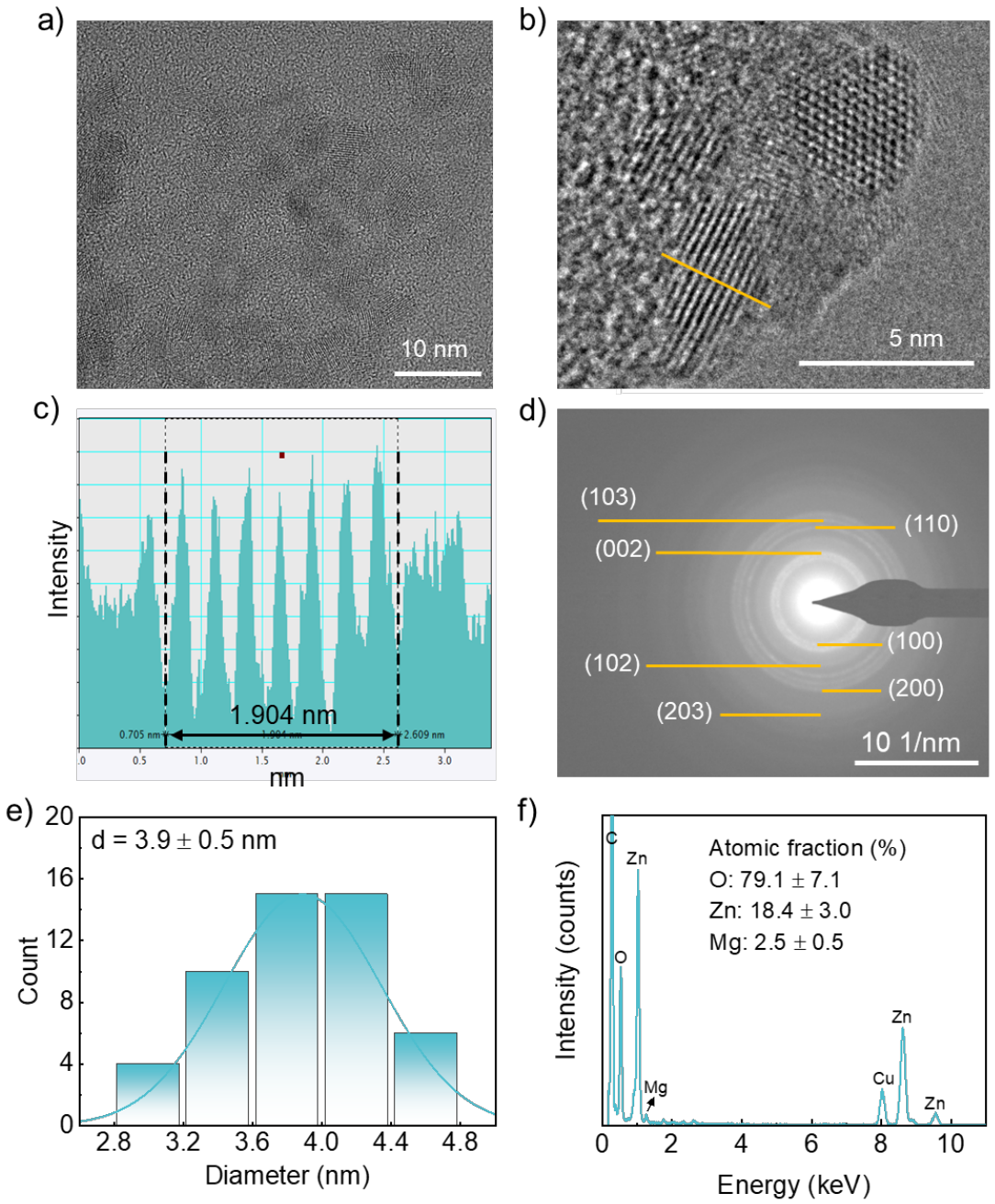

Figure 35. a-b) HR-TEM images and c) corresponding line profile of $Zn_{0.9}Mg_{0.1}O$-EA NPs. The interplanar spacing of 2.73 Å corresponds to the crystalline plane of (100). d) SAED image of $Zn_{0.9}Mg_{0.1}O$-EA NPs. e) Size distribution (fitted by the Gaussian model) and f) EDS spectra with atomic percentage inset of $Zn_{0.9}Mg_{0.1}O$-EA NPs.

3.3.3 XPS of $Zn_{0.9}Mg_{0.1}O$ NPs

Figure 36 shows the XPS spectra of $Zn_{0.9}Mg_{0.1}O$ and $Zn_{0.9}Mg_{0.1}O$-EA NPs, and they exhibited similar XPS peaks of C 1s, Zn 2p, and Mg 1s. The C peak mainly originates from carbon contaminants for $Zn_{0.9}Mg_{0.1}O$ NPs, but the combination of carbon contaminates and surfactant (EA) on the surface for $Zn_{0.9}Mg_{0.1}O$-EA NPs [213, 214].

The main peak positioned at 284.8 eV corresponds to C-C/C-H bonds, and peaks generated at higher BE values of 286.6, 287.9, and 289.1 eV were related to C-O (or C-N from EA), C=O, and -COOH, respectively (Figure 36a), indicating oxidation of carbon contaminants because the NPs were left under the ambient atmosphere for drying the solvent. The Zn 2p spectrum exhibited two contributions due to the spin-orbit splitting of 22.9 eV, Zn $2p_{3/2}$ and Zn $2p_{1/2}$, at 1021.3 and 1044.4 eV, respectively (Figure 36b). The peak positions were slightly higher than those of ZnO NPs after Mg doping [215]. The Mg 1s peak was fitted well with one single peak centered at 1303.6 eV (Figure 36c), in good agreement with previously reported results [216]. The atomic ratios of Mg were 15.1% and 15.8% for $Zn_{0.9}Mg_{0.1}O$ and $Zn_{0.9}Mg_{0.1}O$-EA NPs, respectively, which were similar to the EDS result discussed in section 3.3.2. The O 1s spectrum has two contributions, the peaks present at 530.0 and 531.7 eV were attributed to Zn-O bonding from the O_2 ions in the wurtzite structure surrounded by Zn atoms and surface oxygen, respectively (Figure 36d) [215, 217]. The area of surface oxygen increased from 58.2% to 65.6% for $Zn_{0.9}Mg_{0.1}O$-EA NPs due to the addition of EA.

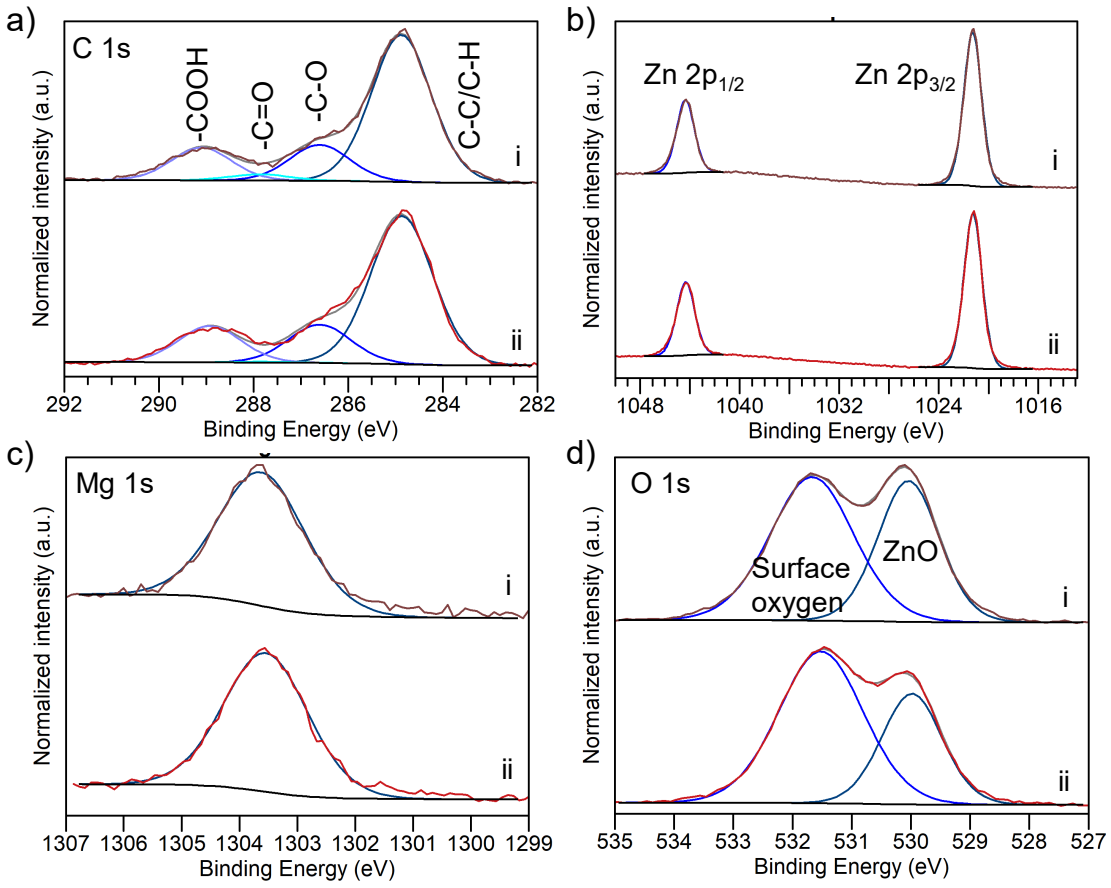

Figure 36. XPS spectra of a) C 1s, b) Zn 2p, c) Mg 1s, and d) O 1s of $Zn_{0.9}Mg_{0.1}O$ (i) and $Zn_{0.9}Mg_{0.1}O$-EA (ii).

3.4 Concluding Remarks

The goal of the work in this chapter was to synthesize high-quality InP/$ZnSe_xS_{1-x}$/ZnS QDs and $Zn_{0.9}Mg_{0.1}O$ by optimizing the synthesis protocols, which were used as the EML and ETL, respectively, in QD-LEDs in Chapter 4. Their optical properties significantly influence the electrical performance of the resultant QD-LEDs.

The red-emitting high-quality InP/$ZnSe_xS_{1-x}$/ZnS QDs were successfully synthesized via the hot-injection method, showing a high PLQY of 81%, an FWHM of 56 nm, and an average lifetime of 63 ns. These excellent optical properties were attributed to the effective multiple-shell encapsulation, passivating the surface trap states in the core. The replacement of ODE with squalane prevented the generation of poly(ODE) which can hinder the carrier transportation in the QD layer. QDs synthesized by squalane slightly reduced the Stokes shift and FWHM. The QDs showed a narrow size distribution of 8.1 ± 0.7 nm, with an estimated core diameter of about 3.6 nm and 4.3 monolayers of the shell. The Se at% in the middle shell was confirmed to be 2.7% by the EDS, which was similar to the value (3.7%) determined by XPS. The optical properties and size of our synthesized red-emitting QDs were comparable to previously reported literature.

Additionally, based on the solution precipitation method of $Zn_{0.9}Mg_{0.1}O$ NPs, the addition of a small amount of EA after synthesis efficiently improved the monodispersity of $Zn_{0.9}Mg_{0.1}O$ NPs in IPA. $Zn_{0.9}Mg_{0.1}O$-EA NPs exhibited a big optical band gap of 3.66 eV and a small size distribution of 3.9 ± 0.5 nm. According to the EDS and XPS results, the chemical formula of Mg-doped ZnO can be expressed as $Zn_{0.9}Mg_{0.1}O$. The high-quality QDs and $Zn_{0.9}Mg_{0.1}O$ NPs are prerequisites of InP QD-LEDs with excellent electrical performance.

4. Inkjet Printing of InP QD-LEDs

Manufacturing high-resolution, large-scale, and low-cost QD-LEDs remains challenging. IJP technology uses fewer materials, creates patterns without masks, and achieves high resolution, making it a promising candidate for industrial QD-LED assembly. Developing printable QD inks and mitigating the CRE are the keys to achieving inkjet-printed QD-LEDs with excellent performance. The viscosity, ST, density, and boiling point of the ink solvents are crucial factors for formulating printable QD inks. The ST and thermal conductivity of ink solvents play a vital role in determining the strength of the solutal and thermal ME, respectively, which in turn impact the CRE and smoothness of the resultant QD patterns.

4.1.Background

The device structure of InP-based QD-LEDs is primarily categorized into conventional and inverted types (Figure 37). In the conventional structure, the hydrosoluble conducting polymer PEDOT:PSS is commonly used as the HIL. PEDOT:PSS modulates the work function of ITO electrodes, reducing the barrier mismatch between the anode and the HTL, and effectively smooths the ITO surface. In the inverted structure, organic HATCN and inorganic MoO_3 are widely used as the HIL, while organic materials like CBP and TCTA are common for HTL. Unlike the solution-processed HIL and HTL in the conventional structure, the inverted structure's layers are typically prepared by high vacuum thermal evaporation, which prevents solvent erosion during the deposition of multiple layers.

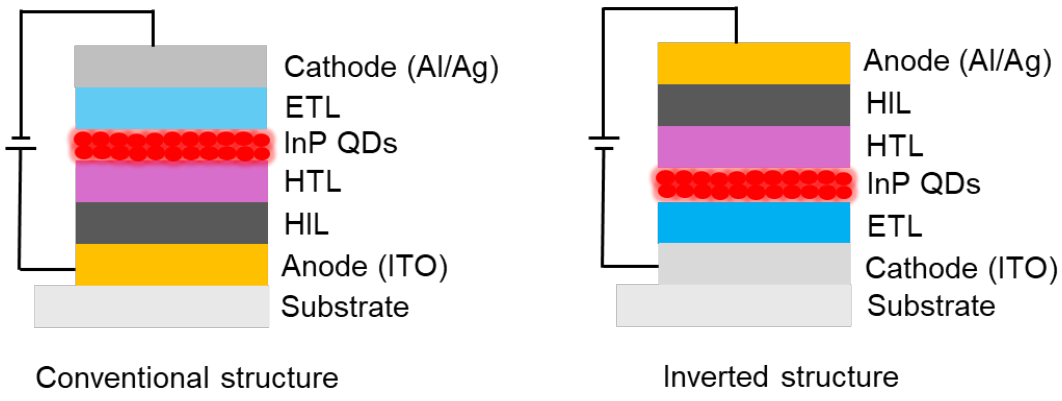

Figure 37. Conventional and inverted structures of InP-based QD-LEDs. Reprinted with permission from [188]. Copyright 2020 ACS.

In general, the assembly of QD-LEDs combines SC and thermal evaporation in low-

oxygen and low-moisture conditions to achieve uniform thin films and avoid the degradation of the functional materials. In contrast, IJP offers advantages such as reduced material usage, high-resolution pattern design without a mask, and no need for post-structuring like wiping or laser scribing, attracting big attention in the industry. The EQE record of inkjet-printed QD-LEDs has been refreshed annually since the first report by Haverinen et al. in 2009 [218]. Yet, the majority of the printed QD-LEDs are based on Cd chalcogenides and Pb-containing perovskites due to their greater optical performance (Table 10). Although spin-coated HMF QDs-based QD-LEDs have been developed, such as InP-based QD-LEDs [219], $CuInS_2$-based QD-LEDs [220], CQDs-based QD-LEDs [221], LFP QDs-based QD-LEDs [222], and SiQDs-based QD-LEDs [223], inkjet-printed HMF QDs-based QD-LEDs are still in its infancy.

Table 10. A performance summary of state-of-the-art QD-LEDs via IJP.

Structure (The QD layers are in bold)	PLQY (%)	λ_{em} (nm)	V_{on} (V)	L_{max} (cd m^{-2})	EQE (%)	Ref.
ITO/PEDOT:PSS/TFB/**InP**/ZnMgO/Ag	83.5	625	2.6	17,759	8.1	[33]
ITO/PEDOT:PSS/PVK:TFB/**InP**/ZnMgO/Al	82	550	5	2540	~0.7	[35]
ITO/PEDOT:PSS/TFB/**InP**/ZnO/Ag	96.2	472	7	91	0.15	[34]
ITO/PEDOT:PSS/poly-TPD/**$FA_{0.8}Cs_{0.2}PbI_3$**/TPBi/LiF:Al	25.8*	769	-	-	14.3	[32]
ITO/PEDOT:PSS/PTAA/**$CsPbBr_3$**/TPBi/LiF/Al	87	688	2.4	43,883	8.5	[26]
ITO/ TFB/PVK/PVP/**CdSe**/ TPBi/LiF/Al	83	624	2.1-2.2	-	7.2-18.3	[76]
ITO/ZnO/**CdSe** /CBP/MoO_3/Al	-	630	2.3-3.0	29,264-73,360	1.0-2.8	[78]
ITO/PEDOT:PSS/PVK/**CdZnSe**/ZnMgO/Al	85-94.6	536-620	2.86-2.88	31,740-59,420	22.4-23.1	[31]
ITO/PEDOT:PSS/TFB:FLTA-V/**CdSe**/MoO_3/Al	60	475	3.1	6710	6.82	[224]
ITO/PEDOT:PSS/TFB/**CdZnSe**/ZnMgO/Al	60-90	465-630	-	2,367-283,996	4.4-19.3	[90]

*PLQY of QD films rather than QD dispersions.

Currently, InP QDs are the only example of HMF QDs that have been applied in inkjet-printed QD-LEDs but still lag behind their spin-coated analogs [50, 225, 226]. The inkjet-printed red, green, and blue InP QD-LEDs have only appeared in the past two years, achieving EQE of 8.1%, 0.7%, and 0.15%, respectively which are much lower than that of CdSe/PQD-based counterparts (Table 10). The low EQE of blue inkjet-printed QD-LEDs is a typical issue of blue QD-LEDs because blue QD emitters have a deeper valence band that creates a great injection barrier impeding the hole transfer [227]. Samsung Display Co., Ltd. fabricated the world's first all-inkjet-printed Cd-free

active matrix QD-LEDs by inkjet printing all the functional layers except the electrodes [228]. Yet, the authors hid many details in the paper such as ink solvents and functional materials.

IJP is typically conducted in an ambient atmosphere rather than an inert atmosphere, and the weak covalent bond between In and P makes InP QDs less stable in ambient conditions compared to HM QDs [148, 229]. The relatively low viscosity of QD dispersion poses a challenge in printing, preventing effective QD packing and accelerating the trapping of O_2/H_2O during manufacturing. This leads to the formation of inhomogeneous and highly void films. Currently, the performance of inkjet-printed environmentally friendly QD-LEDs remains low due to issues such as FRET, less uniform QD film, degradation during air printing, and a significant drop in the PLQY of QD films [26, 79]. In Cd-based QDs, the electron and hole masses are similar, but in InP QDs, the hole mass is much heavier. This difference affects Fermi level adjustment during device operation, altering the CBM and VBM. Consequently, the tendency for electron injection into the QD layer may differ from previous results.

Efforts have been made to improve the performance of inkjet-printed InP QD-LED, some of which refer to the strategies for spin-coated QD-LEDs, including improving the PL of InP QDs and optimizing the device structure. Firstly, suppressing FRET between closed-packed QDs by engineering the thickness of the ZnS shell [34]. The PLQY of the InP/ZnS/ZnS QD film reached 58%, which was twice the value of the InP/ZnS QD film (Figure 38a). The printed blue InP QD-LED showed a maximum luminance and EQE of 91 cd m^{-2} and 0.15% (Figure 38b). Secondly, the inter-QD spacing was reduced by PI-mediated cross-linkage between InP QDs [35]. The cross-linked QD film with PI was more stable than that without PI due to the homogenous QD surface, sustaining the original luminescence for 4000 s (Figure 38c). Additionally, the PI was mixed with ZnMgO NPs to reduce the current leakage from the ETL and Auger recombination (AR) in the high-*J* regime, achieving a high luminescence of 2540 cd m^{-2} for printed QD-LEDs (Figure 38d).

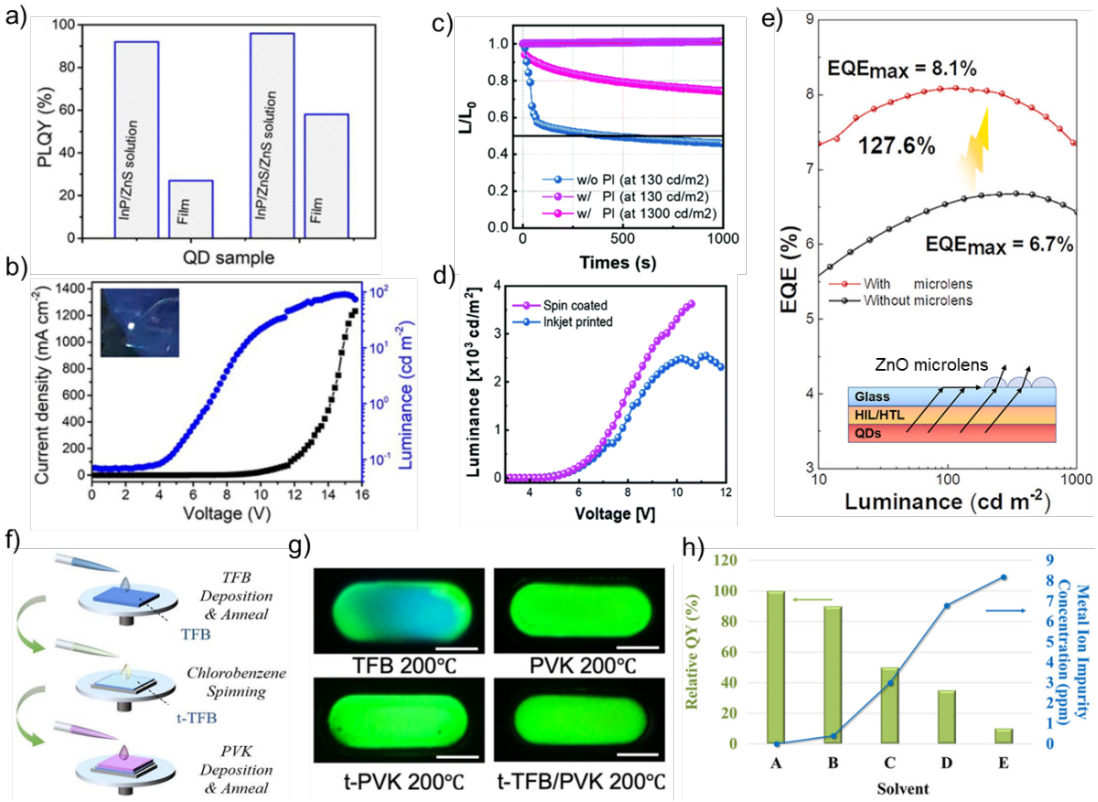

Figure 38. a) The PLQY of InP QD dispersions and films with thin and thick ZnS shells. b) *J-V-L* behavior of a blue InP QD-LED (Inset). Figure a) and b) are reprinted with permission from [34]. Copyright 2022 Elsevier. c) The stability of QD-LEDs with and without adding PI. d) *V-L* curves of spin-coated and inkjet-printed InP QD-LEDs. Figure c) and d) are reprinted from [35]. CC BY 3.0. e) The EQE of inkjet-printed InP QD-LEDs with and without ZnO microlens (Inset). Reprinted with permission from [33]. Copyright 2023 Elsevier. f) A schematic of tailoring the t-TFB/PVK layer. g) EL images of printed InP QD-LEDs based on different HTLs. Figure f) and g) reprinted from [93]. CC BY 4.0. h) PLQY of QD inks varies with the metal ion impurity concentration in different ink solvents. Reprinted with permission from [228]. Copyright 2022 Wiley.

Thirdly, the device structure design was optimized to enhance light extraction efficiency. For example, Bai et al. achieved a red inkjet-printed InP QD-LED with the highest EQE of 8.1% by nanoimprinting periodic ZnO microlens arrays on the glass substrate (Figure 38e). The arrays reduced the total reflection when the angle of incidence of emitted light at the glass/air interface exceeds the critical angle. Efficiency improvements can be made by improved balancing of the injection of holes and electrons, typically by modifying the HTL. TFB is one of the most popular HTLs due to its higher hole mobility than other HTLs; however, it is not compatible with the commonly used ink solvent (CHB) and causes parasitic emission [230]. Zhan et al. tailored the HTL by sequentially SC a layer of TFB, chlorobenzene, and PVK, suppressing ink erosion and maintaining hole transport [93] (Figure 38f and g). Park

and coworkers achieved an all-inkjet-printed large-area active-matrix InP QD-LED with a resolution of 217 PPI by optimizing the ink solvents and getting over the hurdles of all inkjet printing processes (Figure 38h) [228].

To further improve performance and advance commercialization of inkjet-printed InP-based QD-LEDs, additional efforts should focus on the following areas. First, improving the air stability of InP QDs or creating an inert atmosphere for printing. Second, optimizing the InP QD ink for low-cost and greener printing. For example, synthesizing high-quality aqueous InP QDs and formulating environmentally friendly QD inks using greener solvents such as water, alcohols, etc. which are compatible with most CTL materials. Third, develop more effective ways to suppress AR, FRET, and field-induced quenching. Last, exploring new CTL materials for more balanced charge injection.

4.2 Printability of InP QD Inks

The QD inks that meet the criteria for IJP, were formulated as described below. The solvents CHB and decane have BPs of 239 °C and 174 °C, respectively, and were both found suitable to disperse the octanethiol-stabilized QDs. The QD inks with 3 vol. %, 10 vol. %, 20 vol. %, and 80 vol. % of decane were denoted as ink-3, ink-10, ink-20, and ink-80, respectively. The vol. % of decane was selected based on the QD ink formulation reported by Li et al., where CHB was the primary solvent [72]. They noted that the CHB/decane solvent system was ineffective on the PVK film. However, it can be used by leveraging the thermal Marangoni effect in this work, which will be discussed later. The inks were stable as stored in a glove box, exhibiting nearly the same PLQY and emission peak after 10 days (Figure 39). Table 11 gives a summary of the relevant properties of four inks, and the characterization of these parameters is described in section 2.9, section 2.10, and section 2.11. All inks fall into the range of good printability.

Table 11. Rheological properties, printability, and solutal Marangoni strength of QD inks with different vol. % of decane in CHB.

QD inks	Ink-3	Ink-10	Ink-20	Ink-80
Decane content (Vol. %)	3	10	20	80
Viscosity (η, mPa s)	2.80 ± 0.01	2.44 ± 0.01	2.14 ± 0.01	1.12 ± 0.01
Surface tension (γ, mN m^{-1})	31.5 ± 0.6	30.7 ± 0.1	30.2 ± 0.1	26.1 ± 0.1
Droplet CA (°)	15.3 ± 0.6	12.3 ± 1.7	11.5 ± 1.3	10.8 ± 0.9
Density (ρ, g cm^{-3})	0.93 ± 0.01	0.93 ± 0.01	0.92 ± 0.01	0.77 ± 0.01
Z value	6.7	7.7	8.6	13.8
Ma_s strength ($\Delta\gamma/\eta$)	0.29	0.66	0.98	5.54

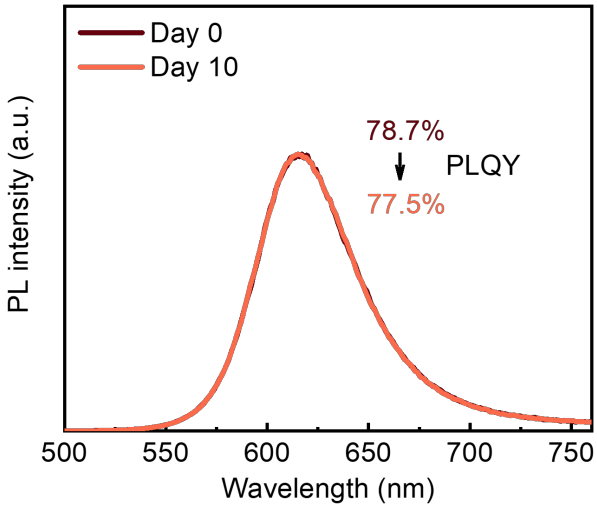

Figure 39. The stability of the ink-20 that was stored in the glove box for 10 days.

The low CA (< 16°) of the CHB/decane mixture on the PVK film demonstrates the high surface energy and excellent surface wettability of PVK [75]. In this study, PVK was chosen as the HTL rather than another commonly used TFB because PVK was reported to be resistant to CHB and decane [75]. The mean thickness of PVK films barely changed after rinsing by the ink solvents, while it significantly decreased for TFB films (Figure 40).

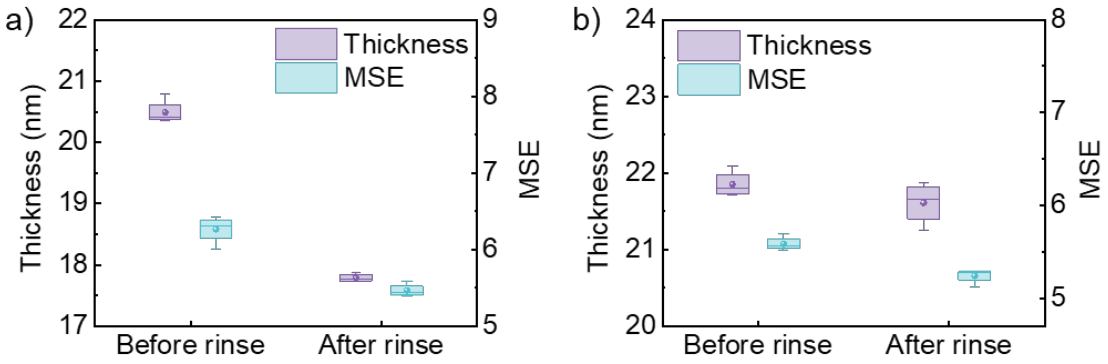

Figure 40. Thicknesses and MSE of a) TFB films and b) PVK films before and after rinsing by the ink solvents.

4.3 Optimisation of Printing Parameters

These inks were printed on the PVK-coated glass substrate without the bank structure. Voids appeared when the DS > 20 μm, so the maximum DS of 20 μm was set to allow the sequential drops to bridge the gap, forming solid patterns (Figure 41). Thicker QD films can be printed by setting a lower DS which extends the printing period. Jetting at higher voltages led to faster drops and bigger drops but the satellite generated when the voltage was greater than 10.0 V (Figure 42a). The velocity of ejected droplets linearly varied with the applied voltages (Figure 42b). The clear spherical droplet was ejected without satellites and off-axis drops under the printing voltage of 9.5 V, corresponding to a falling velocity of ~ 4.3 m/s (Figure 42c).

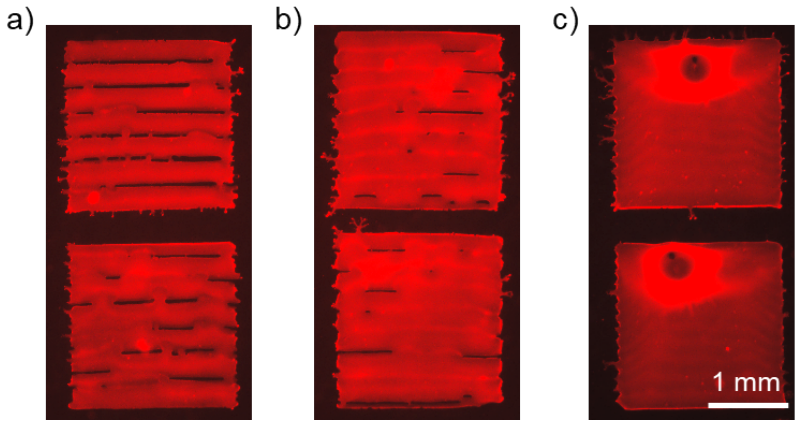

Figure 41. Fluorescence images of inkjet-printed square patterns by applying various DS. a) 30 μm, b) 25 μm, c) 20 μm.

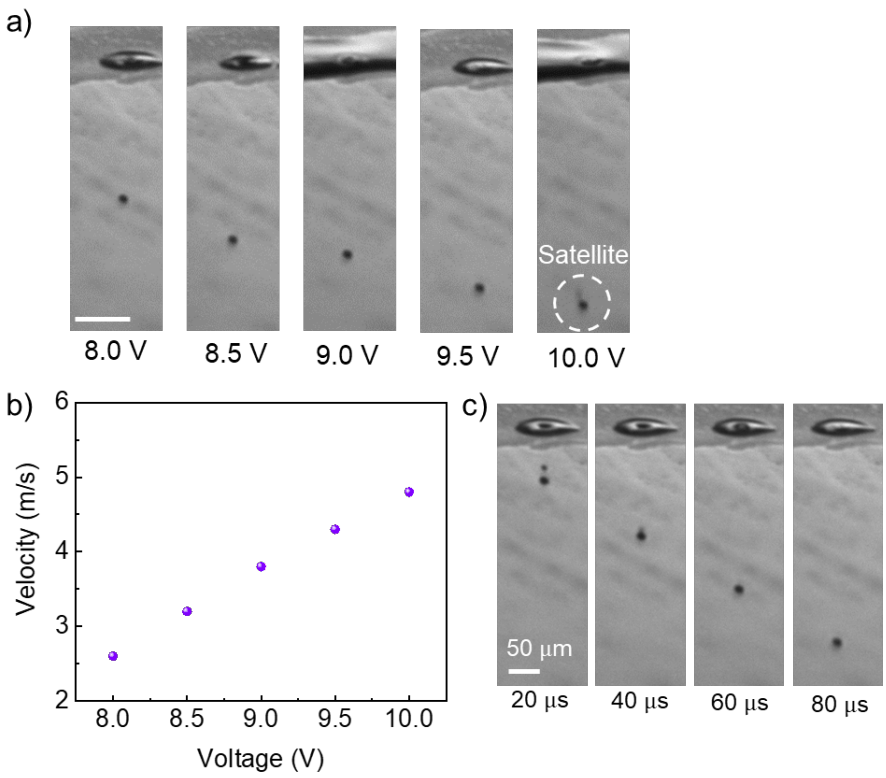

Figure 42. a) The ejection of QD droplets under different printing voltages. Scale bar: 100 µm, at 80 µs. b) The velocity of QD droplets with respect to the printing voltage. c) The evolution of a single droplet over time at 9.5 V, following ejection from the nozzle.

4.4 Droplet Drying

This section studied the impact of the ink solvent's volume ratio and T_{sub} on the CRE and revealed the drying modes of the QD ink at different T_{sub}.

4.4.1 Effect of Solvents' Volume Ratio and T_{sub} on the CRE

The QD inks were printed on the PVK film at different substrate temperatures, T_{sub} of 20 °C, 40 °C, and 60 °C using the above printing parameters. The fluorescent images and corresponding line profiles of the printed circular patterns are shown in Figure 43. The droplets exhibited multiple coffee rings after evaporation except the ink-20 printed at the T_{sub} of 60 °C, indicating multiple times of pinning of the contact line. At the T_{sub} of 20 °C, all ink droplets apart from the ink-10 showed two coffee rings and a dark center due to the prolonged drying time and the longer pinning period (Figure 43 a1, a3, and a4). The non-uniformity of the ink-10 droplets at the T_{sub} of both 20 °C and 40 °C can be attributed to the undesirable dissolvability and aggregation during solvent evaporation (Figure 43 a2 and b2) [72]. As the T_{sub} increased from 20 °C to 40 °C, the number of coffee rings remained the same, but the outermost coffee ring narrowed

because the extra thermal energy shortened the contact line pinning time at the edge (Figure 43 b1 and b3). A small bright center reveals that the contact line of ink-80 droplets was depinned during the final drying stage (Figure 43 b4). When the T_{sub} reached 60 °C, the ink-3 droplets showed the same CRE as at the T_{sub} of both 20 °C and 40 °C because the small decane volume evaporated rapidly initially, leaving a CHB-only solvent system (Figure 43 c1). Due to the very short pinning time, only a weak coffee ring at the edge and a larger bright center were observed for the ink-10 and ink-80 droplets (Figure 43 c2, and c4). Yet, uniform patterns were achieved when the ink-20 was printed at 60 °C (Figure 43 c3).

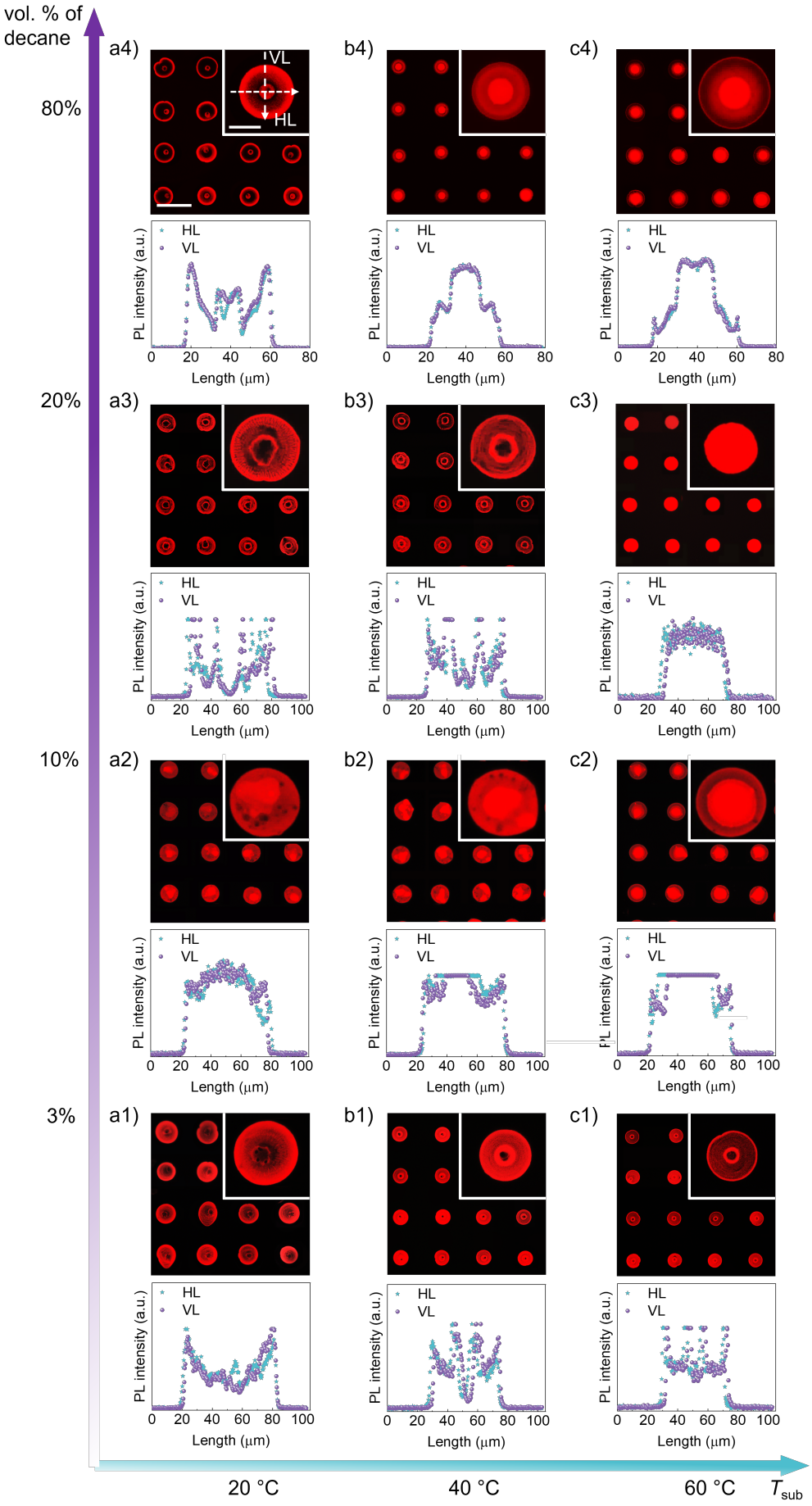
vol. % of decane
80%
20%
10%
3%
a4)
b4)
c4)
a3)
b3)
c3)
a2)
b2)
c2)
a1)
b1)
c1)
VL
HL
PL intensity (a.u.)
Length (μm)
20 °C
40 °C
60 °C
T_{sub}

Figure 43. PL images and corresponding line profiles of QD patterns by printing the QD inks with 3 vol. %, 10 vol. %, 20 vol. %, and 80 vol. % of decane on the PVK-coated glass substrate at the T_{sub} of a1-a4) 20 °C, b1-b4) 40 °C, and c1-c4) 60 °C. Each PL image has an insert at the top right to enlarge the spot. The droplet volume is 25 ± 5 pL. HL and VL indicate horizontal and vertical lines, respectively, passing through the center of the inset spot. The scale bars for the QD array and a single QD spot are 100 μm and 25 μm, respectively.

Apart from varying the volume ratio of decane in CHB, the addition of a small amount of PMMA (0.5 mg/mL, 8 kDa) into the ink-10 can also tune the strength of Ma_s. The fluorescence images and corresponding line profiles of QD patterns by printing the QD-10 with 0.5 and 1.0 mg/mL of PMMA (8 kDa) at the T_{sub} of 20 °C, 40 °C, and 60 °C are provided in Appendix 9.3. Smooth QD patterns were obtained when the ink-10 with 0.5 mg/mL was printed at 40 °C. Additionally, the evaporation of the ink-20 at different T_{sub} on the PVK/glass substrate that was pre-wetted by the ink solvents (20 vol. % decane) was studied. The fluorescence images and corresponding line profiles of printed QD patterns are provided in Appendix 9.3. The ink solvents might reassemble PVK molecules, thus slightly changing the surface morphology and showing different QD patterns after drying.

In terms of the motion of capillary and Marangoni flows during drying, the contact line was fixed after the droplets were deposited, and the evaporation of decane at the edge will have created the outward capillary flow. As the initial homogeneous binary components changed, spatial variations in composition emerged, leading to corresponding interfacial γ gradient and a solutal Marangoni flow (Ma_s) along the interface from the apex to the edge of the droplet. The strength of the Ma_s was reported to be proportional to the ratio of interfacial γ gradient ($\Delta\gamma = \gamma_{CHB} - \gamma_{ink}$) and viscosity, $Ma_s \propto \Delta\gamma/\eta$ [80, 89], where γ_{CHB} is γ of the QD ink with 100 vol. % of CHB (32.3 mN/m). The Ma_s should, therefore, increase by increasing the vol. % of decane (see Table 11). However, if the Ma_s is too weak, then the capillary flow will dominate, and the CRE will be the resultant pattern. To enhance the strength of the Marangoni flow further, the thermal Marangoni flow (Ma_T) must be enhanced by increasing the T_{sub}. The initial flow direction depends on the ratio of thermal conductivity between the glass (K_s = 1.05) and the CHB/decane mixture (K_l = ~0.13) at RT, which is 8.1. As this ratio is >2, thermal energy transferred to the droplet caused the highest temperature at the CL, where the conduction pathway was minimized. In contrast, the droplet apex experienced a lower temperature due to the longer conduction pathway. Therefore, the circulation flow caused by the Ma_T spatially moved inward and then outward. The capillary and net

Marangoni flow were speculated to reach equilibrium for the ink-20 when T_{sub} = 60 °C.

4.4.2 Evaporation Modes of the Ink Droplets

The real-time evaporation of the ink-20 droplets at the T_{sub} of 20 °C, 40 °C, and 60 °C was observed from both top and side views to study how coffee rings formed through the evolution of droplet diameter and CA (Figure 44). Notably, the droplet size in Figure 44a was smaller than that in Figure 44b because different instruments with varying capabilities were used, resulting in different time scales. For droplets with different sizes, the evaporation, pinning, and depinning times vary during evaporation, but the trends in droplet diameter and contact angle evolution remain consistent [231].

Initially, a plateau in droplet diameter indicated that the contact line was pinned while the CA reduced, forming the outermost coffee ring, a phase that is known as the constant radius mode (CRM) [94]. The pinning time decreased with increasing the T_{sub} (< 1 s at 60 °C, Figure 44a). More optical images of the evolution of droplet diameter of the ink-20 drying at different T_{sub} are provided in Appendix 9.3. Subsequently, the contact line receded, and the CA partially recovered at 20 °C and 40 °C but plateaued at 60 °C (at ~94 s, Figure 44b) until drying was complete, a phase termed the constant angle mode (CAM) [95]. Then, the droplet diameter plateaued again at 38 s, with the CA partially recovering several times at 40 °C, i.e., alternating the CRM and CAM until the contact line receded to zero, forming more coffee rings. At 20 °C, the droplet behaved the same as at 40 °C but repeated more cycles of the CRM and CAM.

At the T_{sub} of 20 °C and 40 °C, the combined effects of Ca and Ma_s initially drive liquid from the center to the periphery, reducing the contact angle while keeping the contact line pinned in a constant radius. This transport of QDs to the edge forms an outmost coffee ring. Subsequently, the Ma_T and Ca restore the droplet's original shape, triggering the contact line to recede. The process then repeats multiple times until the droplet fully evaporates. This evolution is called the stick–jump (SJ) mode (Figure 45a) [98], where multiple coffee rings originated from the CR mode. In contrast, drying at 60 °C, the initial drying phase in the CR mode follows the same pattern, but due to the stronger strength of Ma_T and rapid evaporation, its duration is significantly shorter. The drying process then transitions into the CA mode, continuing until the contact line fully recedes. This evolution belongs to another mixed mode, starting with a CR mode followed by a CA mode until the evaporation was completed, known as the stick–slide (SS) mode (Figure 45b).[97]

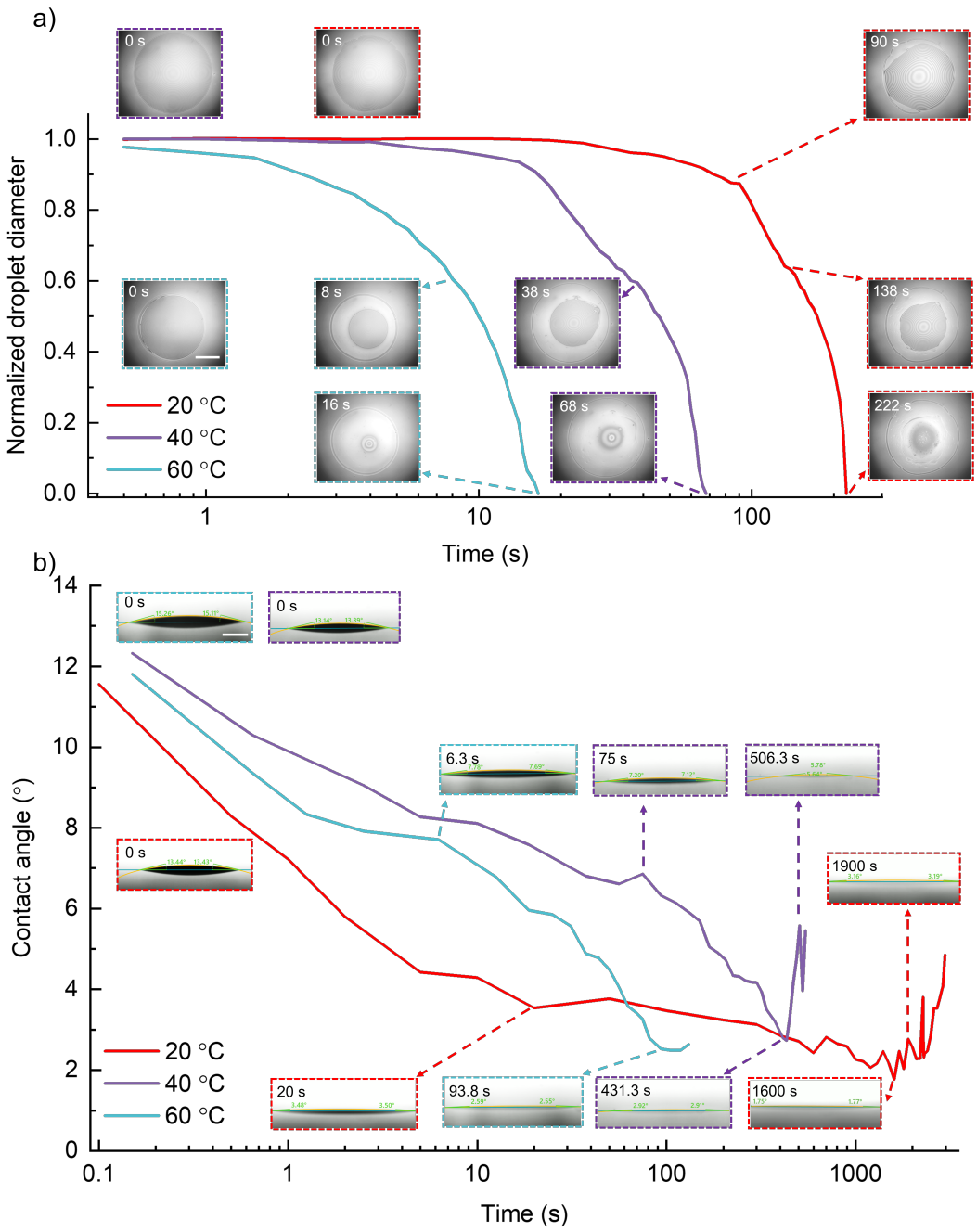

Figure 44. The evolution of a) droplet diameter and b) contact angle of the ink-20 drying on the PVK-coated glass substrate at the T_{sub} of 20 °C, 40 °C, and 60 °C. The scale bars in Figure a) and b) are 200 μm and 300 μm, respectively. The droplet volumes in Figure 3a and 3b are 46 ± 10 nL and 310 ± 70 nL.

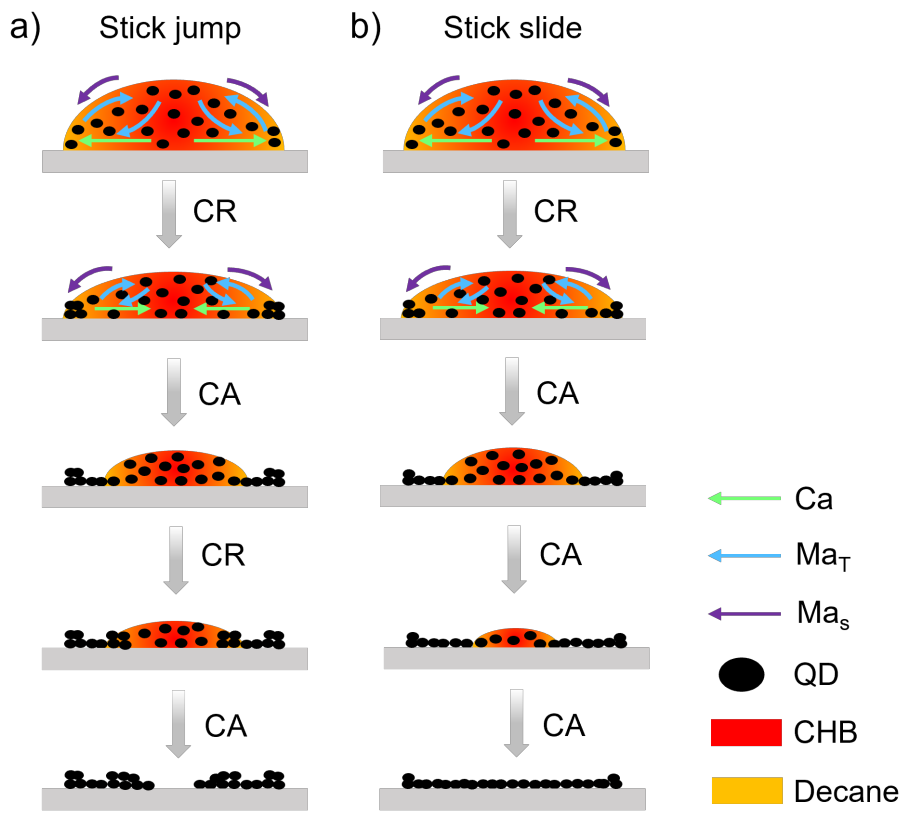

Figure 45. Schematics of the evaporation modes of QD droplets drying at different T_{sub}. a) SJ mode at 20 °C and 40 °C. b) SS mode at 60 °C.

4.5 Spin-coated Functional Layers

This section characterizes the thickness and morphology of spin-coated and inkjet-printed functional films by AFM and ellipsometry.

4.5.1 Thickness of Functional Layers

The thicknesses of functional layers spin-coated with different concentrations and spin speeds were measured by ellipsometry and AFM (Figure 46 and Figure 47) were summarised in Table 12. The SE data, optical constants, and absorbance of these functional materials are shown in Appendix 9.4. MSE is calculated by equation (30) in section 2.8. They showed comparable results, indicating physical modeling for ellipsometry data analysis. The average thickness of one printing layer of QD films was about 18 nm (Figure 47 a2, b2), which was similar to that of the QD films prepared by spin-coating the QD dispersion with a concentration of 15 mg/mL at 2000 RPM. The roughness (R_{ms}, 2.9 nm) of inkjet-printed QD films was slightly greater than that of spin-coated ones (2.4 nm).

Table 12. A summary of the thickness and roughness of spin-coated PEDOT:PSS, PVK, TFB, QDs, and $Zn_{0.9}Mg_{0.1}O$-EA films measured by ellipsometry and AFM, respectively.

Samples	Spin speed (RPM)	Ellipsometry		AFM	
		Thickness (nm)	MSE	Roughness (R_{ms}, nm)	Thickness (nm)
ITO	-	101	5.2 ± 0.2	2.1 ± 0.1	111 ± 2
PEDOT:PSS (20 vol.% IPA)	4000	35 ± 1	6.3 ± 1.9	2.4 ± 0.2	-
PEDOT:PSS (0 vol.% IPA)	4000	27 ± 1	1.8 ± 0.1	2.0 ± 0.3	30 ± 1
PVK	4000	21.6 ± 0.4	2.1 ± 0.1	1.0 ± 0.1	25 ± 2
TFB	3000	24.7 ± 0.3	5.1 ± 0.2	0.8 ± 0.2	23 ± 1
QDs (15 mg/mL)	2000	19 ± 1	1.9 ± 0.3	2.4 ± 0.5	-
QDs (10 mg/mL)	3000	10.0 ± 0.3	4.3 ± 0.8	3.0 ± 0.4	11 ± 2
$Zn_{0.9}Mg_{0.1}O$-EA (14 mg/mL)	4000	40 ± 1	3.3 ± 0.6	2.6 ± 0.2	41 ± 3
$Zn_{0.9}Mg_{0.1}O$-EA (25 mg/mL)	5000	49 ± 1	6.9 ± 0.6	-	-
	3000	60.6 ± 0.1	9.5 ± 0.2	-	-

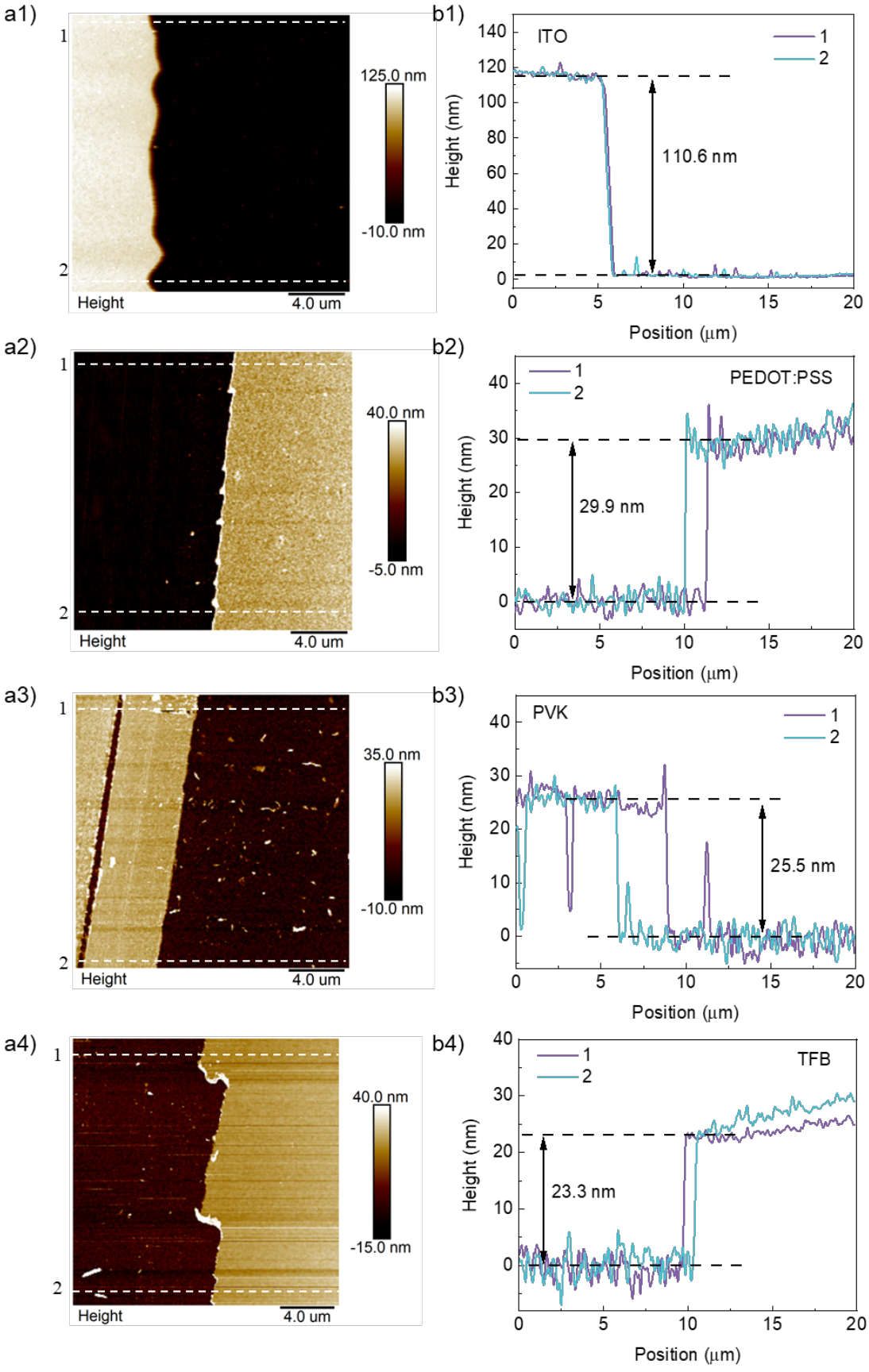

Figure 46. a1-a4) Cross-section AFM images and corresponding b1-b4) line profiles of the functional films. a1-b1) ITO, a2-b2) PEDOT:PSS, a3-b3) PVK, a4-b4) TFB.

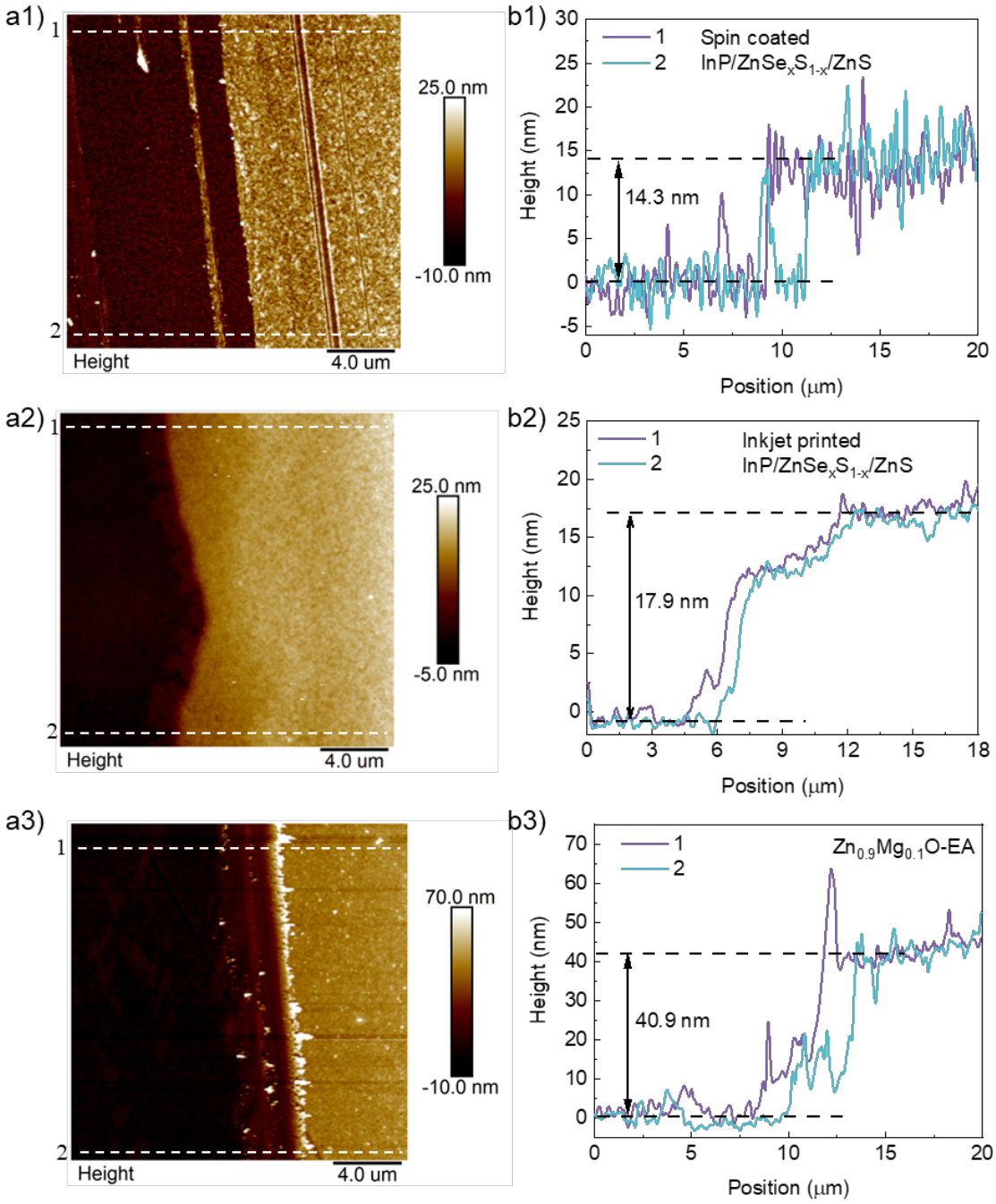

Figure 47. a1-a3) Cross-section AFM images and corresponding b1-b3) line profiles of the functional films. a1-b1) spin-coated QD, a2-b2) inkjet-printed QD, a3-b3) $Zn_{0.9}Mg_{0.1}O$.

4.5.2 Morphology of Functional Layers

It is crucial to obtain uniform and smooth films because the smoothness of each functional layer influences the brightness uniformity of the resultant QD-LEDs. There exist carrier leakages and shorter carrier pathways for films with pin holes. Table 12 summarizes the roughness of each functional layer characterized by AFM, showing smooth and pin-hole-free features (Figure 48 - Figure 54). The optical images of

cleaned ITO glass and PVK-coated ITO glass and fluorescence images of spin-coated QDs on the PVK-coated ITO glass are shown in Appendix 9.3. The smooth morphology makes it possible to deposit upper layers by the solution process. For QD and ETL films, there were clusters in small areas, likely resulting in FRET that caused the redshift and lower efficiency in QD-LEDs [129, 141]. This will be discussed in section 4.6. After adding the EA, the roughness of $Zn_{0.9}Mg_{0.1}O$-EA dramatically decreased from 5.6 to 2.6 nm (Figure 54 and Figure 55).

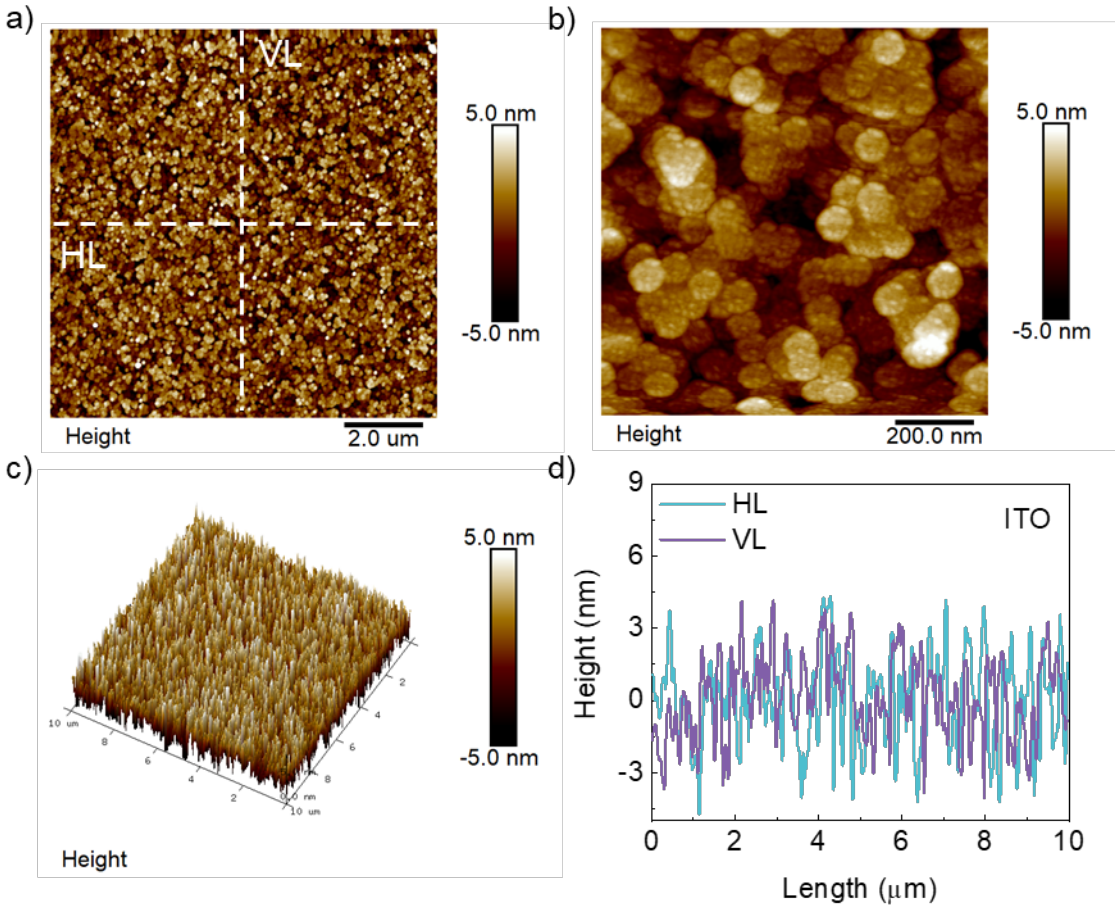

Figure 48. a-b) 2D and c) 3D AFM images and d) corresponding line profiles of ITO films.

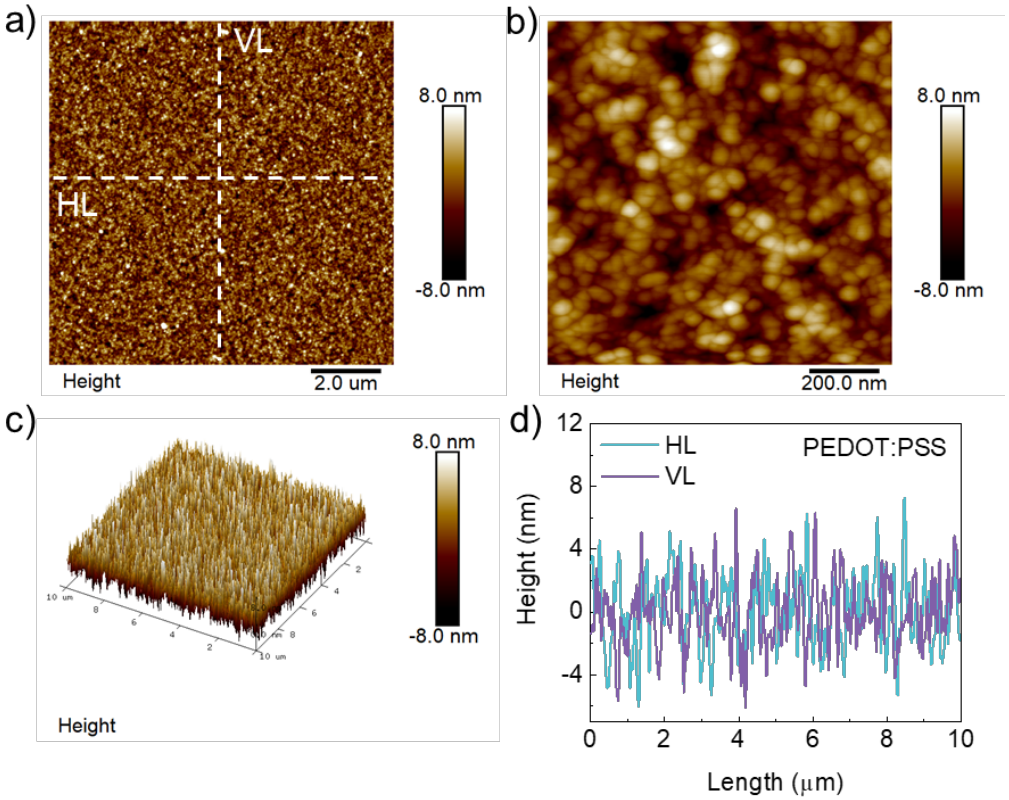

Figure 49. a-b) 2D and c) 3D AFM images and d) corresponding line profiles of PEDOT:PSS films.

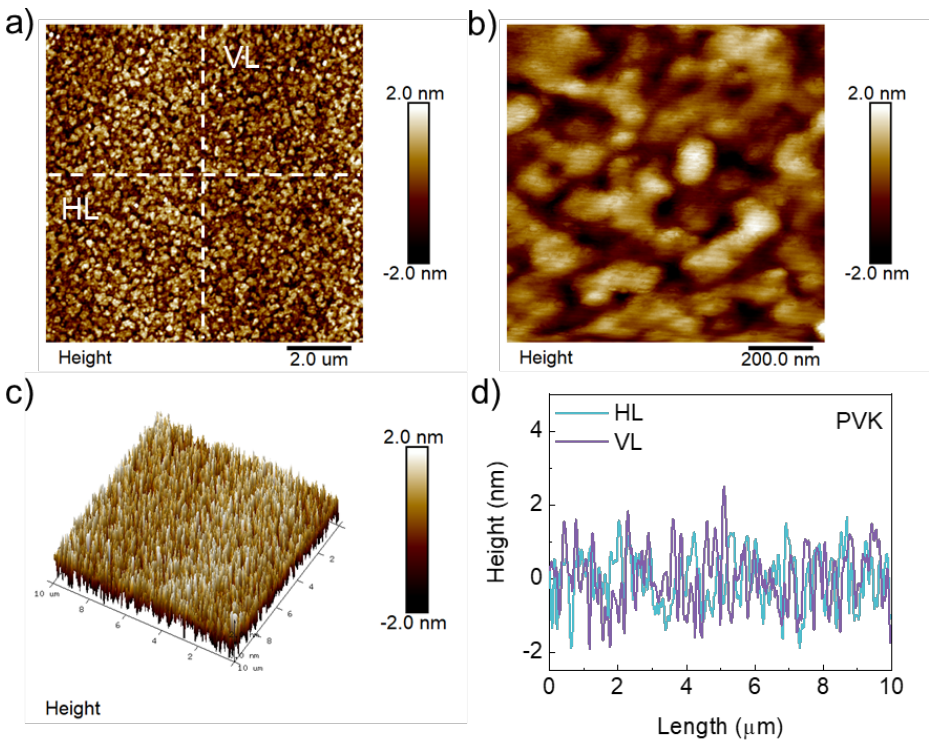

Figure 50. a-b) 2D and c) 3D AFM images and d) corresponding line profiles of PVK films.

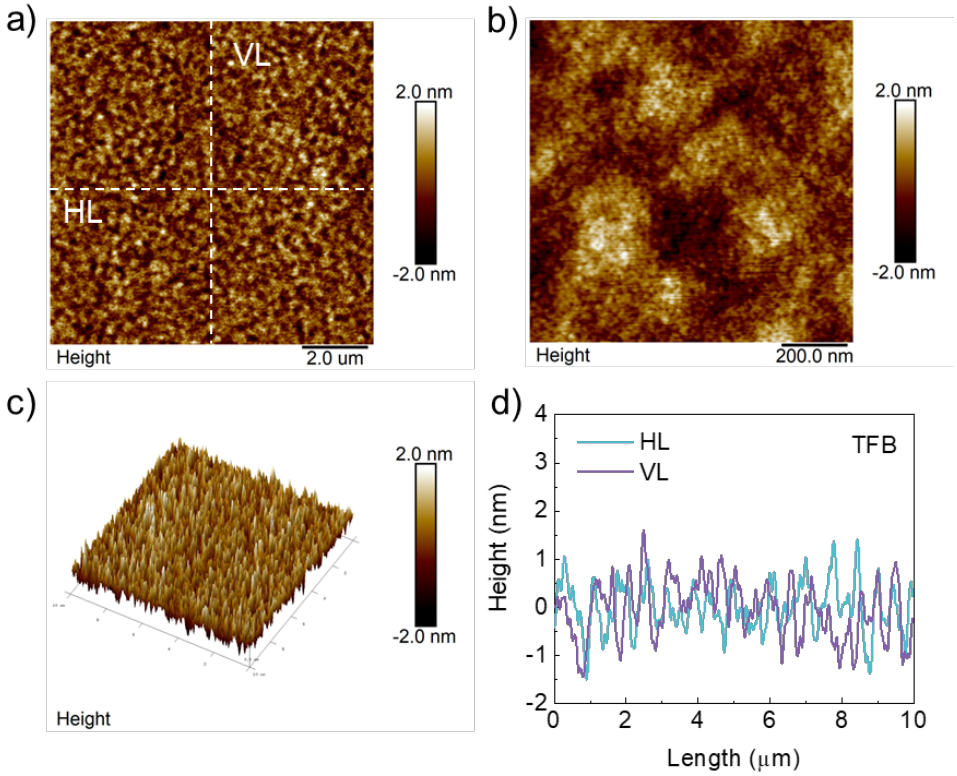

Figure 51. a-b) 2D and c) 3D AFM images and d) corresponding line profiles of TFB films.

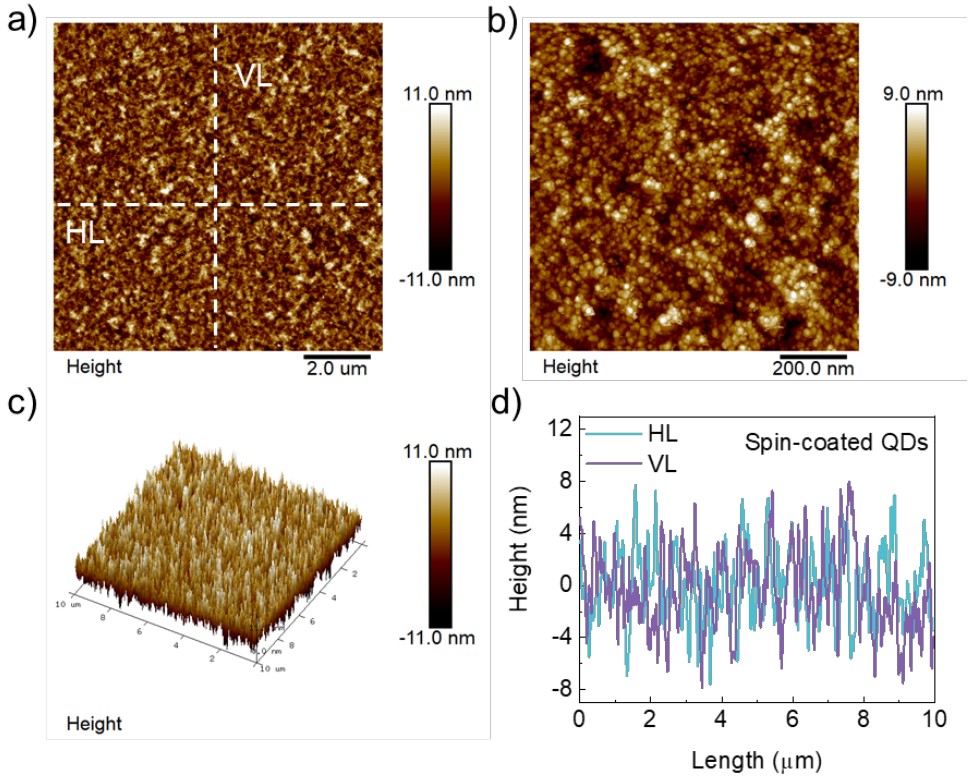

Figure 52. a-b) 2D and c) 3D AFM images and d) corresponding line profiles of spin-coated QD films.

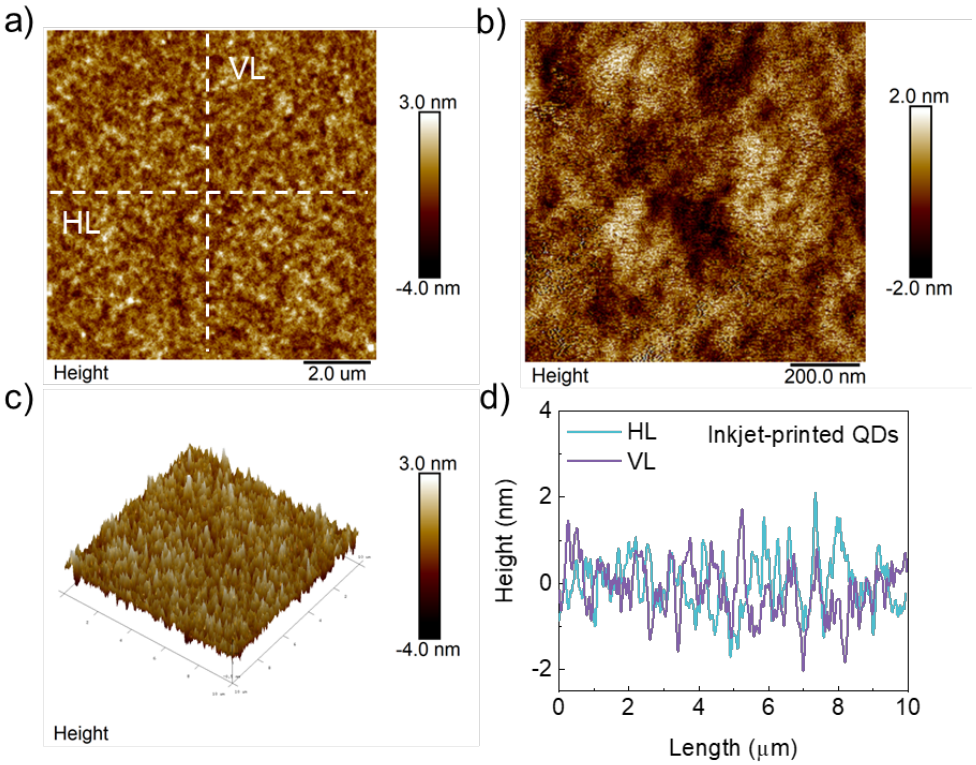

Figure 53. a-b) 2D and c) 3D AFM images and d) corresponding line profiles of inkjet-printed QD films.

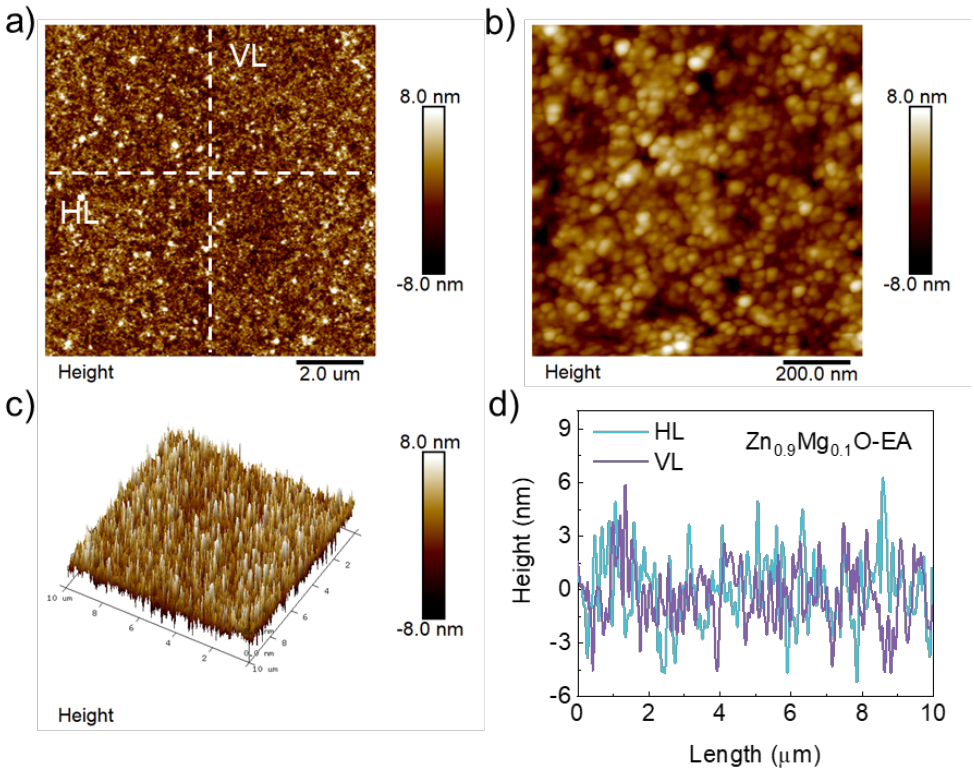

Figure 54. a-b) 2D and c) 3D AFM images and d) corresponding line profiles of $Zn_{0.9}Mg_{0.1}O$-EA NP films.

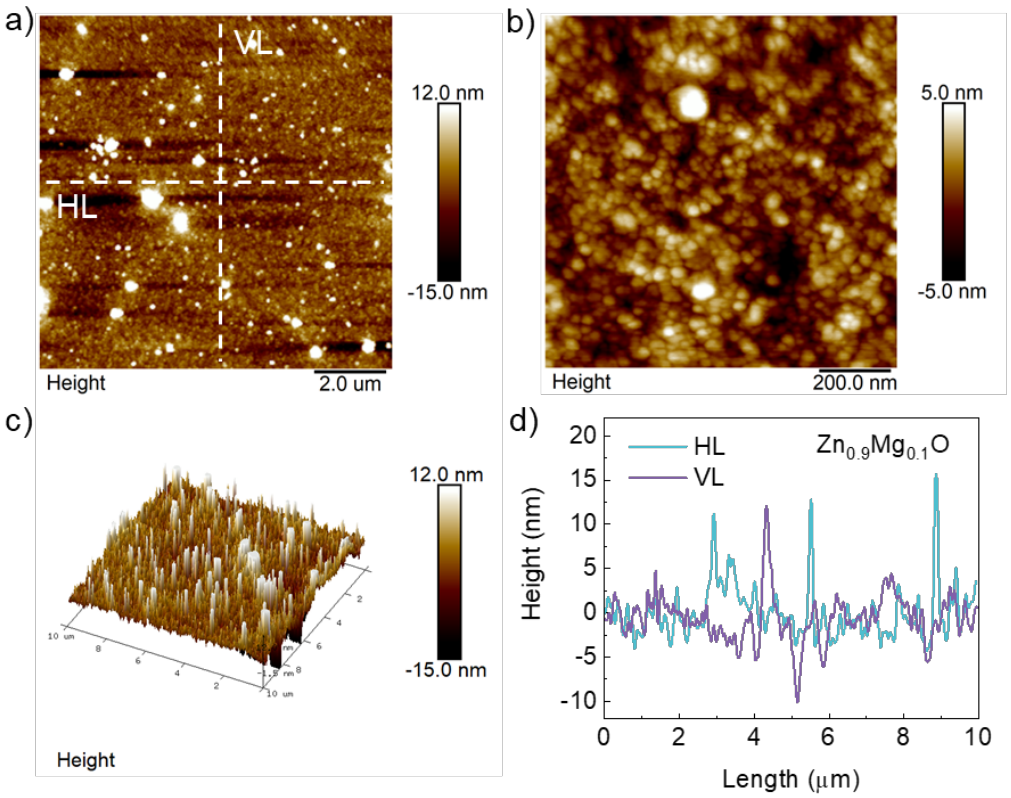

Figure 55. a-b) 2D and c) 3D AFM images and d) corresponding line profiles of $Zn_{0.9}Mg_{0.1}O$ NP films.

4.6 Electrical Performance of InP QD-LEDs

The structure of inkjet-printed QD-LEDs consists of indium tin oxide (ITO, 101 nm), PEDOT:PSS (35 nm), PVK (22 nm), InP/$ZnSe_xS_{1-x}$/ZnS (QDs, 18 nm), $Zn_{0.9}Mg_{0.1}O$ NPs (61 nm), and Al (100 nm), as shown in Figure 56a. Figure 56b shows the corresponding energy band alignment of the function materials in the devices. Adding a small amount of alcohol into the PEDOT:PSS ink was reported to enhance its conductivity due to its clean-off effect on the insulting PSS [232]. In this work, the addition of 20 vol. % of IPA also led to a lower CA on the ITO glass (Figure 57), facilitating the formation of smoother and more uniform PEDOT:PSS films.

In our system, the thermal evaporator was not connected to the glove box, so the ETL was inevitably exposed to the air with a relative humidity (RH) of 55% ± 5% for approximately 15 min. During the transfer, oxygen changes the behavior of charge transport in the ETL because it can trap electrons. Water vapor accumulates on the surface of $Zn_{0.9}Mg_{0.1}O$ film and soaks into the QD layer when RH > 60%, quenching the QD layer and deteriorating device performance [40]. Thicker ETL (> 40 nm) was hypothesized to alleviate the deterioration of the ETL and QD layer, so the electrical

performance of QD-LEDs with different ETL thicknesses was investigated. The ETL thickness of 40 nm was commonly used in literature (without exposure to air) [148], and resistivity was reported to increase for films thicker than 50 nm because more carriers were trapped at grain boundaries [233].

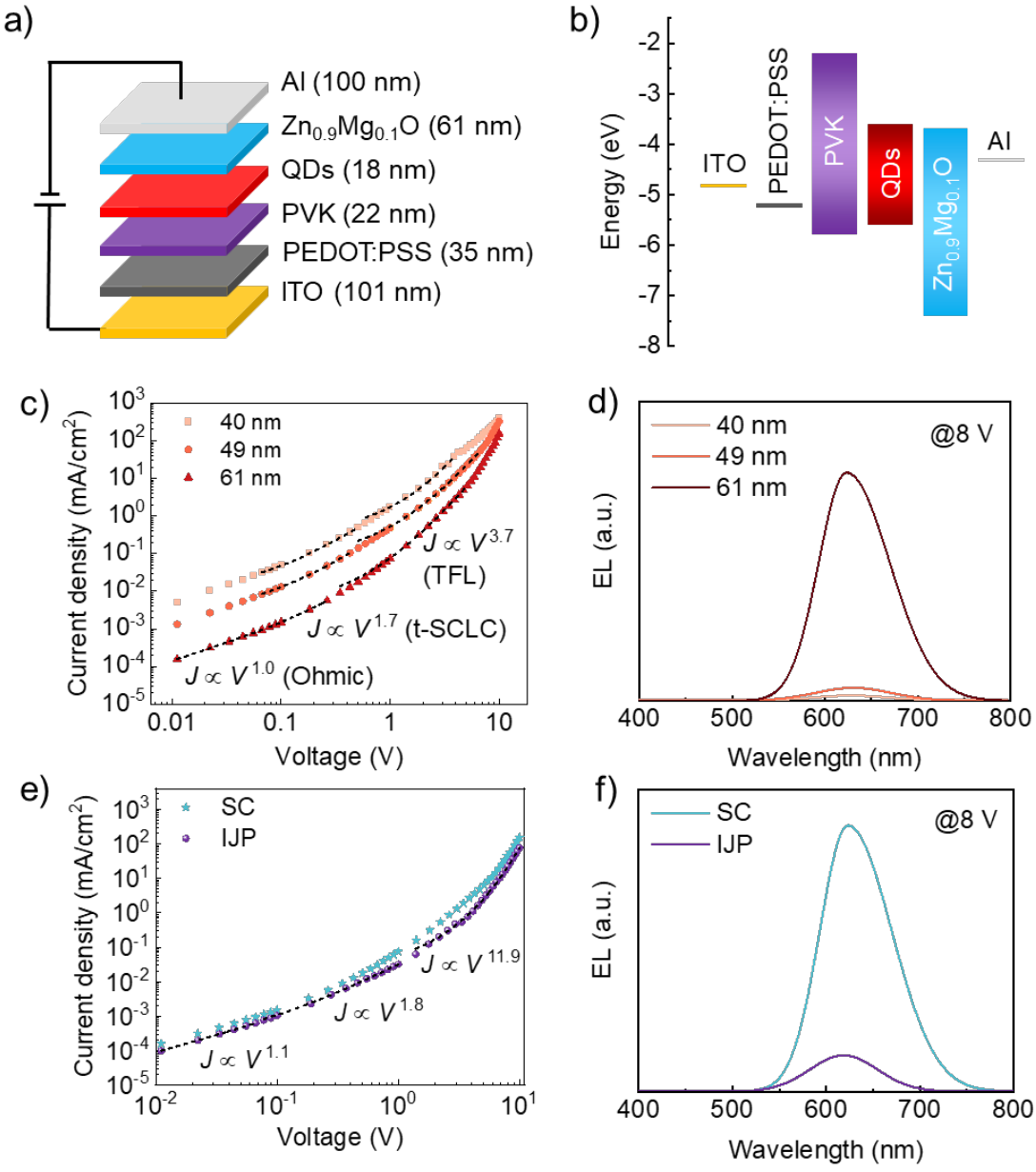

Figure 56. Electrical performance of inkjet-printed InP QD-LEDs. a) The device structure and b) the energy band diagram of QD-LEDs. c) *J-V* behavior and d) EL spectra (at 8 V) of QD-LEDs with different thicknesses of the ETL. e) *J-V* behavior and f) EL spectra (at 8 V) of spin-coated and inkjet-printed QD-LEDs. The black dashed lines in Fig. c) and e) are fitting curves of $J \sim V^n$.

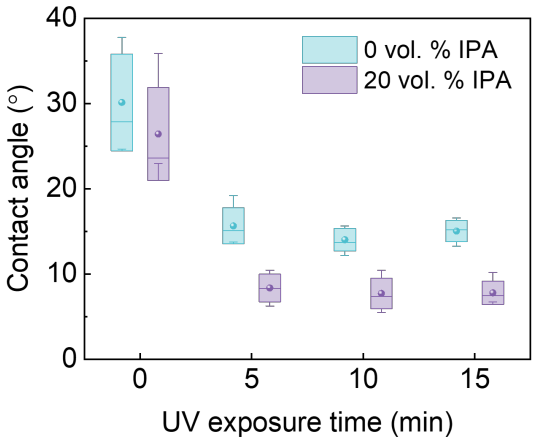

Figure 57. CA of PEDOT:PSS with and without adding 20 vol. % IPA varies with the UV-Ozone exposure time. The substrate is ITO glass.

Thus, thicknesses of 40 nm, 49 nm, and 61 nm were selected for this study. The *J*−*V* characteristics of spin-coated InP QD-LEDs with different thicknesses of $Zn_{0.9}Mg_{0.1}O$ films suggested a $J \sim V^n$ relation (Figure 56c) [170]. The corresponding power exponents are shown in Table 13, the bigger *n* in the TFL region indicates the presence of more trap states. The threshold voltage (V_{TFL}, the voltage transits from the TFL to the t-SCLC region) and trap density (N_t) were reduced by half and two-thirds, respectively when the ETL thickness increased from 40 nm to 61 nm. N_t can be calculated by

$$N_t = \frac{2\varepsilon\varepsilon_0 V_{\mathrm{TFL}}}{eL^2} \tag{45}$$

Where ε, ε_0, e, and L are the relative permittivity of $Zn_{0.9}Mg_{0.1}O$-EA NPs, vacuum permittivity, elementary charge, and the thickness of $Zn_{0.9}Mg_{0.1}O$-EA NP films, respectively [41]. The EL intensity of InP QD-LEDs significantly improved due to the lower trap states (Figure 56d). The lower trap density is likely attributed to a reduction in oxygen vacancies within the ETL, which minimizes defect-related exciton quenching at the ETL/QD interface [234]. The inkjet-printed devices showed higher V_{TFL}, N_t, and *n* in the TFL region than the spin-coated ones, which is likely due to the increasing air exposure time of the QD layer being printed in an ambient atmosphere. This introduces surface oxides and more trap states in the QD layer, thus impacting the QD-ETL interfacial electron transport (Figure 56e) [234]. It could also account for potential contributions from other layers within the device. The PVK film could be slightly corroded by the ink solvents and was exposed to air for a short time before printing the

QD layer. Water and oxygen might physiosorb on the PVK film, reducing the hole injection.

Table 13. Power exponent, V_{TFL}, and N_t of InP QD-LEDs with different ETL thicknesses.

Thickness of the ETL	*n*			V_{TFL} (V)	N_t (N_0)
	ohmic	t-SCLC	TFL		
40 nm (SC)	1.0	2.0	4.9	0.51	1.0
49 nm (SC)	1.0	2.0	3.8	0.43	0.56
61 nm (SC)	1.0	1.7	3.7	0.26	0.34
61 nm (IJP)	1.1	1.8	11.9	1.0	1.31

The luminance of InP QD-LEDs increased with increasing the applied voltage, but it reached a plateau (620 and 250 cd m^{-2}) at approximately 10.0 and 11.5 V for the spin-coated and inkjet-printed ones, respectively, which is likely to be caused by field-induced quenching (Figure 58a) [142]. The maximum EQE of spin-coated and inkjet-printed devices was 0.5% and 0.2%, respectively (Figure 58b). The EL intensity of inkjet-printed devices was just one-seventh of spin-coated devices (Figure 56f and Figure 59), but they exhibited comparable EL peak maxima (620 nm vs 623 nm). Compared with the PL, a red shift of the EL peak and broad EL emission can be attributed to the electric field-accompanying Stark effect and the inter-QD FRET [129, 141]. Apart from the undesirable compatibility of TFB with the ink solvents, the disadvantage of TFB-based InP QD-LEDs also included a parasitic emission centered at 436 nm because the deep-lying lowest unoccupied molecular orbit of TFB led to the flow of electrons from the QD layer to the TFB layer [152] (Figure 60). The emission intensity from the TFB layer increased as the voltage increased.

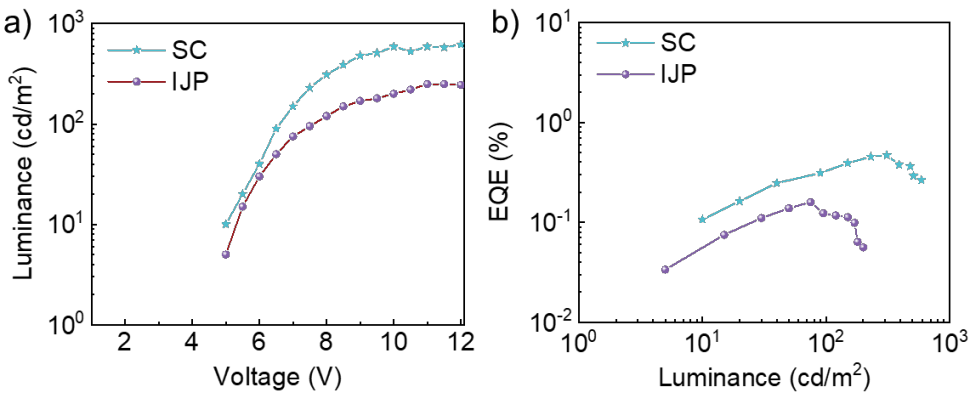

Figure 58. a) Luminance and b) EQE of inkjet-printed and spin-coated InP QD-LEDs.

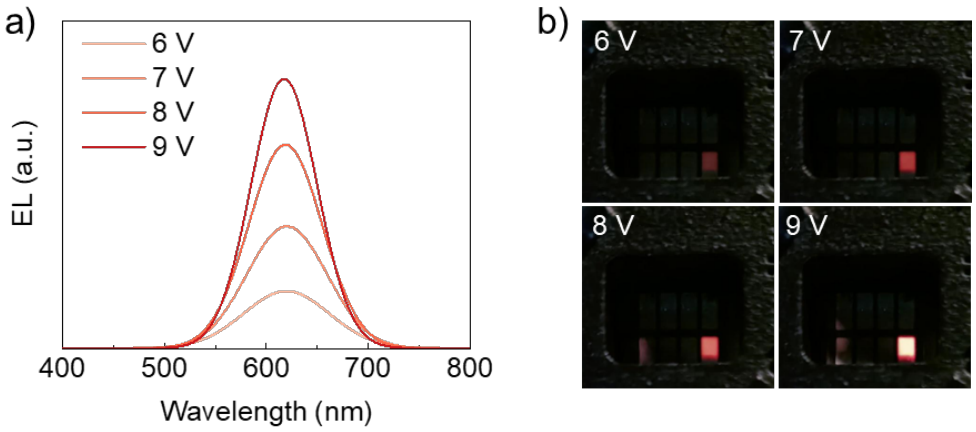

Figure 59. a) EL intensity and b) corresponding photographs of inkjet-printed InP QD-LEDs under various applied voltages. The pixel size is 2 mm by 2 mm.

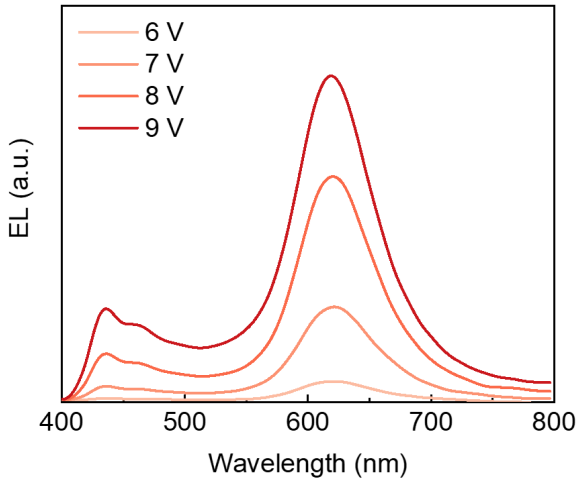

Figure 60. EL spectra of InP QD-LEDs using TFB as the HTL.

The inkjet-printed millimeter-sized QR code, letters, and the University of Leeds icon, which were composed of the InP QDs, demonstrated excellent printing resolution, showing potential for Cd-free QDs-based anti-counterfeiting applications and large-scale manufacturing (Figure 61). These patterns exhibited low roughness, were free of coffee rings, and displayed uniform luminescence, aligning with the previous discussion.

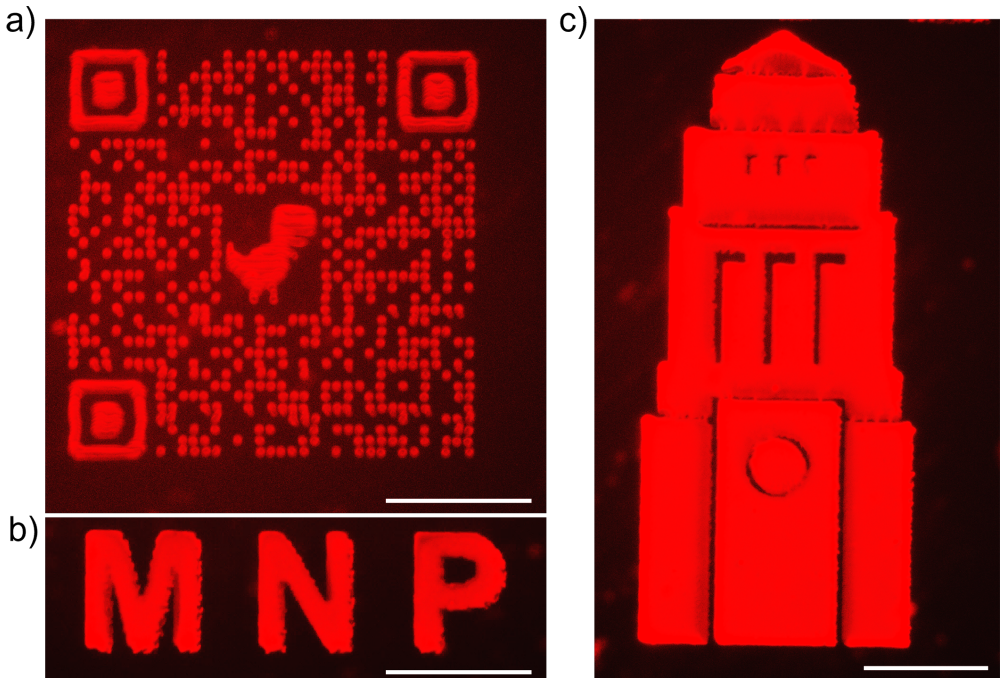

Figure 61. PL images of an inkjet-printed a) MNP QR code, b) letters, and c) Leeds University icon by printing the ink-20 on the PVK/glass substrate at T_{sub} = 60 °C. Scale bars: 1 mm.

4.7 Concluding Remarks

We successfully fabricated Cd-free QD-LEDs without coffee rings based on high-quality InP/$ZnSe_xS_{1-x}$/ZnS QDs via IJP. The ME was introduced to alleviate the CRE, including the solutal and thermal ME, which were achieved by adjusting the vol. % of the ink solvents and heating the substrate during printing, respectively. The smooth and uniform QD patterns were achieved by printing the ink-20 at T_{sub} of 60 °C. The temporal evolution of the ink-20 droplet diameter and CA revealed the SJ mode at 20 °C and 40 °C and the SS mode at 60 °C, giving insight into the fundamental understanding of the coffee ring formation of fluids containing NPs with an extremely small size (<10 nm).

Furthermore, this work highlighted the potential drawbacks of device exposure to air, as well as the challenges and issues that may arise during the open-air manufacturing of inkjet-printed QD-LEDs. Increasing the ETL thickness reduced trap density in the ETL and protected the QD layer from oxygen and water, greatly enhancing the electrical performance of InP QD-LEDs. The electrical performance of inkjet-printed QD-LEDs was inferior to spin-coated analogs because of the quenching of QDs during printing in the ambient atmosphere, leading to a lower EQE of 0.2%. Additionally, the hole mobility of PVK is much less than the electron mobility of $Zn_{0.9}Mg_{0.1}O$, resulting in

less balanced charge injection. To further improve the electrical performance of inkjet-printed InP QD-LEDs, future work can work on printing in an inert atmosphere to avoid the degradation of QDs by water and oxygen and optimizing the ink solvents which are compatible with TFB.

5. Degradation of InP QD Films

Currently, most high-performance QD-LEDs are fabricated in controlled environments, such as nitrogen-filled gloveboxes or vacuum-pumped thermal evaporators, to minimize exposure to atmospheric oxygen and water vapor. These factors are known to significantly degrade organic HTL materials and QDs [235]. However, such stringent fabrication conditions pose a considerable challenge for large-scale production methods, such as IJP. Additionally, the aerobic and thermal stability of QD-LEDs is critical for their practical application under harsh environmental conditions, including extreme temperatures and high humidity [236]. Although state-of-the-art QD-LEDs have achieved high EQEs, a substantial portion of the injected electrical energy—70% or more—is converted into heat [237]. This heat generation can result in elevated device temperatures during operation, particularly under high-power conditions or when using small substrates [54]. In extreme cases, temperatures can exceed 100 °C, leading to significant thermal degradation of the devices. The thermal stability of a QD-LED system is influenced by both the intrinsic and modified charge transport properties of the charge transport layers, as well as the exciton relaxation dynamics within the QD layer [238].

So far, many studies have focused on the air and thermal stability of Cd-based QDs and QD-LEDs [235, 236], which have been reviewed in section 1.6. Yet, Cd-free-based analogs are rarely reported. Therefore, understanding the quenching and chemical variations of InP QD films by air and heat is critical to developing air and thermal-stable InP QD-LEDs. The degradation of InP/$ZnSe_{1-x}S_x$/ZnS QD films by oxygen, water, and heat was characterized using fluorescence spectroscopy and NAP-XPS. To improve the air stability of QD films, a thin encapsulation layer of spin-coated PMMA.

5.1 Background

The air and thermal stability of QDs directly relates to the lifespan of QD-LEDs. The optical properties of QDs can be quenched by oxygen, water, light, and heat. This section discusses the degradation mechanisms of QDs and QD-LEDs when exposed to these factors, along with strategies to improve their stability in the air. QDs are susceptible to degradation due to diverse molecular interactions with oxygen and water under light. This physical and/or chemical adsorption of oxygen and water can significantly impact the overall behavior of QDs, resulting in photoactivation, photooxidation, and photocorrosion (Figure 62).

Photoactivation leads to PL enhancement in a short time when QDs exposed to water under light, which is believed to result from the passivation of surface trap states by adsorbed water molecules [42]. The photoinduced fluorescence enhancement effect highly depends on the environmental humidity levels. This process can be reversed by removing the physisorbed water molecules through inert-gas purging or vacuum degassing [43]. However, excessive water molecules oxidize the surface of QDs, introducing new surface states that lower the PL, and leading to a blue shift of in band-edge emission. Exposure of photoexcited QDs to oxygen, causing surface oxidation, is called photooxidation, which can be accelerated by UV irradiation [44]. Continuous oxygen exposure degrades their optical characteristics irreversibly and creates surface trap states, leading to permanent fluorescence quenching. Photooxidation generates ions like Cd^{2+} and SeO^{x-}, which then detach from the core through a process known as photocorrosion [45]. Photocorrosion results in the formation of surface trap states and a decrease in core size, which irreversibly quenches the PL, broadens the FWHM, and shifts the band-edge emission to shorter wavelengths.

The PL of QDs is quenched after heating but mostly enables it to restore to its initial state upon cooling [239]. Thermal-induced temporary trap states, arising from the ion exchange process, cause reversible PL quenching up to a specific temperature. However, repeated cycles of heating and cooling at elevated temperatures ultimately lead to irreversible degradation due to the formation of permanent trap states. These permanent states likely result from mismatched thermal expansion between the core and shell, as well as increased atomic mobility. The thermal stability of QDs is strongly influenced by their shells and ligands; unstable shells or ligands can readily create surface trap states and extra energy bands near the CB of the heated QDs [240].

The surface oxidation of InP QDs primarily results from water molecules produced during their synthesis. InP QDs, with stronger covalent bonds than II-VI QDs, require a high growth temperature above 170 °C. At this temperature, carboxylic acids commonly used in InP QD synthesis generate water through side reactions. The amorphous phase of the surface oxide (e.g., $InPO_x$, In_2O_3, etc.) can hinder the epitaxial growth of the ZnS shell due to the significant lattice mismatch between the surface oxide and ZnS [205]. Despite coating with multiple shells of ZnSe/ZnS, InP/ZnSe/ZnS QDs can also be oxidized. Oxidation of the ZnS shell results in ZnO formation, causing a lattice mismatch with the host QD lattice and leading to dislocations and strain within the QD [241]. These dislocations prompt the diffusion of In atoms from the core across the QD. Furthermore, ZnO is easily etched from the QD, and poor passivation of the

ZnSe layer creates dangling bonds. InP/ZnS QDs exhibit temperature-induced shifts in exciton absorption and luminescence peaks due to interactions with acoustic phonons [55]. A temperature-dependent Stokes shift reveals the fine structure of exciton states across different configurations. Exciton PL quenching mainly occurs through thermally activated electron migration from the InP core to the ZnS shell.

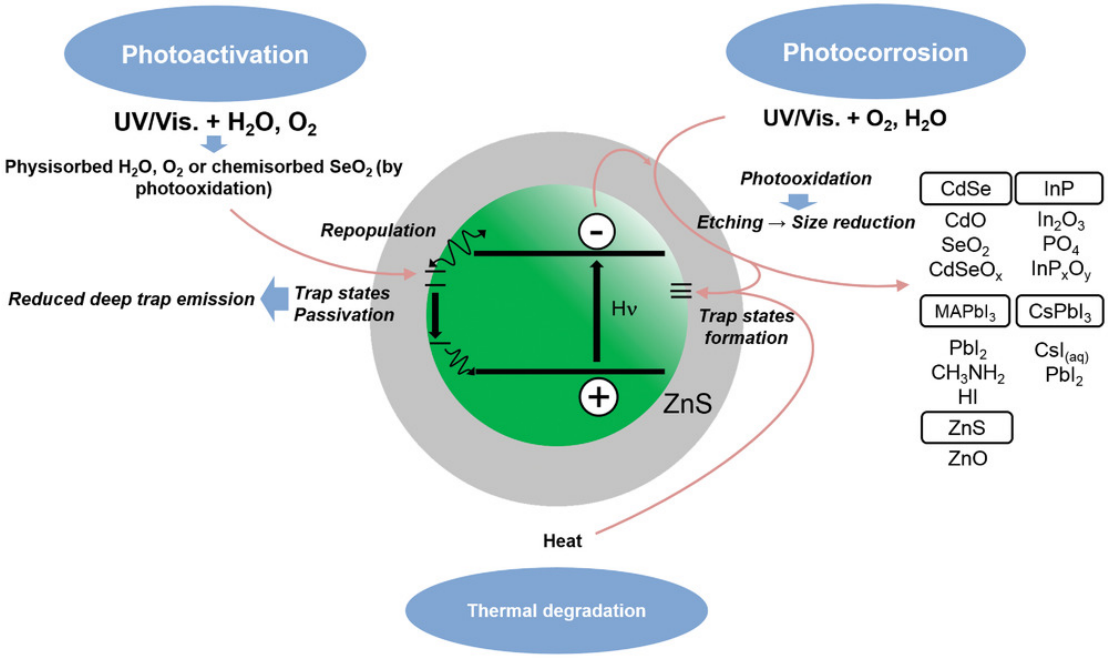

Figure 62. Degradation mechanisms of QDs that are caused by oxygen, water, light, and heat. Reprinted with permission from [242]. Copyright 2019 Wiley.

Ligand engineering and surface encapsulation are effective ways to mitigate the degradation caused by oxygen, moisture, illumination, and heat.

Surface ligands maintain the shape and size of individual dots in solid films, preserve the clean energy band gap, and control charge carrier conduction. This regulation enhances their performance in QD-LEDs. Bulky ligands provide effective coverage of the QD surface, hindering the infiltration of water and oxygen due to their substantial steric hindrance (Figure 63a) [243]. Ligand structure and functional groups significantly influence gas barrier performance [244]. Encapsulation of QDs within a polymer matrix is achieved by managing the polymer's solubility in solvents, eliminating the need for direct bonding between the QDs and polymers. This approach bypasses extra chemical reactions to introduce reactive functional groups on the QD surface. Under controlled processing conditions, polymers and QDs were uniformly blended, and the resulting mixture showed prolonged PL (Figure 63b) [245]. Additionally, inorganic

matrices like ZnS have also been reported to improve the air and thermal stability of QD films efficiently (Figure 63c) [246]. Polymers with shorter intermolecular distances can prevent oxygen and moisture transmission. Strong interactions, such as covalent bonds, decrease the distance between QDs and create a high packing density in the film by crosslinking ligands and crosslinkers, leading to lower oxygen and moisture permeability (Figure 63d) [35].

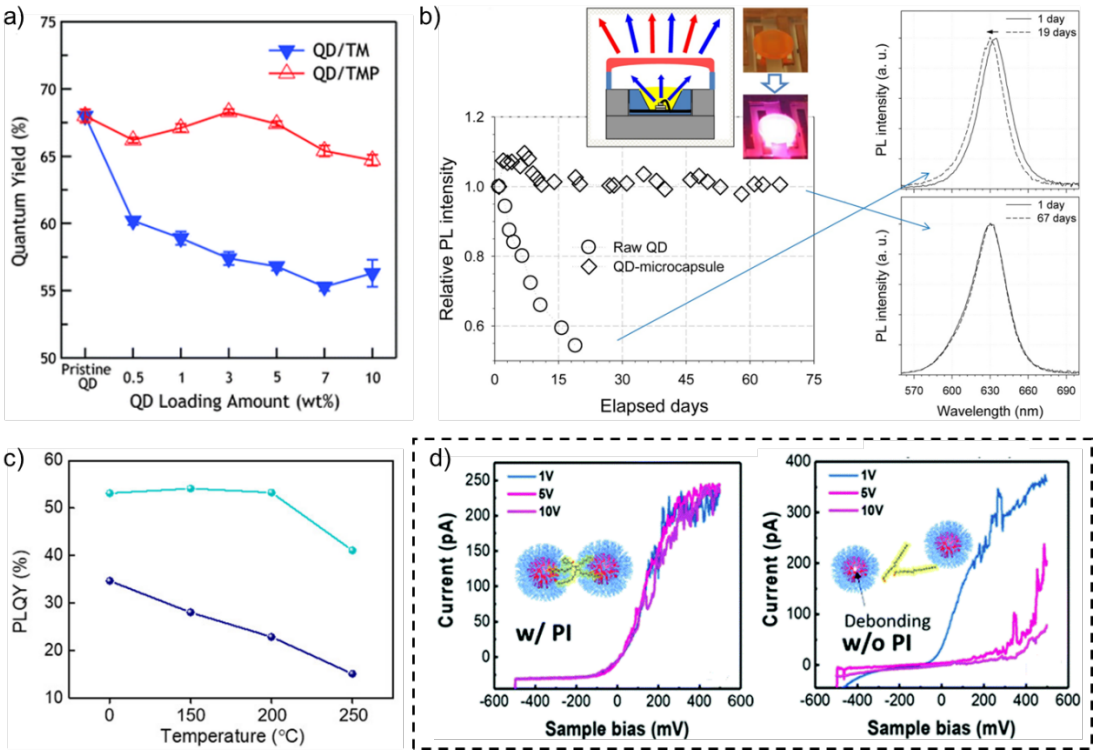

Figure 63. a) PLQY of QD-organosilicate hybrid films with different QD loading amounts. TM and TMP ligands represent the molar ratios of tetraethyl orthosilicate, methyl trimethoxysilane, and (3-mercaptopropyl)trimethoxysilane of 3:7:0 and 3:7:1, respectively. Reprinted with permission from [243]. Copyright 2013 RSC. b) The time-dependent relative PL intensity of raw QDs and the QD-microcapsule–silicone resin composite is measured under blue LED light (450 nm) irradiation. The inset displays a schematic of the experiment and sample images. The right figures are normalized PL spectra for the raw QDs and the QD-microcapsule composite. Reprinted with permission from [245]. Copyright 2015 IOP. c) PLQY stability tests of InP/ZnS QD film and InP/ZnS QDs in the ZnS matrix after annealing at different temperatures for 1 h. Reprinted with permission from [246]. Copyright 2020 ACS. d) *I–V* profile of InP QD films with (left) and without (right) PI measured by the conductive atomic force microscopy. Reprinted from [35]. CC BY 3.0.

Shell design can also enhance the stability of QDs by increasing the shell thickness and selecting appropriate shell materials, which has been discussed in the previous section. Inorganic overcoating with air-stable salts like $BaSO_4$ [247] and metal-organic

complexes [248], has been used to enhance photostability, acid stability, and thermal stability. Inorganic salts can cause a redshift in emission wavelength due to aggregation, whereas metal-organic complexes do not, and they can also improve quantum yield. Oxide overcoating effectively protects QDs from water and oxygen, but careful control is necessary to maintain both PLQY and stability [249].

The degradation mechanism of QD-LEDs is more complicated than the QD film because QD-LEDs comprise more functional layers, which is still unclear. Previous studies have reported that QD-LED aging is highly related to charge balance [56], including current leakage [146], exciton quenching [234], ZnO defect (typically $Zn(OH)_2$) passivation [250], and interaction between neighboring layers [251].

Charge balance has been discussed in Section 1.5.2. The imbalanced injection of carriers in QD-LEDs leads to QD charging with extra electrons [252]. Currently, most HTLs are organic materials which are more easily degraded than inorganic materials due to their inherently poor stability against moisture, oxygen, and heat, deteriorating their electrical properties [253]. Lin et al. ascribed the QD-LED degradation to the HTL, where charge accumulation occurs at the QD-HTL interface [254]. Additionally, PEDOT tends to absorb moisture and, due to its acidity, can deteriorate the electrical performance of the ITO electrode, leading to a gradual decline in device performance and lifespan.[251]. The limited lifetime and efficiency of QD-LEDs are also linked to the exciton quenching in the QD-ETL interface without encapsulation, resulting from oxygen-induced charge transfer [234]. As the emissive layer in QD-LEDs, the stability of QDs plays a crucial role in determining both electrical performance and device longevity. Shin et al. reported that InP-QD layers are more susceptible to exciton and electron-exciton stress compared to Cd-QDs [53]. This vulnerability arises from an increase in surface defects in InP-QDs after such stress, which accelerates non-radiative AR processes.

The degradation of QD-LEDs assembled under an ambient atmosphere at low/high temperatures has also been studied. Ambient gas was reported to change the energy alignment of QD-LED layers and increase the roughness of spin-coated films, resulting in lower efficiency compared with the devices fabricated under N_2 (Figure 64a) [235]. Lee's group discovered that thermal air treatment of the cathode and EML reduced QD-LED performance, likely because of oxidation and ligand stripping [255]. Pahlevani et al. studied the temperature-dependent efficiency parameters and brightness by subjecting devices to four cooling/heating cycles over a wide temperature range (−10

to 85 °C) (Figure 64b) [236]. The results showed that efficiency remained nearly constant after repeated cycles; however, a drop in brightness and a shift in the EL spectrum were observed. These effects were attributed to changes in charge transport characteristics and temperature-induced variations in radiative and non-radiative exciton relaxation dynamics. However, air exposure was reported to positively affect the electrical properties of $Zn_{1-x}Mg_xO$, enhancing the maximum EQE by more than twofold [40]. The findings revealed that H_2O reduces hole leakage, while O_2 influences charge transport by trapping electrons (Figure 64c) .

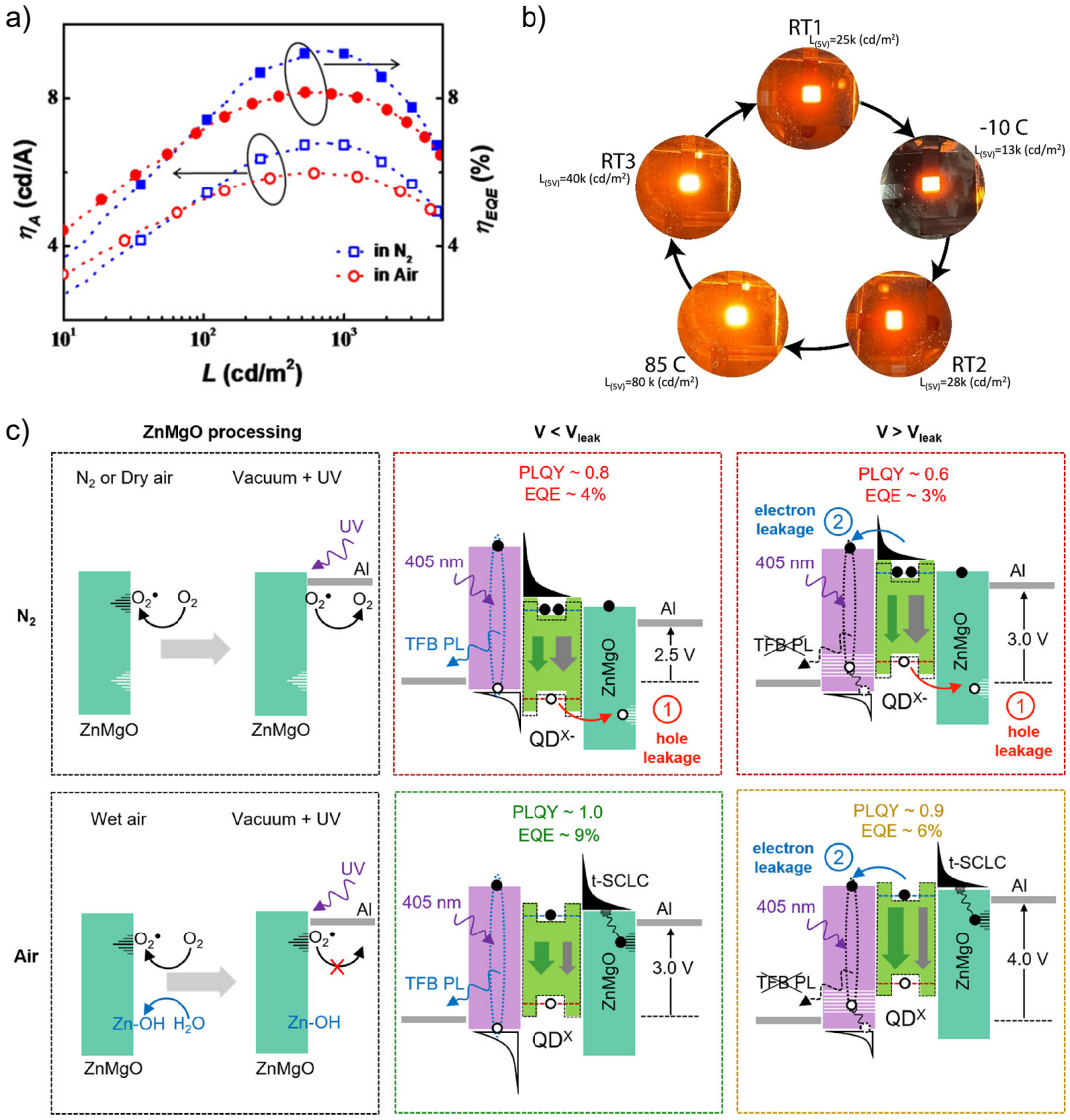

Figure 64. a) Current efficiency–luminance–EQE (η_A–L–η_{EQE}) of QD-LEDs assembled in air and N_2 atmosphere. Reprinted with permission from [235]. Copyright 2016 ACS. b) Photographs of an amber-emitting QD-LED operated at different temperatures. Reprinted from [236]. CC BY 4.0. c) The effect of $Zn_{1-x}Mg_xO$ exposed to oxygen and water on the operation mechanism of QD-LEDs below and above the electron leakage threshold. Reprinted from [40]. CC BY 4.0.

5.2 The Effect of Oxygen and Water

After spin coating the QD films on the glass coverslip, the emission spectra of QD films red-shifted by 10 nm to about 625 nm, this is likely to be due to the inter-QD FRET [129, 141], as shown in Figure 65a. Via inter-QD FRET, excitons migrate from smaller dots to neighboring larger QDs among the close-packed QD solids. This effect significantly reduces the absolute PLQY of 19-nm-thick QD films to 18 ± 2% under 35% RH. The PLQY is comparable to reported values in the literature [256, 257]. The FWHM of QD films (66 nm) was larger than that of QD dispersion (56 nm).

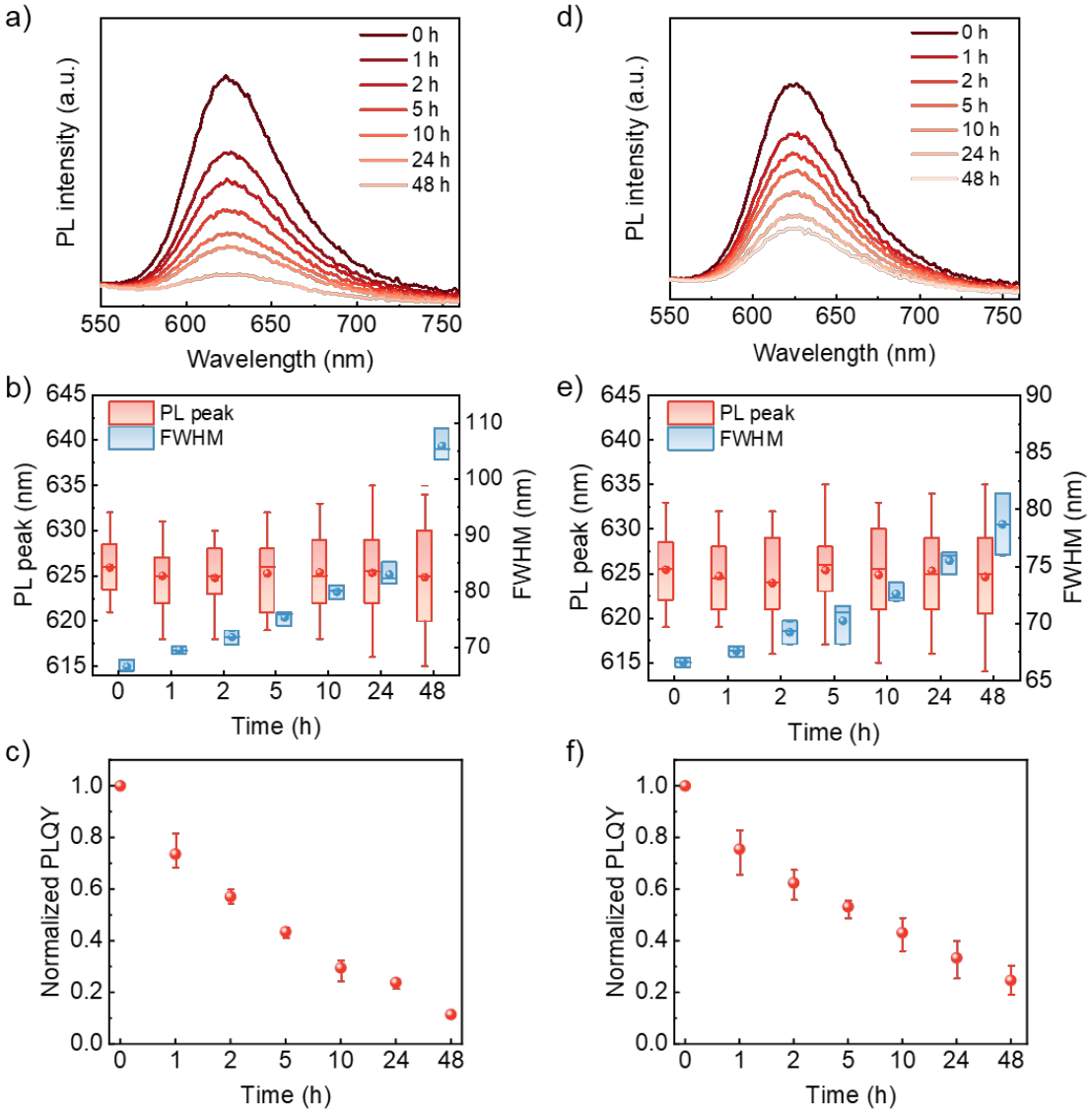

Figure 65. a, d) PL emission spectra, b, e) corresponding PL peaks and FWHM, and c, f) normalized PLQY of 19-nm-thick QD films under different RH over time at 22 °C. a-c) 35%, d-f) 55%.

After 48 h of storage in the dark, the QD films became almost non-emissive. The PL peak maxima remained nearly unchanged (Figure 65b), which might be due to the absence of UV exposure, resulting in inadequate photocorrosion [45]. The FWHM greatly increased by 39 nm because of the presence of impurities such as oxide species in the shell, forming shallow hole traps and causing a broader QD distribution [194]. The PL decay half-life ($\tau_{1/2} = k \ln 2$, Figure 65c and Table 14) was calculated to be 2.5 h and was fitted by an exponential degradation function,

$$I = I_0 e^{-\frac{t}{k}} + I_\infty \tag{46}$$

Where I_0, t, k, and I_∞ are the initial PLQY, time, decay rate, and a constant, respectively. The shift of PL peak and FWHM of QD dispersion under RH of 35% was less considerable than that of the QD films due to the solvent's protection, as shown in Appendix 9.5.

Table 14. The degradation half-life ($\tau_{1/2}$) of QD films under different experimental conditions.

	RH (%)	Temperature (°C)	t_{QD} (nm)	t_{PMMA} (nm)	$\tau_{1/2}$ (h)
Ambient atmosphere	55	22	101 ± 4	-	17.2
	55	22	48 ± 2	-	5.9
	55	22	19 ± 1	-	2.6
	55	22	19 ± 1	47 ± 6	33.5
	55	22	19 ± 1	20 ± 1	15.0
	35	22	19 ± 1	-	2.5
Vacuum (~1.0 mbar)	6	22	19 ± 1	-	-
	6	50	19 ± 1	-	2.7
	6	100	19 ± 1	-	2.2

Under a higher RH of 55%, QD films exhibited a slower degradation rate and smaller change of FWHM (Figure 65d-f). The initial absolute PLQY increased by about 4% and $\tau_{1/2}$ slightly promoted to 2.6 h, which can be attributed to the photoinduced fluorescence enhancement effect (PFEE) [258, 259]. In this process, adsorbed water molecules passivated surface trap states, allowing electrons to repopulate from the trap states to the conduction band of the QDs and resulting in increased band-edge radiative recombination [258]. The PFEE is highly dependent on the humidity levels, which is

predominant with high humidity levels and enhances the PL in a short time (< 30 min) [258]. The absorbance of 19-nm-thick QD films was almost the same under the RH of both 35% and 55% after 48 h (Figure 66).

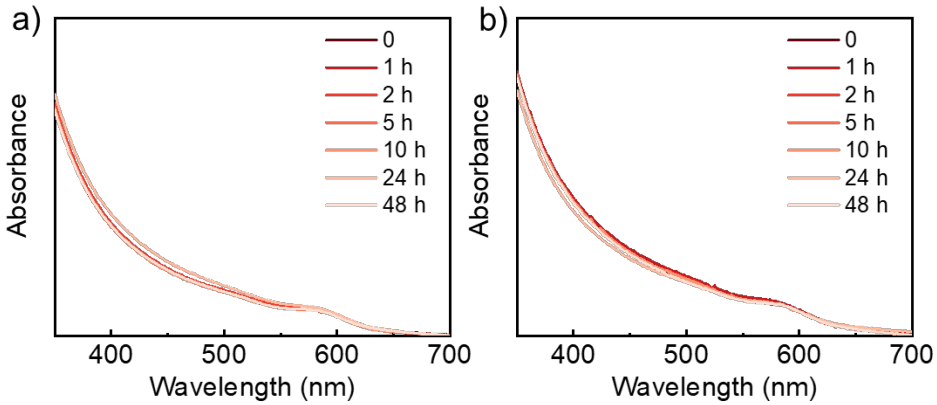

Figure 66. The evolution of absorption of 19-nm-thick QD films under the RH of a) 35% and b) 55% over time at RT.

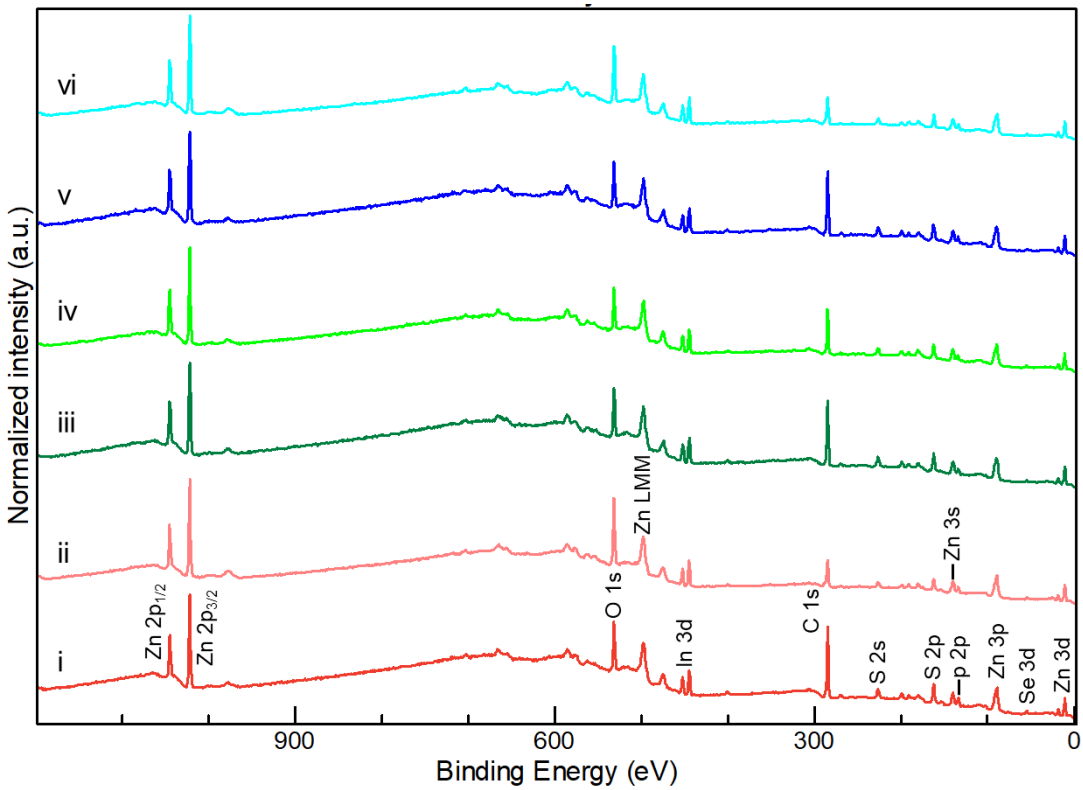

Figure 67. Survey scans of 19-nm-thick QD films under different exposure conditions. i – UHV before oxygen exposure, ii – UHV after oxygen exposure, iii – UHV before water exposure, iv – UHV after water exposure, v – UHV before oxygen and water exposure, vi – UHV after oxygen and water exposure.

To identify the chemical changes in QD films exposed to oxygen and/or water in the

dark, survey scans under UHV (Figure 67) and high-resolution NAP-XPS spectra were recorded for the C 1s, S 2p, Se 3p, Zn 2p, Zn LMM, Se 3d, P 2p, Zn 3s, In 3d, and O 1s core levels. These measurements were taken from spin-coated 19-nm-thick QD films before exposure, during 3 mbar oxygen and/or water exposure at RT, after heating to 100 °C under the same exposure conditions, and under UHV after exposure. Figure 68 illustrates the effect of oxygen exposure.

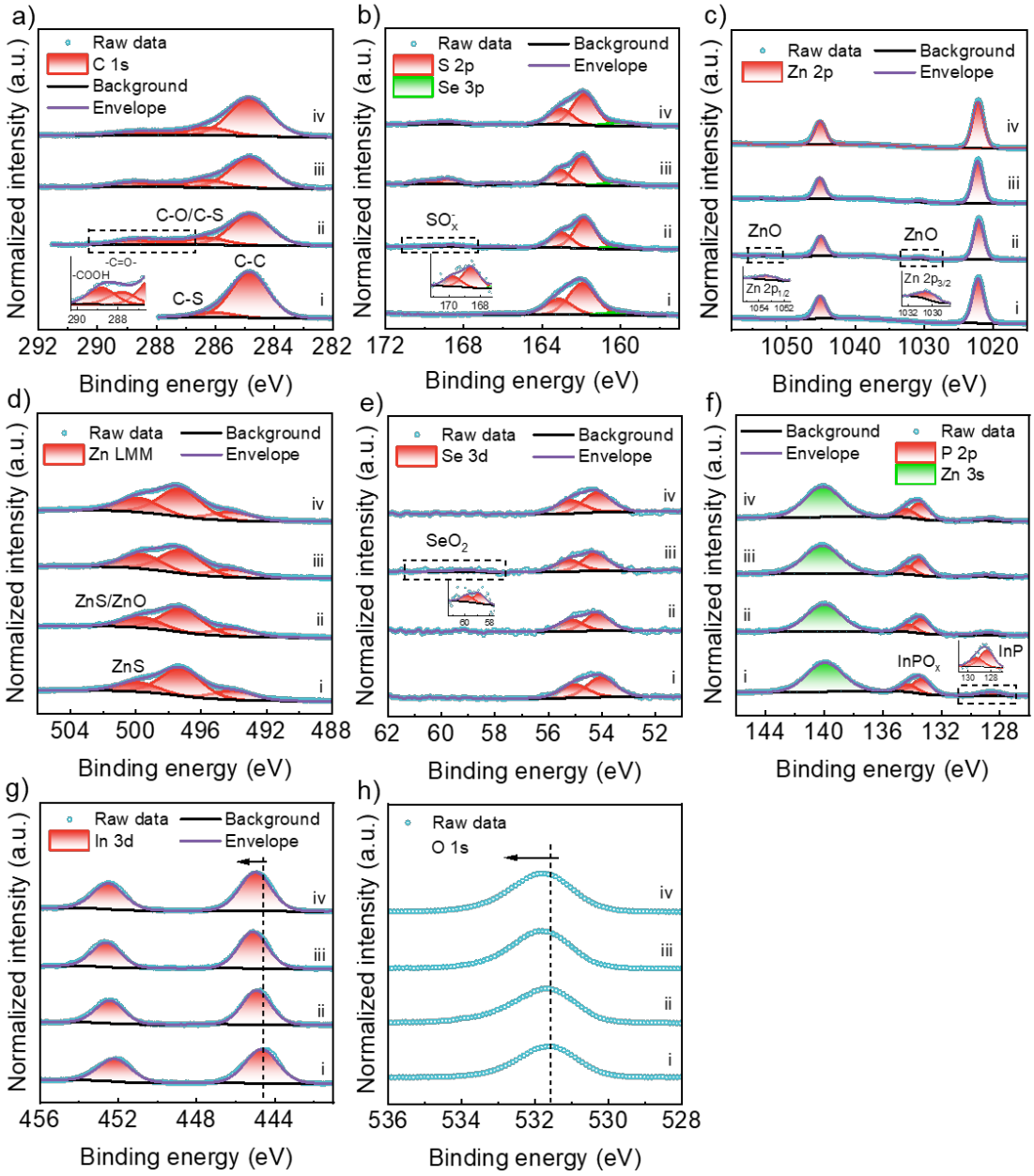

Figure 68. NAP-XPS spectra of a) C 1s, b) S 2p & Se 3p, c) Zn 2p, d) Zn LMM, e) Se 3d, f) P 2p & Zn 3s, g) In 3d, and h) O 1s of 19-nm-thick QD films under different oxygen exposure conditions. i – UHV before oxygen exposure, ii – 3 mbar oxygen exposure at RT, iii – 3 mbar oxygen exposure at 100 °C, iv – UHV after oxygen exposure.

Before oxygen exposure, the main peak positioned at 284.8 corresponds to C-C/C-H, while the tail extending to higher BE (286.0 eV) is associated with the C-S bond of the QD ligands (octanethiol, see Figure 68a) [204]. After oxygen exposure at RT, additional peaks generated at higher BE values of 287.8 and 288.8 eV were related to C=O and RCOOH groups, respectively, indicating oxidation of carbon contaminants [213, 214]. The peak at 286.3 eV likely represents a combination of C-S and C-O bonds due to their proximity. The S 2p spectrum initially exhibited a doublet due to the spin-orbit splitting, $2p_{3/2}$ and $2p_{1/2}$, at 161.9 and 163.1 eV, respectively, which can be assigned to the $ZnSe_xS_{1-x}$/ZnS shell and the QD ligand (Figure 68b inset) [172, 208]. After oxygen exposure, an additional doublet appeared with peaks at 168.4 and 169.6 eV, which are associated with the formation of SO_x^- (x = 2 and/or 3) owing to oxidation of the QD ligand and/or the shell [260] (Figure 68b). The oxidation peak area increased by 4.4 times after elevating the NAP cell temperature from RT to 100 °C. SO_x^- counted for 6.9 at% of the total S 2p (33.5 at%, see Table 15) after oxygen exposure under UHV. The decrease in S at% after oxygen exposure was caused by the removal of ligands. The peaks at 166.0 and 160.0 eV correspond to Se $3p_{1/2}$ and Se $3p_{3/2}$, respectively.

Table 15. Atomic concentrations of Zn, S, Se, In, and P for InP/$ZnSe_xS_{1-x}$/ZnS (excluding O) before and after various exposure conditions.

Atomic ratio (%)	Zn 2p	S 2p	Se 3d	In 3d	P 2p
UHV before O_2 exposure	25.9	40.5	3.3	7.7	22.5
UHV after O_2 exposure	32.1	33.5	3.1	8.6	22.7
UHV before H_2O exposure	27.1	40.2	3.1	7.5	22.0
UHV after H_2O exposure	30.4	36.1	3.2	7.9	22.5
UHV before O_2 + H_2O exposure	27.9	39.9	3.1	7.5	21.6
UHV after O_2 + H_2O exposure	33.8	33.2	3.0	8.3	21.7

Isolated Zn $2p_{3/2}$ and Zn $2p_{1/2}$ peaks present at 1022.1 and 1045.1 eV, respectively, with a spin-orbit splitting of 23 eV (Figure 68c). The presence of a small new doublet at 1030.3 and 1053.3 eV recorded in the NAP cell indicated the generation of ZnO under oxygen exposure [261, 262], in good agreement with recently reported TEM results by Baek et al. [241]. This is also consistent with the increasing area ratio (+7.1%) of the highest BE peak of the Zn LMM spectrum at 499.8 eV which overlaps the peak

of ZnS and ZnO [172, 263] (Figure 68d and Table 16). The doublet of ZnO was not observed after oxygen exposure under UHV because core level Zn 2p peaks are less sensitive to Auger peaks to the change in the environment around zinc, and the spot size in the NAP cell is 3.3 times smaller than that in the UHV chamber.

Table 16. Area ratio of the highest BE peak (ZnS + ZnO) of Zn LMM spectrum.

Area ratio (%)	O_2	H_2O	$O_2 + H_2O$
UHV before exposure	20.8	20.0	20.5
NAP at RT	23.3	19.5	21.2
NAP at 100 °C	29.1	19.9	29.0
UHV after exposure	27.9	22.9	24.9

Table 17. Atomic concentrations of Zn, S, O, Se, In, and P for InP/$ZnSe_xS_{1-x}$/ZnS before and after various exposure conditions.

Atomic ratio (%)	Zn 2p	S 2p	Se 3d	In 3d	P 2p	O 1s
UHV before O_2 exposure	15.7	24.6	2.0	4.7	13.7	39.4
UHV after O_2 exposure	15.3	16.0	1.5	4.1	10.9	52.2
UHV before H_2O exposure	16.9	25.1	2.0	4.7	13.8	37.6
UHV after H_2O exposure	18.6	22.1	1.9	4.8	13.8	38.8
UHV before $O_2 + H_2O$ exposure	17.2	24.6	1.9	4.6	13.3	38.4
UHV after $O_2 + H_2O$ exposure	17.2	16.9	1.5	4.2	11.0	49.1

There was no change for the Se 3d peak after exposure to O_2 at RT (Figure 68e). However, the small peak emerged at 58.8−59.8 eV when exposed to oxygen at 100 °C corresponding to SeO_2 [207, 264], because of increased atomic mobility and longer exposure time. The P 2p spectrum of the QD film in the UHV cell has been discussed in section 3.2.3. The small doublet, appearing at 128.4-129.3 eV, is characteristic of InP (Figure 68f). The more intense doublet is located at higher BE (133.3-134.2 eV) and corresponds to P in an oxidized state, likely as $InPO_x$ (x = 3 or 4). The ratio of oxidized phosphorus atoms ($InPO_x$) increased by 1.5% after oxygen exposure. The Zn 3s peak at 139.9 eV showed no significant change after oxygen exposure. The In $3d_{3/2}$

and In $3d_{5/2}$ peaks, initially at 452.2 and 444.7 eV, respectively, shifted to higher BE (+0.3 eV) after oxygen exposure, indicating the oxidation of In atoms ($\underline{In}_2O_3$, Figure 68g) [207, 249]. $\underline{In}OOH$ and $\underline{In}(OH)_3$ can be excluded as possible oxidation products because the indium source used in this work was indium chloride rather than indium acetate [205, 265]. Quantitative data suggest a phosphorus-rich surface, with an In/P ratio close to 0.34 (Table 15), consistent with previous reports [50, 266]. The high Zn/In ratio of 3.3 (in as-deposited QD films) supports that the InP core was covered by the shell [267], resulting in a low In at% due to XPS's surface sensitivity, which typically detects only a few atom layers on the top. The O 1s peak shifted to higher BE (+0.2 eV) and the O at% increased by 12.3% (Figure 68h and Table 17), which is in line with the oxides discussed above.

The degradation of QD films under 3 mbar water exposure (RH: 10%) was studied separately, revealing that water had a minimal impact on chemical change (Figure 69). The peaks of $\underline{C}$=O and $\underline{C}$OOH were weak after water exposure, with no observable SO_x^- and ZnO peaks, even at 100 °C (Figure 69a-c). The area ratio of the highest BE peak in the Zn LMM spectrum slightly increased after water exposure (Figure 69d and Table 16), and Se oxidation was not detected (Figure 69e). The ratio of oxidized phosphorus atoms was almost the same after water exposure (Figure 69f and Table 15), and the shift of the In doublet was insignificant (Figure 69g). The slight increase of oxygen at% further implies negligible oxidation under water exposure (Table 17). The small peak at 535.0 eV in the NAP cell is assigned to water (Figure 69h) [268].

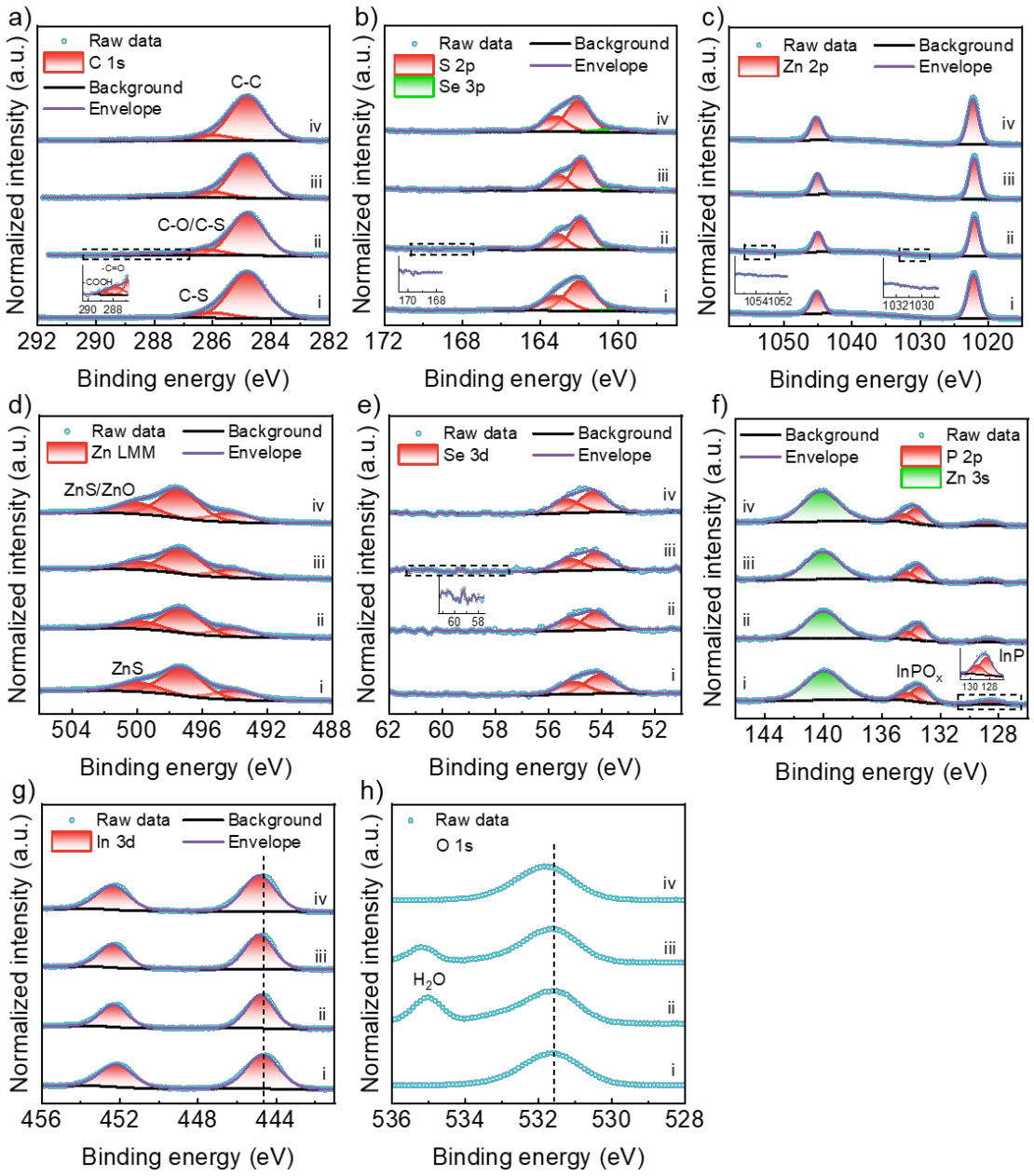

Figure 69. NAP-XPS spectra of a) C 1s, b) S 2p & Se 3p, c) Zn 2p, d) Zn LMM, e) Se 3d, f) P 2p & Zn 3s, g) In 3d, and h) O 1s of 19-nm-thick QD films under different water exposure conditions. i – UHV before water exposure, ii – 3 mbar water exposure at RT, iii – 3 mbar water exposure at 100 °C, iv – UHV after water exposure.

The combined effects of oxygen and water exposure on chemical variations were similar to those of oxygen exposure alone (Figure 70). The slightly weaker oxidation observed under both exposures could be due to the thin capsulation layer of water on QDs, which might alleviate the reaction with oxygen (Table 16 and Table 17).

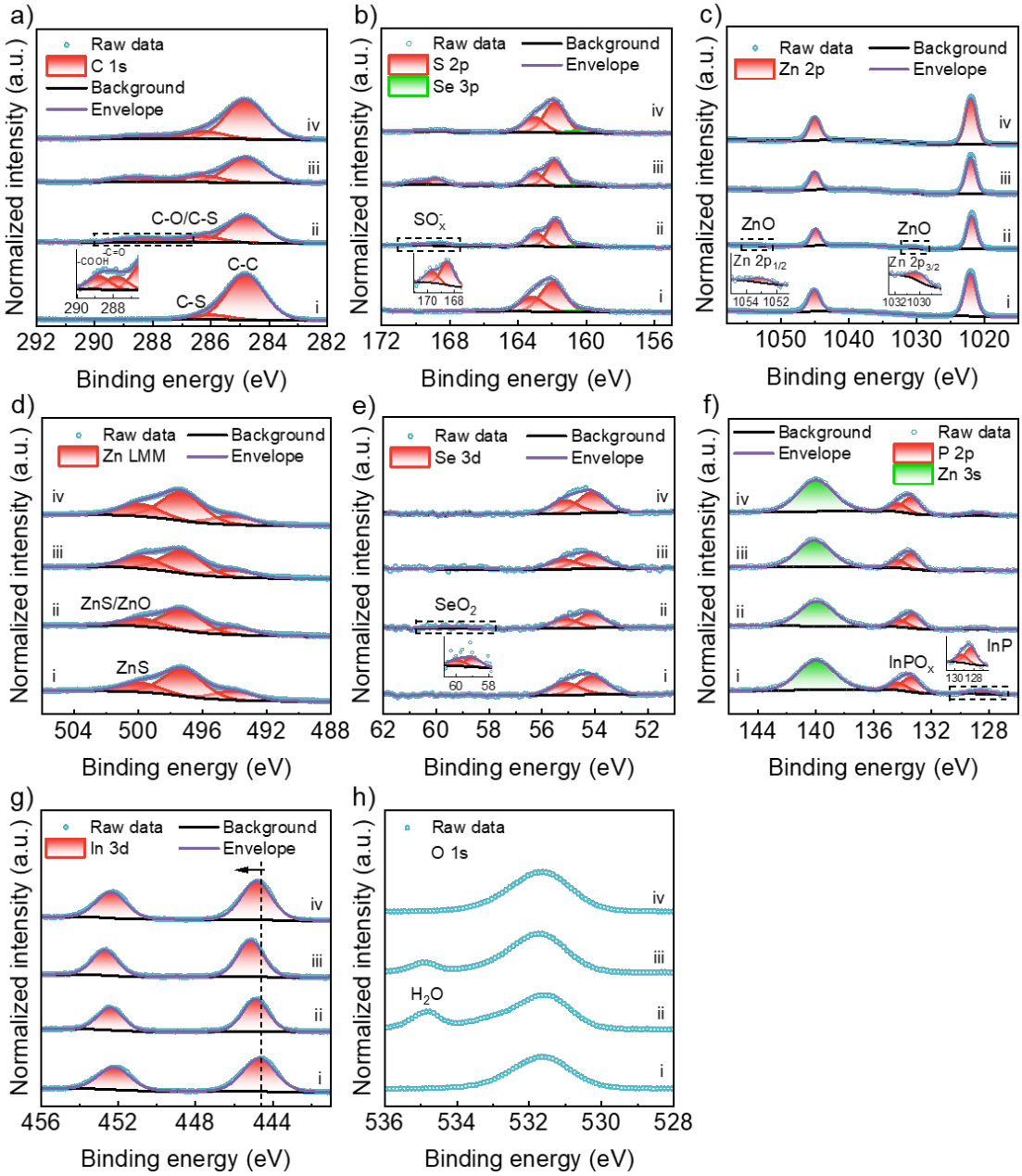

Figure 70. NAP-XPS spectra of a) C 1s, b) S 2p & Se 3p, c) Zn 2p, d) Zn LMM, e) Se 3d, f) P 2p & Zn 3s, g) In 3d, and h) O 1s of 19-nm-thick QD films under different oxygen exposure conditions. i – UHV before oxygen and water exposure, ii – 3 mbar oxygen and water exposure at RT, iii – 3 mbar oxygen and water exposure at 100 °C, iv – UHV after oxygen and water exposure.

5.3 The Effect of Heat

When 19-nm-thick QD films were stored in the vacuum oven (1 mbar, 6% RH) at 22 °C, the emission linewidth did not change significantly, and the PLQY preserved 87% of its initial value after 24 h (Figure 71a-c). The drop in PLQY was primarily due to air exposure during measuring, which took approximately 5 min per sample, with three

samples tested under each condition. Notably, the PLQY remained stable within 3 h due to the short exposure time, and the PL could be recovered by vacuum degassing the physisorbed water molecules [43]. As the vacuum oven temperature was elevated to 50 °C and 100 °C, the PL quenching accelerated, resulting in broader emissions and reducing the PLQY by half and three-fifths, respectively (Figure 71d-i). The $\tau_{1/2}$ of QD films at 22 °C under 55% RH was comparable to that of QD films at 50 °C under vacuum. Heat-facilitated PL quenching was attributed to thermally created permanent trap states, caused by the difference in the thermal expansion of the core and shell, and increased atomic mobility [239]. This increased the diffusion of oxygen and water into the QD core.

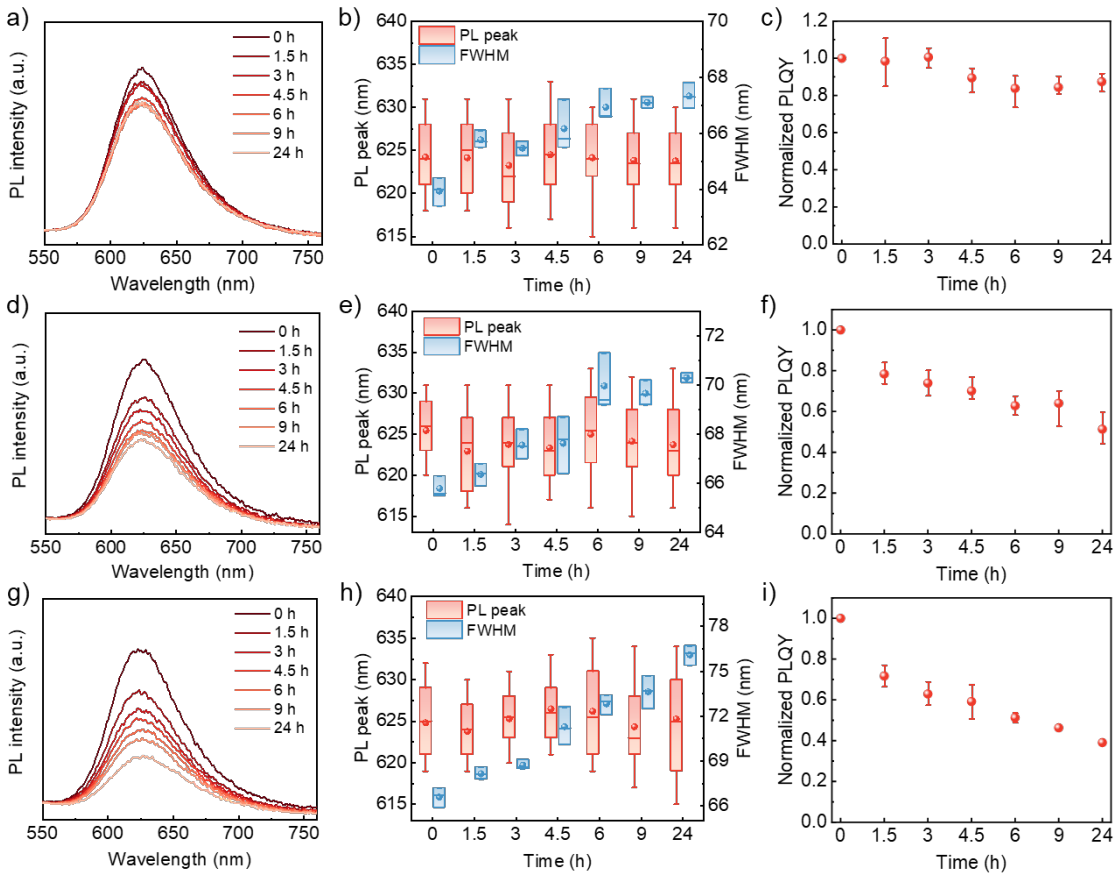

Figure 71. a, d, and g) PL emission spectra, corresponding b, e, and h) PL peaks and FWHM, and c, f, and i) normalized PLQY of 19-nm-thick QD films under vacuum (1.0 mbar) over time at different temperatures. a-c) 22 °C, d-f) 50 °C, g-i) 100 °C.

5.4 The Effect of the Thickness of QD Films

Increasing the QD film's thickness (t_{QD}) from 19 nm to 48 and 100 nm led to redder and broader PL emissions, indicating more pronounced inter-QD FRET (Figure 72a, d). The spin-coated QD films with different thicknesses using various dispersion

concentrations and spin speeds were summarised in Table 18. The PL maxima were almost the same after 10 days (Figure 72b, e), and the $\tau_{1/2}$ extended to 5.9 h and 17.2 h, respectively (Table 14). The PLQY of 48-nm-thick QD films (13.9%) was half that of 100-nm-thick QD films (26.8%) after 240 h (Figure 72c, f). Notably, the PLQY of 100-nm-thick QD films reached a plateau with exposure time between 10 and 24 h, which is likely because thicker samples contained more QDs that did not deteriorate at the bottom, maintaining their PL property for a longer period.

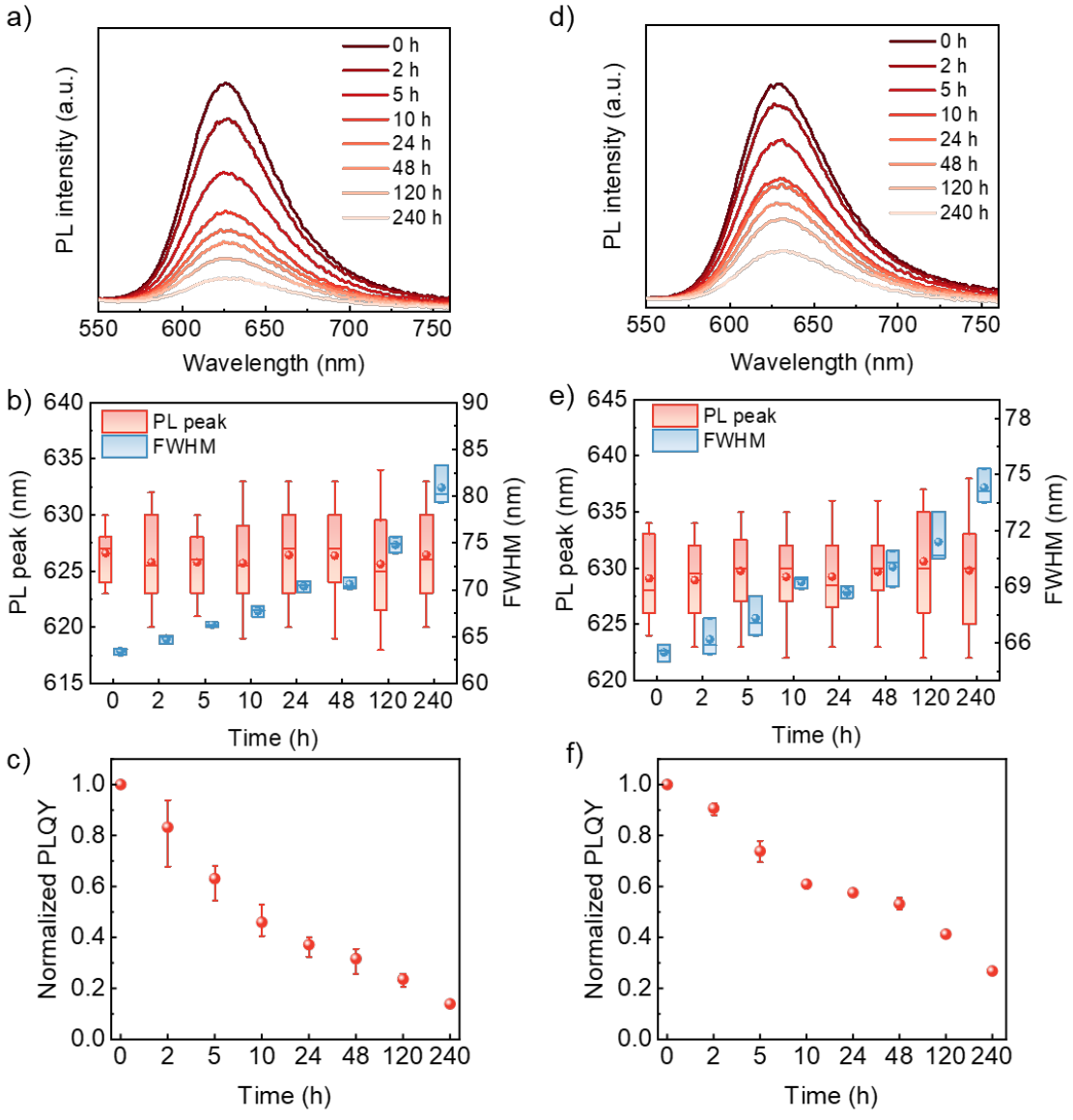

Figure 72. a, d) PL emission spectra, b, e) corresponding PL peaks and FWHM, and c, f) normalized PLQY of QD films with different thicknesses under the RH of 55% over time at 22 °C. a-c) 48 ± 2 nm; d-f) 100 ± 4 nm.

Table 18. A summary of the thickness of QD films that spin-coated by varying concentrations and spin speeds.

C of QD dispersion (mg/mL)	Spin speed (RPM)	Thickness (nm)	MSE
15	2000	19 ± 1	1.9 ± 0.3
	3000	16 ± 1	1.7 ± 0.1
30	2000	67 ± 3	7 ± 2
	3000	48 ± 2	5 ± 3
60	2000	100 ± 4	8 ± 1
	3000	90 ± 1	5 ± 2

5.5 The Effect of the Encapsulation Layer

To enhance the air stability of QD films, a thin PMMA film with different thicknesses (t_{PMMA}) was spin-coated on 19-nm-thick QD films as a protection barrier (Table 19). PMMA is an excellent organic optical material, offering minimal dispersion, good environmental inertness, and high transparency across the visible spectrum [269]. QD-PMMA nanocomposites have been used in active planar waveguides [270] and the alleviation of the CRE in inkjet printing [78]. Additionally, Dai et al. spin-coated a thin PMMA layer between the QD layer and electron transport layer to balance the charge injection in QD-LEDs, thus dramatically boosting the EQE to 20.5% [56].

Table 19. A summary of the thickness of PMMA films that spin-coated by varying concentrations and spin speeds.

C of PMMA solution (mg/mL)	Spin speed (RPM)	Thickness (nm)	MSE
2.00	4000	65 ± 3	4.4 ± 0.3
0.50	4000	47 ± 6	1.6 ± 0.4
0.05	4000	20 ± 1	1.4 ± 0.1

The PL was quenched extremely slowly under 55% RH at 22 °C, sustaining about 50% of the PL with t_{PMMA} of 20 ± 1 nm and 47 ± 6 nm after 24 h and 48 h, respectively (Figure 73a, d). FWHM moderately increased to 74 nm and 69 nm, respectively, smaller than that of QD films without PMMA after 48 h (79 nm), and PL peaks remained stable after 10 days (Figure 73b, e). Weak emissions were still detectable after 5 days, with the $\tau_{1/2}$ increased by 5 and 12 times, respectively (Figure 73c, f). The enhanced air stability

of QD films with PMMA layers can be explained by Frick's first law of diffusion [271], the diffusion flux through a thin layer of PMMA can be expressed as

$$J = \frac{D(C_1 - C_2)}{t_{\mathrm{PMMA}}} \tag{47}$$

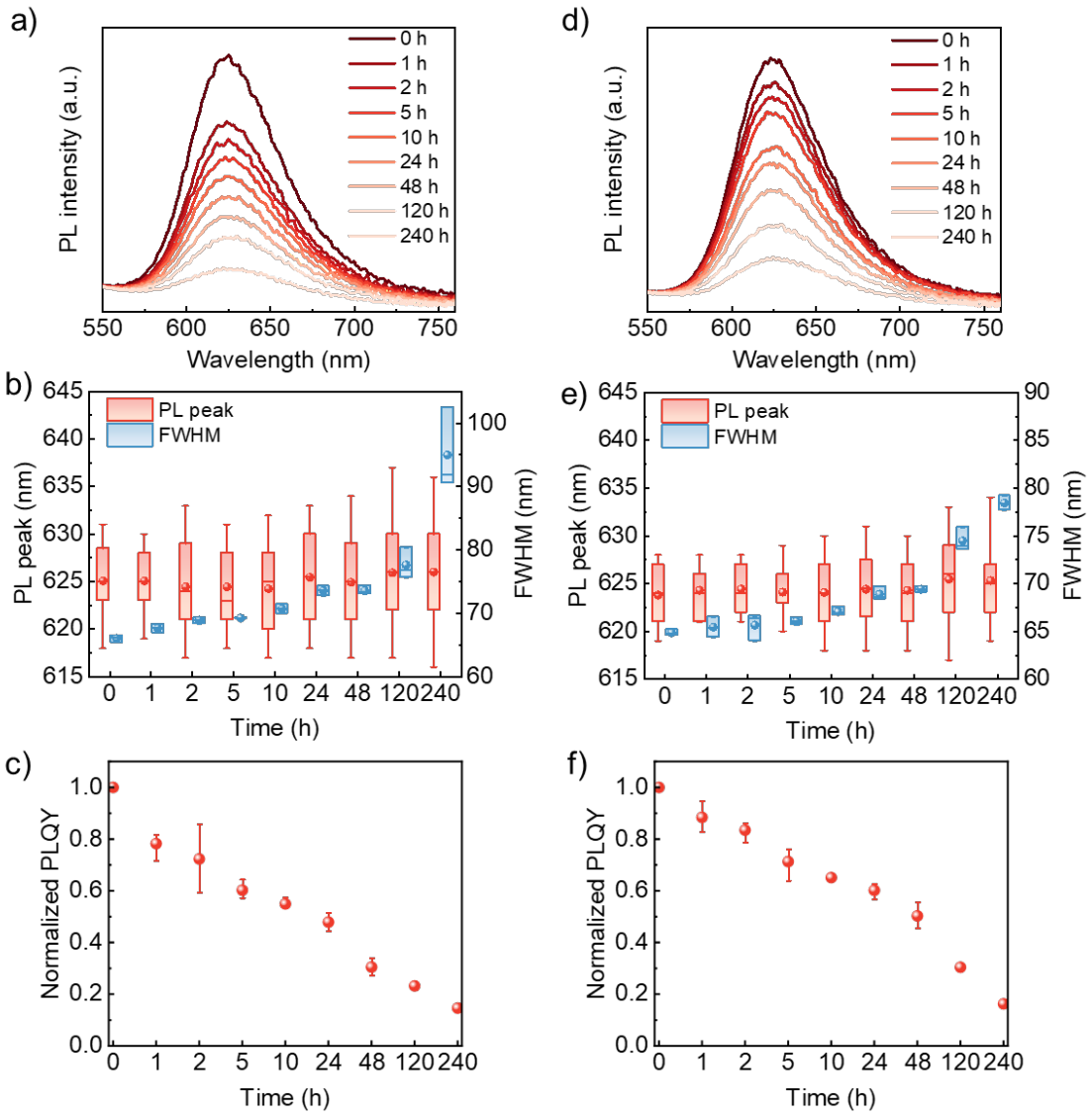

Figure 73. a, d) PL emission spectra, b, e) corresponding PL peaks and FWHM, and c, f) normalized PLQY of 19-nm-thick QD films coated with different thicknesses of PMMA films under the RH of 55% over time at 22 °C. a-c) 20 ± 1 nm, d-f) 47 ± 6 nm.

Where D, C_1, and C_2 represent the diffusion coefficient, and the concentration on the top and bottom of PMMA film, respectively. D is dependent on the ambient temperature and PMMA's molecular weight but independent of t_{PMMA} [272]. D of water at 25 °C is two orders greater than D of oxygen for PMMA [273]. QD films encapsulated with a

thicker PMMA layer reduced the diffusion flux of oxygen and water because J is inversely proportional to t_{PMMA}, thereby achieving more air-stable QD films.

5.6 Concluding Remarks

The PL quenching and chemical state changes in InP/$ZnSe_xS_{1-x}$/ZnS QD films were studied in this chapter. NAP-XPS results indicated that chemical state changes were primarily caused by oxidation rather than water exposure, forming oxides that include In_2O_3, $InPO_x$, SeO_2, ZnO, and SO_x^- (Figure 74). Notably, $InPO_x$ was detected before oxygen or water exposure, indicating that it was formed during the synthesis. However, oxygen, water, or heat can introduce permanent trap states, leading to PL quenching. The PL decayed more slowly under higher RH due to the PFEE, which passivated surface trap states and temporarily enhanced the PL. Thicker QD films showed better air stability and greater $\tau_{1/2}$ because they contained more QDs and QDs on the top layer protected the bottom layer from degradation. Thermal energy increases atomic mobility and expands the structure deformation between the shell and core, introducing permanent trap states that quenched the PL.

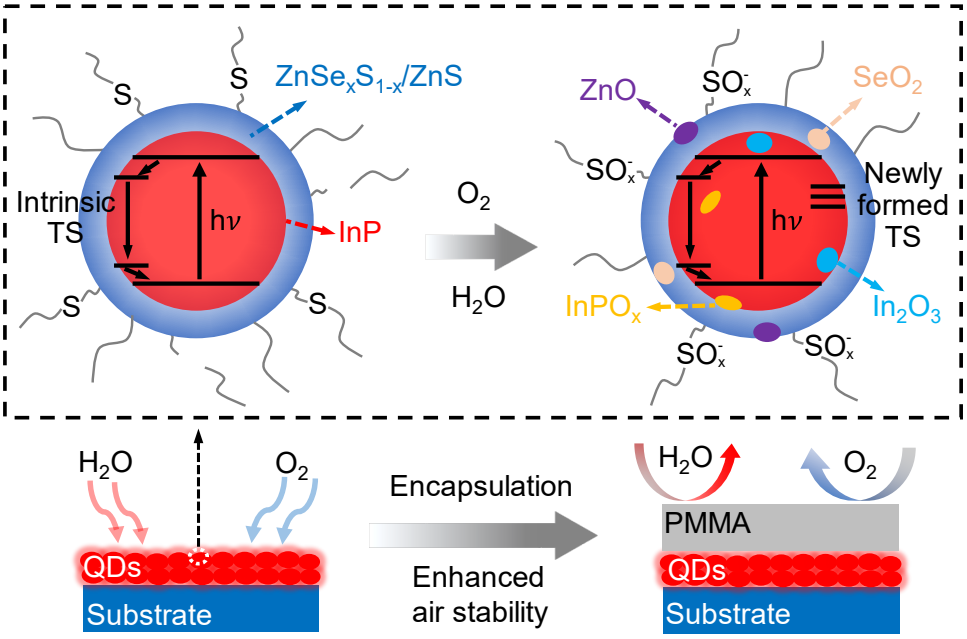

Figure 74. Schematics of QD films with enhanced air stability by encapsulating a thin layer of PMMA. The top figure shows the degradation of QD films under the air, forming trap states and several oxides.

Apart from engineering the QD surface during synthesis such as increasing the shell thickness and coating multiple inorganic shells, encapsulating QD films with a polymer

barrier layer is an easier way to maintain the optical properties of QD films under ambient atmosphere. In this work, encapsulating a PMMA barrier layer proved to be an effective strategy to improve the air stability of QD films by reducing the diffusion flux of oxygen and moisture. The $\tau_{1/2}$ increased by 5 and 12 times with PMMA thickness of 20 and 47 nm, respectively. This study provides insight into the effect of oxygen and/or water on InP/$ZnSe_xS_{1-x}$/ZnS QD films, paving the way to develop more air-stable QD films for InP-based optoelectronic devices like QD-LEDs.

6. Conclusions

In this study, the aim is to fabricate cadmium-free QDs-based electroluminescent devices by IJP and investigate the degradation of InP/$ZnSe_{1-x}S_x$/ZnS QD films. The InP QDs are one of the most promising HMF QDs with excellent optical properties, especially for the red InP QDs. The work was split into three key sections: firstly, synthesizing and characterizing the optical properties, chemical composition, and morphology of core-shell InP QDs and Mg-doped ZnO NPs. Secondly, inkjet printing the QD layer without the CRE, assembling the QD-LEDs, and studying the effect of the thickness of the ETL on the electrical performance of InP QD-LEDs. Finally, investigated the PL quenching of InP QD films varied with the thickness, RH, and temperature and detected the chemical state variations under oxygen and/or water exposure.

In Chapter 3, the optical properties, chemical composition, and morphology of synthesized red-emitting InP QDs and $Zn_{1-x}Mg_xO$ NPs were characterized. InP core with a diameter of 3.6 nm showed almost no PL with a PLQY of nearly zero due to the formation of a large number of surface defects like In_2O_3 and $InPO_x$ (x = 3 and/or 4) on the core's surface. By encapsulating a single shell of $ZnSe_xS_{1-x}$ and multiple shells of $ZnSe_xS_{1-x}$/ZnS (c.a. 4.3 monolayers), the PLQY was greatly enhanced to 58% and 81%, respectively, successfully passivating the defect states and confining the carriers in QDs. Although the Se doping amount was small (2.7 at%), the composition-gradient $ZnSe_xS_{1-x}$ intermediate shell relieved interfacial compressive strain at the InP/ZnS interface, contributing to the higher PLQY. The relatively thick shell can enhance the stability and suppress nonradiative FRET in core/shell QDs, contributing to more stable and efficient QD-LEDs. The relatively broader emission than Cd-based QDs associated with structural and electronic disorders but it is comparable to other reported analogues. The peak was slightly asymmetric with a slight tail into the red region due to the presence of a small amount of larger QDs and trap states. TRPL measurements revealed a decrease of τ_1% and an increase of τ_2% in core-shell QDs, further proving the effective surface passivation.

Mg-doped ZnO ($Zn_{1-x}Mg_xO$) is beneficial for balancing the carrier injection in QD-LEDs due to the smaller electron mobility and reduced energy barrier between the QD layer and ETL than pure ZnO. The doping ratio was confirmed to be 12.0 at% and 15.6 at% according to the EDS and XPS results. The addition of a small amount of EA enhanced the monodispersity of $Zn_{1-x}Mg_xO$ NPs with an average size of 3.9 nm, facilitating more

even and uniform films by spin coating. The relatively larger optical band gap of $Zn_{1-x}Mg_xO$ NPs than bulk ZnO indicated greater spatial confinement of photogenerated charge carriers in the smaller ZnO NPs.

In Chapter 4, CHB and decane were selected to formulate the printable QD inks with different vol. %, and the impact of the vol. % of decane and T_{sub} on the CRE was investigated. Uniform patterns were obtained with 20 vol. % decane and T_{sub} of 60 °C, balancing the capillary effect and ME (including solutal and thermal ME). To further study how coffee rings formed at different T_{sub}, the real-time evaporation of QD inks was observed from both top and side views. The results showed stick jump mode at 20 °C and 40 °C and stick slide mode at 60 °C. The electrical performance of QD-LEDs deteriorates when the ETL ($Zn_{0.9}Mg_{0.1}O$) is exposed to air for a short time. The $J \sim V^n$ relation indicated that increasing the ETL thickness to 61 nm reduced trap density under air exposure and prevented the deterioration of the QD layer. The maximum brightness and EQE of inkjet-printed devices were 250 cd m^{-1} and 0.2%, respectively. The electrical performance of inkjet-printed QD-LEDs was lower than that of spin-coated counterparts, primarily due to QD quenching from ambient exposure during printing. Additionally, the hole mobility of PVK is much lower than the electron mobility of $Zn_{0.9}Mg_{0.1}O$, leading to unbalanced charge injection. To enhance the performance of inkjet-printed InP QD-LEDs, the air and thermal stability need to be studied.

In Chapter 5, the degradation of InP/$ZnSe_{1-x}S_x$/ZnS QD films by oxygen, water, and heat was characterized using fluorescence spectroscopy and NAP-XPS. The PL quenching of InP/$ZnSe_xS_{1-x}$/ZnS QD films in the dark over time was studied by tuning film thicknesses (19 nm, 48 nm, and 100 nm), relative humidity (RH: 6%, 35%, and 55%), and temperatures (22 °C, 50 °C, and 100 °C). Oxygen, moisture, or heat can create permanent trap states, causing PL quenching. PL decay slowed at higher relative humidity due to the PFEE, which temporarily passivated surface traps and enhanced PL. Thicker QD films demonstrated better air stability and higher $\tau_{1/2}$, as the top-layer QDs shielded lower layers from degradation. Thermal energy increased atomic mobility, intensifying structural deformation between the shell and core and introducing permanent traps that quenched PL. Chemical variations were detected by NAP-XPS under oxygen and/or water exposure at RT and 100 °C. The results indicated that chemical state changes were primarily caused by oxidation rather than water exposure, forming oxides that include In_2O_3, $InPO_x$, SeO_2, ZnO, and SO_x^-. To improve the air stability of QD films, a thin encapsulation layer of spin-coated PMMA, with thicknesses of 20 nm and 47 nm, was employed to protect QD films from oxygen

and moisture. A 47-nm-thick layer of PMMA can dramatically increase the $\tau_{1/2}$ by 12 times compared to QD films without the PMMA barrier, proving to be an effective strategy to improve air stability of QD films by reducing the diffusion flux of oxygen and moisture.

7. Future Work

Future research will focus on two main areas. The first involves investigating fully inkjet-printed InP QD-LEDs, which hold significant potential for large-scale manufacturing but remain largely underexplored. A critical aspect will be developing printable inks for all functional materials including QDs, while ensuring compatibility between ink solvents and underlying layers. Additionally, the impact of air exposure on each functional layer's electrical performance will be studied to identify the primary influencing factors.

The second area of research will explore inkjet printing for high-resolution, flexible, full-color InP QD-LEDs. This will involve fabricating micro-sized bank structures on flexible substrates prior to depositing functional layers. The resolution of the resulting QD-LEDs will depend on the density of the array. The evaporation behavior of ink droplets within the bank structures, which differs from drying on open surfaces, will also be examined. Furthermore, dual HTL layers combining the advantages of TFB and PVK will be employed to enhance hole injection and achieve better charge injection balance. The electrical performance of the flexible QD-LEDs will be evaluated under compressive and bending conditions.

7.1 Fully-inkjet-printed InP QD-LEDs

The inkjet-printed InP QD-LEDs in Section 4 only include the inkjet-printed QD layer. For fully-inkjet-printed QD-LEDs, the electrodes and functional layers will be inkjet printed instead of spin coating in the glove box. The structure of fully-inkjet-printed InP QD-LEDs includes glass, ITO, PEDOT:PSS, TFB, QDs, $Zn_{1-x}Mg_xO$, and Ag (Figure 75). Inkjet printing of single ITO [274], PEDOT:PSS [275], ZnO [276], and Ag [277] films have been reported previously.

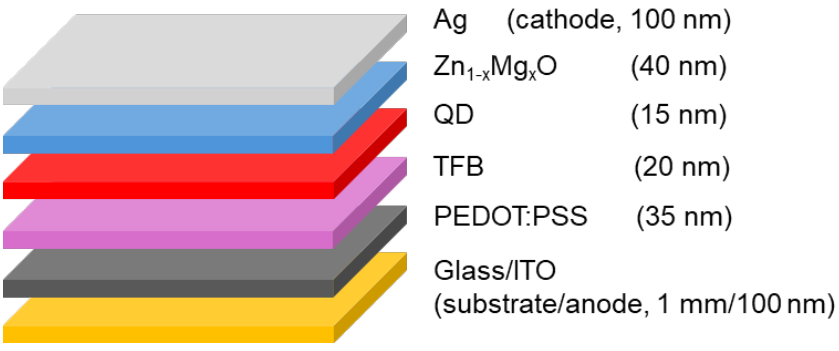

Figure 75. The structure of fully-inkjet-printed InP QD-LEDs.

Table 20. Physical properties of solvents used to dissolve the functional materials in fully-inkjet-printed InP QD-LEDs [161].

Materials	Solvent	BP (°C)	Viscosity (mPa s)	ST (mN/m)	Density (g/cm^3)
ITO NPs	Ethanol	78	1.1	22.1	0.79
Ag NPs	Tetradecane	254	2.1	26.6	0.76
TFB	COB	132	0.8	33.5	1.11
QDs	Decalin	196	3.4	31.5	0.90
	n-Tridecane	235	1.7	25.6	0.76
PEDOT:PSS	Water	100	1.0	72.8	1.00
$Zn_{1-x}Mg_xO$	IPA	83	2.0	23.0	0.79
	Propylene glycol	188	42	71.6	1.04

It is crucial to select appropriate solvents to dissolve/disperse each material, which should have proper viscosity, ST, BP, and density, and be compatible with the bottom layers. The physical properties of the corresponding solvents are shown in Table 20. There is commercial ITO (Advanced Nano Products), ZnO (Sigma-Aldrich), and Ag (Harima Chemical Co.) NP inks for IJP, which disperse in ethanol, the mixture of IPA and propylene glycol, and tetradecane, respectively. To obtain uniform ITO and Ag films with excellent conductivity, the annealing temperature needs to be optimized after printing. Regarding the Mg-doped ZnO NP ink, the same solvents used for dispersing ZnO NPs will work. TFB will be used as the HTL because of its higher hole mobility than PVK, so the solvents for dispersing QDs will be a mixture of decalin and n-tridecane with a volume ratio of 7:3 rather than the mixture of CHB and decane [76].

The physical properties of PEDOT:PSS inks with various concentrations have been tested, as shown in Table 21. The viscosity decreased as the volume ratio of Milli Q water increased, and all inks showed shear-thinning behavior (Figure 76). The inks with volume ratios of 2:1, 1:1, and 1:2 have proper ST and viscosity, which can be selected for printing. Apart from the selection of solvents, the printing parameters also need to be examined, including waveform, voltage, firing frequency, substrate temperature, DS, and annealing parameters.

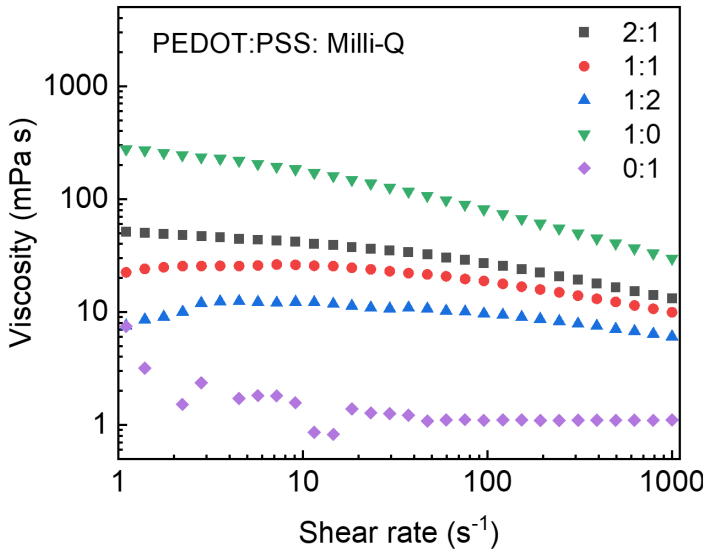

Figure 76. Dynamic viscosity of PEDOT:PSS inks with different concentrations.

Table 21. Physical properties of PEDOT:PSS inks with different concentrations.

PEDOT:PSS: Milli Q (v/v)	Viscosity (mPa s)	Surface tension (mN/m)	CA (°)
1:0	29.7	38.1 ± 0.1	33.0 ± 3.3
2:1	13.1	38.7 ± 0.3	26.6 ± 5.0
1:1	10.0	41.2 ± 0.1	28.6 ± 7.6
1:2	6.1	43.4 ± 0.1	46.2 ± 3.6
0:1	1.1	71.9 ± 0.4	37.8 ± 4.0

7.2 Inkjet Printing of High-Resolution Flexible Full-color InP QD-LEDs

The size of InP QDs can be tuned using different Zn halides ($ZnCl_2$, $ZnBr_2$, and ZnI_2) with the same synthesis protocol described in Section 2.1. Smaller green and blue InP QDs with the same ligands can also be dispersed in the same binary solvent system (CHB and decane) to formulate green and blue QD inks. The inks will be inkjet-printed in the glove box using the same printing parameters aforementioned in Section 4.2 with slight adjustments. The structure and band alignment of full-color flexible InP QD-LEDs are shown in Figure 77. Here, double HTLs including TFB and PVK will be used, and the substrate will be the ITO-coated Polyethylene naphthalate (PEN). The compatibility of different configurations of TFB+PVK films with the ink solvents (CHB and decane) was measured by the ellipsometer and UV-Vis spectrometer (Figure 78).

The optimal configuration is 31-nm-thick PVK and 13-nm-thick TFB films, with minimal reduction of the thickness and absorbance.

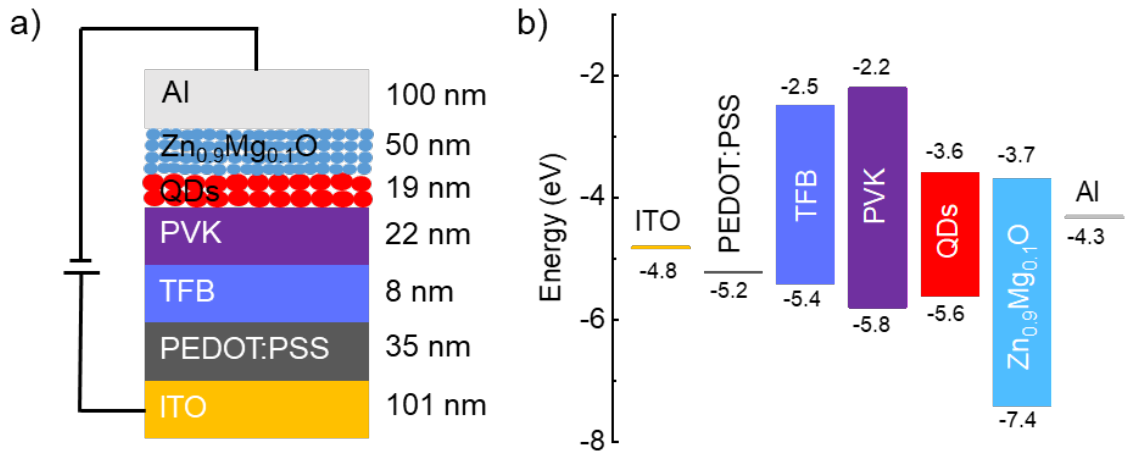

Figure 77. a) The structure and b) band alignment of the flexible InP QD-LEDs.

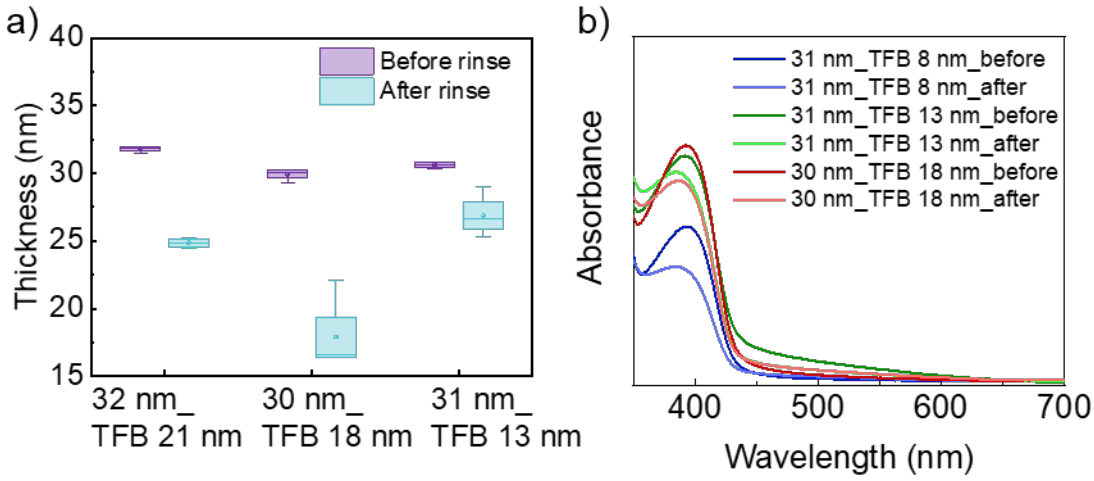

Figure 78. a) Thickness and b) absorbance variations of PVK+TFB films with different thickness configurations before and after rinsing by the mixture of CHB and decane.

To achieve full-color QD-LEDs with high resolution, it is necessary to fabricate micro-pixel photoresist bank arrays by photolithography on the substrate. The typical dimension of the bank structure is 60 μm (L) * 180 μm (W) * 1.3 μm (H). The CRE of the ink-20 was studied on the flexible substrate (Figure 79), showing minimal CRE on the flat ITO/PEN glass substrate at 60 °C. As PEN is a poor conductor, the ratio of K_s (~0.18) to K_l is about 1.38 (<1.45), so there is insufficient energy to sustain the droplet's temperature, causing the contact line to be cooler than the rest of the droplet due to the highest evaporative flux occurring in this region (Figure 79a). The Ma_T flow spatially moved outward and then inward at T_{sub} = 20 °C (Figure 79b). As the T_{sub} increased to

40 °C and 60 °C, the external energy sustained the temperature at the contact line, and the droplet behaved in the SJ mode and SS mode, respectively (Figure 79c, d). However, there was an obvious coffee ring at the edge when printed at T_{sub} = 60 °C which might be due to the longer pinning time. To obtain more uniform patterns, the ITO PEN film was then attached to the glass substrate to keep the same heat transfer pathway (Figure 79e).

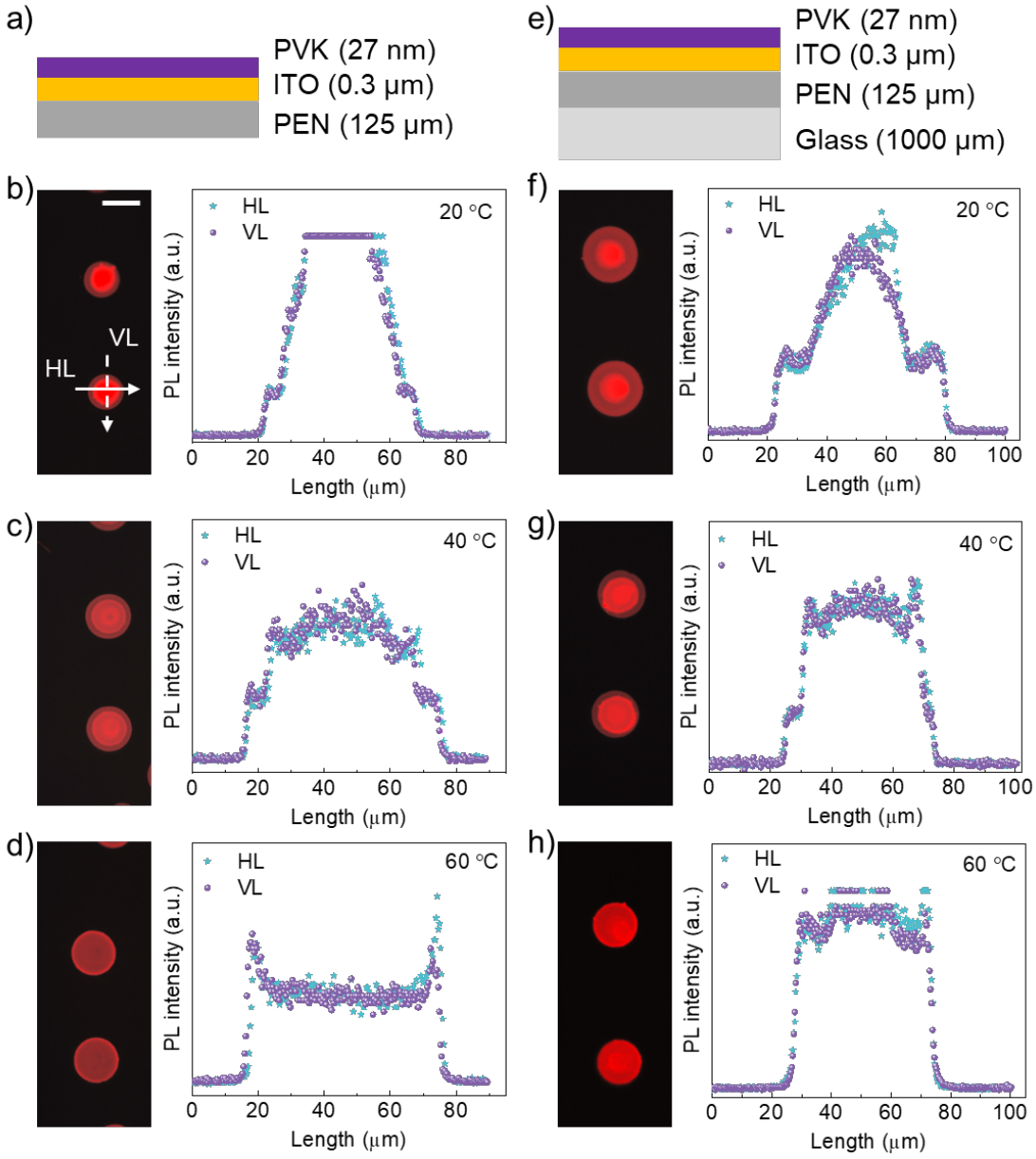

Figure 79. Inkjet printing the ink-20 on PVK-coated a) PEN and e) PEN/glass substrates. b-d, f-h) PL images and corresponding line profiles of the inkjet-printed patterns on the two substrates at T_{sub} of 20 °C, 40 °C, and 60 °C.

The substrate combines PEN and glass, and their total thermal conductivity (k_t = 5.25 >

2) can be estimated by

$$\frac{d_\mathrm{p} + d_\mathrm{g}}{k_t} = \frac{d_\mathrm{p}}{k_\mathrm{p}} + \frac{d_\mathrm{g}}{k_\mathrm{g}} \tag{48}$$

Here, d_p, d_g, k_p, and k_g are the thickness and thermal conductivity of PEN and glass, respectively. The outermost coffee ring was thicker at T_sub of 20 °C (Figure 79f), but the CRE was alleviated at higher T_sub owing to more balanced CRE and ME (Figure 79g,h).

However, the droplet evaporation on the bank differs from droplets dried on the flat surface. The final droplet profile is significantly influenced by the ST of the photoresist bank walls and PVK, which was identified by Ely et al. (Figure 80) [278]. Tailoring the ST of the bank walls and base to similar values facilitates more even deposition and improves the uniformity of printed QD patterns.

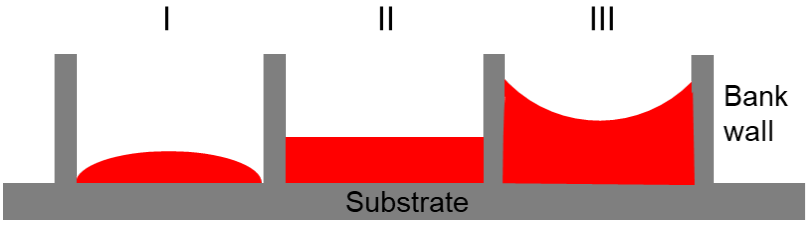

Figure 80. A schematic of droplet profiles at the end of evaporation in the photoresist well. The wettability of the bank walls is I) lower and III) greater than that of the base. II) The wettability of the bank walls is roughly equal to the base.

8. References

[1] de Arquer F P G et al. 2021 Semiconductor quantum dots: Technological progress and future challenges *Science* **373** eaaz8541

[2] Mishra S et al. 2019 Heavy metal contamination: an alarming threat to environment and human health *Environmental biotechnology: For sustainable future* 103-25

[3] Commission E 2011 Directive 2011/65/EU of the European parliament and of the council of 8 June 2011 on the restriction of the use of certain hazardous substances in electrical and electronic equipment *Off. J. Eur. Union* **174** 88

[4] Al-Douri Y et al. 2023 Synthesis and optical properties of II-VI semiconductor quantum dots: a review *J. Mater. Sci. Mater. Electron.* **34** 993

[5] Kim Y et al. 2020 III-V colloidal nanocrystals: control of covalent surfaces *Chem. Sci.* **11** 913-22

[6] Jain S et al. 2020 I-III-VI core/shell QDs: Synthesis, characterizations and applications *J. Lumin.* **219** 116912

[7] Fan Q Q et al. 2020 Lead-free halide perovskite nanocrystals: Crystal structures, synthesis, stabilities, and optical properties *Angew. Chem. Int. Ed.* **59** 1030-46

[8] Wang L et al. 2020 Full-color fluorescent carbon quantum dots *Sci. Adv.* **6** eabb6772

[9] Yan Y et al. 2019 Recent Advances on Graphene Quantum Dots: From Chemistry and Physics to Applications *Adv. Mater.* **31** 1808283

[10] Beri D 2023 Silicon quantum dots: surface matter, what next? *Mater. Adv.* **4** 3380-98

[11] Jalali H et al. 2022 Past, present and future of indium phosphide quantum dots *Nano Res.* **15** 4468-89

[12] Click S and Rosenthal S 2023 Synthesis, Surface Chemistry, and Fluorescent Properties of InP Quantum Dots *Chem. Mater.* **35** 822-36

[13] Jang E and Jang H 2023 Review: Quantum dot light-emitting diodes *Chem. Rev.* **123** 4663-92

[14] Lehnen T et al. 2012 Phase-selective microwave synthesis and inkjet printing applications of Zn_2SnO_4 (ZTO) quantum dots *J. Mater. Chem.* **22** 17732-36

[15] Ding L et al. 2020 Preparation of ZnO quantum dots@SiO_2/PVA for multifunctional coating on PET *New J. Chem.* **44** 2122-28

[16] Liang K et al. 2022 Fully printed optoelectronic synaptic transistors based on quantum dot-metal oxide semiconductor heterojunctions *ACS Nano* **16** 8651-61

[17] Cook B et al. 2017 Quantum dots-facilitated printing of ZnO nanostructure photodetectors with improved performance *ACS Appl. Mater. Interfaces* **9** 23189-94

[18] Zhao J W et al. 2020 Graphene quantum dots as full-color and stimulus responsive fluorescence ink for information encryption *J. Colloid Interface Sci.* **579** 307-14

[19] Lee S Y et al. 2023 Controlling the Surface Modification by CF4 Plasma Treatment for Inkjet Printed Color Conversion Layer With InP‐Based QDs Ink *Adv. Mater. Interfaces* **10** 2201851

[20] Eggenhuisen T M et al. 2015 High efficiency, fully inkjet printed organic solar cells with freedom of design *J. Mater. Chem. A* **3** 7255-62

[21] Pichumani M et al. 2013 Dynamics, crystallization and structures in colloid spin coating *Soft Matter* **9** 3220-29

[22] Bauri J et al. 2021 Recent advances in efficient emissive materials-based OLED applications: a review *J. Mater. Sci.* **56** 18837-66

[23] Park S et al. 2023 Patterning Quantum Dots via Photolithography: A Review *Adv. Mater.* **35** 2300546
[24] Fu M and Critchley K 2024 Inkjet printing of heavy-metal-free quantum dots-based devices: a review *Nanotechnology* **35** 302002
[25] Deegan R D et al. 1997 Capillary flow as the cause of ring stains from dried liquid drops *Nature* **389** 827-29
[26] Wei C T et al. 2022 A universal ternary-solvent-ink strategy toward efficient inkjet-printed perovskite quantum dot light-emitting diodes *Adv. Mater.* **34** 2107798
[27] Dou R and Derby B 2012 Formation of coffee stains on porous surfaces *Langmuir* **28** 5331-38
[28] Eral H B et al. 2011 Suppressing the coffee stain effect: how to control colloidal self-assembly in evaporating drops using electrowetting *Soft Matter* **7** 4954-58
[29] Pahlavan A A et al. 2021 Evaporation of binary-mixture liquid droplets: The formation of picoliter pancakelike shapes *Phys. Rev. Lett.* **127** 024501
[30] Ristenpart W D et al. 2007 Influence of substrate conductivity on circulation reversal in evaporating drops *Phys. Rev. Lett.* **99** 234502
[31] Wei C et al. 2024 Highly ordered inkjet-printed quantum-dot thin films enable efficient and stable QLEDs with EQE exceeding 23% *eScience* **4** 100227
[32] Liu H et al. 2024 Large-Area Flexible Perovskite Light-Emitting Diodes Enabled by Inkjet Printing *Adv. Mater.* **36** 2309921
[33] Bai J Y et al. 2023 Achieving high performance InP quantum dot light-emitting devices by using inkjet printing *Org. Electron.* **113** 106705
[34] Yang Z et al. 2022 Inkjet-printed blue InP/ZnS/ZnS quantum dot light-emitting diodes *Chem. Eng. J.* **450** 138413
[35] Lee H et al. 2022 Air stable eco-friendly quantum dots with a light-mediated photoinitiator for an inkjet printed flexible light emitting diode *J. Mater. Chem. C* **10** 10708-18
[36] Wang S et al. 2024 Efficient and Long Lifetime Red InP-Based QLEDs Enabled by Simultaneously Improved Carrier Injection Balance and Depressed Leakage *Adv. Opt. Mater.* 2402677
[37] Bian Y et al. 2024 Efficient green InP-based QD-LED by controlling electron injection and leakage *Nature* **635** 1-6
[38] Zhang W et al. 2022 High Quantum Yield Blue InP/ZnS/ZnS Quantum Dots Based on Bromine Passivation for Efficient Blue Light-Emitting Diodes *Adv. Opt. Mater.* **10** 202200685
[39] Cros-Gagneux A et al. 2010 Surface Chemistry of InP Quantum Dots: A Comprehensive Study *J. Am. Chem. Soc.* **132** 18147-57
[40] Chrzanowski M et al. 2021 Effect of Air Exposure of ZnMgO Nanoparticle Electron Transport Layer on Efficiency of Quantum-Dot Light-Emitting Diodes *ACS Appl. Mater. Interfaces* **13** 20305-12
[41] Ning M et al. 2023 Improving Performance of InP-Based Quantum Dot Light-Emitting Diodes by Controlling Defect States of the ZnO Electron Transport Layer *J. Phys. Chem. C* **127** 824-30
[42] Muller J et al. 2004 Air-induced fluorescence bursts from single semiconductor nanocrystals *Appl. Phys. Lett.* **85** 381-83
[43] Cordero S et al. 2000 Photo-activated luminescence of CdSe quantum dot monolayers *J. Phys. Chem. B* **104** 12137-42
[44] van Sark W et al. 2001 Photooxidation and photobleaching of single CdSe/ZnS quantum dots probed by room-temperature time-resolved spectroscopy *J. Phys. Chem. B* **105** 8281-84
[45] van Sark W et al. 2002 Blueing, bleaching, and blinking of single CdSe/ZnS quantum dots *Chemphyschem* **3** 871-79
[46] Brown R et al. 2018 Synthesis and Degradation of Cadmium-Free InP and InPZn/ZnS Quantum Dots in Solution *Langmuir* **34** 13924-34

[47] Duan X et al. 2023 Study of the Interfacial Oxidation of InP Quantum Dots Synthesized from Tris(dimethylamino)phosphine *ACS Appl. Mater. Interfaces* **15** 1619-28
[48] Yang X et al. 2012 Full Visible Range Covering InP/ZnS Nanocrystals with High Photometric Performance and Their Application to White Quantum Dot Light-Emitting Diodes *Adv. Mater.* **24** 4180-85
[49] Shen W et al. 2017 Synthesis of highly fluorescent InP/ZnS small-core/thick-shell tetrahedral-shaped quantum dots for blue light-emitting diodes *J. Mater. Chem. C* **5** 8243-49
[50] Yu P et al. 2022 Highly efficient green InP-based quantum dot light-emitting diodes regulated by inner alloyed shell component *Light: Sci. Appl.* **11** 162
[51] Liu P et al. 2021 Green InP/ZnSeS/ZnS Core Multi-Shelled Quantum Dots Synthesized with Aminophosphine for Effective Display Applications *Adv. Funct. Mater.* **31** 2008453
[52] Jo J et al. 2021 Stability enhancement of InP quantum dot/poly(methyl methacrylate) nanocomposites for light-emitting diode applications by grafting thermoresponsive poly(N-isopropylacrylamide) *J. Mater. Chem. C* **9** 14606-12
[53] Shin D et al. 2022 Understanding the Origin of Degradation of InP-Quantum Dot Light-Emitting Diodes *Adv. Electron. Mater.* **8** 2200256
[54] Zhang T et al. 2020 Factors influencing the working temperature of quantum dot light-emitting diodes *Opt. Express* **28** 34167-79
[55] Savchenko S et al. 2024 Thermally assisted optical processes in InP/ZnS quantum dots *Phys. Chem. Chem. Phys.* **26** 18727-40
[56] Dai X et al. 2014 Solution-processed, high-performance light-emitting diodes based on quantum dots *Nature* **515** 96-99
[57] Wang S J et al. 2018 Enhanced light out-coupling efficiency of quantum dot light emitting diodes by nanoimprint lithography *Nanoscale* **10** 11651-56
[58] Kim S H et al. 2017 A study on thin film uniformity in a roll-to-roll thermal evaporation system for flexible OLED applications *Int. J. Precis. Eng. Manuf.* **18** 1111-17
[59] Singh M et al. 2010 Inkjet Printing-Process and Its Applications *Adv. Mater.* **22** 673-85
[60] Zhan Z et al. 2017 Inkjet-printed optoelectronics *Nanoscale* **9** 965-93
[61] Li H et al. 2020 High-Resolution Pixelated Light Emitting Diodes Based on Electrohydrodynamic Printing and Coffee-Ring-Free Quantum Dot Film *Adv. Mater. Technol.* **5** 2000401
[62] Park J et al. 2007 High-resolution electrohydrodynamic jet printing *Nat. Mater.* **6** 782-89
[63] Lee D H et al. 2009 Screen-printed white OLED based on polystyrene as a host polymer *Curr. Appl. Phys.* **9** 161-64
[64] Zhong Z Y et al. 2020 Roll-to-roll reverse-offset printing combined with photonic sintering process for highly conductive ultrafine patterns *Adv. Eng. Mater.* **22** 2000463
[65] Kopola P et al. 2009 Gravure printed organic light emitting diodes for lighting applications *Thin Solid Films* **517** 5757-62
[66] Wu W 2017 Inorganic nanomaterials for printed electronics: a review *Nanoscale* **9** 7342-72
[67] Kaçar R et al. 2023 A review of high-end display technologies focusing on inkjet printed manufacturing *Mater. Today Commun.* **35** 105534
[68] Mackley M R et al. 2016 *Fundamentals of Inkjet Printing* (Wiley-VCH) pp 339-64
[69] Fromm J E 1984 Numerical-calculation of the fluid-dynamics of drop-on-demand jets *IBM J. Res. Dev.* **28** 322-33
[70] Jang D et al. 2009 Influence of Fluid Physical Properties on Ink-Jet Printability *Langmuir* **25** 2629-35

[71] Derby B and Reis N 2003 Inkjet printing of highly loaded particulate suspensions *MRS Bull.* **28** 815-18
[72] Liu Y et al. 2017 Efficient All-Solution Processed Quantum Dot Light Emitting Diodes Based on Inkjet Printing Technique *ACS Appl. Mater. Interfaces* **9** 25506-12
[73] Shen H et al. 2015 High-Efficiency, Low Turn-on Voltage Blue-Violet Quantum-Dot-Based Light-Emitting Diodes *Nano Lett.* **15** 1211-16
[74] Kim J H et al. 2021 Solvent mixture formulation for orthogonal inkjet processing and uniform pixel patterning of quantum dot light-emitting diode *J. Korean Phys. Soc.* **78** 1116-27
[75] Xiong X et al. 2019 Realizing 17.0% external quantum efficiency in red quantum dot light-emitting diodes by pursuing the ideal inkjet-printed film and interface *Org. Electron.* **73** 247-54
[76] Chen M et al. 2021 High performance inkjet-printed QLEDs with 18.3% EQE: improving interfacial contact by novel halogen-free binary solvent system *Nano Res.* **14** 4125-31
[77] Hu Z et al. 2020 Inkjet printed uniform quantum dots as color conversion layers for full-color OLED displays *Nanoscale* **12** 213-11
[78] Roh H et al. 2021 Enhanced performance of pixelated quantum dot light-emitting diodes by inkjet printing of quantum dot-polymer composites *Adv. Opt. Mater.* **9** 2002129
[79] Jiang C et al. 2016 Coffee-Ring-Free Quantum Dot Thin Film Using Inkjet Printing from a Mixed-Solvent System on Modified ZnO Transport Layer for Light-Emitting Devices *ACS Appl. Mater. Interfaces* **8** 26162-68
[80] Gao A et al. 2020 Printable $CsPbBr_3$ perovskite quantum dot ink for coffee ring-free fluorescent microarrays using inkjet printing *Nanoscale* **12** 2569-77
[81] Sliz R et al. 2019 Stable Colloidal Quantum Dot Inks Enable Inkjet-Printed High-Sensitivity Infrared Photodetectors *ACS Nano* **13** 11988-95
[82] Soltman D and Subramanian V 2008 Inkjet-printed line morphologies and temperature control of the coffee ring effect *Langmuir* **24** 2224-31
[83] Shi S et al. 2021 In situ inkjet printing patterned lead halide perovskite quantum dot color conversion films by using cheap and eco-friendly aqueous inks *Small Methods* **5** 2000889
[84] Young T 1805 III. An essay on the cohesion of fluids *Philos. Trans. R. Soc. London* 65-87
[85] Marangoni C 1865 On the expansion of a drop of liquid floating on the surface of another liquid *Tipographia dei fratelli Fusi, Pavia*
[86] Larson R 2014 Transport and deposition patterns in drying sessile droplets *AIChE J.* **60** 1538-71
[87] Still T et al. 2012 Surfactant-induced marangoni eddies alter the coffee-rings of evaporating colloidal drops *Langmuir* **28** 4984-88
[88] Lim J A et al. 2008 Self-organization of ink-jet-printed triisopropylsilylethynyl pentacene via evaporation-induced flows in a drying droplet *Adv. Funct. Mater.* **18** 229-34
[89] Poulard C and Damman P 2007 Control of spreading and drying of a polymer solution from Marangoni flows *Europhys. Lett.* **80** 64001
[90] Jia S Q et al. 2021 High performance inkjet-printed quantum-dot light-emitting diodes with high operational stability *Adv. Opt. Mater.* **9** 2101069
[91] Cui L Y et al. 2012 Avoiding coffee ring structure based on hydrophobic silicon pillar arrays during single-drop evaporation *Soft Matter* **8** 10448-56
[92] Girard F et al. 2010 Infrared thermography investigation of an evaporating sessile water droplet on heated substrates *Langmuir* **26** 4576-80
[93] Zhan S J et al. 2022 Inkjet-printed multi-color arrays based on eco-friendly quantum dot light emitting diodes with tailored hole transport layer *J. Soc. Inf. Disp.* **30** 748-57

[94] Birdi K S et al. 1989 A study of the evaporation rates of small water drops placed on a solid-surface *J. Phys. Chem.* **93** 3702-03
[95] Erbil H et al. 2002 Drop evaporation on solid surfaces: Constant contact angle mode *Langmuir* **18** 2636-41
[96] Wilson S K and D'Ambrosio H-M 2023 Evaporation of Sessile Droplets *Annu. Rev. Fluid Mech.* **55** 481-509
[97] Hu D and Wu H 2016 Volume evolution of small sessile droplets evaporating in stick-slip mode *Phys. Rev. E* **93** 042805
[98] Debuisson D et al. 2016 Stick-Jump (SJ) Evaporation of Strongly Pinned Nanoliter Volume Sessile Water Droplets on Quick Drying, Micropatterned Surfaces *Langmuir* **32** 2679-86
[99] Li Y et al. 2019 Stoichiometry-controlled InP-based quantum dots: Synthesis, photoluminescence, and electroluminescence *J. Am. Chem. Soc.* **141** 6448-52
[100] Baskoutas S and Terzis A F 2006 Size-dependent band gap of colloidal quantum dots *J. Appl. Phys.* **99** 1
[101] Yu P et al. 2021 Inorganic solid phosphorus precursor of sodium phosphaethynolate for synthesis of highly luminescent inp-based quantum dots *ACS Energy Lett.* **6** 2697-703
[102] Kittel C and McEuen P 2018 *Introduction to solid state physics* (John Wiley & Sons)
[103] Singleton J 2001 *Band theory and electronic properties of solids* vol 2 (OUP Oxford)
[104] Pauli W 1924 Pauli exclusion principle *Naturwiss* **12** 741
[105] Cohen M L and Chelikowsky J R 2012 *Electronic structure and optical properties of semiconductors* vol 75 (Springer Science & Business Media)
[106] Lim M et al. 2019 Synthesis of far-red- and near-infrared-emitting Cu-doped InP/ZnS (core/shell) quantum dots with controlled doping steps and their surface functionalization for bioconjugation *Nanoscale* **11** 10463-71
[107] Takagahara T and Takeda K 1992 Theory of the quantum confinement effect on excitons in quantum dots of indirect-gap materials *Phys. Rev. B* **46** 15578-81
[108] Kim J et al. 2024 Recent Advances and Challenges of Colloidal Quantum Dot Light-Emitting Diodes for Display Applications *Adv. Mater.* **36** 2212220
[109] Brus L E 1983 A simple-model for the ionization-potential, electron-affinity, and aqueous redox potentials of small semiconductor crystallites *J. Chem. Phys.* **79** 5566-71
[110] Sun J and Goldys E 2008 Linear absorption and molar extinction coefficients in direct semiconductor quantum dots *J. Phys. Chem. C* **112** 9261-66
[111] Ferreira D and Alves J 2004 The effects of shape and size nonuniformity on the absorption spectrum of semiconductor quantum dots *Nanotechnology* **15** 975-81
[112] Othonos A 1998 Probing ultrafast carrier and phonon dynamics in semiconductors *J. Appl. Phys.* **83** 1789-830
[113] Klimov V et al. 1999 Electron and hole relaxation pathways in semiconductor quantum dots *Phys. Rev. B* **60** 13740-49
[114] Pandey A and Guyot-Sionnest P 2008 Slow Electron Cooling in Colloidal Quantum Dots *Science* **322** 929-32
[115] Hendry E et al. 2006 Direct observation of electron-to-hole energy transfer in CdSe quantum dots *Phys. Rev. Lett.* **96** 057408
[116] Qi W et al. 2005 Shape factor of nonspherical nanoparticles *J. Mater. Sci.* **40** 2737-39
[117] Xu Y et al. 2024 Shell thickness influence on the carrier dynamics of InP/ZnS QDs *Chem. Phys. Impact* **8** 100579

[118] Cordones A and Leone S 2013 Mechanisms for charge trapping in single semiconductor nanocrystals probed by fluorescence blinking *Chem. Soc. Rev.* **42** 3209-21
[119] Vishnu E et al. 2024 Trap States in Semiconductor Quantum Dots: Friends or Foes *J. Phys. Chem. C* **128** 4373-82
[120] Vasudevan D et al. 2015 Core-shell quantum dots: Properties and applications *J. Alloys Compd.* **636** 395-404
[121] Yun Z et al. 2022 Solvent-mediated surface ligand exchange to enhance the performance of quantum-dot light-emitting diodes *Org. Electron.* **108** 106561
[122] Shin S et al. 2023 Ligand-Crosslinking Strategy for Efficient Quantum Dot Light-Emitting Diodes via Thiol-Ene Click Chemistry *Small Methods* **7** 2300206
[123] Sugimoto T 1987 Preparation of monodispersed colloidal particles *Adv. Colloid Interface Sci.* **28** 65-108
[124] Chen B et al. 2020 InP quantum dots: Synthesis and lighting applications *Small* **16** 2002454
[125] Kim H-M et al. 2018 Li and Mg Co-Doped Zinc Oxide Electron Transporting Layer for Highly Efficient Quantum Dot Light-Emitting Diodes *ACS Appl. Mater. Interfaces* **10** 24028-36
[126] Kagan C R et al. 2016 Building devices from colloidal quantum dots *Science* **353** aac5523
[127] Spinicelli P et al. 2009 Bright and grey states in CdSe-CdS nanocrystals exhibiting strongly reduced blinking *Phys. Rev. Lett.* **102** 136801
[128] Liu Z et al. 2020 Micro-light-emitting diodes with quantum dots in display technology *Light: Sci. Appl.* **9** 83
[129] Anikeeva P et al. 2008 Electronic and excitonic processes in light-emitting devices based on organic materials and colloidal quantum dots *Phys. Rev. B Condens. Matter* **78** 085434
[130] Mashford B et al. 2013 High-efficiency quantum-dot light-emitting devices with enhanced charge injection *Nat. Photon.* **7** 407-12
[131] Deng Y et al. 2020 Deciphering exciton-generation processes in quantum-dot electroluminescence *Nat. Commun.* **11** 2309
[132] Wood V et al. 2011 Electroluminescence from Nanoscale Materials via Field-Driven Ionization *Nano Lett.* **11** 2927-32
[133] Koo J H et al. 2018 Flexible and stretchable smart display: Materials, fabrication, device design, and system integration *Adv. Funct. Mater.* **28** 1801834
[134] Yuan Q et al. 2021 A review on the electroluminescence properties of quantum-dot light-emitting diodes *Org. Electron.* **90** 106086
[135] Park Y et al. 2014 Auger Recombination of Biexcitons and Negative and Positive Trions in Individual Quantum Dots *ACS Nano* **8** 7288-96
[136] Klimov V I et al. 2000 Quantization of multiparticle Auger rates in semiconductor quantum dots *Science* **287** 1011-13
[137] Nirmal M et al. 1996 Fluorescence intermittency in single cadmium selenide nanocrystals *Nature* **383** 802-04
[138] Galland C et al. 2011 Two types of luminescence blinking revealed by spectroelectrochemistry of single quantum dots *Nature* **479** 203-07
[139] Lee Y et al. 2022 Effectual Interface and Defect Engineering for Auger Recombination Suppression in Bright InP/ZnSeS/ZnS Quantum Dots *ACS Appl. Mater. Interfaces* **14** 12479-87
[140] Dai X et al. 2017 Quantum-Dot Light-Emitting Diodes for Large-Area Displays: Towards the Dawn of Commercialization *Adv. Mater.* **29** 1607022
[141] Kagan C R et al. 1996 Electronic energy transfer in CdSe quantum dot solids *Phys. Rev. Lett.* **76** 1517-20
[142] Baldo M A et al. 1999 Very high-efficiency green organic light-emitting devices based on electrophosphorescence *Appl. Phys. Lett.* **75** 4-6

[143] Moon H et al. 2019 Composition-tailored ZnMgO nanoparticles for electron transport layers of highly efficient and bright InP-based quantum dot light emitting diodes *Chem. Commun.* **55** 13299-302
[144] Qasim K et al. 2012 Enhanced Electrical Efficiency of Quantum Dot Based LEDs with TiO2 as the Electron Transport Layer Fabricated Under the Optimized Annealing-Time Conditions *J. Nanosci. Nanotechnol.* **12** 7879-84
[145] Vu H-T et al. 2016 Solution-Processable MoOx for Efficient Light-Emitting Diodes Based on Giant Quantum Dots *IEEE Photonics Technol. Lett.* **28** 2156-59
[146] Zhang H et al. 2016 Ultrastable Quantum-Dot Light-Emitting Diodes by Suppression of Leakage Current and Exciton Quenching Processes *ACS Appl. Mater. Interfaces* **8** 31385-91
[147] Liang F et al. 2017 Polymer as an Additive in the Emitting Layer for High-Performance Quantum Dot Light-Emitting Diodes *ACS Appl. Mater. Interfaces* **9** 20239-46
[148] Won Y-H et al. 2019 Highly efficient and stable InP/ZnSe/ZnS quantum dot light-emitting diodes *Nature* **575** 634-38
[149] Vu H et al. 2018 Ultrathin PVK charge control layer for advanced manipulation of efficient giant CdSe@ZnS/ZnS quantum dot light-emitting diodes *Org. Electron.* **63** 349-54
[150] Thesen M et al. 2010 Hole-Transporting Host-Polymer Series Consisting of Triphenylamine Basic Structures for Phosphorescent Polymer Light-Emitting Diodes *J. Polym. Sci. Part A: Polym. Chem.* **48** 3417-30
[151] Wang T et al. 2019 Exploring Electronic and Excitonic Processes toward Efficient Deep-Red $CuInS_2$/ZnS Quantum-Dot Light-Emitting Diodes *ACS Appl. Mater. Interfaces* **11** 36925-30
[152] Jo J H et al. 2016 High-efficiency red electroluminescent device based on multishelled InP quantum dots *Opt. Lett.* **41** 3984-87
[153] Buffard A et al. 2016 Mechanistic Insight and Optimization of InP Nanocrystals Synthesized with Aminophosphines *Chem. Mater.* **28** 5925-34
[154] Song W-S et al. 2013 Amine-derived synthetic approach to color-tunable InP/ZnS quantum dots with high fluorescent qualities *J. Nanopart. Res.* **15** 1750
[155] Jiang W et al. 2021 Efficient green indium phosphide quantum dots with tris(dimethylamino)-phosphine phosphorus precursor for electroluminescent devices *J. Mater. Sci. Mater. Electron.* **32** 4686-94
[156] Ristic M et al. 2005 Sol-gel synthesis and characterization of nanocrystalline ZnO powders *J. Alloys Compd.* **397** L1-L4
[157] Pan Y M et al. 2022 On axisymmetric dynamic spin coating with a single drop of ethanol *J. Fluid Mech.* **951** A30
[158] Company E K 1967 *Proceedings of the Second Kodak Seminar on Microminiaturization, April 4 and 5, 1966, at Monterey, California*
[159] Meyerhofer D 1978 Characteristics of resist films produced by spinning *J. Appl. Phys.* **49** 3993-97
[160] Wu M G et al. 2018 High-luminance perovskite light-emitting diodes with high-polarity alcohol solvent treating PEDOT:PSS as hole transport layer *Nanoscale Res. Lett.* **13** 1-9
[161] Smallwood I 2012 *Handbook of organic solvent properties* (Butterworth-Heinemann)
[162] Young J F 1967 Humidity control in the laboratory using salt solutions—a review *J. Appl. Chem.* **17** 241-45
[163] Reiss P et al. 2009 Core/Shell Semiconductor Nanocrystals *Small* **5** 154-68
[164] Yamada S 2002 General shear-thinning dynamics of confined fluids *Tribol. Lett.* **13** 167-71
[165] WOODCOCK L 1984 Origins of shear dilatancy and shear thickening phenomena *Chem. Phys. Lett.* **111** 455-61

[166] Hu H and Larson R G 2002 Evaporation of a Sessile Droplet on a Substrate *J. Phys. Chem. B* **106** 1334-44
[167] Chandra S et al. 1996 Effect of liquid-solid contact angle on droplet evaporation *Fire Saf. J.* **27** 141-58
[168] Shen X Y et al. 2010 Minimal Size of Coffee Ring Structure *J. Phys. Chem. B* **114** 5269-74
[169] Guild J 1932 The colorimetric properties of the spectrum *Proc. R. soc. Lond. Ser. A-Contain. Pap. Math. Phys. Character.* **230** 149-87
[170] ROSE A 1955 Space-charge-limited currents in solids *Phys. Rev.* **97** 1538-44
[171] Kim S et al. 2019 Control of carrier injection and transport in quantum dot light emitting diodes (QLEDs) via modulating Schottky injection barrier and carrier mobility *J. Appl. Phys.* **126** 185702
[172] Krishna V and Mahesha M 2021 XPS analysis of $ZnS_{0.4}Se_{0.6}$ thin films deposited by spray pyrolysis technique *J. Electron. Spectrosc. Relat. Phenom.* **249** 147072
[173] Cho B et al. 2016 Highly conductive air-stable ZnO thin film formation under *in situ* UV illumination for an indium-free transparent electrode *RSC Adv.* **6** 69027-32
[174] Gary D C et al. 2014 Investigation of indium phosphide quantum dot nucleation and growth utilizing triarylsilylphosphine precursors *Chem. Mater.* **26** 1734-44
[175] Tessier M D et al. 2015 Economic and size-tunable synthesis of InP/ZnE (E = S, Se) colloidal quantum dots *Chem. Mater.* **27** 4893-98
[176] Harris D K and Bawendi M G 2012 Improved precursor chemistry for the synthesis of iii-v quantum dots *J. Am. Chem. Soc.* **134** 20211-13
[177] Clark M D et al. 2011 Focusing nanocrystal size distributions via production control *Nano Lett.* **11** 1976-80
[178] Allen P M et al. 2010 Mechanistic insights into the formation of InP quantum dots *Angew. Chem. Int. Ed.* **49** 760-62
[179] Joung S et al. 2012 Facile synthesis of uniform large-sized InP nanocrystal quantum dots using tris(tert-butyldimethylsilyl)phosphine *Nanoscale Res. Lett.* **7** 1-8
[180] Franke D et al. 2015 The unexpected influence of precursor conversion rate in the synthesis of iii-v quantum dots *Angew. Chem. Int. Ed.* **54** 14299-303
[181] Gao S M et al. 2002 Aqueous synthesis of III-V semiconductor GaP and InP exhibiting pronounced quantum confinement *Chem. Commun.* **24** 3064-65
[182] Li L et al. 2008 Economic synthesis of high quality InP nanocrystals using calcium phosphide as the phosphorus precursor *Chem. Mater.* **20** 2621-23
[183] Thomas A et al. 2018 How Trap States Affect Charge Carrier Dynamics of CdSe and InP Quantum Dots: Visualization through Complexation with Viologen *ACS Energy Lett.* **3** 2368-75
[184] Pietra F et al. 2016 Tuning the Lattice Parameter of In_xZn_yP for Highly Luminescent Lattice-Matched Core/Shell Quantum Dots *ACS Nano* **10** 4754-62
[185] Vinokurov A et al. 2018 Optical properties and structure of Ag-doped InP quantum dots prepared by a phosphine synthetic route *Dalton Trans.* **47** 12414-19
[186] Micic O I et al. 2000 Core-shell quantum dots of lattice-matched $ZnCdSe_2$ shells on InP cores: Experiment and theory *J. Phys. Chem. B* **104** 12149-56
[187] Kim T-G et al. 2018 Trap passivation in indium-based quantum dots through surface fluorination: Mechanism and applications *ACS Nano* **12** 11529-40
[188] Wu Z et al. 2020 Development of InP Quantum Dot-Based Light-Emitting Diodes *ACS Energy Lett.* **5** 1095-106
[189] Zhang G et al. 2018 Dual-Emissive and Color-Tunable Mn-Doped InP/ZnS Quantum Dots via a Growth-Doping Method *Nanoscale Res. Lett.* **13** 170

[190] Xu Y et al. 2020 Preparation of Highly Stable and Photoluminescent Cadmium-Free InP/GaP/ZnS Core/Shell Quantum Dots and Application to Quantitative Immunoassay *Part. Part. Syst. Charact.* **37** 1900441
[191] Lim J et al. 2013 Highly efficient cadmium-free quantum dot light-emitting diodes enabled by the direct formation of excitons within InP@ZnSeS quantum dots *ACS Nano* **7** 9019-26
[192] Dennis A M et al. 2019 Role of interface chemistry in opening new radiative pathways in InP/CdSe giant quantum dots with blinking-suppressed two-color emission *Adv. Funct. Mater.* **29** 1809111
[193] Karatum O et al. 2019 Light-emitting devices based on type-II InP/ZnO quantum dots *ACS Photonics* **6** 939-46
[194] Janke E et al. 2018 Origin of Broad Emission Spectra in InP Quantum Dots: Contributions from Structural and Electronic Disorder *J. Am. Chem. Soc.* **140** 15791-803
[195] Nguyen A et al. 2021 Extremely Slow Trap-Mediated Hole Relaxation in Room-Temperature InP/ZnSe/ZnS Quantum Dots *J. Phys. Chem. C* **125** 4110-18
[196] Freymeyer N et al. 2020 Effect of indium alloying on the charge carrier dynamics of thick-shell InP/ZnSe quantum dots *J. Chem. Phys.* **152** 16
[197] Huang P et al. 2023 Deep-Red InP Core-Multishell Quantum Dots for Highly Bright and Efficient Light-Emitting Diodes *Adv. Opt. Mater.* **11** 2300612
[198] Zhang W et al. 2022 High Quantum Yield Blue InP/ZnS/ZnS Quantum Dots Based on Bromine Passivation for Efficient Blue Light‐Emitting Diodes *Adv. Opt. Mater.* **10** 2200685
[199] Battaglia D and Peng X 2002 Formation of high quality InP and InAs nanocrystals in a noncoordinating solvent *Nano Lett.* **2** 1027-30
[200] Dhaene E et al. 2019 The Trouble with ODE: Polymerization during Nanocrystal Synthesis *Nano Lett.* **19** 7411-17
[201] Tisdale W A et al. 2010 Hot-Electron Transfer from Semiconductor Nanocrystals *Science* **328** 1543-47
[202] Rodosthenous P et al. 2020 Tuning the Radiative Lifetime in InP Colloidal Quantum Dots by Controlling the Surface Stoichiometry *J. Phys. Chem.* **11** 10124-30
[203] Adachi S 1999 *Optical Constants of Crystalline and Amorphous Semiconductors: Numerical Data and Graphical Information* (Springer US) pp 445-58
[204] Sette-Ducati J et al. 2023 Understanding the Two-Dimensional Mixing Behavior of 1-Naphthalenethiol and Octanethiol *J. Phys. Chem. C* **127** 6531-42
[205] Virieux H et al. 2012 InP/ZnS Nanocrystals: Coupling NMR and XPS for Fine Surface and Interface Description *J. Am. Chem. Soc.* **134** 19701-08
[206] Ding L et al. 2023 Synchronous generation of green oxidants H_2O_2 and O_3 by using a heterojunction bifunctional ZnO/ZnS@C electrocatalyst *J. Mater. Chem. A* **11** 3454-63
[207] Kazmerski L L et al. 1981 Initial oxidation of $CuInSe_2$ *J. Vac. Sci. Technol* **19** 467-71
[208] Jiang K et al. 2023 Photobreeding Heterojunction on Semiconductor Materials for Enhanced Photocatalysis *Adv. Funct. Mater.* **33** 2304351
[209] Shallenberger J and Hellgren N 2020 Zinc selenide analyzed by XPS *Surf. Sci. Spectra* **27** 014020
[210] Heo D et al. 2023 Modified Zinc Magnesium Oxide for Optimal Charge‐Injection Balance in InP Quantum Dot Light‐Emitting Diodes *Adv. Opt. Mater.* **11** 2202256
[211] Pan J et al. 2016 Size Tunable ZnO Nanoparticles To Enhance Electron Injection in Solution Processed QLEDs *ACS Photonics* **3** 215-22

[212] Ozgür U et al. 2005 A comprehensive review of ZnO materials and devices *J. Appl. Phys.* **98** 4
[213] Bourlier Y et al. 2018 Investigation of InAlN Layers Surface Reactivity after Thermal Annealings: A Complete XPS Study for HEMT *ECS J. Solid State Sci. Technol* **7** P329-P38
[214] Lee W et al. 2001 XPS study of carbon fiber surfaces treated by thermal oxidation in a gas mixture of $O_2/(O_2+N_2)$ *Appl. Surf. Sci.* **171** 136-42
[215] Kim H et al. 2019 Optimization of the electron transport in quantum dot light-emitting diodes by codoping ZnO with gallium (Ga) and magnesium (Mg) *RSC Adv.* **9** 32066-71
[216] Yin Z et al. 2016 Controllable ZnMgO Electron-Transporting Layers for Long-Term Stable Organic Solar Cells with 8.06% Efficiency after One-Year Storage *Adv. Energy Mater.* **6** 1501493
[217] Lee Y et al. 2019 Electron transport phenomena at the interface of Al electrode and heavily doped degenerate ZnO nanoparticles in quantum dot light emitting diode *Nanotechnology* **30** 035207
[218] Haverinen H M et al. 2009 Inkjet printing of light emitting quantum dots *Appl. Phys. Lett.* **94** 7
[219] Wang S et al. 2023 Development and challenges of indium phosphide-based quantum-dot light-emitting diodes *J. Photochem. Photobiol. C* **55** 100588
[220] Lim L et al. 2023 Non-Toxic $CuInS_2$/ZnS Colloidal Quantum Dots for Near-Infrared Light-Emitting Diodes *Adv. Mater.* **35** 2301887
[221] Shi Y et al. 2023 Carbon Dots for Electroluminescent Light-Emitting Diodes: Recent Progress and Future Prospects *Adv. Mater.* **35** 2210699
[222] Zhang J et al. 2017 High quantum yield blue emission from lead free inorganic antimony halide perovskite colloidal quantum dots *ACS Nano* **11** 9294-302
[223] Saitow K 2024 Bright silicon quantum dot synthesis and LED design: insights into size-ligand-property relationships from slow- and fast-band engineering *Bull. Chem. Soc. Jpn.* **97** uoad002
[224] Xie L et al. 2022 High‐Performance Inkjet‐Printed Blue QLED Enabled by Crosslinked and Intertwined Hole Transport Layer *Adv. Opt. Mater.* **10** 2200935
[225] Li H et al. 2022 High Performance InP-based Quantum Dot Light-Emitting Diodes via the Suppression of Field-Enhanced Electron Delocalization *Adv. Funct. Mater.* **32** 2204529
[226] Mei G et al. 2022 Light extraction employing optical tunneling in blue InP quantum dot light-emitting diodes *Appl. Phys. Lett.* **120** 091101
[227] Li D et al. 2019 Blue quantum dot light-emitting diodes with high luminance by improving the charge transfer balance *Chem. Commun.* **55** 3501-04
[228] Park M et al. 2022 All inkjet-printed 6.95" 217 ppi active matrix QD-LED display with RGB Cd-free QDs in the top-emission device structure *J. Soc. Inf. Disp.* **30** 433-40
[229] Song J J et al. 2019 Over 30% external quantum efficiency light-emitting diodes by engineering quantum dot-assisted energy level match for hole transport layer *Adv. Funct. Mater.* **29** 1808377
[230] Hubner T et al. 2021 Parasitic emission in inkjet-printed InP-based quantum dot light-emitting diodes *Org. Electron.* **93** 106156
[231] Fukai J et al. 2006 Effects of droplet size and solute concentration on drying process of polymer solution droplets deposited on homogeneous surfaces *Int. J. Heat Mass Transfer* **49** 3561-67
[232] Pan J Y et al. 2016 Application of Solvent Modified PEDOT:PSS in All-Solution-Processed Inverted Quantum Dot Light-Emitting Diodes *J Disp. Technol.* **12** 1157-61
[233] Shariffudin S et al. 2012 Effect of film thickness on structural, electrical, and optical properties of sol-gel deposited layer-by-layer ZnO nanoparticles *Trans.*

Electr. Electron. Mater. **13** 102-05
[234] Qu X et al. 2023 Does interfacial exciton quenching exist in high-performance quantum dot light-emitting diodes? *Nanoscale* **15** 3430-37
[235] Lin Q et al. 2016 Influence of Ambient Gas on the Performance of Quantum-Dot Light-Emitting Diodes *ACS Appl. Mater. Interfaces* **8** 11557-63
[236] Zanjani S et al. 2023 An investigation on the cyclic temperature-dependent performance behaviors of ultrabright air-stable QLEDs *Sci. Rep.* **13** 12713
[237] Sun Y et al. 2019 Investigation on Thermally Induced Efficiency Roll-Off: Toward Efficient and Ultrabright Quantum-Dot Light-Emitting Diodes *ACS Nano* **13** 11433-42
[238] Zanjani S et al. 2022 Tailored ZnO Functional Nanomaterials for Solution-Processed Quantum-Dot Light-Emitting Diodes *Adv. Photon. Res.* **3** 2200159
[239] Zhao Y et al. 2012 High-Temperature Luminescence Quenching of Colloidal Quantum Dots *ACS Nano* **6** 9058-67
[240] Rowland C et al. 2014 Thermal Stability of Colloidal InP Nanocrystals: Small Inorganic Ligands Boost High-Temperature Photoluminescence *ACS Nano* **8** 977-85
[241] Baek H et al. 2024 Insights into structural defect formation in individual InP/ZnSe/ZnS quantum dots under UV oxidation *Nat. Commun.* **15** 1671
[242] Moon H et al. 2019 Stability of Quantum Dots, Quantum Dot Films, and Quantum Dot Light-Emitting Diodes for Display Applications *Adv. Mater.* **31** 1804294
[243] Woo H et al. 2013 Robust, processable, and bright quantum dot/organosilicate hybrid films with uniform QD distribution based on thiol-containing organosilicate ligands *J. Mater. Chem. C* **1** 1983-89
[244] Burrows P et al. 2001 Gas permeation and lifetime tests on polymer-based barrier coatings *Organic Light-Emitting Materials and Devices IV* **4105** 75-83
[245] Park S et al. 2015 Long-term stability of CdSe/CdZnS quantum dot encapsulated in a multi-lamellar microcapsule *Nanotechnology* **26** 275602
[246] Lee S et al. 2020 InP-Quantum-Dot-in-ZnS-Matrix Solids for Thermal and Air Stability *Chem. Mater.* **32** 9584-90
[247] Chang Y et al. 2015 Preparation of highly luminescent $BaSO_4$ protected CdTe quantum dots as conversion materials for excellent color-rendering white LEDs *J. Mater. Chem. C* **3** 2831-36
[248] Jo J et al. 2018 Effective surface passivation of multi-shelled InP quantum dots through a simple complexing with titanium species *Appl. Surf. Sci.* **428** 906-11
[249] Jo J et al. 2015 Photostability enhancement of InP/ZnS quantum dots enabled by In_2O_3 overcoating *J. Alloys Compd.* **647** 6-13
[250] Acharya K et al. 2017 High efficiency quantum dot light emitting diodes from positive aging *Nanoscale* **9** 14451-57
[251] You J et al. 2016 Improved air stability of perovskite solar cells via solution-processed metal oxide transport layers *Nat. Nanotechnol.* **11** 75
[252] Bae W et al. 2013 Controlling the influence of Auger recombination on the performance of quantum-dot light-emitting diodes *Nat. Commun.* **4** 2661
[253] Yun D et al. 2020 In-Situ Photoelectron Spectroscopy Study on the Air Degradation of PEDOT:PSS in Terms of Electrical and Thermoelectric Properties *Adv. Electron. Mater.* **6** 2000620
[254] Lin B et al. 2021 Lifetime elongation of quantum-dot light-emitting diodes by inhibiting the degradation of hole transport layer *RSC Adv.* **11** 20884-91
[255] Lee J and Lee H 2024 Enhancing CdSe/ZnS Quantum-Dot Light-Emitting Diode Performance: The Impact of Thermal Treatment Atmospheres on Fabrication Processes *J. Nanoelectron.* **19** 600-04
[256] Wegner K et al. 2019 Influence of the Core/Shell Structure of Indium Phosphide Based Quantum Dots on Their Photostability and Cytotoxicity *Front. Chem.* **7** 466

[257] Tran A et al. 2024 Encapsulation of InP/ZnS Quantum Dots into MOF-5 Matrices for Solid-State Luminescence: Ship in the Bottle and Bottle around the Ship Methodologies *Materials* **17** 3155
[258] Pechstedt K et al. 2010 Photoluminescence of Colloidal CdSe/ZnS Quantum Dots: The Critical Effect of Water Molecules *J. Phys. Chem. C* **114** 12069-77
[259] Jones M et al. 2003 Photoenhancement of luminescence in colloidal CdSe quantum dot solutions *J. Phys. Chem. B* **107** 11346-52
[260] Chauvin J and Pratt D 2017 On the Reactions of Thiols, Sulfenic Acids, and Sulfinic Acids with Hydrogen Peroxide *Angew. Chem. Int. Ed.* **56** 6255-59
[261] Nakamura A and Temmyo J 2011 Schottky contact on ZnO nano-columnar film with H_2O_2 treatment *J. Appl. Phys.* **109** 093517
[262] Fouad O et al. 2006 Zinc oxide thin films prepared by thermal evaporation deposition and its photocatalytic activity *Appl. Catal. B* **62** 144-49
[263] Hellgren N et al. 2020 Effect of etching on the oxidation of zinc selenide surfaces characterized by X-ray photoelectron spectroscopy *Appl. Surf. Sci.* **528** 146604
[264] Würz R et al. 2005 In situ X-ray photoelectron spectroscopy study of the oxidation of $CuGaSe_2$ *Surf. Sci.* **580** 80-94
[265] Granada-Ramirez D et al. 2020 Chemical synthesis and optical, structural, and surface characterization of InP-In_2O_3 quantum dots *Appl. Surf. Sci.* **530** 147294
[266] Chen W et al. 2022 Synthesis and characterization of InP/ZnSe/ZnS quantum dots for photo-emissive color conversion *Opt. Mater. Express* **12** 1717-30
[267] Byun H et al. 2011 Solvothermal synthesis of InP quantum dots and their enhanced luminescent efficiency by post-synthetic treatments *J. Colloid Interface Sci.* **355** 35-41
[268] Dinh C et al. 2019 Multi-site electrocatalysts for hydrogen evolution in neutral media by destabilization of water molecules *Nat. Energy* **4** 107-14
[269] Ali U et al. 2015 A Review of the Properties and Applications of Poly (Methyl Methacrylate) (PMMA) *Polym. Rev.* **55** 678-705
[270] Suárez I et al. 2011 Photoluminescence waveguiding in CdSe and CdTe QDs-PMMA nanocomposite films *Nanotechnology* **22** 435202
[271] Fick A 1995 On liquid diffusion *J. Membr. Sci.* **100** 33-38
[272] Klinger M et al. 2009 Effect of Polymer Cross-Links on Oxygen Diffusion in Glassy PMMA Films *ACS Appl. Mater. Interfaces* **1** 661-67
[273] KJELDSEN P 1993 Evaluation of gas diffusion through plastic materials used in experimental and sampling equipment *Water Res.* **27** 121-31
[274] Hwang M et al. 2011 Inkjet-printing of indium tin oxide (ITO) films for transparent conducting electrodes *Mater. Sci. Eng. B* **176** 1128-31
[275] Singh A et al. 2015 Understanding the formation of PEDOT:PSS films by ink-jet printing for organic solar cell applications *RSC Adv.* **5** 78677-85
[276] Sánchez J et al. 2018 Impact of inkjet printed ZnO electron transport layer on the characteristics of polymer solar cells *RSC Adv.* **8** 13094-102
[277] Lee D and Oh J 2010 Inkjet printing of conductive Ag lines and their electrical and mechanical characterization *Thin Solid Films* **518** 6352-56
[278] Ely F et al. 2011 Patterning quality control of inkjet printed PEDOT:PSS films by wetting properties *Synth. Met.* **161** 2129-34

9. Appendix

9.1 Different combinations of lifetime fitting of QDs

Table 22. Different combinations of lifetime fitting of InP core, InP/$ZnSe_xS_{1-x}$, and InP/$ZnSe_xS_{1-x}$/ZnS QDs.

	InP core	InP/$ZnSe_xS_{1-x}$	InP/$ZnSe_xS_{1-x}$/ZnS
A_1	4095.9	58763.7	56752.2
τ_1 (ns)	0.5	0.5	0.5
A_2	3.8	2461.9	2938.8
τ_2 (ns)	114.9	114.9	114.9
χ^2	1.0	135.1	136.5
A_1	36.7	12579.5	1263.9
τ_1 (ns)	10.5	10.5	10.5
A_2	0.006	2090.4	2523.7
τ_2 (ns)	114.9	114.9	114.9
χ^2	1.5	53.5	58.6
A_1	16.0	8307.7	8803.5
τ_1 (ns)	33.6	33.6	33.6
A_2	-2.4	1140.7	1466.5
τ_2 (ns)	114.9	114.9	114.9
χ^2	1.6	1.5	1.8
A_1	3553.2	-53160.6	-59830.7
τ_1 (ns)	0.5	0.5	0.5
A_2	18.7	17891.4	19022.2
τ_2 (ns)	11.8	11.8	11.8
χ^2	1.0	203.7	242.2
A_1	4063.1	17101.9	10626.1
τ_1 (ns)	0.5	0.5	0.5
A_2	6.4	7742.5	8779.0
τ_2 (ns)	50.0	50.0	50.0
χ^2	1.0	12.6	12.8
A_1	4083.6	43787.9	39669.3
τ_1 (ns)	0.5	0.5	0.5
A_2	4.7	4339.3	5077.5
τ_2 (ns)	80.0	80.0	80.0
χ^2	1.0	59.2	53.8

9.2 Interpretation of SAED Patterns

Table 23. Crystal facets of InP/$ZnSe_xS_{1-x}$/ZnS QDs interpreted from its SAED pattern.

1/*d* (1/nm)	1/*r* (1/nm)	*r* (nm)	*a* (Å)	hkl
6.552	3.276	0.3053	3.053	(111)
10.333	5.167	0.1936	1.936	(220)
12.328	6.164	0.1622	1.622	(311)

Table 24. Crystal facets of $Zn_{0.9}Mg_{0.1}O$ NPs interpreted from its SAED pattern.

1/*d* (1/nm)	1/*r* (1/nm)	*r* (nm)	*a* (Å)	hkl
6.8755	3.4378	0.2909	2.909	100
7.6545	3.8273	0.2613	2.613	002
10.3195	5.1598	0.1938	1.938	102
11.9235	5.9618	0.1677	1.677	110
13.1605	6.5803	0.1520	1.520	103
14.2125	7.1063	0.1407	1.407	200
18.239	9.1195	0.1097	1.097	203

9.3 Optical and Fluorescence Images

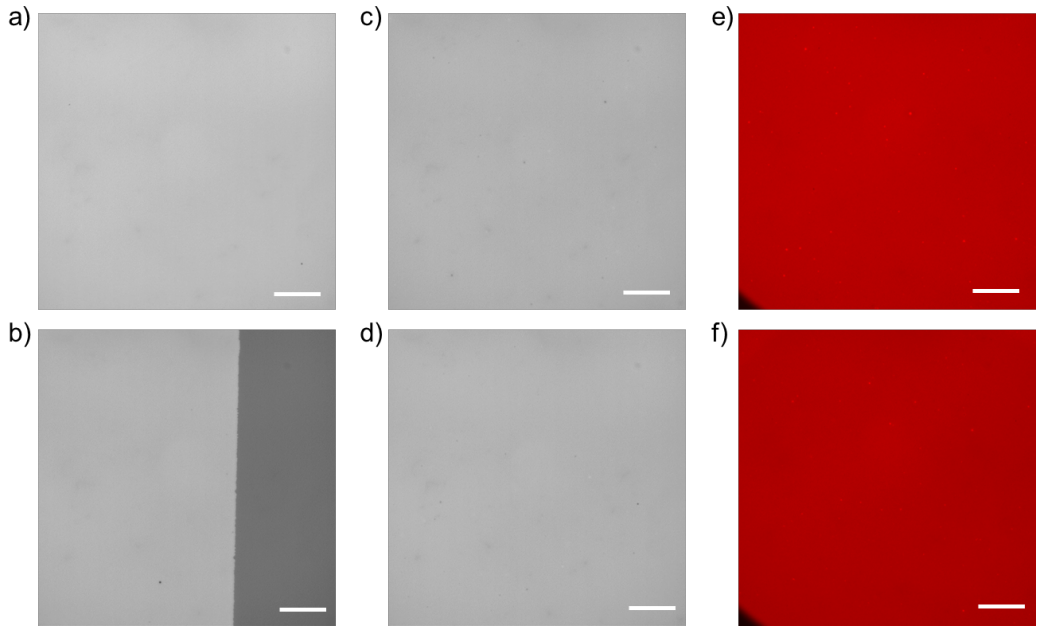

Figure 81. Optical images of a-b) cleaned ITO glass and c-d) PVK-coated ITO glass. e-f) Fluorescence images of spin-coated QDs on the PVK-coated ITO glass. Scale bars: 50 μm.

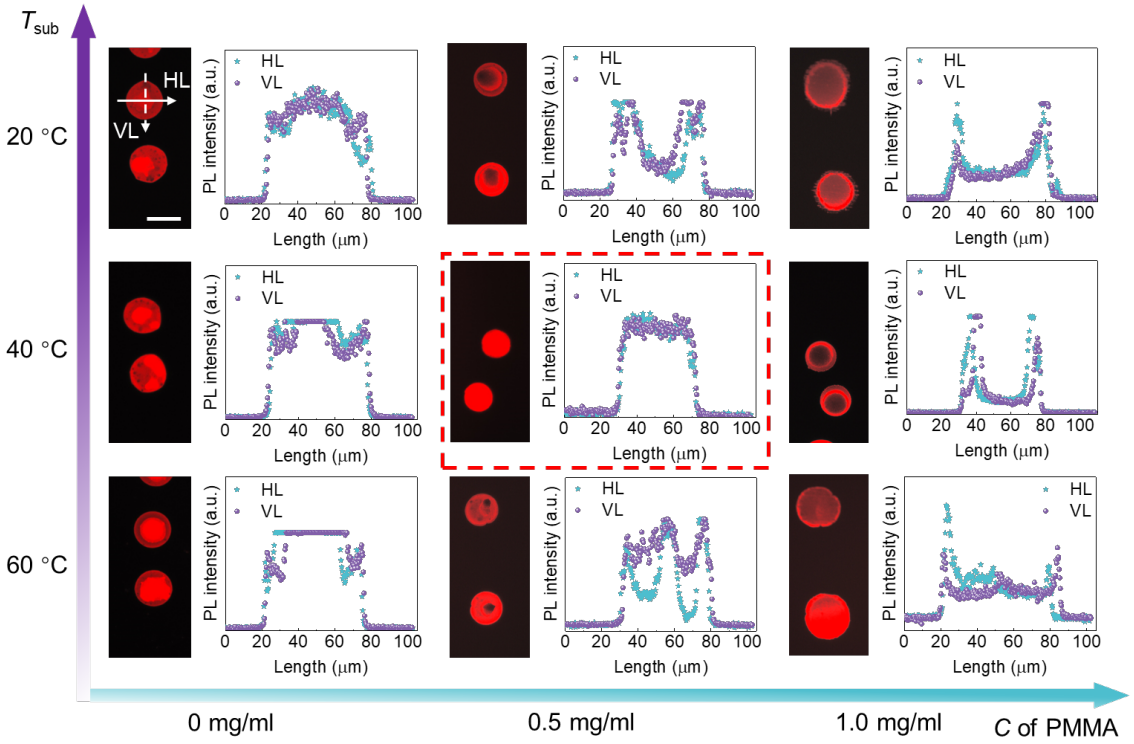

Figure 82. Fluorescence images and corresponding line profiles of patterns by printing the ink-10 with different concentrations of PMMA (8 kDa) at T_{sub} of 20 °C, 40 °C, and 60 °C. Scale bar: 50 μm. HL and VL indicate horizontal and vertical lines, respectively, passing through the center of the inset spot.

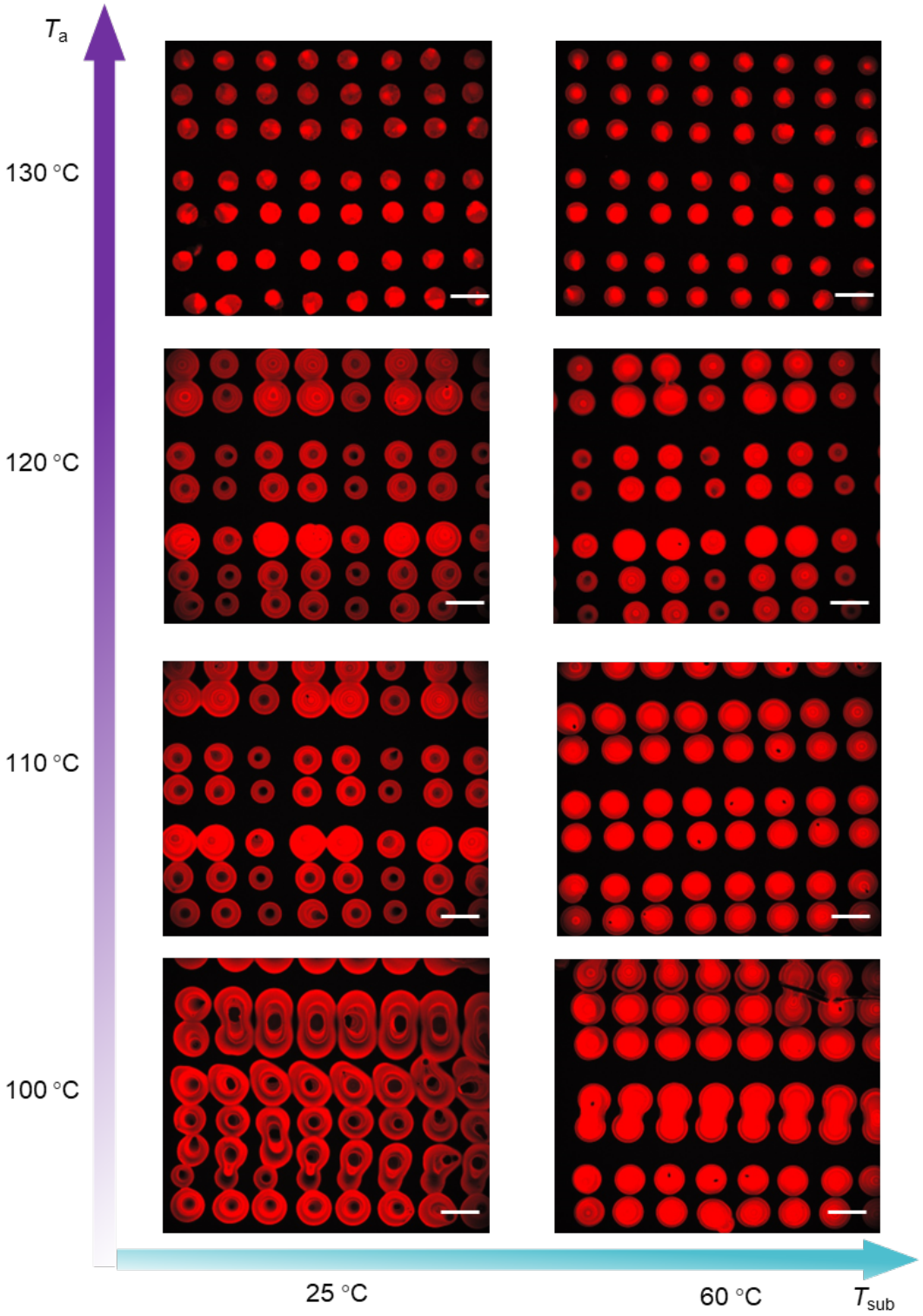

Figure 83. Fluorescence images of inkjet-printed circular patterns by printing the ink-10 with different T_{sub} and annealing temperatures (T_a). Scale bars: 100 μm.

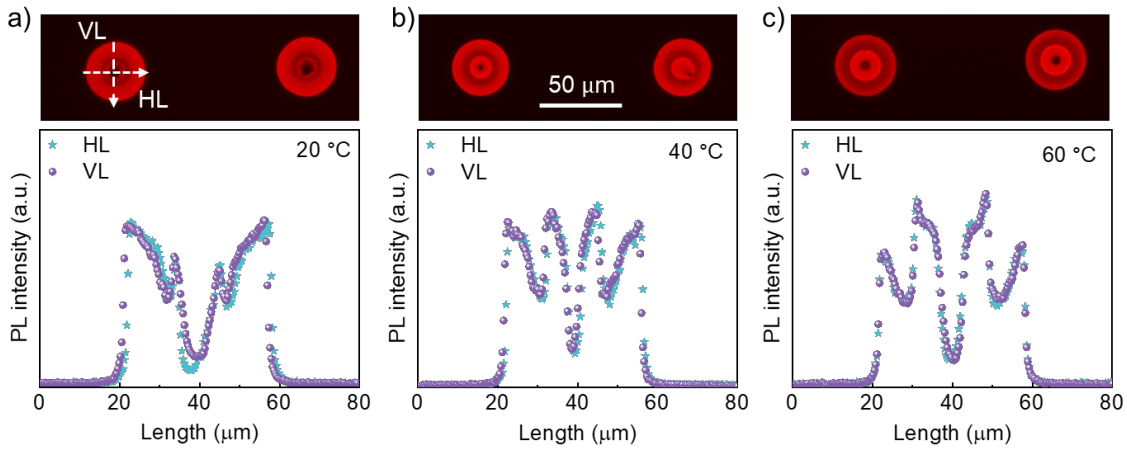

Figure 84. Fluorescence images and corresponding line profiles of patterns by printing the ink-20 at different T_{sub} on the PVK/glass substrate that was pre-wetted by the ink solvents. HL and VL indicate horizontal and vertical lines, respectively, passing through the center of the inset spot. Scale bar: 50 μm.

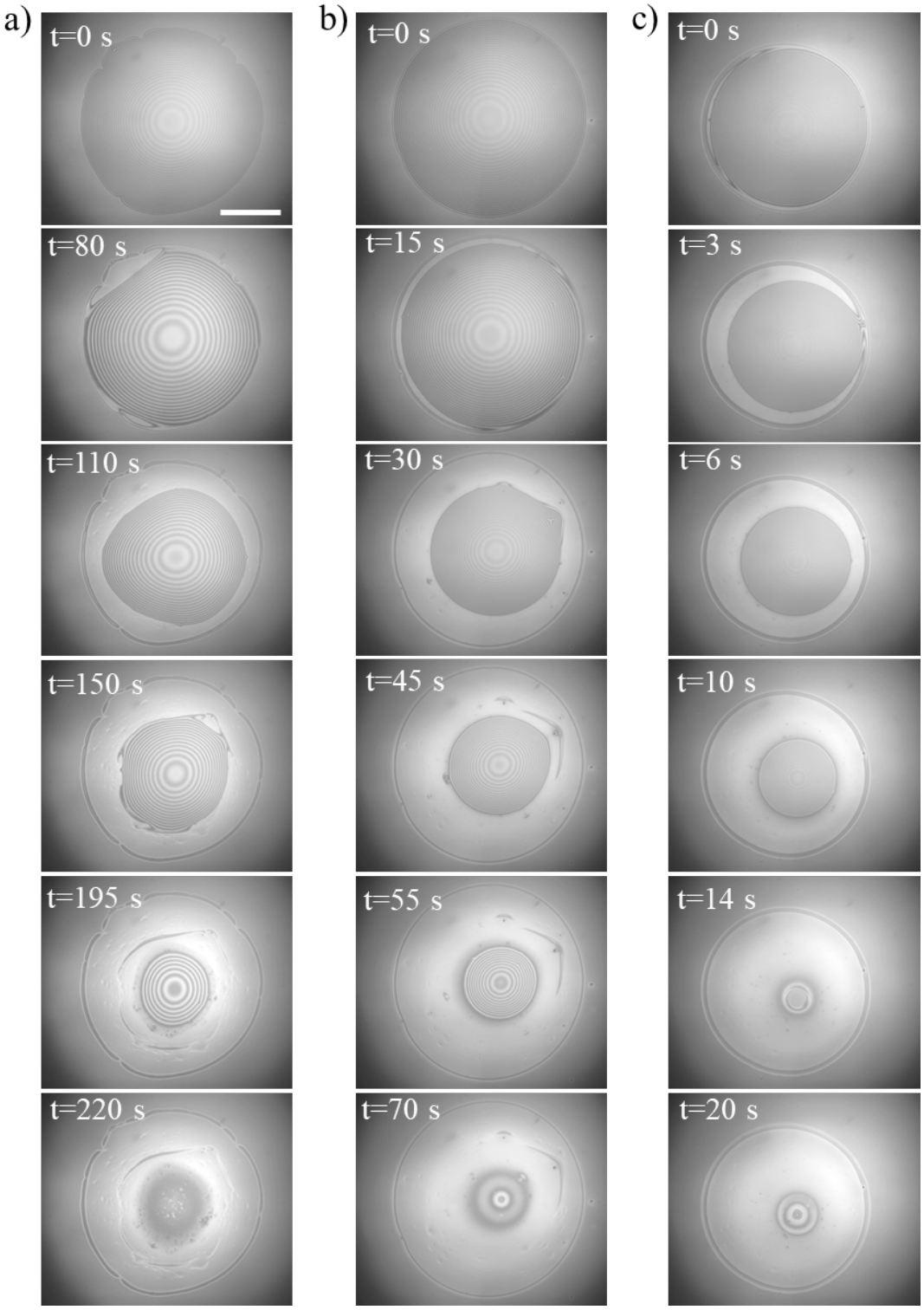

Figure 85. Optical images of the ink-20 droplets dried on PVK films at a) 20 °C, b) 40 °C, and c) 60 °C over time.

9.4 SE Data of Functional Materials

a)

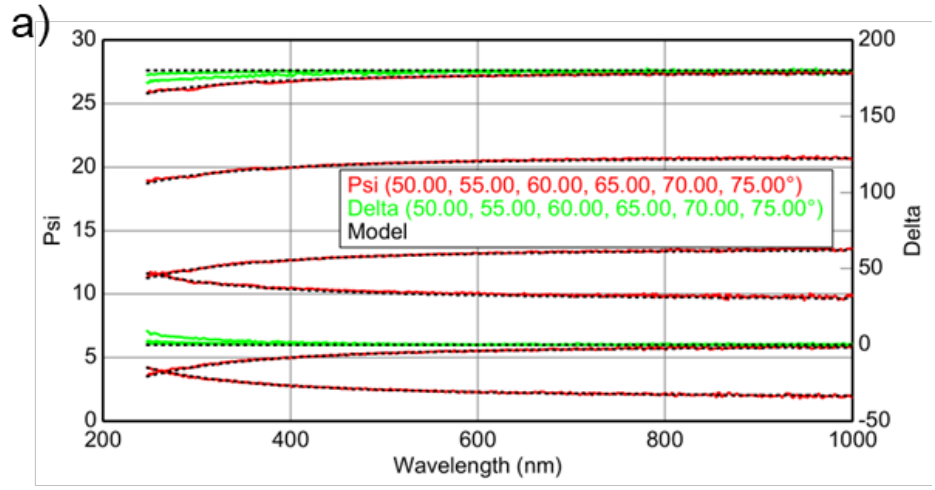

b)

Include Surface Roughness = OFF

- Substrate = Cauchy Substrate Thickness = 1.0000 mm
  A = **1.493** (fit) B = **0.00553** (fit) C = 0.0000
  + **Urbach Absorption Parameters**

- **MODEL Options**
  Angle Offset = 0.00
  Include Substrate Backside Correction = ON
  Transmission SE Data = OFF Reverse Direction = OFF
  # Back Reflections = 0.00
  % 1st Reflection = 100.00
  Model Calculation = Ideal

Figure 86. a) SE spectra of glass slides fitted with the Cauchy model. b) Fitting results (A, B, and C) of glass slides.

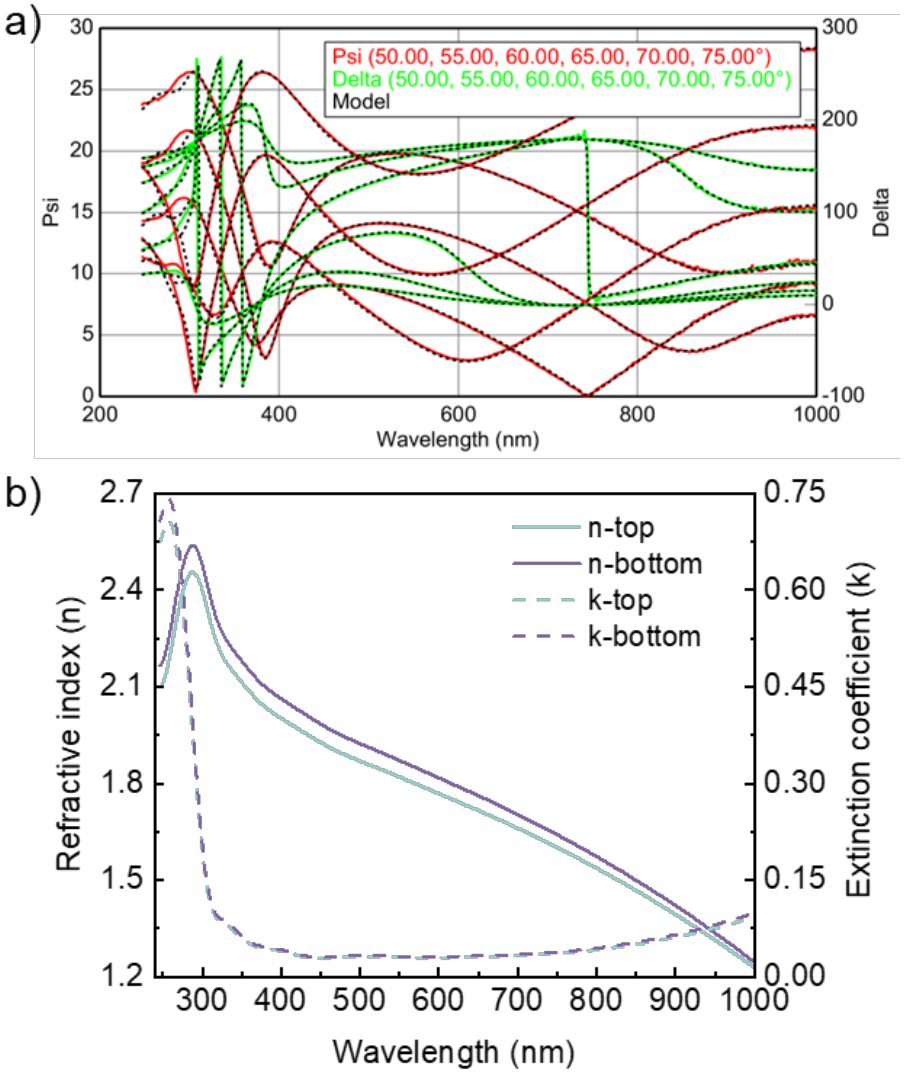

Figure 87. a) SE spectra of ITO films fitted with the B-spline model. b) Fitted refractive index of ITO films.

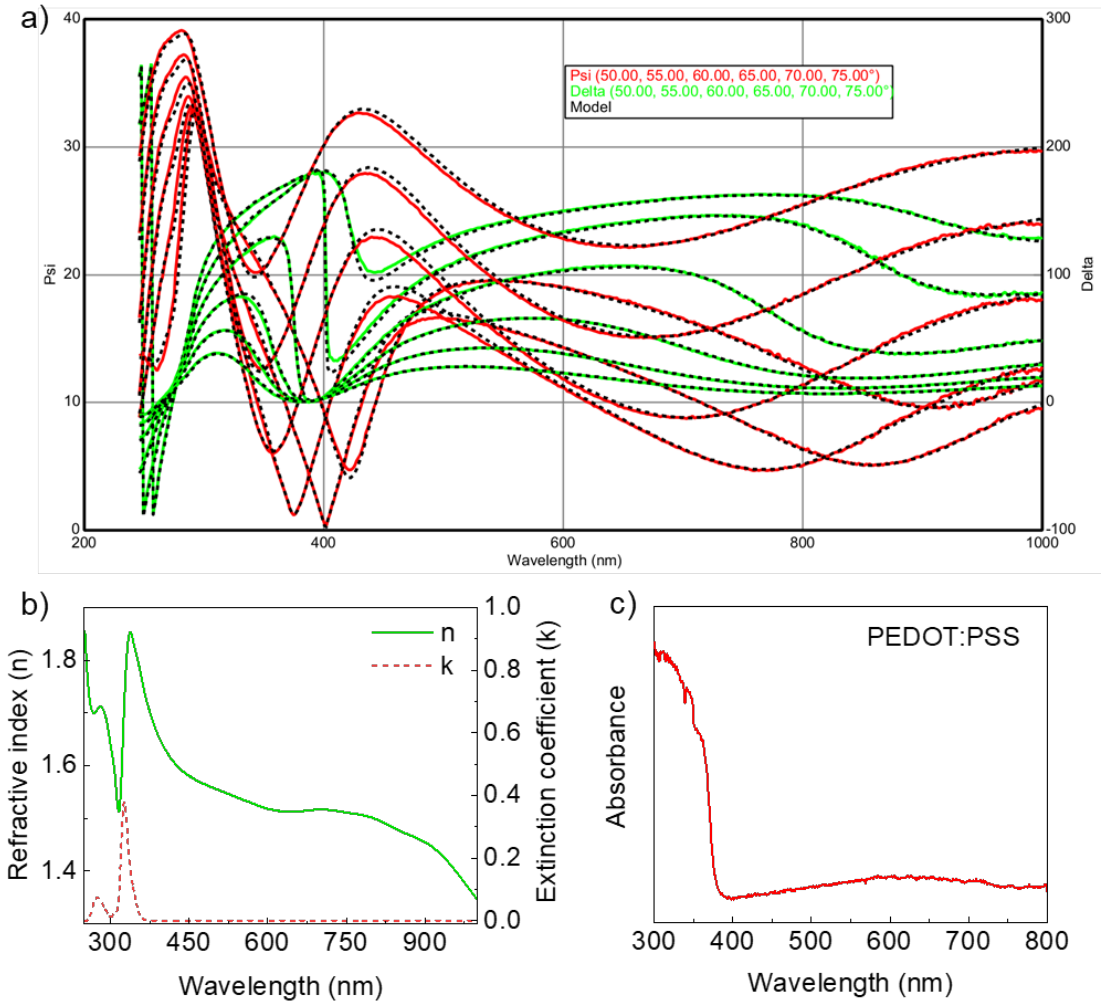

Figure 88. a) SE spectra of PEDOT:PSS films fitted with the Tauc-Lorentz model. b) Fitted refractive index of PEDOT:PSS films. c) Absorbance of PEDOT:PSS dispersion.

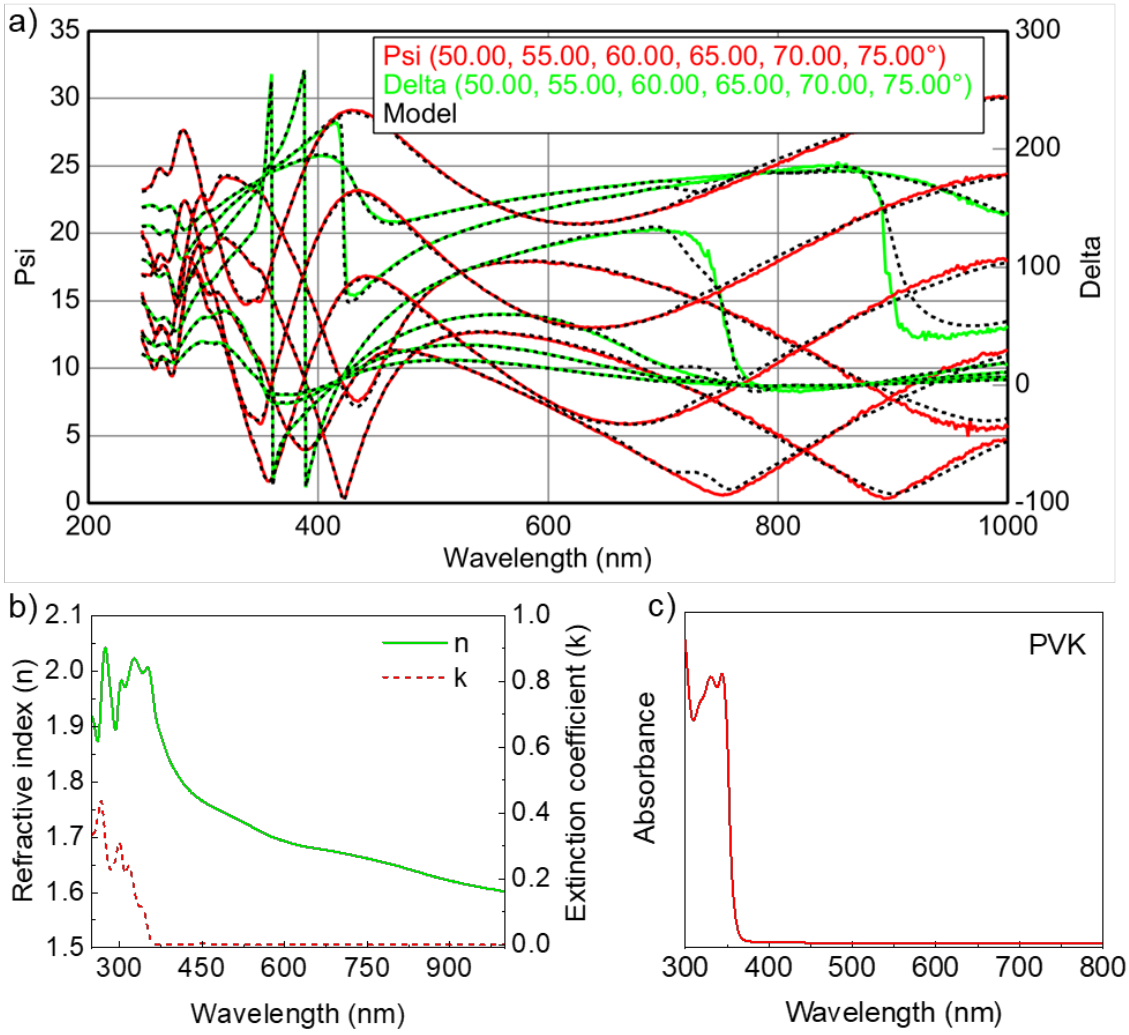

Figure 89. a) SE spectra of PVK films fitted with the Tauc-Lorentz model. b) Fitted refractive index of PVK films. c) Absorbance of PVK solution.

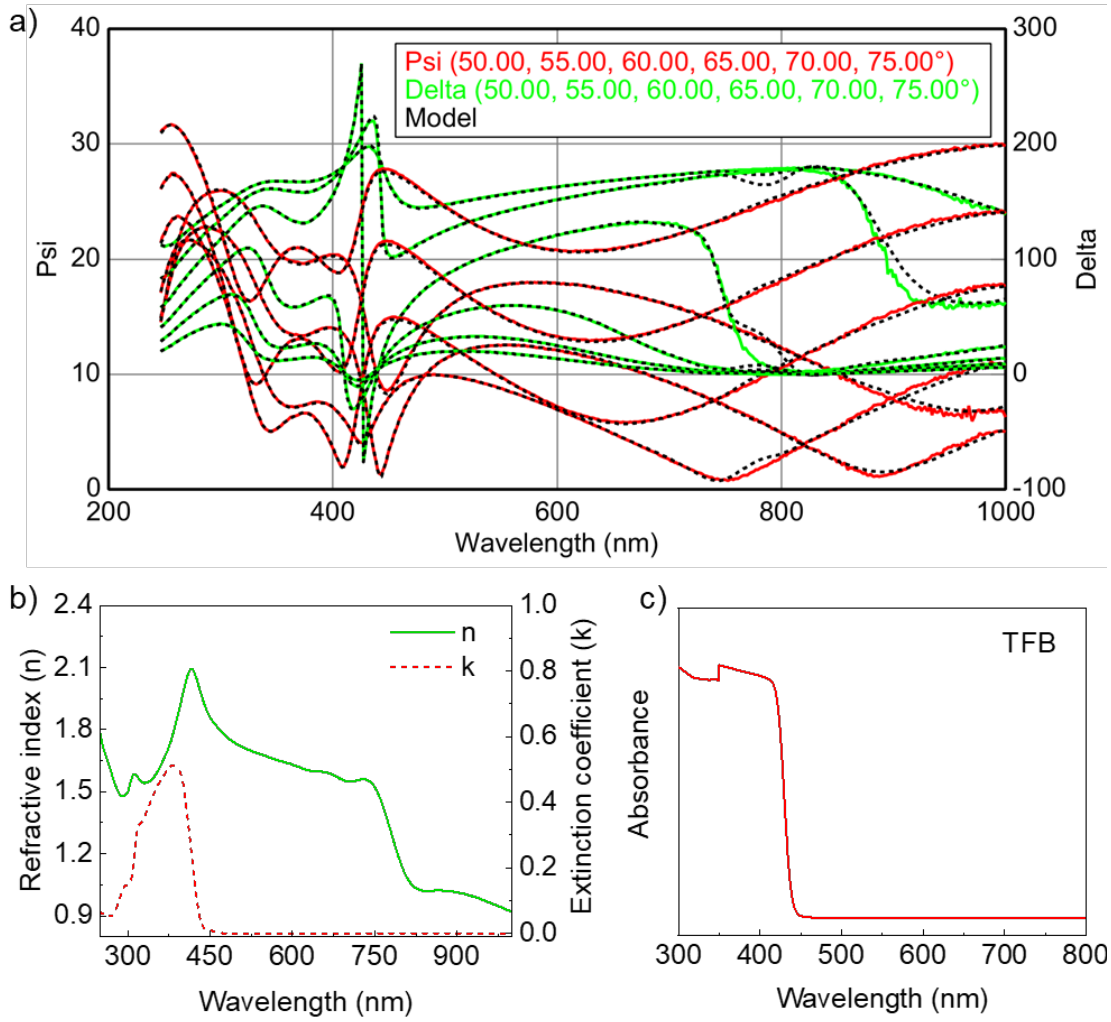

Figure 90. a) SE spectra of TFB films fitted with the Tauc-Lorentz model. b) Fitted refractive index of TFB films. c) Absorbance of TFB solution.

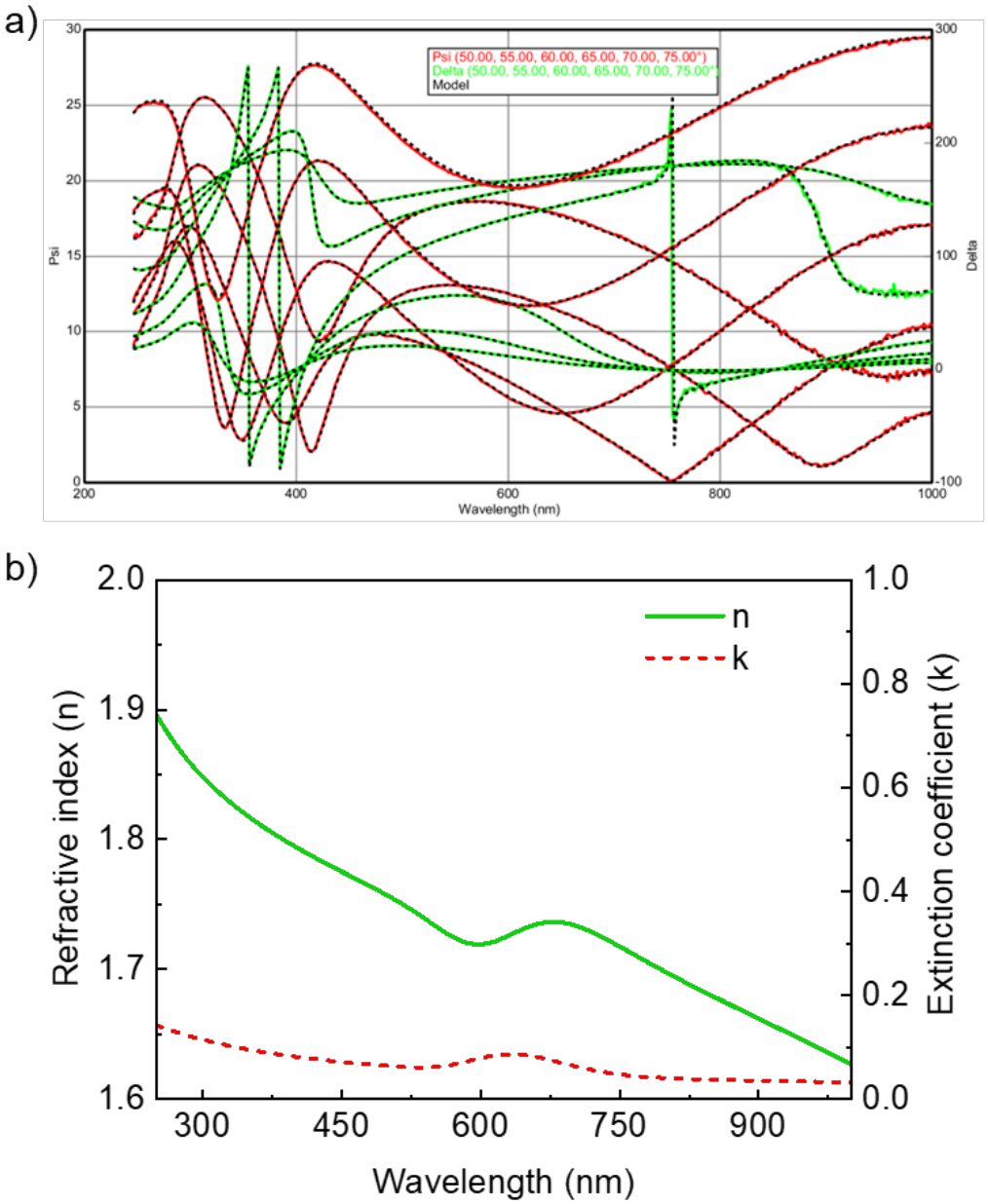

Figure 91. a) SE spectra of QD films fitted with the Tauc-Lorentz model. b) Fitted refractive index of QD films.

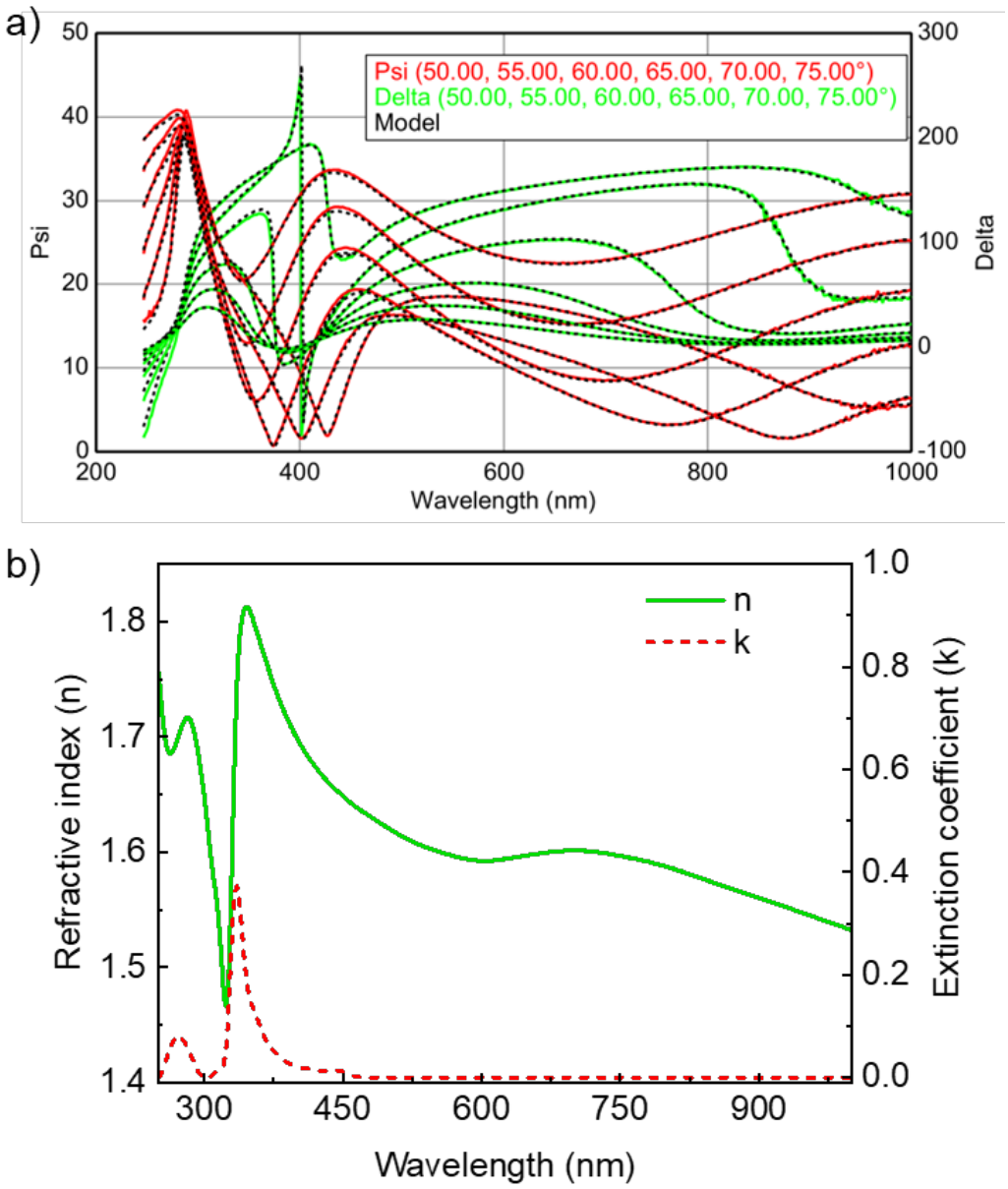

Figure 92. a) SE spectra of $Zn_{0.9}Mg_{0.1}O$ films fitted with the Tauc-Lorentz model. b) Fitted refractive index of $Zn_{0.9}Mg_{0.1}O$ films.

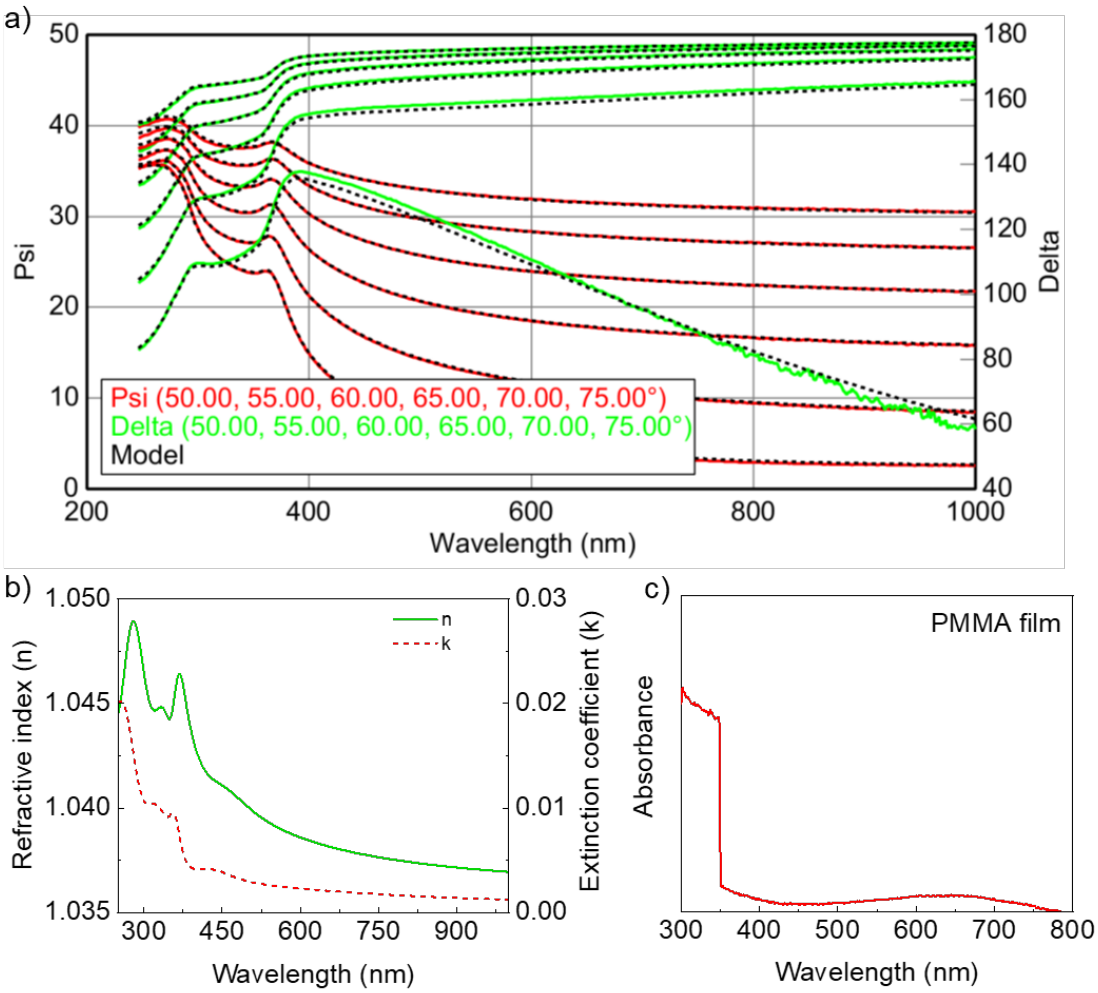

Figure 93. a) SE spectra of PMMA films fitted with the Tauc-Lorentz model. b) Fitted refractive index and c) absorbance of PMMA films.

9.5 Stability of Inks Under Ambient Atmosphere

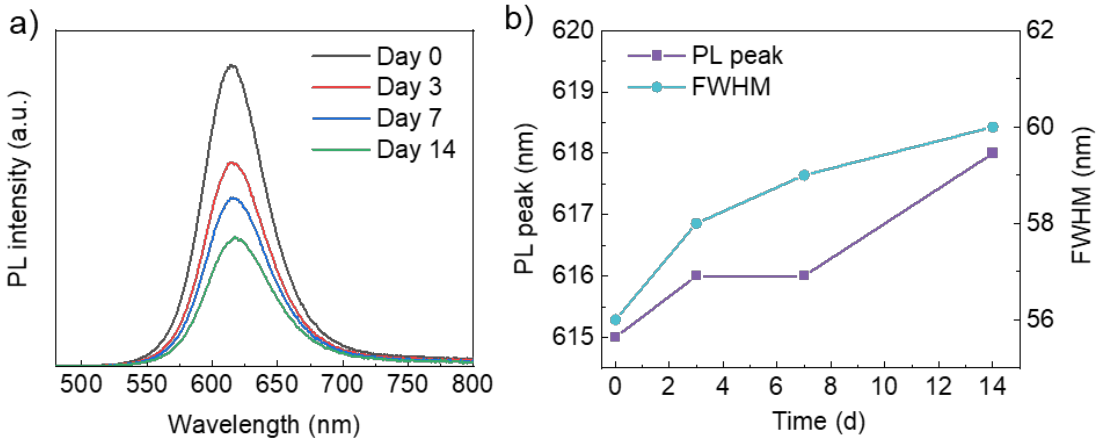

Figure 94. a) PL emission spectra and corresponding b) PL peaks and FWHM of the ink-10 under ambient atmosphere over time.